Tailoring Tunable Interactions in Superconducting Circuits Using Many to No Modes

Thesis by
Gihwan Kim

In Partial Fulfillment of the Requirements for the
Degree of
Doctor of Philosophy

CALIFORNIA INSTITUTE OF TECHNOLOGY
Pasadena, California

2026
Defended March 27, 2026

Gihwan Kim
ORCID: 0009-0009-3695-8118

ACKNOWLEDGEMENTS

7 years! I still remember my first visit to Caltech almost exactly seven years ago, during the visit days. I was very lucky to catch some cloudy days in Pasadena. At the time, I did not expect that by the end of this journey I would have spent more years in the United States than in Korea as an adult.

I would like to begin by thanking my advisor, Prof. Oskar Painter. This journey would not have been possible without your endless support. In my first year, I was a nervous international student who could barely speak English and had very limited knowledge. In retrospect, I clearly had little idea what I would work on or even what I was talking about. And yet, I felt secure because you welcomed me into your group. I always sensed enormous patience and support from you. That trust, and later the recognition of my work, encouragement, and advice you gave me over the years meant a great deal to me and gave me the confidence to grow further as a scientist.

I would like to express special gratitude to my colleague Andreas Butler. We joined the same group in the same year, shared the same offices, took the same courses, worked on the same projects, had the same mentor, and even used the same model of laptop for most of those years. I am so proud that we managed to remain indistinguishable particles for so long. It has been a great fortune to have one of my best friends also be my closest colleague in the lab, and someone who happens to be one of the nicest people I have known. I learned a great deal from you, not only about science, but also about having a broader view of life, ethics, maintaining balance, and of course, English.

I owe special thanks to our mighty mentor, Vinicius Ferreira. I wish I could have made the certificate of mentorship I gave you bigger and shinier. You literally carried us from our very first day and throughout the pandemic, all while working toward your own graduation. Several years after your graduation, it has become even clearer to me how influential your mentorship was in shaping my understanding, my way of thinking, and my enthusiasm for science. I also treasure the unforgettable memories we shared, and the feeling we had when we prayed for red dots and first saw the first cluster state. That is something money cannot buy.

Piero Chiappina, Sameer Sonar, Utku Hatipoglu, and Andreas Butler, the Painter group class of 2026, I want to thank you all for your friendship and for supporting

one another throughout this long PhD. It could not have been easy for all seven years, especially with the pandemic, but having friends with whom I can share this experience, at such a similar stage of life and career, was always a great source of comfort to me. We could ask silly questions, have serious discussions, and rebuild our understanding from the ground up together. This made the entire experience feel much less lonely and much more meaningful.

I was also fortunate to learn from the senior graduate students and postdocs. Eunjong Kim, thank you for showing the way as a Korean senior graduate student who had already walked many of the paths I might later take, and for showing the rigor and systematic approach to science. Xueyue (Sherry) Zhang, thank you for sharing your know-how, answering my silly questions, and offering an extra dose of physical intuition. Alex Hadley, thank you for boosting our productivity so much and for being so understanding when we struggled to explain what we wanted to implement. Mo Chen, I really appreciate the many times you listened to my questionable "new project ideas," gave thoughtful feedback, and tried to help us. Lucia De Rose, I deeply appreciate how much positivity you brought to us; I still miss that energy. Srujan Meesala, Steven Wood, and David Lake, thank you for showing such passion for science while always staying chill and approachable. I would also like to thank the SURF students I worked with, Alexander Deters and Alan Zhu, for trusting me and giving me the opportunity to solidify my knowledge.

I also want to acknowledge our technical staff member, Barry Baker, who always asks how I am doing, shares funny and positive words, and helps us whenever and wherever we need something. I would like to thank Matthew Davidson, Jamison Stevens, Olivia Pitcl, Bastien Bakker, Ricky Parada, John Parker, Sara Magdalena Gomez, and Parthorn Ammawat, who joined the group during the latter part of my PhD, for helpful discussions and lunch conversations. I would like to thank all Painter group staff, Angie Riley, Matthew McCoy, Brendon Larrowe, Chris Freestone, Trevor Nash, and Ewan Painter. I also thank APh staff, Jennifer N. Blankenship, Christy Jenstad, and Connie M. Rodriguez.

Outside of Caltech, I also want to thank wonderful people I encountered during my PhD. Or Golan, Prof. Alexey Gorshkov, and Prof. Alex Retzker, thank you for all the discussions and thoughtful science in our long-range collaboration on long-range connectivity. I thank Michal Goldenshtein, Kevin Villegas, and Chun-Ju Wu at Quantum Machines for their technical help. I also want to express my gratitude to the people I met at conferences for sharing physics, ideas, and insights.

A PhD consists not only of research, but also of the ordinary experience of living as a human being. I am especially grateful to Caltech's Korean community, my dispersed SNU ECE friends in the United States and Korea, my Berkeley EECS friends, P-orbi, the Watson Boys, and the Free Radicals softball team for filling my life with joy and encouragement.

Finally, I want to thank my family for their endless love and support. To my parents, Giosig Kim and Geumye Shin, I cannot express enough how much unconditional love I have received from you. That love has become one of the strongest pillars in my life, and because of it I always feel grounded. Thank you for bringing me into this world and raising me with the curiosity to enjoy and explore it. To my sisters, Jiyoung Kim and Minyoung Kim, who came into the world 11 and 10 years before I did, thank you for being the best babysitters in my childhood and for giving me another layer of unconditional love. I was fortunate to receive realistic advice from those only a half generation ahead of me, which helped me prepare for the future. Thanks to you all, I am so lucky to be an uncle to my wonderful nieces and nephews, Juwon Lee, Jua Park, Seoa Park, and Seowon Lee.

ABSTRACT

Tunable couplings are a central requirement for scalable quantum processing with superconducting quantum circuits. Practical quantum processors must dynamically reconfigure their interaction landscape to accommodate different quantum operations, including idle, single-qubit gates, two-qubit gates, readout, and reset, while maintaining high coherence and suppressing spurious couplings. While widely used tunable interaction approaches rely on single-mode mediation, they are often constrained by nearest-neighbor connectivity, limited on-off ratios, and stringent requirements on qubit frequency allocation.

This thesis develops and studies novel strategies for tailoring tunable interactions by moving beyond single-mode mediation, spanning multimode engineered interactions and modeless interaction schemes ("many to no modes"), while accounting for realistic constraints in superconducting hardware. Using a microwave metamaterial waveguide realized by coupled resonator arrays, I demonstrate tunable dissipative interactions that allow on-demand, fast, and high switching-ratio photon emission from a transmon used as a multi-level quantum emitter. This capability is leveraged to achieve deterministic generation of multidimensional photonic cluster states, as well as unconditional reset and leakage reduction of frequency-tunable superconducting qubits.

Complementary to these multimode dissipative tunable interactions, this thesis also introduces architectures that realize tunable interactions mediated by many coherent modes or by no mediating modes. I discuss a long-range interaction scheme between superconducting dual-rail qubits mediated by spatially extended eigenmodes of a coupled-resonator array bus. Finally, I propose and analyze a novel modeless coupling architecture based on a SQUID coupler which provides intrinsic cross-Kerr interactions, enabling fast, hybridization-free CZ gates for far-detuned pairs, and discuss its implications for miniaturization of superconducting quantum processors.

PUBLISHED CONTENT AND CONTRIBUTIONS

[1] G. Kim, A. Butler, and O. Painter. "A Tunable, Modeless, and Hybridization-free Cross-Kerr Coupler for Miniaturized Superconducting Qubits". In: *arXiv preprint* (2026). DOI: 10.48550/arXiv.2602.03186.
G.K. came up with the concept, performed mathematical and numerical analysis, and wrote the manuscript.

[2] G. Kim, A. Butler, V. S. Ferreira, X. Zhang, A. Hadley, E. Kim, and O. Painter. "Fast unconditional reset and leakage reduction of a tunable superconducting qubit via an engineered dissipative bath". In: *Phys. Rev. Appl.* 24 (1 July 2025), p. 014013. DOI: 10.1103/6wc6-78y3.
G.K. came up with the concept and planned the experiment, performed the measurements, analyzed the data, and wrote the manuscript.

[3] V. S. Ferreira, G. Kim, A. Butler, H. Pichler, and O. Painter. "Deterministic generation of multidimensional photonic cluster states with a single quantum emitter". In: *Nat. Phys.* 20.5 (2024), pp. 865–870. DOI: 10.1038/s41567-024-02408-0.
G.K. participated in developing key concepts, planning the experiment, and design and nanofabrication of the device. G.K. performed the measurements, analyzed the data, and participated in the writing of the manuscript.

TABLE OF CONTENTS

LIST OF ILLUSTRATIONS

LIST OF TABLES

Chapter 1

INTRODUCTION

Quantum mechanics provides an exceptionally accurate description of nature when the energy scales are sufficiently low and the physical degrees of freedom are confined to microscopic dimensions [1–10]. Beyond its explanatory power, this realization naturally raises a complementary question: can quantum systems be deliberately engineered to model physical processes and provide practical utility stemming fundamentally from their quantumness? Such an idea was articulated by Richard Feynman in the early 1980s [11]. Since then, quantum information science has developed the perspective that certain physical processes and computational tasks may be most naturally and efficiently addressed using quantum hardware, such as quantum computers and quantum simulators [12, 13], rather than through indirect mappings onto classical binary architectures. Strikingly, it was subsequently discovered that some problems admit substantial computational speedups on quantum computers compared to their best-known classical counterparts, including integer factorization [14], black-box search [15], and linear algebraic problems [16].

At the same time, significant progress over the past several decades has been made in understanding and achieving precise control over microscopic quantum systems, reinforcing the prospect of realizing the advantages discussed above. A wide range of physical platforms, including optical lattices, trapped ions, semiconductor quantum dots, neutral atom arrays, and superconducting quantum circuits, have demonstrated a high degree of experimental control, each with distinct strengths and limitations [17–26].

However, the intrinsic fragility of quantum states and the difficulty of scaling coherent control to large systems impose significant challenges across all platforms, necessitating carefully designed strategies. Central among these challenges is establishing fault-tolerance, which is substantially more demanding than in classical information processing systems [27–33]. In addition, systematic engineering concepts such as hierarchical abstraction, modularity, and design automation, which have been critical to the success of modern technologies, for example, very large-scale integrated (VLSI) circuits [34–39], have not yet been clearly formulated and broadly demonstrated in quantum hardware.

Among the various platforms aimed at tackling such challenges, circuit quantum electrodynamics (circuit QED) based on superconducting quantum circuits is particularly attractive because of their strong light-matter interactions and relatively low decoherence, enabling fast and accurate quantum operations [21, 40]. The solid-state and engineered nature of superconducting circuits allows their properties to be readily designed and fabricated. Moreover, the existence of simple qubit designs and interaction schemes has provided easy understanding and engineering of the system [41–47]. These features have led to significant experimental progress, including demonstrations of many-body quantum simulators, multi-qubit processors, and quantum error correction experiments [48–53]. In the following, I briefly review superconducting quantum circuits and define the scope of this thesis.

Superconducting quantum circuits

Superconductivity enables the flow of persistent currents with effectively zero electrical resistance [54, 55]. As a result, superconducting circuits can support bosonic resonators with exceptionally low dissipation, allowing long-lived quantum states. Moreover, the presence of Josephson junctions and fluxoid quantization introduces non-dissipative nonlinearities, making it possible to engineer artificial atoms with tailored energy-level structures [24, 26, 56, 57]. These features have enabled the discovery of extremely simple qubit designs and control principles [41, 58].

One of the key requirements for advancing superconducting quantum processors is achieving both coherent and dissipative control of qubits. The coherence times of superconducting qubits have steadily grown due to efforts to improve qubit design and material properties, achieving coherence times exceeding a millisecond and stabilization of high coherence [59–65]. Single-qubit gates continue to achieve close to coherence-limits, with infidelities below 10^{-4} [66, 67]. Dispersive readout of superconducting qubits has also crossed the error correction threshold with improvements in readout speed and suppression of spurious measurement-induced state transitions [46, 68–71]. These accomplishments have led to experimental demonstrations towards low physical error rates and scalable integration [52, 53, 72–75].

Interaction design is as central as qubit design

Despite the substantial progress achieved in superconducting quantum circuits, several core components, including qubits, couplers, and readout architectures, still require improvement at both the fundamental and engineering levels to achieve

performances on a utility scale [76, 77]. Central to many of these challenges is the manner in which interactions are generated and controlled among qubits, resonators, and waveguides. This is because interaction schemes can expose quantum processors to unintended couplings, additional decoherence channels, and physical constraints that may limit the quantum hardware's performance regardless of how coherent individual qubits may be [42, 78–81]. In addition, such interactions must be fast tunable *in situ*, as various quantum operations, such as idle, single-qubit gate, readout, reset, and two-qubit gate, require distinct operating conditions that are not usually compatible with each other [82, 83].

Existing approaches have predominantly relied on tunable couplings mediated or tailored by a single bosonic mode, a strategy that has been successfully employed in microwave quantum optics experiments and in elementary quantum operation primitives such as two-qubit gates and qubit reset [44, 47, 84]. However, the increasing demands of larger and more complex quantum systems, such as reducing leakage errors, allowing more operating frequencies, and enabling long-range connectivity, call for novel interaction schemes [84–86]. At the same time, candidate interaction schemes should also be compatible with scaling strategies, such as tilability, maintaining low crosstalk, mitigating frequency crowding and collisions, and keeping qubit coherences high [60, 87–90]. These new engineering challenges motivate the exploration of alternative interaction schemes that extend beyond single-mode mediation.

Contribution and outline of the thesis

In this thesis, motivated by the aforementioned challenges, I investigate richer tunable interaction schemes based on either many bosonic modes or effectively no explicit bosonic modes, with the goal of expanding the performance and operational capabilities of superconducting quantum circuits.

The outline of the thesis is as follows. First, in Chapter 2, I provide background on tunable dissipative and coherent interactions and outline capabilities that extend beyond those accessible with single-mode-mediated interaction schemes.

In Chapter 3, I present an implementation of tunable dissipative interactions using a structure called a metamaterial waveguide (MMWG), which consists of many bosonic modes forming a narrow passband. When coupled to a qutrit quantum emitter implemented as a transmon, this system enables on-demand frequency-selective qutrit-waveguide coupling for single-photon emission and qubit-photon interactions.

The narrow passband of the MMWG provides much stronger frequency-selectivity in emission rate than what is possible with existing single-mode-mediated approaches, which typically entails a long-tailed Lorentzian lineshape. This capability is leveraged to deterministically generate two-dimensional photonic cluster states with only a single quantum emitter. The results in this chapter are published in [91].

In Chapter 4, I demonstrate fast unconditional reset and leakage reduction of a flux-tunable superconducting qubit with state-of-the-art performance, enabled by tunable dissipative interactions mediated by many bosonic modes. By employing a broadband MMWG, rather than the narrowband MMWG used in Chapter 3, simultaneous reset of multiple excited states of a transmon is achieved, thereby suppressing error propagation caused by excitations shelved in higher excited states. By introducing frequency selectivity into this scheme, selective reset of higher excited states while preserving the qubit subspace, referred to as a leakage reduction operation, is realized. The results in this chapter are published in [92].

In Chapter 5, I discuss how simultaneous long-range tunable interactions can be achieved using multiple coherent bosonic modes. By leveraging a coupled-resonator array bus (CRAB) and their orthogonal long-range eigenmodes, multiple long-range interactions can exist simultaneously without allowing fundamental crosstalk channels. In this context, we use dual-rail transmons to eliminate unwanted static interactions, highlighting the interplay between qubit design and interaction schemes. An implementation strategy and design considerations are presented. This chapter is based on an ongoing collaboration with external collaborators, a manuscript in preparation [93], and materials presented in [94, 95].

In Chapter 6, I present a galvanic interaction scheme based on superconducting quantum interference device (SQUID) couplers. Such couplers enable tunable, modeless, and hybridization-free cross-Kerr coupling, which can be used for implementing controlled-Z (CZ) gates. In addition, I discuss design strategies for fully miniaturized quantum processors using merged-element transmons. The results in this chapter have been posted as a preprint [96].

Taken together, this "many to no modes" framing of the thesis reflects the broader perspective that the interaction design space for superconducting quantum circuits remains rich with unexplored possibilities. The chapters that follow explore each direction, with the shared goal of expanding the toolkit available to superconducting quantum processors.

Chapter 2

TUNABLE INTERACTIONS IN SUPERCONDUCTING CIRCUITS

2.1 Tunable dissipation engineering for superconducting qubits

Although quantum systems must remain coherent, controlled dissipation plays an essential role in transferring and extracting information from quantum systems. A representative example is a superconducting qubit used as a single photon emitter, which provides a platform for microwave quantum optics, quantum communication, and measurement-based quantum information processing [97–100]. In such a system, a superconducting qubit is coupled to a waveguide that supports propagating microwave photons, enabling the controlled transfer of quantum information from the localized qubit to an itinerant photon. Such systems, in which quantum emitters interact with propagating modes of a waveguide, are studied within the framework of waveguide quantum electrodynamics (waveguide QED) [101–103].

At the same time, it is necessary to preserve the nonclassical character of the qubit prior to photon emission, which arises from the intrinsic nonlinearity of the qubit (e.g., anharmonicity). If the qubit is continuously strongly damped by the waveguide, as illustrated in Fig. 2.1a, excitations can leave the qubit element almost immediately. Consequently, the system dynamics are dominated by the linear waveguide modes, and the system response becomes increasingly similar to that of a linear resonator. In contrast, if the damping of the qubit to the waveguide can be tuned *in situ*, the state preparation stage can be separated from the emitter-waveguide interaction steps. Such tunable dissipation enables the preparation of nonclassical states while still allowing efficient release of quantum information into the waveguide.

A natural way to engineer such *in situ* tunability in emitter-waveguide coupling is to introduce frequency selectivity in the interactions. However, typical microwave waveguides, such as coplanar waveguides (CPWs), support an extremely broad passband, spanning frequencies from near DC to tens of gigahertz. As a result, some portion of this continuum inevitably overlaps with the qubit transition frequency, leading to continuous strong damping of the qubit. Therefore, additional frequency selectivity must be introduced through engineered circuit elements.

A commonly used approach in superconducting quantum circuits is to insert a

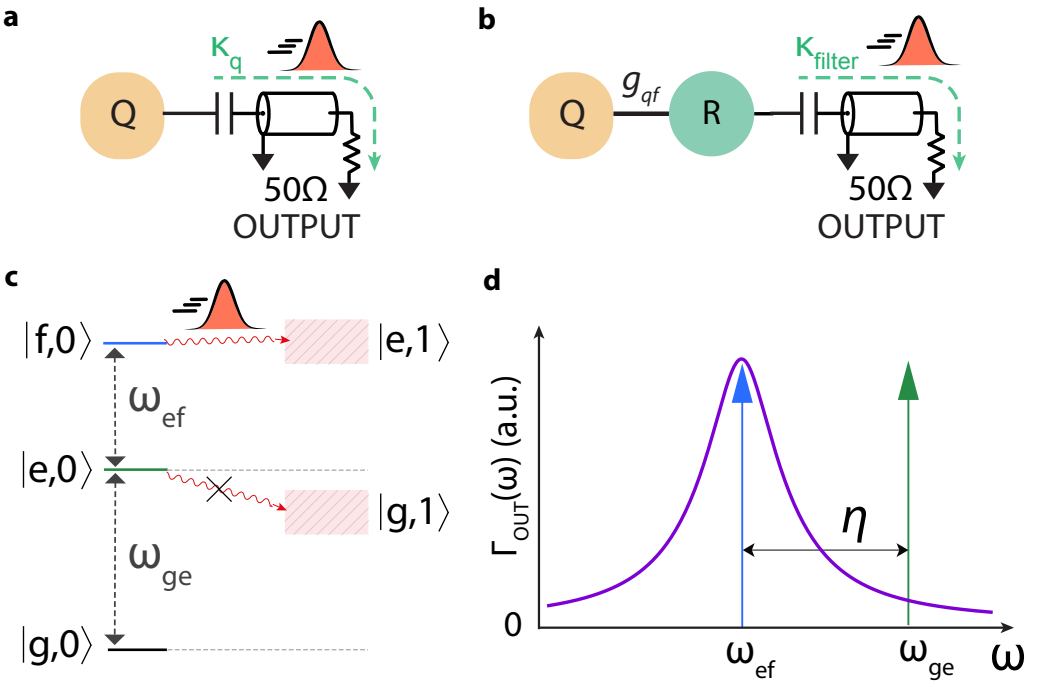

Figure 2.1: **Qubit as a single photon emitter.** **a**, Schematic of a qubit (orange, Q) coupled to output waveguide (50Ω OUTPUT), with a broadband emission rate κ_q into the output waveguide. **b**, Schematic of a qubit coupled to output waveguide filtered by an intermediate resonator mode R. **c**, Illustration of the spectral requirement for photon emission in the qubit-photon entanglement protocol described in the main text. **d**, Emission rate into the output waveguide as a function of frequency, shaped by the filter resonance.

microwave resonator or an auxiliary qubit ("coupler") between the qubit and the waveguide to act as a filter, as shown in Fig. 2.1b [42]. In this configuration, the qubit-like dressed eigenmode, which has participation of the filter mode, becomes the mode relevant for quantum information storage. Only the component of this dressed mode that resides in the filter mode couples directly to the environment. The hybridization between the qubit and the filter follows a Lorentzian response, which results in a Lorentzian spectral filtering of the density of states (DOS) seen by the qubit. This can be formulated as follows:

$$
\begin{aligned}
|\tilde{e}\rangle &= \sqrt{1-|c_{\text{filter}}|^2}|e,0\rangle + c_{\text{filter}}|g,1_f\rangle \\
\Gamma^{ge}_{\text{OUT}}(\omega_{ge}) &= |c_{\text{filter}}|^2\kappa_{\text{filter}} \approx \frac{g_{qf}^2}{\Delta^2 + \left(\frac{\kappa_{\text{tot}}}{2}\right)^2}\kappa_{\text{filter}},
\end{aligned}
\tag{2.1}
$$

where $|g\rangle$ and $|e\rangle$ denote the ground state and the first excited state of the qubit,

respectively. $|\tilde{e}\rangle$ is the dressed qubit-like excited state, $|i, j_f\rangle$ denotes the tensor product of the bare qubit state $|i\rangle$ and the bare filter state $|j_f\rangle$, and c_{filter} is the hybridization amplitude in the filter excitation in the dressed state. Γ^{ge}_{OUT} is the emission rate of the qubit $g-e$ transition into the output waveguide, and ω_{ge} is the qubit transition frequency. ω_{filter} is the resonance frequency of the filter, and $\Delta \equiv \omega_{ge} - \omega_{\text{filter}}$ is the qubit-filter detuning. κ_{filter} is the damping rate of the filter into the output waveguide, g_{qf} is the qubit–filter linear coupling rate, and κ_{tot} is the total linewidth of the filter including all decay channels. The approximation assumes the bad-cavity limit $g_{qf} \ll \kappa_{\text{tot}}$, where excitation transferred to the filter mode escapes into the waveguide before significant population builds up in the filter.

This can be viewed from the perspective of the local DOS of the waveguide seen by the qubit. The connection between eq.(2.1) and Fermi's golden rule can be written as

$$\begin{aligned} \Gamma^{ge}_{\text{OUT}}(\omega_{ge}) &= 2\pi g_{qf}^2 \rho(\omega_{ge}) \\ \rho(\omega_{ge}) &= \frac{1}{2\pi} \frac{\kappa_{\text{filter}}}{\Delta^2 + \left(\frac{\kappa_{\text{tot}}}{2}\right)^2}, \end{aligned} \tag{2.2}$$

where $\rho(\omega_{ge})$ is the DOS seen by the qubit at frequency ω_{ge}.

Such a filter provides a minimally functional emitter-waveguide system when combined with the tunability available in superconducting circuits. One approach is to exploit frequency tunability of qubits, which is typically realized by incorporating a SQUID composed of two Josephson junctions [41]. In flux-tunable transmons, an external magnetic flux threading the SQUID modifies the effective Josephson energy and consequently shifts the transition frequency of the transmon. During idle or state preparation, the qubit transition frequency can be tuned far away from the filter resonance so that the detuning is much larger than the filter linewidth, thereby suppressing emission into the waveguide. During the photon emission step, the qubit frequency can then be dynamically brought closer to the filter resonance, resulting in a strongly enhanced emission rate.

For typical quantum information processing, we aim to achieve low probability of errors by ensuring that the time required for individual operations is much shorter than the coherence time of the qubits. This requirement also applies to the emitter-waveguide or qubit-photon system, and motivates the use of the figure of merit known as the *cooperativity* of the emitter-waveguide system, analogous to atom-

cavity cooperativity in cavity QED framework [104]. Cooperativity quantifies how efficiently quantum information is emitted into the desired waveguide channel compared to other decay channels:

$$C \equiv \frac{\Gamma_{\mathrm{OUT}}}{\Gamma'}, \tag{2.3}$$

where Γ' represents the undesired decay rate, and Γ_{OUT} is the desired emission rate into the output waveguide. The cooperativity is directly related to the fidelity of the qubit-photon operations, as the typical error probability scales inversely with cooperativity.

It is important to note that $\Gamma_{\mathrm{OUT}}^{ge}$ at the idle or state preparation operating point should be included in Γ', since emission into the waveguide at this stage contributes to undesired decay. Therefore, the achievable cooperativity in the setup discussed above is given by

$$C = \frac{\max \Gamma_{\mathrm{OUT}}^{ge}}{\Gamma_{\mathrm{OUT}}^{ge}(\omega_0) + \Gamma_0'} < \frac{4\Delta_0^2}{\kappa_{\mathrm{tot}}^2}, \tag{2.4}$$

where ω_0 is the idle qubit frequency, and $\Delta_0 = \omega_0 - \omega_{\mathrm{filter}}$ is the corresponding detuning from the filter resonance, and Γ_0' is the qubit relaxation rate in the absence of coupling to the filter and waveguide. The inequality is obtained by setting $\Gamma_0' = 0$.

Eq. (2.4) implies that the qubit must be sufficiently detuned such that $\kappa_{\mathrm{tot}} \ll |\Delta_0|$. This upper bound on cooperativity therefore sets the minimum required detuning or, if the detuning is fixed while κ_{filter} is varied, establishes a trade-off between the maximum achievable emission rate and cooperativity. For instance, achieving a cooperativity on the order of 10^4 requires $|\Delta_0|/2\pi \approx 1$ GHz when $\kappa_{\mathrm{filter}}/2\pi \approx 20$ MHz that allows up to photon emission within tens of nanoseconds ($1/\kappa_{\mathrm{filter}} \approx 8$ ns), which is readily achievable in typical superconducting circuits.

However, even relatively basic quantum information processing protocols require spectral selectivity beyond what single–pole Lorentzian filtering can provide. A representative example is the generation of a qubit–photon entangled state while preserving a long-lived qubit storage state. In such a system, the emitter supports two distinct excited states: a radiative state that transfers excitation into the waveguide and a long-lived state that stores quantum information. Such a system can be realized by using a transmon as a three–level emitter, where the first excited state $|e\rangle$ serves as the storage state and the second excited state $|f\rangle$ as the radiative state. An example

protocol is as follows: The transmon is first prepared in an equal superposition of $|g\rangle$ and $|e\rangle$. The population in $|e\rangle$ is then transferred to $|f\rangle$. Finally, emission from $|f\rangle$ generates a photon in the waveguide, producing a qubit–photon entangled (GHZ) state. The process can be summarized as

$$|g\rangle|vac\rangle \xrightarrow{\text{prep}} (|g\rangle+|e\rangle)|vac\rangle \xrightarrow{\text{load}} (|g\rangle+|f\rangle)|vac\rangle \xrightarrow{\text{emit}} |g\rangle|vac\rangle+|e\rangle|1\rangle, \quad (2.5)$$

where $|vac\rangle$ denotes the vacuum of the waveguide and $|1\rangle$ is a Fock state of a collective mode of the waveguide. Normalization factors are omitted.

In such a protocol, it is important to protect the $g-e$ transition during emission from the $|f\rangle$ into the waveguide, as illustrated in Fig. 2.1c. Such state-selective decay is also useful for leakage reduction operations, where population in higher excited states is selectively removed without disturbing the computational subspace [85, 105, 106].

However, this removes the freedom to tune the detuning $\Delta_{ge} \equiv \omega_{ge} - \omega_{\text{filter}}$, since the $e-f$ transition frequency ω_{ef} must be close to ω_{filter} to enable photon emission. In this situation, the relevant cooperativity can be defined as the ratio between the desired emission from the $e-f$ transition and the unwanted emission from the $g-e$ transition. Assuming no other loss channels, this gives

$$C = \frac{\Gamma^{ef}_{\text{OUT}}(\omega_{ef})}{\Gamma^{ge}_{\text{OUT}}(\omega_{ge})} = 2\frac{\Delta_{ge}^2 + \left(\frac{\kappa_{\text{tot}}}{2}\right)^2}{\Delta_{ef}^2 + \left(\frac{\kappa_{\text{tot}}}{2}\right)^2} \approx \frac{8\eta^2}{\kappa_{\text{tot}}^2}, \quad (2.6)$$

where $\Delta_{ef} = \omega_{ef} - \omega_{\text{filter}}$, $\eta \equiv \omega_{ef} - \omega_{ge}$ is the transmon anharmonicity, and the approximation assumes $\Delta_{ef} \approx 0$ and $\kappa_{\text{tot}} \ll |\eta|$. The factor of two originates from the $\sqrt{2}$ enhancement of the linear coupling associated with the second-excitation matrix elements.

Thus, achievable cooperativity is already limited by the anharmonicity and the filter linewidth, leaving little room for further improvement in cooperativity. Moreover, the $|e\rangle$ state is subject to the long tail of the Lorentzian as shown in Fig. 2.1d. For a typical transmon anharmonicity of $\eta/2\pi \approx -200$ MHz, achieving a cooperativity on the order of 10^4 requires $\kappa_{\text{tot}}/2\pi \approx 5$ MHz ($1/\kappa_{\text{tot}} \approx 32$ ns). Furthermore, anharmonicity of a transmon is typically constrained in order to suppress sensitivity to charge noise, leaving the filter linewidth κ_{tot} as the primary remaining tuning knob. Since κ_{tot} sets the maximum achievable photon emission rate, this imposes a significant limitation.

2.1.1 Shaping qubit relaxation with a metamaterial waveguide

The limitations imposed by single-pole Lorentzian filtering can be overcome by implementing stronger spectral filtering using a multimode structure. For example, consider the tight-binding waveguide illustrated in Fig. 2.2 where a flux-tunable transmon is coupled to one end of a coupled resonator array. Such a structure is referred to as a coupled-resonator-array metamaterial waveguide, or simply a *metamaterial waveguide* (MMWG) in this thesis [107, 108]. A MMWG is a one-dimensional array of microwave resonators with nearest-neighbor coupling, where all resonators share the same resonance frequency and a uniform hopping rate, as shown in Fig. 2.2a. Such a structure can be simply implemented by superconducting circuits with the circuit schematic shown in Fig. 2.2b, and will be discussed in Chapter 3. The Hamiltonian of the system is given by

$$\begin{aligned}\hat{H}_{q-MMWG} =&\omega_q \hat{q}^\dagger \hat{q} + \frac{\eta}{2}\hat{q}^\dagger\hat{q}^\dagger\hat{q}\hat{q} - g_{qf}(\hat{q}-\hat{q}^\dagger)(\hat{a}_1 - \hat{a}_1^\dagger) \\ &+ \sum_{x=1}^{M}\omega_{MM}\hat{a}_x^\dagger\hat{a}_x + \sum_{x=1}^{M-1} J(\hat{a}_x - \hat{a}_x^\dagger)(\hat{a}_{x+1} - \hat{a}_{x+1}^\dagger), \end{aligned} \tag{2.7}$$

where ω_{MM} and J denote the resonance frequency of the resonators and the nearest-neighbor hopping rate in the MMWG, x labels the resonator index, M is the number of resonators in the MMWG, and $\hat{q}$ and $\hat{a}_x$ are the annihilation operators of the transmon and the x–th resonator, respectively.

The protection of the qubit-like eigenstate $|\tilde{e}\rangle$ provided by the MMWG can be estimated by evaluating the participation of the last (M–th) resonator in $|\tilde{e}\rangle$, following Ref. [109]. Intuitively, when the qubit frequency is sufficiently detuned from the resonator frequencies in the MMWG, the excitation hybridized with the qubit cannot propagate through the chain and instead remains localized near the qubit. Under rotating-wave approximation, we consider the following Hamiltonian:

$$\begin{aligned}\hat{H}^{RWA}_{q-MMWG} =& \omega_q \hat{q}^\dagger\hat{q} + \frac{\eta}{2}\hat{q}^\dagger\hat{q}^\dagger\hat{q}\hat{q} + \sum_{x=1}^{M}\omega_{MM}\hat{a}_x^\dagger\hat{a}_x \\ &+ g_{qf}\left(\hat{q}\hat{a}_1^\dagger + \hat{q}^\dagger\hat{a}_1\right) + \sum_{x=1}^{M-1} J\left(\hat{a}_x\hat{a}_{x+1}^\dagger + \hat{a}_x^\dagger\hat{a}_{x+1}\right), \end{aligned} \tag{2.8}$$

where $\Delta = \omega_q - \omega_{MM}$ is the detuning. Since the RWA Hamiltonian is excitation-number-conserving,

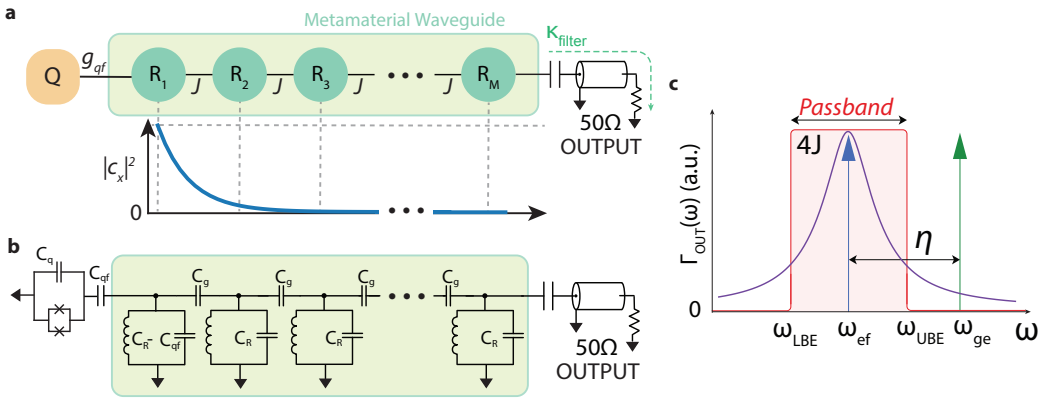

Figure 2.2: **Qubit coupled to metamaterial waveguide.** **a**, Schematic of a qubit (orange) coupled to a metamaterial waveguide (MMWG, green enclosure), and the hybridization amplitudes c_x as a function of resonator index x. The opposite end of the MMWG is coupled to an output waveguide. **b**, Circuit schematic of a flux-tunable transmon coupled to a metamaterial waveguide. **c**, Decay rate into the output port filtered by the MMWG as a function of frequency (red) and comparison with Lorentzian filtering (purple).

$$[\hat{H}^{RWA}_{q-MMWG}, \hat{q}^\dagger \hat{q} + \sum_x \hat{a}^\dagger_x \hat{a}_x] = 0, \tag{2.9}$$

the dressed qubit-like excited state can be written as a linear combination of single-excitation states. The corresponding eigenvalue equation in real space is

$$\begin{aligned} |\tilde{e}\rangle &= c_0|e, vac\rangle + \sum_{x=1}^{M} c_x|g, 1_x\rangle \\ (\omega_q - E)c_0 + g_{qf}c_1 &= 0 \\ (\omega_{MM} - E)c_1 + g_{qf}c_0 + Jc_2 &= 0 \\ (\omega_{MM} - E)c_n + J(c_{n-1} + c_{n+1}) &= 0, \end{aligned} \tag{2.10}$$

where E is the dressed eigenenergy, $|1_x\rangle \equiv \hat{a}^\dagger_x|vac\rangle$ is the bare single-excitation Fock state of the x–th resonator, and c_x is the hybridization amplitude. The recurrence relation can be solved using the ansatz $c_n = p^n$, which yields

$$-\Delta_E + J(\frac{1}{p} + p) = 0 \rightarrow p_\pm = \frac{\Delta_E}{2J} \pm \sqrt{\left(\frac{\Delta_E}{2J}\right)^2 - 1}, \tag{2.11}$$

where $\Delta_E = E - \omega_{MM}$, and the bulk solution takes the form:

$$c_x = A p_-^x + B p_+^x. \tag{2.12}$$

When $|\Delta_E| > 2J$, the roots $p_\pm$ are real, corresponding to an exponentially localized bound state. In this case, the physical solution is dominated by the root satisfying $|p| < 1$. Therefore, asymptotically,

$$c_x \propto \begin{cases} p_-^x & \Delta_E > 2J \\ p_+^x & \Delta_E < -2J \end{cases} \quad \rightarrow \quad |c_M|^2 \propto \left(\frac{1}{\frac{|\Delta_E|}{2J} + \sqrt{\left(\frac{\Delta_E}{2J}\right)^2 - 1}} \right)^{2M}. \tag{2.13}$$

Thus, the resonator component of the qubit-like eigenstate decays exponentially away from the qubit, as illustrated in Fig. 2.2a, strongly suppressing the participation of distant resonators and the coupling of the qubit-like eigenstate to an external port attached at the far end.

On the other hand, if $|\Delta_E| < 2J$, the roots have complex components and the system supports propagating solutions, meaning that the excitation becomes completely delocalized across the MMWG. Therefore, by controlling the transmon's $e - f$ transition from the detuned (bound state) regime to resonant (propagating state) regime, one can on-demand emit a photon into the MMWG. Still, if the *g–e* transition satisfies the condition $|\Delta_E| > 2J$, it enjoys the exponential suppression of decay rate. This provides a huge improvement in cooperativity compared to single-pole Lorentzian filtering, as shown in Fig. 2.2c. Therefore, a MMWG can provide stronger filtering of qubit emission and frequency selectivity in photon emission, compared to a single-mode filter, showing that tunable dissipative interactions tailored by multiple modes can outperform single-mode filters.

2.2 Tunable coherent interaction between superconducting qubits

In this section, we review how multimode couplers can improve tunable coherent interactions between superconducting qubits, which form the basis of entangling gates. A native approach to realize entanglement between two transmon qubits is to couple them using a linear coupling element, such as a capacitor as illustrated in Fig. 2.3a, which produces a transverse coupling:

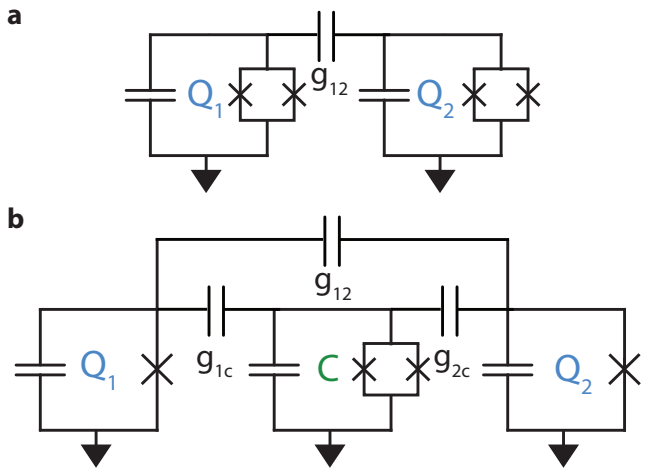

Figure 2.3: **Qubit-qubit coherent coupling.** **a**, Schematic of two transmons (Q1, Q2) coupled transversely via a coupling capacitor. **b**, Schematic of two transmons coupled both directly (g_{12}) and through a tunable coupler (C).

$$\hat{H}_{q-q} = \omega_1 \hat{a}^\dagger \hat{a} + \omega_2 \hat{b}^\dagger \hat{b} - g_{12}(\hat{a} - \hat{a}^\dagger)(\hat{b} - \hat{b}^\dagger) + \frac{\eta_1}{2}\hat{a}^\dagger \hat{a}^\dagger \hat{a}\hat{a} + \frac{\eta_2}{2}\hat{b}^\dagger \hat{b}^\dagger \hat{b}\hat{b}, \quad (2.14)$$

where $\hat{a}$ and $\hat{b}$ denote the annihilation operators of the two transmon modes, ω_1, ω_2 are the $g-e$ transition frequencies, η_1, η_2 are the anharmonicities, and g_{12} is the transverse coupling rate.

There are two native entangling mechanisms. First, the transverse coupling produces an iSWAP interaction described by $g_{12}(\hat{a}\hat{b}^\dagger + \hat{a}^\dagger \hat{b})$ when the two transmons are resonant with each other. Second, a ZZ (controlled-phase) interaction can arise either through nonadiabatic swap between $|ee\rangle$ and the noncomputational states $|gf\rangle$ or $|fg\rangle$, or through an adiabatic interaction under sufficient detuning. In the latter case, the interaction rate is given by

$$\zeta = \omega_{|ee\rangle} - \omega_{|eg\rangle} - \omega_{|ge\rangle} - \omega_{|gg\rangle} \approx \frac{2g_{12}^2}{(\omega_1 - \omega_2 - \eta_2)(\omega_1 - \omega_2 + \eta_1)}(\eta_1 + \eta_2). \quad (2.15)$$

However, this system is not ideal because turning off the interaction relies on substantial tuning of the individual transmon frequencies. During idle, readout, and single-qubit gates, the entangling interactions should be turned off. This includes the static ZZ interaction, which is given by the same expression in eq.(2.15). Suppressing this interaction requires detuning the two qubits away from each other. For example, with $g_{12}/2\pi = 10$ MHz and $\eta_1/2\pi = \eta_2/2\pi = -200$ MHz, achieving

a sufficiently small ZZ interaction rate of $\zeta/2\pi = 40$ kHz requires about 1 GHz of detuning. This implies that the qubits must be *in situ* tuned over a frequency range of roughly ≈ 1 GHz for each two-qubit gate. As a result, each qubit occupies a large spectral window, which exacerbates frequency crowding and increases the probability of Landau-Zener tunneling to other modes, such as spectator qubits and two-level system (TLS) defects. Furthermore, strong flux tunability increases sensitivity to flux noise and therefore degrades dephasing performance. Finally, during frequency tuning, the $|ee\rangle$ state collides with either the $|gf\rangle$ or $|fg\rangle$ state, which complicates the implementation of iSWAP interactions.

A commonly used solution to this problem is to incorporate a tunable coupler that relocates the required tunability from the qubits to an auxiliary element [43]. One of the most successful architectures is the tunable transmon coupler [47, 110], which consists of a flux-tunable transmon, as shown in Fig. 2.3b. In this architecture, the coupling between two qubits is mediated by the coupler and can be controlled *in situ* by tuning the coupler frequency relative to the frequencies of the two qubits. The effective interaction is given by

$$g_{12}^{\text{eff}} = g_{12} - \frac{g_{1c}g_{2c}}{2}\left(\frac{1}{\omega_1 - \omega_c} + \frac{1}{\omega_2 - \omega_c}\right), \tag{2.16}$$

where g_{12}^{eff} is the effective transverse coupling strength between transmon 1 and transmon 2, g_{1c} and g_{2c} are the coupling strengths between each transmon and the coupler, and ω_c is the $g-e$ transition frequency of the coupler transmon.

As the expression implies, the direct coupling rate g_{12} and the mediated coupling term can cancel out for an appropriate choice of the coupler frequency ω_c during idle. In addition, the tunability can be controlled solely by ω_c, which eliminates the need to tune the qubit frequencies ω_1 and ω_2. Strong interactions can be achieved by engineering the coupling rates and the coupler frequency, without requiring significant modifications to the qubits themselves. Variants of this tunable coupler architecture have led to steady improvements, including improved suppression of ZZ interactions and greater flexibility in qubit frequency placement. Such designs have enabled two-qubit gates with nearly coherence-limited fidelities approaching 99.9% and have supported quantum error-correction experiments [52, 84, 111].

However, as quantum processors become more precise, more stringent architectural requirements emerge. One notable demand is long-range connectivity and a larger number of couplings per qubit, which are required for implementing quantum low-density parity-check (qLDPC) codes that offer (asymptotically) improved logical-

to-physical qubit encoding rates [86, 112]. Achieving such connectivity requires extending the coupler structure to reach distant qubits, motivating new coupling architectures.

Furthermore, placing multiple couplers on each qubit increases the capacitive loading of the qubit through the coupling capacitors. This can introduce additional interfacial dielectric loss [60, 113] and complicate the physical layout, which is already demanding for weight-4 connectivity with a readout resonator per qubit. Although such dielectric loss issues have been mitigated through improved fabrication techniques and larger device geometries that reduce surface participation, these approaches begin to limit the achievable qubit packing density.

2.2.1 Multimode-mediated coherent interactions

Long-range coupling between qubits, especially over distances longer than the relevant wavelength λ, inevitably involves multiple modes. For instance, an open-ended waveguide supports multiple resonances: $\lambda/2$, λ, $3\lambda/2$ ..., yielding eigenmodes at frequencies $\omega_n = n\omega_0$, $n \in \{1, 2, 3, \ldots\}$.

When two qubits are coupled through a waveguide over a distance much smaller than λ, the electromagnetic profile varies only weakly between the two qubits, and the mediated interaction can be approximated as a simple capacitive coupling. However, when the qubits are placed near the ends of a waveguide whose length significantly exceeds λ, multiple eigenmodes appear near the qubit frequencies and can mediate the interaction.

Thus, engineering long-range interactions requires careful treatment of the eigenmodes supported by the coupling structure. In general, two approaches can be considered. The first approach is to use a single distributed element spanning the entire distance, which supports multiple eigenmodes. This approach is suitable for distances exceeding a few centimeters, for example using low-loss coaxial cables. It has been successfully demonstrated to provide high-fidelity entanglement over long distances and shows promise for chip-to-chip quantum operations and quantum communication [114, 115]. Such structures require careful handling of low-frequency modes that can be thermally populated, as well as mitigation of potential frequency collisions between integer-multiple eigenmodes through multiphoton processes.

The second approach is to use a chip-scale multimode structure to mediate long-range coupling through its collective modes, such as a MMWG, which is comparatively less explored. Coupled-resonator-array buses have been shown to provide

high-contrast coupling over chip-scale distances [116, 117]. In these systems, the interaction arises from spatial broadening of the qubit-like eigenmode as the qubit frequency approaches the bus band, as discussed in Subsection 2.1.1. Notably, although these structures can mediate long-distance coupling, they do not inherently support low-frequency geometric modes due to the periodic enforcement of voltage nodes and anti-nodes. In addition, the coupling between the bus structure and the qubits can be engineered to be strong because the resonators can be implemented as lumped-element circuits. Furthermore, multiple qubits can naturally be coupled to a single bus, enabling hardware-efficient realization of higher connectivity per qubit. In Chapter 5, we propose microwave-activated simultaneous long-range gate schemes by leveraging the rich multimode structure of coupled-resonator-array buses.

2.2.2 Galvanic and modeless tunable interactions

As discussed above, tunable couplings are typically engineered through mediating modes. However, such modes can provide channels for leakage errors, spurious coupling and crosstalk, and frequency crowding [85, 88, 118]. In addition, these schemes intrinsically rely on hybridization between qubits and couplers, where nonadiabatic transitions during tuning can limit achievable gate fidelity and speed. Furthermore, the mediated couplings are typically about an order of magnitude smaller than the underlying physical coupling rates. This often necessitates large coupling capacitances, which introduce interfacial dielectric losses, increase the physical footprint of qubits, and constrain capacitance budgets relevant to anharmonicity and field localization.

Alternatively, one can engineer pure nonlinear coupling through galvanic coupling schemes, which provide the required nonlinearity without introducing mediating modes. A representative example is the Quarton coupler [119], in which a SQUID composed of multiple Josephson junctions is series-connected to two elements. The Quarton coupler can be designed to produce cross-Kerr coupling while canceling self-Kerr nonlinearities. Such a design does not introduce additional mediating modes at low frequency while still allowing tunability through external magnetic flux. In addition, it directly connects phase variables in the circuit, enabling extremely strong coupling rates while requiring only a minimal circuit footprint for the coupling elements and does not rely on coupling capacitances.

Another representative example is the recently developed junction readout tech-

nique [71, 120], which leverages the intrinsic nonlinearity (cross-Kerr) of Josephson junctions for readout while canceling hybridization between the qubit and the readout resonator, thereby maintaining localization of the qubit eigenmode. Motivated by these approaches, in Chapter 6 I propose a tunable coupling architecture with a SQUID coupler that provides intrinsic cross-Kerr coupling without introducing additional modes.

These observations suggest that scalable superconducting quantum processors, demanding greater functionalities while relaxing some of the design trade-offs imposed by existing approaches, will likely require interaction schemes that go beyond single-mode mediation. The following chapters explore three complementary directions: engineering dissipative interactions using many modes, engineering coherent interactions using multimode buses, and engineering nonlinear interactions directly without mediating modes.

Chapter 3

DETERMINISTIC GENERATION OF MULTIDIMENSIONAL PHOTONIC CLUSTER STATES WITH A SINGLE QUANTUM EMITTER

With the capabilities of metamaterial waveguide (MMWG) discussed in Chapter 2, we present a microwave quantum optics platform consisting of a transmon operated as a qutrit quantum emitter coupled to a MMWG. Here, the MMWG serves not only as a state-selective filter for photon emission but also as a waveguide operating in the slow-light regime. The slow-light waveguide reduces the group velocity of itinerant photons and provides enhanced Purcell protection, while still allowing extremely fast on-demand photon emission. Leveraging this capability, we demonstrate deterministic generation of multidimensional microwave photonic cluster states. This chapter is adapted from Ref. [91].

3.1 Introduction

Quantum entanglement is generally regarded as a necessary resource for exceeding classical performance limits in tasks such as quantum computing, quantum communication, and quantum metrology [121–125]. In the optical domain, where photons are the ubiquitous carriers of quantum information, multi-partite entangled states are key resources for various quantum computation and networking protocols [98, 126]. Of particular importance are multi-dimensional cluster states, a subset of the family of entangled graph states with utility in measurement-based quantum computing [97, 127–129].

Reliable generation of cluster states of photonic qubits by conventional optical means remains an outstanding challenge due to the reliance on probabilistic photon entanglement heralding schemes [130–132]. Thus, there has been significant interest in achieving generation of such multi-dimensional cluster states by deterministic, resource-efficient means. Notable among these are schemes and experiments that involve sequential emission of entangled photons via control of only one or a small number of quantum emitters [133–136]. Note that while sequential emission from a single coherent emitter is sufficient to generate 1D cluster states, higher dimensional cluster states require more emitters or an additional memory element [137]. A promising approach is based on delay lines generating a time-delayed feedback

mechanism, expanding the class of cluster states that can be generated with a single emitter [138–142].

Superconducting circuit QED systems are a natural fit to implement such protocols. In contrast to atomic-optical systems where the finite atom-photon cooperativity is often a limiting factor [143, 144], superconducting circuit QED systems enjoy a strong qubit-photon coupling that far exceeds the strength of other dissipative channels due to the ease of creating microwave circuits at a deep subwavelength scale [40]. There has been significant progress over the last decade in leveraging superconducting qubits to generate, manipulate, and measure non-classical states of light, including 1D cluster states [99, 100, 145–148]. However, deterministic generation of higher dimensional photonic cluster states via a single quantum emitter has yet to be realized. Here we go beyond the previous state-of-the-art by using time-delayed quantum feedback, implemented using an integrated slow-light waveguide, for the generation of multipartite entangled photonic states, thereby achieving generation of a 2D cluster state of microwave photons.

3.2 Cluster state generation protocol

Our approach is based on the proposal in Ref. [138], and is illustrated in Fig. 3.1a. We couple a quantum emitter to the terminated end of a single-ended, low-group velocity waveguide. This quantum emitter has two stable states $|g\rangle$ and $|e\rangle$, as well as a radiative state $|f\rangle$ which is highly damped to the waveguide and decays to the $|e\rangle$ state.

Starting with the emitter in $|g\rangle$, the protocol first involves the generation of entanglement between the emitter and a photon mode: sequential use of a $\pi_{ge}/2$ pulse and a π_{ef} pulse generates an equal superposition of the $|g\rangle$ and $|f\rangle$ state, followed by the decay of the fraction of the emitter in $|f\rangle$ to $|e\rangle$ by emission of a photon into the waveguide. This leaves the emitter and the first emitted photon in the maximally entangled state $|\psi\rangle = (|g\rangle|0\rangle_1 + |e\rangle|1\rangle_1)/\sqrt{2}$. Repeating this control sequence primitive leads to sequential emission of a pulse train of entangled photonic time-bin qubits into the slow-light waveguide, with nearest-neighbor entanglement structure equivalent to that of a 1D cluster state [134, 135], illustrated in Fig. 3.1a as the blue colored pulses.

This pulse train is then reflected back towards the emitter by a switchable mirror at the other end of the delay line. After a full roundtrip the photons scatter from the quantum emitter and pick up a state-dependent scattering phase, illustrated

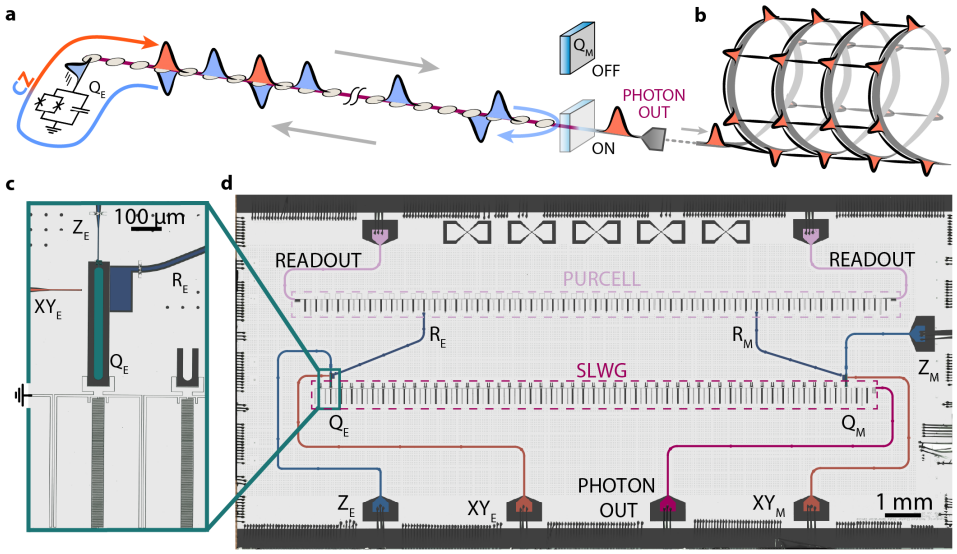

Figure 3.1: **Deterministic generation of 2D cluster states with a single emitter qubit. a,** General scheme for generation of 2D cluster states of photons via a single quantum emitter qubit and time-delayed feedback. The qubit is made to emit a pulse train of nearest-neighbor entangled photons (colored blue) into a delay line. Via control of a switchable mirror, each emitted photon pulse is reflected at the end of the delay line for re-scattering (blue to orange color change) by the emitter qubit. In the device used in this work, superconducting transmon qubits are used as both the quantum emitter (Q_E) and the switchable mirror (Q_M), and an array of weakly coupled resonators comprise a slow-light waveguide, which serves as a single-ended delay line. **b,** Visualization of the resulting entanglement structure. **c, d,** False-color optical images of the device, comprising a slow-light waveguide (SLWG) and two transmon qubits (false color green), with each qubit coupled to a readout resonator (false color dark blue), a XY control-line (false color orange), and a Z fast flux-line (false color light blue). The readout resonators (R) are probed through a coupled resonator array Purcell filter connected to CPW feed-lines (false color light pink). The emitted photons exit the slow-light waveguide and device via a CPW feedline (false color dark pink).

in Fig. 3.1a as a color change in the pulses from blue to orange. This scattering process effectively implements an entangling controlled CZ gate between the emitter qubit and the returning photonic qubit of the form $|g\rangle\langle g| \bigotimes \mathbb{I} + |e\rangle\langle e| \otimes \sigma_z$. The entanglement of the emitter to the most-recently scattered photon is inherited by the next emitted photonic qubit.

This combination of the sequential emission process and the state-dependent scattering process allows for the synthesis of a 2D cluster state with shifted periodic boundary conditions, as illustrated in Fig. 3.1b ([138], Supplementary Section IV). One of the two dimensions of the entanglement connectivity of such a 2D cluster state is derived from the sequential emission of photons, whereas entanglement along the other dimension results from the time-delayed scattering process. The extent of the first dimension is set by the number of photon pulses that can be generated during one round trip time τ_d, highlighting the role of the time-delayed feedback.

We fabricated the device shown in Fig. 3.1c,d in order to achieve a practical realization of this scheme. We implement the requisite delay line as a single-ended slow-light waveguide comprising a periodic array of 52 coupled resonators [149] with a round-trip delay of $\tau_\mathrm{d} = 240$ ns. The output port of the slow-light waveguide is impedance-matched to a 50 Ω coplanar waveguide (CPW) through which emitted itinerant photons leave the device for amplification and subsequent measurement at the digitizer (Supplementary Section 3.7.2).

The resulting transfer function of such a slow-light waveguide is that of a flat "passband" of finite bandwidth for guided modes, and a sharp extinction of transmission outside of the passband due to the sharp decline in the photonic density of states (DOS) of the periodic structure occurring at the band edges. The width of the passband is $4J$, where J is the coupling between unit cells in the resonator array [109, 150]; in our device $J/2\pi = 34$ MHz and the passband center frequency is $\omega_p/2\pi = 4.823$ GHz.

On the terminated end of the slow-light waveguide we couple the emitter qubit Q_E, while at the other end of waveguide we couple another qubit Q_M. The mirror qubit is effectively side-coupled to the slow-light waveguide, allowing it to act as a high reflectivity mirror for single photons if the ratio between its decay rate into the waveguide and its decoherence rate into other channels, $\Gamma_{1\mathrm{D}}/\Gamma'$, is sufficiently high [101].

Crucially, due to the finite width of the slow-light waveguide passband and its sharp band edges in conjunction with an emitter anharmonicity $|\eta|/2\pi$ of ~280 MHz, it is possible to tune the $|e\rangle \rightarrow |f\rangle$ transition frequency ω_{ef} into resonance with ω_p while simultaneously situating $|g\rangle \rightarrow |e\rangle$ transition frequency ω_{ge} outside the passband of the waveguide, where the DOS of the periodic structure is negligible. This allows for a remarkably large $|f\rangle$ to $|e\rangle$ emission rate of $\Gamma_{1D}^{ef}/2\pi \approx 140$ MHz for Q_E, while strongly suppressing $|e\rangle$ to $|g\rangle$ decay to single kHz rates.

3.3 Shaped photon emission

Shaping the emitted photon pulses allows us to mitigate the effects of the waveguide's residual dispersion near ω_p, and to improve the fidelity of the CZ gate after a photon round trip. For this it is necessary to control the photon pulse shape as well as its bandwidth, reducing it to less than Γ_{1D}^{ef} [138]. We shape the pulse of the emitted photons by a tunable qubit-waveguide interaction strength for Q_E via parametric flux modulation at frequency ω_{mod} of the qubit frequency [151–153], creating multiple sidebands of each transition spaced by integer multiples of ω_{mod}. By choosing the qubit frequency $\omega_{ge}/2\pi = 5.55$ GHz and modulation frequency $\omega_{\text{mod}}/2\pi = 450$ MHz such that $\omega_{ef} - \omega_{\text{mod}} = \omega_p$, we can control emission into the waveguide solely through the first-order sideband of the $|f\rangle \rightarrow |e\rangle$ transition. This is shown schematically in Fig. 3.2a,b; in Fig. 3.2a we illustrate this emission process through a level diagram, whereas in Fig. 3.2b we show a simplified frequency spectrum of the particular configuration of qubit frequencies and sideband frequencies used in our experiment.

By continuously varying the amplitude of the flux modulation AC drive during the emission time we can vary the strength of the first-order e-f sideband and achieve arbitrary time-dependent modulation of Q_E's emission rate $\Gamma_{1D}^{ef}(t)$ (Supplementary Section 3.7.3). With this capability, time-bin qubits comprising Gaussian shaped photonic pulses are generated with excellent accuracy, as demonstrated in Fig. 3.2c. We plot the measured photon flux of three emitted Gaussian pulses with different bandwidths along with their respective fits, where photon flux is plotted in normalized units (Supplementary Section 3.7.3). Emission is achieved with high efficiency, enabling deterministic high-fidelity preparation of entangled photonic states (Supplementary Section 3.7.3, 3.7.3).

Further, in Fig. 3.2d, we plot Q_E's population dynamics during emission, as well as the integral of the photon fluxes plotted in Fig. 3.2c which, in the absence of

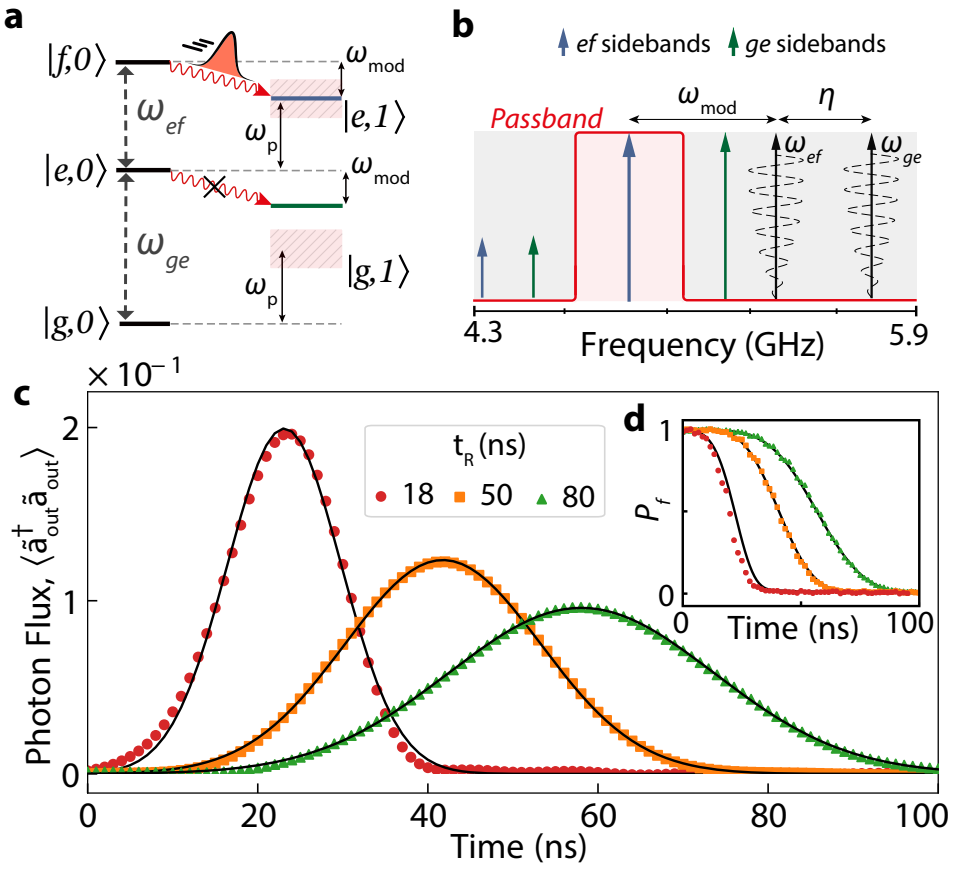

Figure 3.2: **Emission of shaped photons pulses via flux-modulation. a,** Effective level diagram of the qubit-waveguide system, showing the photon emission process. In the $|i,n\rangle$ notation, i denotes the state of the transmon emitter qubit, and n denotes the number of photons in the slow-light waveguide; when $\omega_{ef} - \omega_{\text{mod}} = \omega_p$, the qubit's levels assume a three-state ladder system where only the $|f\rangle$ state is selectively damped to the slow-light waveguide. **b,** Simplified frequency spectrum of the emitter qubit under flux-modulation, where η is the qubit anharmonicity. The flux-modulation waveform is depicted as a dashed black line; the modulated amplitude directly maps to a modulated emission rate into the waveguide that allows for shaped emission of photon pulses. **c,** Measured photon flux $\langle a^\dagger{}_{\text{out}} a_{\text{out}}\rangle$ (dots) of shaped emitted pulses, in normalized units. Black lines are Gaussian fits. **d,** Measured $|f\rangle$ population during shaped emission. Black lines are the scaled integral of the photon fluxes of subfigure **c**.

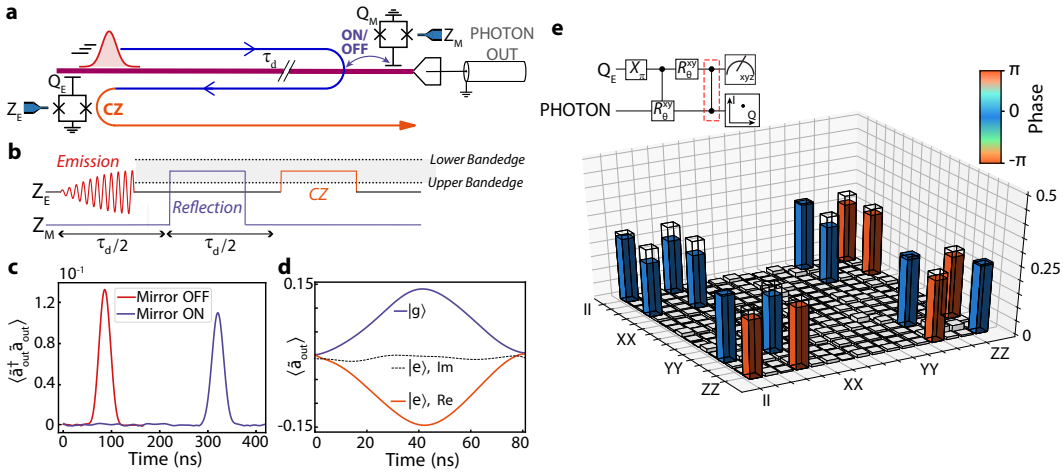

Figure 3.3: **CZ gate between emitter qubit and previously emitted photons via time-delayed feedback.** **a,** Illustration of the time-delayed feedback process realizing the CZ gate between Q_E and its emitted photon. The photon travels one round-trip of the slow-light waveguide and re-scatters on Q_E. **b,** Z-control of the qubits implementing the CZ gate. Square pulses on Z_M and Z_E tune their respective qubit frequencies to the middle of the passband. **c,** Measured photon flux of qubit emission with the Z_M pulse for mirror reflection ON vs OFF. **d,** Measured $\langle a_{\text{out}} \rangle$ of the reflected pulse after it re-interacts with Q_E, where Q_E is prepared in either the $|g\rangle$ or the $|e\rangle$ state. The complex phase of $\langle a_{\text{out}} \rangle$ in both cases is normalized to the phase of the measurement where Q_E is prepared in the $|g\rangle$ state. **e,** Reconstructed Pauli process matrix χ_{CZ} of the CZ gate between Q_E and its emitted photon, demonstrating a 90% fidelity relative to the ideal gate; the procedure is shown on the top left.

waveguide-induced distortion, would coincide with the population dynamics of Q_E. We find excellent agreement between the two, indicating that the effects of the slow-light waveguide dispersion are minimal for Gaussian pulses. Finally, we stress that our large $\Gamma_{1\text{D}}$ allows high-efficiency emission of pulses that are tightly confined to a time-bin window of length as small as 30 ns, which not only is crucial to increase the size of generated cluster states given a fixed τ_{d}, but also demonstrates significant improvement in emission speed of shaped photons over previous shaped emission demonstrations in circuit QED systems [154–157].

3.4 Qubit-photon CZ gate implementation

In Fig. 3.3a we show a schematic of the time-delayed feedback process that implements a high-fidelity qubit-photon CZ gate. An itinerant photon emitted by Q_E propagates through the waveguide, is reflected by Q_M, and propagates back towards Q_E. Scattering on Q_E with ω_{ef} tuned to be resonant with the incoming photon

realizes the CZ gate in the following way: if the emitter is in the $|e\rangle$ state, then the returning photon will couple to the resonant e-f transition and pick up a π scattering phase. If the emitter is in the $|g\rangle$ state the photon will see a far-detuned transition and pick up no scattering phase.

In Fig. 3.3c,d we illustrate the actions of reflection by Q_M and photon re-scattering by Q_E on an emitted photon. In Fig. 3.3c we show the emitted photon's flux measured at the digitizer with the square pulse on the Z_M line turned on or turned off. With the Z_M square pulse turned on, the photon's arrival at the digitizer is delayed by τ_d, while negligible photon flux is measured at all prior times, demonstrating that the Q_M reflects the itinerant photon with high efficiency. The discrepancy in pulse magnitude between the two cases is attributable to an additional 0.6 dB loss suffered by the reflected photon during its round-trip.

In Fig. 3.3d we show the emitted photon's average measured *field* when Q_E is prepared in either the $|g\rangle$ state or the $|e\rangle$ state. It is evident that the sign of the real part of the re-scattered photon's complex field changes when the state of Q_E is changed from $|g\rangle$ to $|e\rangle$, while the imaginary part of the re-scattered photon's complex field is negligible. This corresponds to a state-dependent π difference in the phase of the photon, as desired for the CZ gate implementation.

In addition, we perform quantum process tomography in order to quantitatively characterize the CZ gate, following a procedure inspired by the tomography procedure described in the work of Eichler et al [158]. We prepare a tomographically complete set of states within the two-qubit subspace of the joint qubit-photon system, apply the qubit-photon CZ gate to the prepared state, and then perform single shot joint measurement of the emitter qubit in one of the three axial Bloch bases and heterodyne measurement of the photon field. From these measurements, correlations between the single shot qubit measurements and single shot heterodyne field measurements can be computed, and form a tomographically sufficient set of data for reconstructing the full process matrix of the qubit-photon CZ gate. From the reconstructed process matrix we extract a process fidelity $\mathrm{Tr}\left(\sqrt{\sqrt{\chi_\mathrm{CZ}}\chi_\mathrm{ideal}\sqrt{\chi_\mathrm{CZ}}}\right)^2$ of 90%. We attribute most of the infidelity to dephasing and state preparation and measurement (SPAM) errors, given that a measurement of the $\mathbb{I}\bigotimes\mathbb{I}$ idling process matrix yields a fidelity of 92.5% (Supplementary Section 3.7.5). We note that a similar qubit-photon CZ gate was implemented before by Reuer et al. [157] with a fidelity of 74%. We attribute the fidelity improvement in our system to the large ratio between the slow-light-enhanced emission rate of the emitter qubit to our waveguide

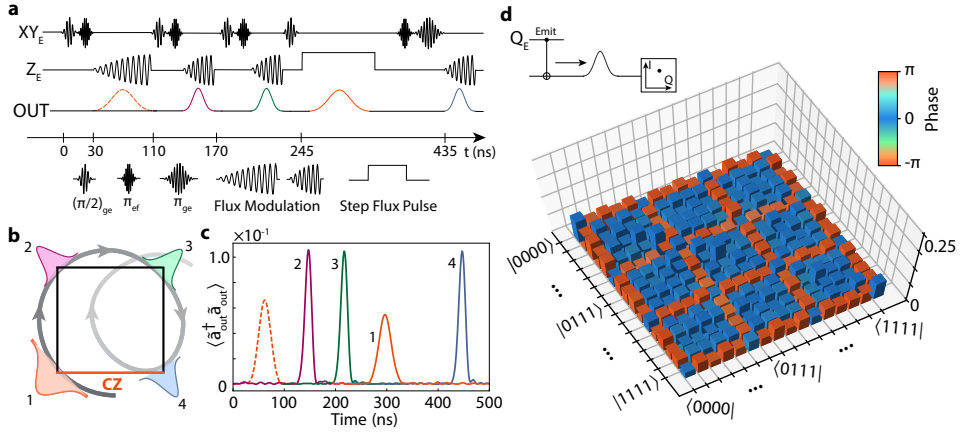

Figure 3.4: **Deterministic generation of a 4-photon 2D cluster state. a,** Pulse sequence of Q_E control lines, and illustration of outgoing photon flux from Q_E. Depiction of Z_M line control can be found in Fig. 3.3. Photons 1,2,3, and 4 are represented by the colors orange, purple, green, and blue, respectively. **b,** Illustration of the generated entangled state. "CZ" signifies the entanglement that arises due to the CZ gate between Q_E and photon 1. **c,** Photon flux of individual time-bin photonic qubits. The dotted orange line corresponds to the photon flux of the first emitted photon in the absence of reflection by the mirror qubit, and is only shown for illustration purposes. **d,** Density matrix ρ of the generated 2D cluster state obtained from photonic quantum state tomography. The height of the bars represent the magnitudes of the elements of ρ, while the color of the bars represent the phases of the elements of ρ. The fidelity of the generated state $F = \mathrm{Tr}\left(\sqrt{\sqrt{\rho}\rho_{\mathrm{ideal}}\sqrt{\rho}}\right)^2$ is 70%.

and the linewidth of the itinerant photon participating in the gate, where this larger ratio was enabled by the unique properties of our slow-light waveguide circuit.

3.5 2D cluster state generation and measurement

Finally, with our high efficiency shaped photon preparation and high fidelity CZ gate, we demonstrate generation of a 2D cluster state of four microwave photons. In Fig. 3.4a, we show the full Q_E control we used to generate the cluster state, resulting in the entangled state shown in Fig. 3.4b. The control sequence consists of four cycles of the 1D cluster state generation primitive with a CZ gate between photon 1 and Q_E prior to emission of photon 4. Before the last π_{ef} pulse we also apply a π_{ge} to Q_E in order to disentangle it from the photonic state upon its final emission. The measured photon flux of the individual time-bin photonic qubits is shown in Fig. 3.4c, where their position in time corresponds to their arrival time at the digitizer. Note that photon 1 is emitted with a lower bandwidth than other

photons in order to maintain the high fidelity of the CZ gate between photon 1 and Q_E, while photons 2, 3, and 4 are emitted more rapidly in order to more efficiently use the fixed τ_d delay available.

Again following Eichler et al [158], we perform MLE-based state tomography of the generated four-photon state using the joint moments of the photon fields, calculated from their measured single-shot field quadratures I_i and Q_i. (Supplementary Section 3.7.4) We calculate a fidelity $F = \mathrm{Tr}\left(\sqrt{\sqrt{\rho}\rho_\mathrm{ideal}\sqrt{\rho}}\right)^2$ of 70% between the generated and the ideal expected density matrix ρ_ideal shown in Fig. S12b, with 95% confidence interval of [69.1%, 70.4%], indicating achievement of genuine four-partite entanglement and successful implementation of the protocol of ref. [138]. The achieved fidelity is in good agreement with our estimated state fidelity limit of 76%, which we calculate from contributions to preparation infidelity that include the dephasing of Q_E (the primary source of infidelity, $T_2^* = 561$ ns in this work), the round-trip loss suffered by photon 1, and measured qubit preparation and control errors (Supplementary Section 3.7.6).

While the four photon square cluster state that we have generated demonstrates the viability of Pichler et al.'s protocol for multidimensional cluster state generation, it is known that four photon square cluster states are equivalent to one-dimensional linear cluster states of four photons under local unitary operations and graph isomorphism. [159]. In order to demonstrate the generation of genuinely multidimensional cluster states, we have also generated a five photon pentagon state that is not equivalent to any one-dimensional cluster state under such transformations, with a fidelity of 61.3%, with a 95% confidence interval of [61.1%, 61.4%] (Supplementary Section 3.7.4). Future improvements to the round trip loss of the waveguide and the coupling architecture between the emitter and the waveguide would allow for the generation of larger, more complex states of microwave photons with higher fidelity.

3.6 Conclusion and outlook

We have successfully implemented a resource-efficient protocol for generation of multidimensional cluster states, utilizing a single superconducting qubit as a source of entangled photons and a coupled resonator array as a slow-light waveguide for time-delayed feedback, and we have used the protocol for the generation of a 2D cluster state of four microwave photons. We accomplished this using rapid, shaped emission of single microwave photons, as well as a high fidelity CZ gate between the quantum emitter and previously emitted photons through the controllable time-

delayed feedback of our system.

The protocol discussed here allows for generation of larger 2D cluster states without incorporation of additional quantum emitters. Increasing one dimension of the entanglement connectivity in the schematic 2D cluster state in 3.1b is achievable by increasing the number of photons that can be emitted within a single round-trip time of the waveguide, either by introducing a delay line with increased round-trip delay or using photon pulses with a shorter temporal extent, in conjunction with improving the waveguide loss. Longer delays could be engineered by further reducing the footprint of our unit cell resonators, for example by leveraging compact high kinetic inductance superconducting resonators [160, 161], or by incorporation of acoustic delay lines [162–164]. The other dimension of the entanglement connectivity could be elongated by improving the coherence time of the emitter qubit, allowing for a larger total number of coherent photon emission events (see Supplementary 3.7.6).

Furthermore, our protocol is directly extensible to protocols for generation of more exotic entangled photonic states. As an example, the generation of 3D cluster states, which have been proposed as a resource for realizing fault-tolerance in measurement based quantum computation [128], could be realized by adding another time-delayed feedback event with a second, longer delay for every photon [139, 140], achievable by incorporation of another mirror qubit and a delay line with increased round-trip delay. As a preliminary demonstration of performing multiple time-delayed feedback operations on a single photon we have successfully generated a 5-photon tetrahedral-like photonic graph state using a scheme that required two feedback operations on one photon (see Supplementary 3.7.4). Additional progress towards fault-tolerant applications could be realized in a conceptually straightforward manner by modifying the photonic qubit encoding scheme to a dual-rail implementation that would allow for unambiguous detection of photon loss events in generated graph states [139, 165].

We therefore expect the deterministic techniques presented here using the rich toolbox of circuit QED to not only improve upon the conventional optics-based approaches for realizing multidimensional cluster states, but to also broaden the scope and applicability of such states for quantum information processing.

3.7 Supplementary Information for Chapter III

3.7.1 Measurement setup

Device fabrication

The device used in this work is fabricated on a 2 cm × 1 cm high-resistivity (10 kΩ) silicon substrate. Fabrication details follow closely those of references [149, 166]. A resist layer is deposited on the silicon substrate, and the ground plane, waveguides, resonator and qubit capacitors are patterned on this resist using electron-beam lithography. This is followed by deposition of 120 nm of aluminum (Al) at a rate of 1 nm/s using an electron-beam evaporator. The device is left in N-methyl-2-pyrrolidinone at 80°C for 2.5 hours to perform liftoff of the resist layer.

The junctions are fabricated by double-angle evaporation of a suspended Dolan bridge patterned using electron beam lithography. A 60 nm Al evaporation at 1 nm/s constitutes the first junction layer, and a 120 nm Al evaporation constitutes the second, between which there is an intervening 20 minute oxidation period when 10 mBar of oxygen gas is admitted to the chamber of the electron beam evaporator to grow the insulating aluminum oxide layer of the junction. After deposition of the two junction layers, electron beam lithography is again used to pattern a 'bandage' layer comprising regions of aluminum that galvanically connect the bottom and top layers of the junctions. Before deposition of the Al bandages, the device is Argon milled for 5 minutes to remove surface oxides and facilitate galvanic connection of the top and bottom junction layers to the bandage.

Air bridges connecting the ground plane on either side of our coplanar waveguides are patterned using a grayscale electron-beam lithography technique. After development of the airbridges, resist is made to reflow by placing the device on a hot plate at 105°C, after which 140 nm of Al is deposited at 1 nm/s on the developed resist. Prior to the Al deposition, the device is Argon milled for 5 minutes to remove surface oxide of the ground plane to facilitate galvanic connection between it and the feet of the air bridges.

Measurement setup

A schematic of the fridge wiring and our room-temperature analog signal processing electronics is shown in Fig. 3.S1. Measurements are performed in a 3He/4He dry dilution refrigerator. The sample is wirebonded to a CPW printed circuit board (PCB) with coaxial connectors, and is housed inside a copper box that is mounted to

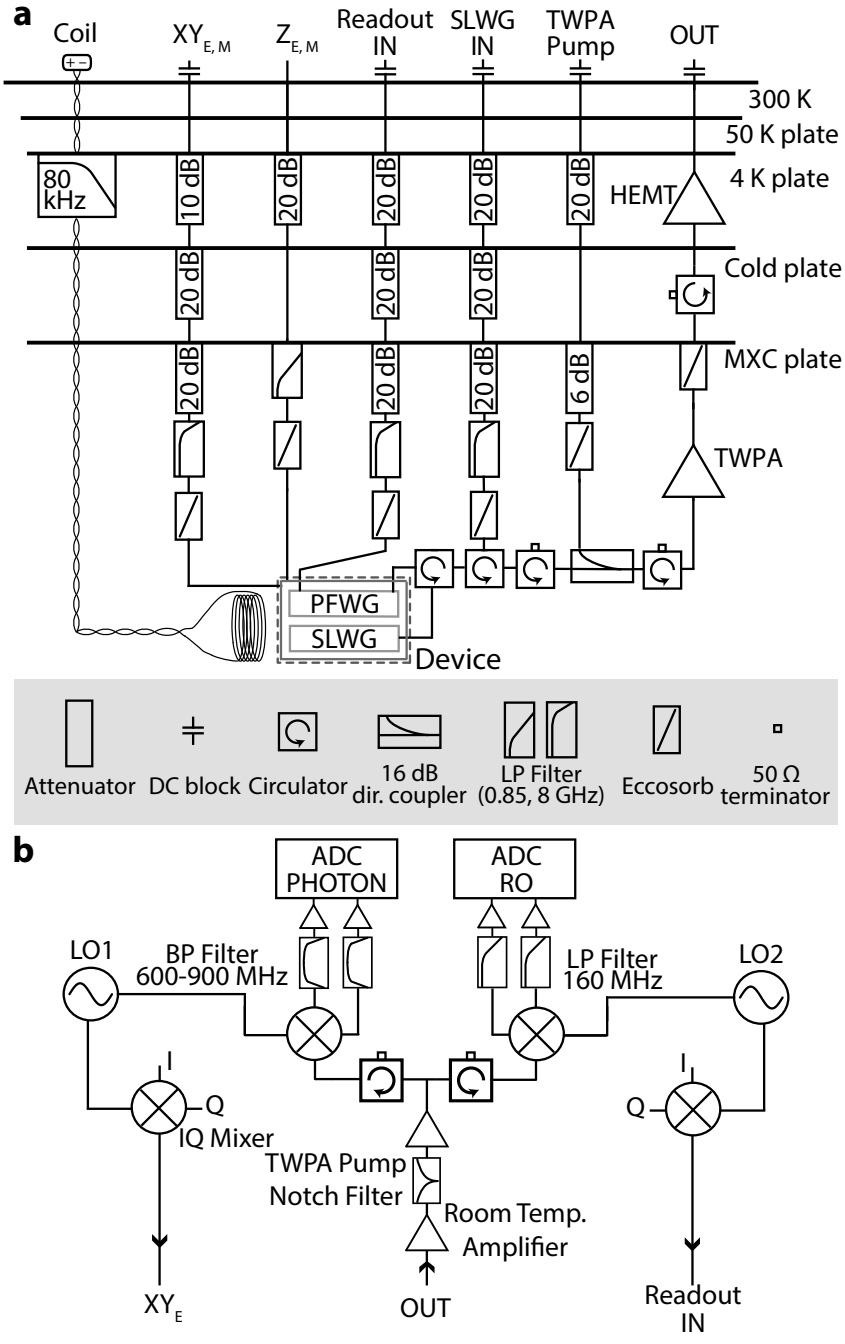

Figure 3.S1: **Measurement setup. a**, Schematic of the measurement wiring inside the dilution refrigerator. See Supplementary text for further details ("dir." is shorthand for "directional", "LP" is shorthand for "Low Pass", and "BP" is shorthand for "Band Pass".). See Fig. 1 for electrical connections at the sample. **b**, Simplified diagram of measurement wiring outside the dilution refrigerator.

the MXC plate of the fridge with T_{MXC} = 7 mK. A coil is placed on top of the copper box for static flux tuning of the qubits, and the sample is enclosed in two layers of magnetic shielding to suppress effects of stray magnetic fields. See refs [149, 166, 167] for more details on device fabrication.

Attenuators are placed at several temperature stages of the fridge to provide thermalization of the coaxial input lines and to reduce thermal microwave noise at the input to the sample. Our gigahertz microwave lines (XY_E, XY_M, Readout IN, SLWG IN, TWPA Pump) have significantly more attenuation than our fast flux lines (Z_E, Z_M) for reasons explained in ref. [168]. In addition, fast flux lines are filtered by an 850 MHz low-pass filter below the MXC plate, which suppresses thermal noise photons at higher frequencies while still maintaining short rise and fall times of square flux pulses, as well as allowing transmission of AC flux drives. The tuning coil is differentially biased by two DC input lines, with 80 kHz low-pass filters at the 4K stage to further suppress noise photons. Furthermore, Gigahertz microwave input lines are filtered by an 8GHz lowpass filter and all microwave lines have an Eccosorb filter, in order to ensure strong suppression of thermal noise photons at very high frequencies. Note also that all 50-Ω terminations are thermalized to the MXC plate in order to suppress thermal noise from their resistive elements.

Output signals from the Purcell filter waveguide (PFWG) and slow-light waveguide (SLWG) device lines are merged to a single amplifier chain in the following manner. Their corresponding coaxial lines are connected to a circulator as shown in Fig. 3.S1a, such that signals exiting the SLWG continue directly to the output chain, while signals exiting the Purcell filter are first routed to the SLWG device line and subsequently reflect off of the finite-bandwidth structure, thus finally routing them to the output chain. Note that input signals to the SLWG IN line undergo similar routing in order to arrive at the device.

Our amplifier chain at the "OUT" line consists of a quantum-limited traveling-wave parametric amplifier (TWPA) [169] as the initial amplification stage, followed by a Low Noise Factory LNF-LNC4_8C high mobility electron transistor (HEMT) amplifier mounted at the 4K plate. For operation of the TWPA, a microwave pump signal from Rohde & Schwarz SMB100A is added to the amplifier via the coupled port of a 16 dB directional coupler, with its isolated port terminated in 50-Ω. We include two isolators between the directional coupler and the sample in order to shield the sample from the strong TWPA pump.

Outside the fridge, we further amplify output signals with amplification that is

suitable for the dynamic range of our ADC. We note that we use a Micro Lambda Wireless MLBFR-0212 tunable notch filter to reject the TWPA pump signal in order to prevent saturation of the following room temperature electronics. Additionally, we use IF amplifiers (0-1GHz bandwidth) for downconverted signals due to IQ mixer saturation power limits.

Due to their different frequencies, we route SLWG and PFWG signals to different downconversion stages via a 2-way power splitter, followed by a circulator at each branch to prevent crosstalk between the two branches. The "PHOTON" branch is connected to a IQ mixer for downconversion of ~ 4.8 GHz photonic signals, which are then measured by an Alazartech ATS9371 digitizer (ADC PHOTON); measurement of both photonic signal quadratures $I(t)$ and $Q(t)$ comprise the heterodyne measurement of time-dependent photon signals alluded to in Supplementary Section 3.7.4. Meanwhile, the other branch of the power splitter is also connected to an IQ mixer for downconversion of ~ 7.5GHz readout signals, which are then measured by a Keysight M3102 digitizer (ADC RO). We note that downconversion mixers share LO signals (generated by Rohde & Schwarz SMB100A microwave signal generators) with their upconversion counterparts (where a Zurich HDAWG is used), in order to ensure phase drift/jitter of LO's during upconversion are cancelled out during downconversion. And crucially, we place additional filters before measurement at the ADC in order to suppress noise outside of the IF measurement band of interest. This not only allows for better utilization of the ADC dynamic range, but also rejects noise at irrelevant Nyquist bands that "fold" over to the bandwidth of measured signals; we note that this effectively improved the n_{noise} of our photon measurement chain by almost a factor of 2 (see Supplementary Section 3.7.4 for more details).

3.7.2 Device characterization

Slow-light waveguide

As discussed in the 2D cluster state generation protocol proposed in ref [138], one of the dimensions of the resultant cluster state is limited by the number of photons that can be held in the delay line simultaneously, necessitating a delay line with a sufficiently large round trip time τ_{d}. In this work, we realize such a delay line via implementation of a slow-light waveguide (SLWG), which provides large group delay for time-delayed feedback. In addition, the SLWG also provides spectral constriction of propagating modes to a passband with a finite bandwidth,

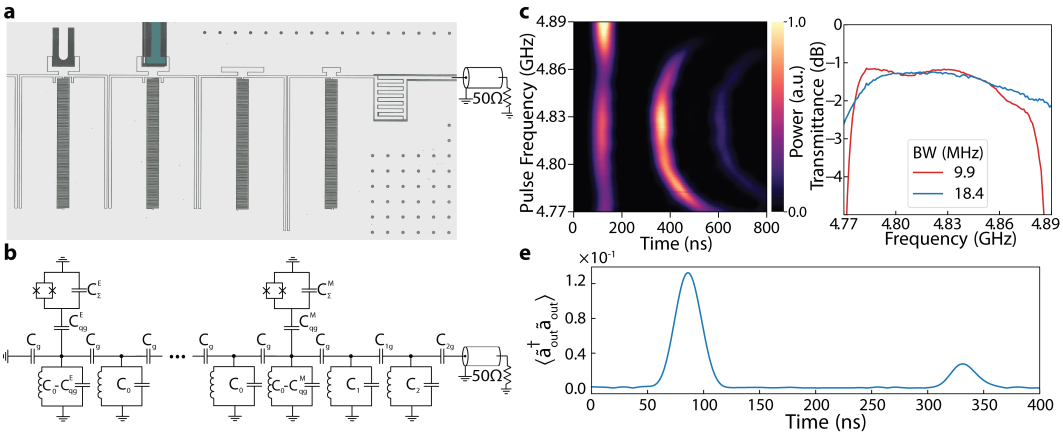

Figure 3.S2: **Metamaterial slow-light waveguide characterization.** **a**, False-colored optical image of the end of the slow-light waveguide that is connected to the CPW output waveguide, including the "tapered" boundary matching circuit consisting of the last two resonators. The mirror qubit shunt capacitance is false colored in green **b**, Full circuit model of the slow-light waveguide and coupled qubits. **c**, Transient response of slow-light waveguide with narrow-band input pulses of frequencies near around the passband. **d**, Transmittance of the tapered end of slow-light waveguide, calculated from the data in subfigure **c** and a separate measurement of round-trip loss. **e**, Photon flux of emitter qubit emission, measured for 400 ns. After one round-trip delay of the slow-light waveguide, the initially non-transmitted portion of the qubit's emitted pulse can be observed.

where the photonic density of states (DOS) sharply decreases at the band edges and is negligible outside the passband, thus enabling selective emission of the Q_E's $|f\rangle \rightarrow |e\rangle$ transition, as discussed in the main text. The SLWG is physically realized as a periodic array of capacitively coupled lumped-element superconducting microwave resonators, with low resonator loss and negligible resonator frequency disorder, as was demonstrated in our prior work [149]. It can be shown that such a design allows for large group delay per resonator $\sim \frac{1}{2J}$, where J is the photon hopping rate between adjacent resonators, as well as strong emission of transmon qubits only at qubit frequencies within the SLWG passband.

The SLWG is implemented by periodically placing $N = 50$ unit cells across the device as seen in Fig. 1d, where a unit cell consists of a lumped-element resonator realized with tightly meandered lines providing the majority of the inductance, wider rectangular features providing the majority of the capacitance, and with capacitive coupling between adjacent resonators achieved via their long capacitive wings, as shown in Fig. 1c. At the output side of the SLWG, the Bloch impedance of the SLWG is matched to its output 50 Ω CPW via a "taper section" comprising two

lumped element resonators, where their coupling capacitances towards the output are gradually increased, and their capacitances to ground are correspondingly gradually decreased to compensate for resonance frequency changes. Crucially, in order to prevent distortion of Q_E photon emission, at the terminated side of the single-ended SLWG a capacitance to ground via a long capacitive wing is placed at the left of the first unit cell resonator (Fig. 1c), thus maintaining the resonance frequency of the first resonator to be the same as the frequency of the other resonators, which ensures monotonic emission from Q_E (as observed in separate modeling).

The corresponding circuit model of the SLWG waveguide coupled to Q_E and Q_M is depicted in Fig. 3.S2b. In the regime of $C_g \ll C_0$, the dispersion of the SLWG is approximately

$$\omega_k = \omega_p + 2J\cos(k), \tag{3.1}$$

where $\omega_0 = 1/\sqrt{L_0 C_0}$ is the resonance frequency of unit cell resonators, $J = \omega_0 \frac{C_g}{2C_0}$, $\omega_p = \omega_0 - 2J$ is the center frequency of the passband, and the passband width is $4J$. To mitigate the deleterious effects in the time-domain shape of emitted photons emerging from the higher-order dispersion [170], a sufficiently large J is required. On the other hand, our requirement for large group delay $\tau_d = \frac{N}{J}$ necessitates a sufficiently small J. In order to balance the conflicting requirements of large delay and manageable dispersion, we chose $J = 33.5$ MHz as a target parameter that corresponds to the round-trip delay of $\tau_d = 237$ ns.

We thus aimed for the following target circuit parameters: $L_0 = 3.1$ nH, $C_0 = 353$ fF, $C_g = 5.05$ fF, $C_1 = 347$ fF, $C_{1g} = 8.6$ fF, $C_2 = 267$ fF, and $C_{2g} = 87$ fF, yielding $J/2\pi = 33.5$ MHz, $\omega_p/2\pi = 4.744$ GHz, and the requisite impedance matching at the boundary. As seen in Fig. 3.S2a, for the taper section the increasing coupling capacitances are implemented as longer capacitive wings or interdigitated capacitors, and adjustments to the resonance frequencies are achieved by both shortening the length of the meandered lines and modifying the head capacitances. In addition, the coupling capacitance of Q_E and Q_M to their respective unit cells, as depicted in Fig. 1c and Fig. 3.S2a, were designed to be 2.41 fF and 5.37 fF, respectively. This yields the qubit-unit cell coupling $g_{uc} = 38.5$ MHz of Q_E and $g_{uc}^M = 85.6$ MHz of Q_M via the following relation:

$$g_{uc} = \frac{C_{qg}^E}{2\sqrt{(C_0 + 2C_g)(C_\Sigma^E + C_{qg}^E)}}\omega_p, \tag{3.2}$$

where g_{uc}^{M} is obtained by a similar calculation. As discussed in the next subsection of the Supplementary, these small coupling capacitances lead to large emission rates due to the slow-light nature of the SLWG, where a small group velocity $v_g = \frac{\partial \omega}{\partial k}$ is commensurate with a large density of states $\sim 1/|v_g|$, which enhances emission rates [6, 109].

In order to characterize the SLWG, we investigated the transmittance of the SLWG boundary for an itinerant pulse by sending coherent gaussian pulses of variable carrier frequency through the SLWG IN line and measuring their outgoing intensity at ADC PHOTON after they pass through the device. The measurement result, comprising distinct features separated in time that correspond to different reflection events, is shown in 3.S2c. First, when the pulses arrive at the SLWG boundary, due to the finite reflectance of the taper section, a fraction of the incident pulse is reflected (and thus does not enter the SLWG) and is measured as the first bright feature in Fig. 3.S2c. Next, the transmitted fraction of the pulse propagates through the SLWG, completes a round-trip, and arrives at the SLWG boundary again. While a small fraction of the pulse is again reflected due to finite reflectance, most of the energy transmits through the boundary to constitute the second bright feature in Fig. 3.S2c. Finally, this reflected fraction of the pulse completes a second round-trip, and is found as the last bright feature of in Fig. 3.S2c. Note that this process continues with more round-trips, while the measured data up to the second round-trip is used for analysis.

We estimated the transmittance T of the SLWG boundary via comparing the energy contained in the second bright feature E_2 and the energy contained in the last bright feature E_3, where we define the energy of the "feature" $E = \int |\langle V(t) \rangle|^2 dt$, where $V(t)$ is the measured voltage at the ADC for a particular "feature". As discussed, the pulse corresponding to the last bright feature undergoes an additional incidence at the SLWG boundary and an additional round-trip in the SLWG relative to the pulse corresponding to the second bright feature. Thus, we can compare their energies via the following relation:

$$E_3 = R(1 - L)E_2, \tag{3.3}$$

where $R = 1 - T$ is the reflectance of the boundary, and L is the photon loss during a round-trip. By using $L \approx 0.1$, which is obtained from the measurement of Fig. 3, we estimate transmittance $T \approx -1.2$ dB at the center of the SLWG passband. The transmittance, shown in Fig. 3.S2d, is measured for two different bandwidths of the incident Gaussian pulses, such that the slow pulses (red curve) have approximately

the same bandwidth as photon 1 of the generated cluster state (see Fig. 4) and the fast pulses (blue curve) have approximately the same bandwidth as photon 2-4 of the generated cluster state. The difference of the transmittance between the two cases demonstrates the necessity of adjustment of the power calibration scaling factor G of the output chain according to the bandwidth of the photons (see Supplementary Section 3.7.4 for further details). Note that we measured T via the transient response of the SLWG because the transient response more directly captured the SLWG transmissivity for broadband itinerant signals, as well as because the transient response is less susceptible than the steady-state response to the compounding effects of multiple reflection events due to all impedance mismatches at the output of the SLWG and throughout the OUT line.

Additionally, we directly investigated the effect of reflection at the SLWG boundary on photon pulses emitted from the Q_E. For this measurement, shown in Fig. 3.S2e, a photon pulse with bandwidth of 9.8 MHz is emitted from Q_E prepared in the $|f\rangle$ state via shaped emission. This photon first propagates through the SLWG and is partially transmitted at the tapered boundary due to the finite transmissivity of the taper with transmittance T; this transmitted fraction then arrives at the ADC and the photon flux is measured. Meanwhile, the reflected fraction of the photon undergoes an additional round-trip in the SWLG, and thus arrives at the ADC time $t = \tau_\mathrm{d}$ later, as seen in Fig. 3.S2e. If this returning portion of the photon field interacts with the qubit during subsequent photon emissions, it can lead to qubit control errors as well as an overlap of our desired photon signal with this spurious reflected signal, which leads to measurement errors. Thus, when generating the four photon 2D cluster state presented in Fig. 4, and the 5 photon state presented in Fig. 3.S11, we had to ensure that photon emission did not overlap with the returning reflected portion of previously emitted pulses. Thus, for photons emitted after $t = \tau_\mathrm{d}$ into the generation sequence, their emission time was judiciously chosen to avoid this overlap. This is why there is a gap in time between the measured photon flux of photon 1 and photon 4 in Fig. 4c.

Qubits

To characterize the system consisting of Q_E and Q_M coupled to our SLWG, we performed multiple dynamical measurements. The central parameters of the system Hamiltonian, ω_p, J, g_{uc}, and g_{uc}^M were obtained via fitting the results from these measurements to the expected results from a time-domain simulation of a

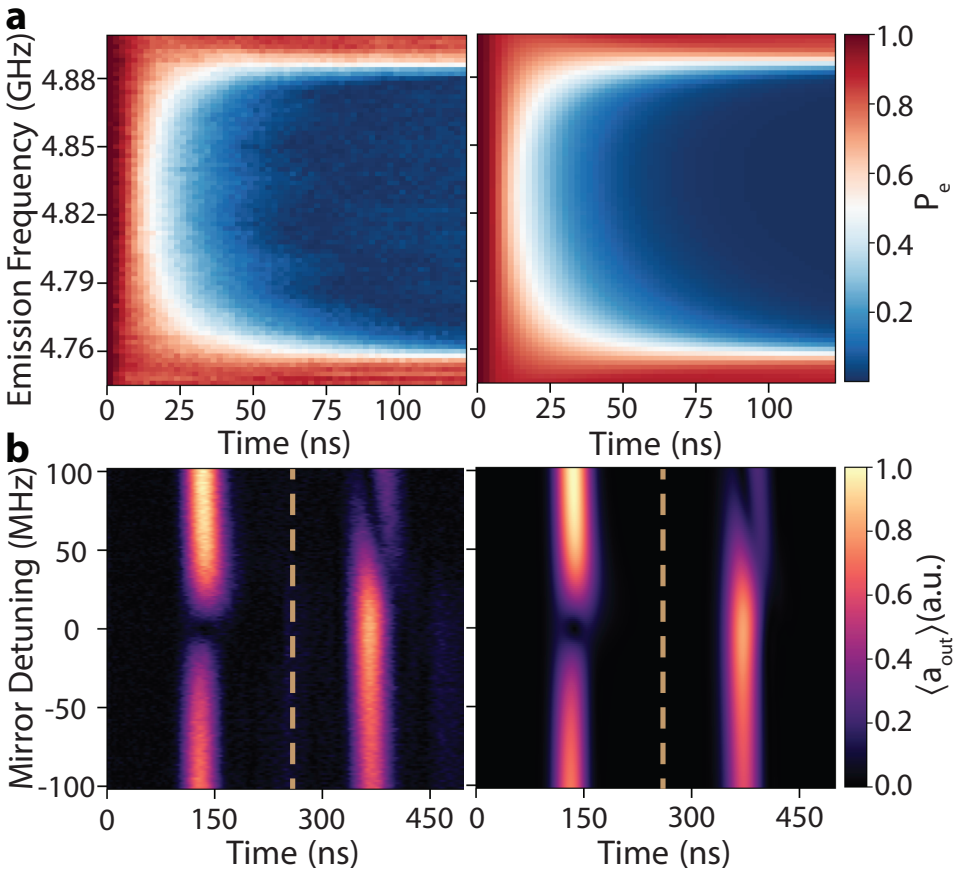

Figure 3.S3: **Emitter and mirror qubit characterization.** **a**, Left: Measured emission dynamics of Q_E prepared in $|e\rangle$, where emission to the ground state is induced via flux modulation with $\omega_{\text{mod}} = 450$ MHz. Right: fit to tight-binding model of equation 3.4. The fit yields SLWG center frequency of $\omega_p = 4.823$ GHz, Q_E to first unit cell coupling of $g_{uc}/2\pi = 35.16$ MHz, Q_E to second unit cell coupling of $g_{nuc}/2\pi = 2.27$ MHz, and unit cell to unit cell coupling $J/2\pi = 33.96$ MHz. **b**, Left: Measured averaged field of Q_E emission with different mirror detuning from the center of the passband; right: fit to single-excitation Hamiltonian yielding an effective mirror qubit to unit cell coupling of $g_{uc}^M/2\pi = 57$ MHz. In both cases, the mirror is detuned away from the passband after the time indicated by the dashed yellow line.

model Hamiltonian. In the following paragraphs, we discuss how we performed the measurements, and the simulation methods.

In order to investigate the interaction between Q_E and the SLWG, we measured the decay dynamics of Q_E prepared in $|e\rangle$ interacting with the SLWG, as found in Fig. 3.S3a (left). First, Q_E is prepared in the first excited state $|e\rangle_E$, following which flux modulation of Q_E's transition frequency induces an interaction between a sideband of Q_E and the SLWG. This interaction time (during which the flux modulation is on) is varied, and the sideband frequency is swept across the passband, as indicated on the x- and y-axis of Fig. 3.S3a, respectively. Finally, the interaction is deactivated by turning off the flux modulation, followed by readout of Q_E to measure the remaining population in $|e\rangle_E$. In this experiment, the flux modulation altered the effective qubit-unit cell coupling rate $g_{uc}^{\text{eff}} = \xi g_{uc}$, where ξ is the sideband amplitude. We implemented $\xi = 0.22$ (see Supplementary Section 3.7.3 for details on flux modulation) in order to slow down Q_E's intrinsic emission rate, such that we were able to perform time-resolved measurements of Q_E's dynamics without being restricted by the limited sampling rate of our instruments. However, the resulting decay rate is sufficiently strong such that the population in $|e_E\rangle$ completely decays to ground state when the sideband is resonant with the passband of the SLWG, as seen in Fig. 3.S3a.

The measured decay dynamics are fit to the following tight-binding interaction picture Hamiltonian:

$$\begin{aligned}\hat{H}^E = &(\omega_1^E - \omega_p)\,|e\rangle\langle e|_E + g_{uc}^{\text{eff}}(\hat{\sigma}_+^E \hat{a}_1 + \hat{\sigma}_-^E \hat{a}_1^\dagger) \\ &+ g_{nuc}^{\text{eff}}(\hat{\sigma}_+^E \hat{a}_2 + \hat{\sigma}_-^E \hat{a}_2^\dagger) + J\sum_{x=1}^{50}(\hat{a}_x^\dagger \hat{a}_{x+1} + \hat{a}_x \hat{a}_{x+1}^\dagger),\end{aligned} \tag{3.4}$$

where ω_1^E is the frequency of the sideband Q_E that is resonant with the SLWG, $\hat{\sigma}_+^E$, $\hat{\sigma}_-^E$ are the raising and lowering operators of Q_E, $\hat{a}_x^\dagger$, $\hat{a}_x$ are the raising and lowering operators of the unit cell resonator at position x, g_{nuc} is the parasitic coupling rate of Q_E to the second unit cell resonator, and $\xi = 0.35$ is the sideband amplitude that renormalizes the following coupling rates to $g_{uc}^{\text{eff}} = \xi g_{uc}$ and $g_{nuc}^{\text{eff}} = \xi g_{nuc}$. Note that g_{nuc}^{eff} accounts for the asymmetry of the decay dynamics at frequencies near the upper band edge and the lower band edge of the SLWG that is observed in the data, as discussed in [149]. Also note that the interaction time of Q_E with the SLWG

is shorter than τ_{d}, and thus the Hamiltonian terms involving the boundary taper resonators of the SLWG and Q_M can be neglected in this model.

With this Hamiltonian, we simulated the decay dynamics of Q_E initially prepared in $|e\rangle_E$ for various values of ω_1^E, as done in experiment. We restricted the simulation Hilbert space to the vacuum state and single-excitation manifold of the system, which is appropriate for simulation of the decay dynamics. The fit is performed with ω_p, J, g_{uc}^{eff}, and g_{nuc}^{eff} as fit parameters, yielding $\omega_p = 4.823$ GHz, $J = 33.96$ MHz, $g_{uc} = 35.16$ MHz, and $g_{nuc} = 2.27$ MHz, with the simulated dynamics shown in Fig. 3.S3a (right), demonstrating excellent agreement to the data.

With these parameters, we calculate the intrinsic $\Gamma_{1\mathrm{D}}$ of Q_E when it is tuned to the middle of the passband via the formula $2g_{\mathrm{uc}}^2/J$ [109, 150], where $2J$ is the group velocity (per unit cell) in the middle of the passband, while g_{uc} also corresponds to the coupling of the qubit to each propagating mode of the passband (note that this formula applies to a qubit end-coupled to a waveguide, while for a side-coupled qubit the effective $\Gamma_{1\mathrm{D}}$ is g_{uc}^2/J). The dependence of $\Gamma_{1\mathrm{D}}$ on J is reflective of the slow-light effect on the emission dynamics of the qubit, where a smaller J leads to a smaller group velocity $v_g = \frac{\partial\omega}{\partial k}$, which in 1D systems corresponds to a large density of states $1/\pi|v_g|$. Per Fermi's Golden Rule, a large density of states boosts emission rates for a given coupling [6]. Thus, due to the slow group velocity of the SLWG, we are able to achieve strong emission rates without relying on bulky coupling capacitors of the qubit to the waveguide, and instead achieve sufficient coupling by simply bringing the qubit island within enough proximity to the unit cell of the SLWG. This allows us to hew to the qubit design principles outlined in ref. [171] that ensure high qubit T_1. Note that we utilize this value of $\Gamma_{1\mathrm{D}}$ for absolute power calibration of measured field amplitudes (see App. 3.7.4).

In addition, the interaction of Q_M with an incident photon pulse as a function of Q_M's frequency was also investigated experimentally. The measurements consisted of emitting a Gaussian photon pulse from Q_E with a bandwidth of 9.8 MHz and carrier frequency ω_p via shaped photon emission, followed by rapid tuning of Q_M's frequency to the vicinity of the passband after the photon's one-way propagation time of $t = \tau_{\mathrm{d}}/2$ through the waveguide. This tuning is maintained for the duration of the emitted pulse's interaction with the mirror and then is subsequently turned off. These measurements are performed for various Q_M bias frequencies during the rapid tuning; the measured average SLWG output photon field $\langle a_{\mathrm{out}}\rangle$ as a function of Q_M frequency (see Supplementary Section 3.7.4 for details on measurement of

$\langle a_{\text{out}} \rangle$) is plotted in Fig. 3.S3b (left).

The transmitted fraction of the photon pulse upon the first incidence at the SLWG boundary is measured as the first bright feature at time 140 ns. When Q_M is tuned close to the center of the passband ("Mirror ON"), Q_M scatters the photon pulse with large Γ_{1D} and thus reflects most of the energy, which is observed as the disappearance of the first bright feature near zero detuning in Fig. 3.S3b. The second bright feature corresponds to the fraction of the photon pulse that was reflected at the SLWG boundary, traveled a round-trip through the waveguide, and subsequently exited the SLWG for measurement. Note that the yellow line in Fig. 3.S3b corresponds to the time when the Q_M fast flux bias is turned off, thus turning off the interaction of Q_M with subsequently incident photon fields.

The measured data of Fig. 3.S3b are fit to the expected output photon field, which is simulated with the following model Hamiltonian:

$$\begin{aligned} \hat{H}^{EM} &= \hat{H}^{E}(t) \\ &+ \Delta^{M}(t)\,|e\rangle\langle e|_{M} + g_{uc}^{M}(\hat{\sigma}_{+}^{M}\hat{a}_{50} + \hat{\sigma}_{-}^{M}\hat{a}_{50}^{\dagger}) \\ &+ \Delta_1 \hat{a}_{51}^{\dagger}\hat{a}_{51} + \Delta_2 \hat{a}_{52}^{\dagger}\hat{a}_{52} + J_1(\hat{a}_{51}^{\dagger}\hat{a}_{52} + \hat{a}_{51}\hat{a}_{52}^{\dagger}), \end{aligned} \tag{3.5}$$

where $\Delta^M(t)$, Δ_1, and Δ_2 are the detunings of Q_M, the left taper cell resonator, and the right taper cell resonator from the center of the passband ω_p respectively, σ_+^M, σ_-^M are the raising and lowering operators of Q_M, and J_1 is the photon hopping rate between the taper cell resonators. We replicate the described rapid tuning of Q_M used in the experiment via the Hamiltonian time-dependent term $\Delta^M(t)$. In addition, the external loading of the system to the output 50 Ω waveguide is implemented in the model via a dissipation collapse operator in the last taper resonator with rate $\kappa = 148$ MHz (calculated from circuit parameters of the system). $\hat{H}^E(t)$ corresponds to the Hamiltonian of equation 3.4 where ξ is time-dependent, which allows us to model shaped photon emission. The envelope of output field $|\langle a_{out}(t)\rangle|$ is obtained in the simulation via taking the time derivative of the accumulated population in the zero-excitation ground state. This output field obtained from the simulation is fit to the measured data by utilizing Δ_1, Δ_2, g_{uc}^M, and J_1 as fit parameters, yielding $\Delta_1 = -6$ MHz, $\Delta_2 = -70$ MHz, $g_{uc}^M = 57$ MHz, and $J_1 = 45.4$ MHz. The simulated dynamics, shown in Fig. 3.S3b (right), demonstrates excellent agreement to the data.

In our modeling, the non-zero Δ_1 and Δ_2 fit values account for the asymmetry of the measured photon field at positive detunings of Q_M and negative detunings

of Q_M that is observed in the data. Moreover, in our model we do not include parasitic couplings of Q_M to neighboring resonators, and thus any effect of parasitic couplings on the overall Γ_{1D} and reflectance of Q_M are incorporated into the one effective coupling rate g_{uc}^M. We note that the fitted value of g_{uc}^M is consistent with the amount of transmitted energy from an incident photon that Q_M does not reflect, calculated as 0.03 from the data in Fig. 3c; this corresponds to a "mirror efficiency" of 0.97 as we have defined it.

Purcell filter

We perform conventional dispersive readout of the state of our qubits by probing $\lambda/4$ coplanar waveguide resonators that are capacitively coupled to the qubits in the dispersive regime. There is an implicit speed-fidelity tradeoff in such readout schemes due to the Purcell decay of the qubit into the readout lines mediated by the readout resonator to which it is coupled. Reducing the Purcell decay without adding auxiliary circuit components requires reducing the dispersive shift of the cavity, thus reducing readout SNR, or the readout resonator decay rate κ, thus reducing readout speed [172]. The common method for bypassing the implicit speed-accuracy tradeoff of such a readout scheme is to add an extra layer of bath engineering via a Purcell filter that modifies the environmental impedance seen by the qubit-resonator system so as to maintain a desirably large κ (for rapid information gain about the qubit state) while simultaneously suppressing decay at the qubit center frequency [172–174].

A Purcell filter can be modeled by replacing the series impedance of the output CPW seen by the qubit-resonator system with a frequency-dependent environmental impedance $Z_{\text{ext}}(\omega)$. Within such a model the qubit Purcell decay is given by [175]:

$$\gamma_P^{\text{filt}} = \kappa \frac{g^2}{\Delta^2} \frac{\text{Re}\, Z_{\text{ext}}(\omega_q)}{\text{Re}\, Z_{\text{ext}}(\omega_r)} \tag{3.6}$$

which is just the bare Purcell decay weighted by the ratio of the real impedances of the external load at the qubit and readout resonator frequencies. Thus, by engineering the frequency-dependence of Z_{ext} to be matched to the output CPW at ω_r, while have negligible real part at ω_q, we can surpress Purcell decay while efficiently probing the readout resonator.

A coupled resonator array, such as the one we use to implement the SLWG used in our experiment, can be used as a Purcell filter due to its highly flexible impedance properties, allowing for a purely imaginary Bloch impedance at frequencies outside of its passband and a purely real Bloch impedance inside [176]. Ideally this allows

for complete extinction of qubit Purcell decay by placing ω_Q outside the passband of the array, while maintaining high readout speed by placing ω_r within the passband. In essence, the coupled resonator array has a large nonzero density of states through which the readout resonator can decay if ω_r is within the passband, while having no density of states, and thus no available decay channels, at the qubit frequency [149].

To that end, we engineered a Purcell Filter Waveguide (PFWG) serving as a single Purcell filter for the two readout resonators of both the emitter and mirror qubits. The Purcell filter, which can be seen in Fig. 3.S4 a. and b., extends between two ports of our device and replaces the usual CPW readout lines to which readout resonators are coupled to on chip. It has the same circuit topology as the SLWG designed for the cluster state generation scheme, comprising 54 lumped element resonator unit cells coupled to their nearest neighbors capacitively. Referring to the model of Fig. 3.S4b., the circuit parameters $L_0' = 1.2$ nH, $C_0' = 323.5$ fF, $C_g' = 19.5$ fF, $C_1' = 315.0$ fF, $C_{1g}' = 27.4$ fF, $C_2' = 218.2$ fF, $C_{2g}' = 126.4$ were targeted for the PFWG using the same principles employed in designing the SLWG.

The transmission spectrum of the PFWG, including the two resonances of the readout resonators, can be seen in Fig. 3.S4 c. The passband of the PFWG is situated from 7.24 GHz to 7.9 GHz so as to safely encompass the resonances of both Q_E and Q_M readout resonators centered at $\omega_{RM} \sim 7.4$ GHz and $\omega_{RE} \sim 7.7$ GHz respectively, while excluding the entire tuning ranges of the qubits and the frequency of a pump tone at ~ 7.95 GHz used for driving a Josephson Travelling Wave Parametric Amplifier (TWPA) for output signal amplification. The qubit frequency ω_{ge}, anharmonicity $\eta = \omega_{ef} - \omega_{ge}$, and dispersive shift χ related to single shot readout are listed in Table. 3.1.

Table 3.1: List of measured qubit frequency ω_{ge}, anharmonicity η, and dispersive shift χ for Q_E and Q_M at zero flux bias.

	$\omega_{ge}/2\pi$ (GHz)	$\eta/2\pi$ (MHz)	$\chi/2\pi$ (MHz)
Q_E	6.21	-276	2.1
Q_M	6.44	-280	3.4

The readout resonators are inductively side-coupled to the PFWG by bringing the current anti-node of the $\lambda/4$ resonator into close proximity to the grounded end of a unit cell's meander trace, as can be seen in Fig 3.S4a, for a target resonator decay rate of $\kappa = 10$ MHz. Due to geometric constraints each resonator was coupled to one of the eleventh unit cells of the PFWG counted from its ends. Note that we

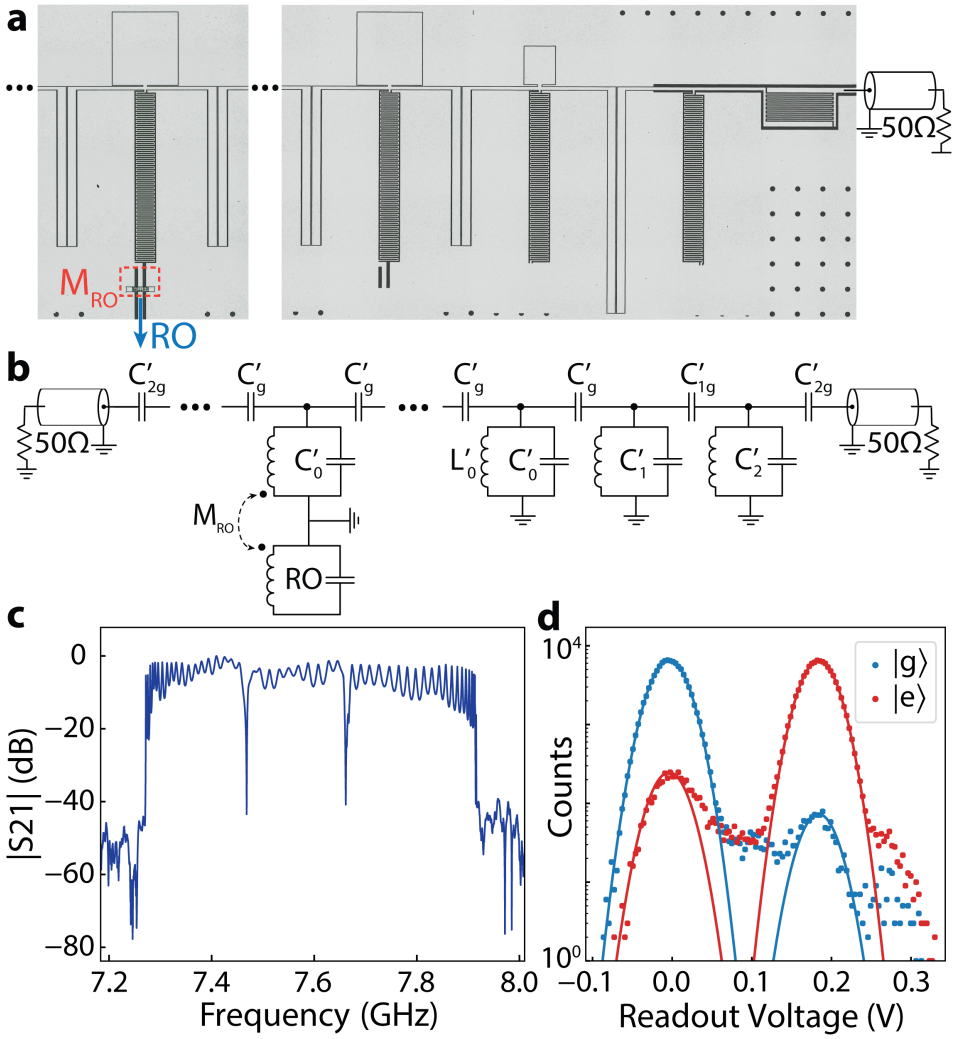

Figure 3.S4: **Purcell filter waveguide and readout characterization a**, False-colored optical image of the on-chip Purcell filter waveguide. The image on the right depicts one end of the Purcell filter waveguide, while the image on the left depicts the unit cell inductively coupled to one of the CPW readout resonators of the qubits **b**, Full circuit model of the purcell filter and an inductively coupled readout resonator. **c**, Transmission spectrum of the full purcell filter waveguide with two side-coupled readout resonators R_E and R_M. **d**, Log-linear raw histogram of single-shot readout measurement results for 100,000 ground state preparations and 100,000 excited states preparations. Solid lines are fits to a bimodal normal distribution. Readout fidelity = 97.6% was obtained from this histogram.

chose inductive coupling to the PFWG via the current anti-node of the resonator because that afforded strong coupling to the PFWG, while still allowing for capacitive coupling to the qubit at the resonator's charge anti-node.

The readout-unit cell coupling strength was adjusted in design by changing the distance between the last airbridge of the readout resonator and the current anti-node of the resonator near the meander trace of the PFWG unit cell. Moving the airbridge closer to the coupling point reduces the overall strength of the inductive coupling, while moving it away increases the strength. We believe the presence of the airbridge screens the extent of magnetic fields generated by the current near the coupling point and thus reduces the overall overlap volume of fields generated by the resonator and the PFWG unit cell. The fabricated resonator decay rate was found to be approximately $\kappa \sim 11$ MHz. Moreover, the dispersive shift of the readout resonator was measured to be $2\chi = 4.2$ MHz for a qubit-readout resonator detuning of $\Delta = 1.45$ GHz, yielding a qubit-resonator coupling strength $g \sim 140$ MHz that agrees well with the design value. The measured Purcell-protected T_1 time of Q_E at its upper sweet spot was measured to be $20\mu s$, which is more than one order of magnitude larger than what would be expected in the absence of a Purcell filter; we believe this T_1 is ultimately limited by sample loss.

In order to optimize Q_E's single shot readout, we first found the readout probe pulse carrier frequency and length that maximized the complex voltage contrast between the readout transmission when Q_E was initialized to either $|g\rangle$ or $|e\rangle$. Due to the distorting effects of the ripples in the PFWG transmission spectrum, the optimal frequency of the readout probe tone was found empirically. We also chose the optimal readout power by maximizing contrast while avoiding any powers that led to spurious features in the 2D single shot readout signal histograms in the IQ plane (which we attributed to readout-induced qubit transitions). To characterize the readout fidelity we prepared Q_E in either the $|g\rangle$ or $|e\rangle$ state, and measured histograms of demodulated single shot signals resulting from probing the readout resonator. These histograms were fit to a double-Gaussian model seen in Fig 3.S4 d. from which a ground-excited discrimination boundary was determined. The readout fidelity with respect to this discrimination boundary was found to be 97.6%; this high single shot readout fidelity was an important resource for the joint qubit-photon measurements required for the quantum process tomography of the CZ gate used in the cluster state generation protocol.

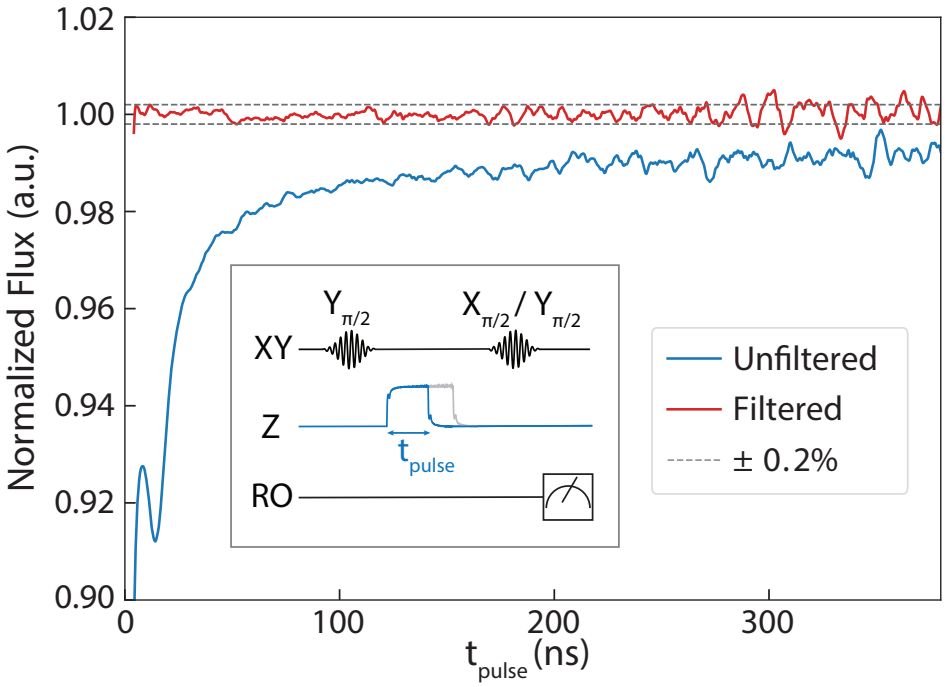

Figure 3.S5: Reconstructed step response of flux line with and without "Cryoscope" distortion pre-compensation. The pulse sequence used for reconstructing the step response is illustrated as an inset; see Supplementary text for further details.

3.7.3 Flux control for shaped photon emission and qubit-photon CZ gate

As alluded to in the main text, sophisticated flux control techniques for dynamical control of the qubit frequency were critical in achieving both shaped photon emission as well as a high fidelity qubit-photon CZ gate. Below we present a summary of the techniques we employed in order to achieve distortion free square flux pulses at Q_E and Q_M, and precise control of the time-dependent coupling between Q_E and the SLWG via flux modulation.

Distortion pre-compensation of square flux pulses

Contributions from dilution refrigerator wiring to signal distortions from flux control lines are often temperature dependent, necessitating techniques for *in situ* characterization of such distortions via the controlled qubit itself. We used the so-called "Cryoscope" technique [177], consisting of Ramsey-type measurements to reconstruct the step-response of the flux line followed by iterative digital pre-compensation, to mitigate distortion in our Z_E and Z_M lines. With pre-compensation, we achieved a desired flat step response within ±0.2% of error, as depicted in Fig. 3.S5, for both qubits. The qubit measurements undertaken to

reconstruct the step response of the flux line are shown in the inset of Fig. 3.S5. We refer the reader to ref. [177] for a detailed description of the entire "Cryoscope" process, and discuss small modifications to what is presented in ref. [177] below.

Firstly, we observe that we did not require real-time digital filtering given that our pulse sequences were only $\sim$ 500 ns in length, and thus chose to use pre-compiled waveforms in order to have more computational flexibility for pre-distortion. Additionally, we note that we observed residual long-time transient responses when applying pre-compensated flux pulses, as discussed in ref. [178]. To address this problem, rather than waiting for decay of the transient response, a negative copy of the flux signal is appended at the end of every sequence.

Moreover, when obtaining the reconstructed step response, we found it useful to digitally filter the $\langle X \rangle(t) + i\langle Y \rangle(t)$ data, in order to eliminate data contributions from phase errors in the gates or population offsets, which manifest themselves as spurious features in the spectrum of the data. Moreover, we apply oscillating decaying exponential IIR filters of the form $1 + Ae^{-t/\tau_{\mathrm{IIR}}} \cos(\omega_{\mathrm{IIR}} t + \phi_{\mathrm{IIR}})$ in addition to solely decaying exponential IIR filters to achieve better pre-compensation. Finally, for the FIR short-scale precompensation, we mention that it is important to include the smoothing effects of the Savitzky-Golay filter in calculation of the predicted signal from the optimized FIR coefficients.

Photonic pulse shaping

As described in the main text, it is important to properly control the time-domain shape of emitted photon pulses in order to ameliorate the effects from the SLWG's non-linear dispersion and to improve the fidelity of the qubit-photon CZ gate. Arbitrary photon pulse shapes can be achieved by controlling the time-dependent decay rate of the Q_E, which necessitates a tunable interaction between Q_E and the SLWG.

For flux-tunable transmon qubits, such tunable interaction can be attained via sinusoidal flux modulation of the qubit frequency (depicted in Fig. 3.S6a) which induces a sideband-mediated interaction with the SLWG whose strength is controlled by the amplitude of the flux modulation AC flux drive [151–153]. In this work, we utilize amplitude modulated AC flux pulses to dynamically control the sideband interaction strength between Q_E and the SLWG, thereby achieving shaped photon pulses. In the following paragraphs, we discuss the theory and technical details of our flux modulation based pulse shaping technique.

We first review the underlying physics of flux modulation by analyzing the following Hamiltonian of a qubit coupled to a waveguide:

$$\hat{H} = \frac{1}{2}\omega_Q(\Phi(t))\hat{\sigma}_z + \int_k \omega_k \hat{a}_k^\dagger \hat{a}_k + g_Q \int_k (\hat{\sigma}_- \hat{a}_k^\dagger + \hat{\sigma}_+ \hat{a}_k), \tag{3.7}$$

where $\omega_Q(\Phi(t))$ is the qubit frequency of Q_E as a function of the time-dependent flux $\Phi(t)$, ω_k is the frequency of a propagating waveguide mode with wavevector k, g_Q is the unit cell coupling of Q_E, $\hat{\sigma}_+$, $\hat{\sigma}_-$ are the raising and lowering operators of Q_E (note that in this model, the two levels of the qubit correspond to the $|e\rangle$ and $|f\rangle$ levels of Q_E that participate in photon emission in our experiment) and $\hat{a}_k^\dagger$, $\hat{a}_k$ are the raising and lowering operators of mode k. By going into the interaction picture by the unitary transformation $U(t) = \exp[-i\int_0^t \frac{1}{2}\omega_Q(\Phi(t'))\hat{\sigma}_z dt' - it\int_k \omega_k \hat{a}_k^\dagger \hat{a}_k]$, we arrive at the following interaction Hamiltonian:

$$\hat{H}_{int} = g_Q \int_k e^{-i(\phi(t)-\omega_k t)} \hat{\sigma}_- \hat{a}_k^\dagger + \text{h.c.}, \tag{3.8}$$

where $\phi(t) = \int_0^t \omega_Q(\Phi(t'))dt'$. Note that g_Q here is independent of k, as is the case for a qubit coupled to a single unit cell of an infinite periodic array of coupled resonators [109].

Under sinusoidal modulation of external flux $\Phi(t)$, we can write $\Phi(t) = \Phi_B + \Phi_{AC}\sin(\omega_{\text{mod}}t)$, where Φ_B is the the static flux bias of Q_E, Φ_{AC} is the AC flux ampltiude, and ω_{mod} is the modulation frequency. The periodicity of the flux signal allows for the $e^{-i\phi(t)}$ term to be expanded by the following Fourier series [179]:

$$\hat{H}_{int} = g_Q \int_k \sum_s \xi_s e^{-i(\tilde{\omega}_Q - s\omega_{\text{mod}} - \omega_k)t} \hat{\sigma}_- \hat{a}_k^\dagger + h.c., \tag{3.9}$$

where $\tilde{\omega}_Q$ is the average of ω_Q, and ξ_s is the Fourier coefficient of the s-th term, which we refer to as the "sideband amplitude". We note that because the tuning curve is non-linear (as depicted in Fig. 3.S6a), sinusoidal flux modulation will result in an average DC shift to the static qubit frequency $\omega_Q(\Phi_B)$, which is captured by the term $\tilde{\omega}_Q$. Moreover, note that one can obtain the magnitudes of ξ_s by simply taking the Fourier transform of $e^{-i\phi(t)}$, as shown in Fig. 3.S6b for one set of flux modulation and qubit parameters.

According to the RWA, we expect that only non-fast rotating terms of the Hamiltonian of equation 3.9 would appreciably contribute to the qubit dynamics; hence

we seek terms where $\tilde{\omega}_Q - s\omega_{\text{mod}} - \omega_k \approx 0$. Assuming that the waveguide has a finite bandwidth passband, and that only the first lower sideband ($s = 1$) is resonant with one of the passband modes, we can assume terms involving all other s are fast-rotating terms and discard them. This results in the final Hamiltonian:

$$\hat{H}_{mod} = g_Q \xi \int_k e^{-i(\omega_Q^1 - \omega_k)t} \hat{\sigma}_- \hat{a}_k^\dagger + \text{h.c.}, \tag{3.10}$$

where $\omega_Q^1 \equiv \tilde{\omega}_Q - \omega_m$ is the frequency of the first lower sideband, and $\xi \equiv \xi_1$. Thus, $\omega_k = \omega_Q^1$ will be the center frequency of emission, while photon emission will also occur at surrounding frequencies where $\omega_Q^1 - \omega_k$ is small; thus imparting a finite bandwidth to any emitted photon. Note that the resultant Hamiltonian is in an equivalent form as Eq. (3.8) up to a renormalization of the effective coupling rate. Thus, we can tune the strength of interaction between Q_E and the SLWG by controlling the sideband amplitude ξ and locating the first lower sideband inside the passband.

We are able to accurately predict the necessary AC flux drive amplitudes to achieve desired values of ξ by numerical calculation of the "sideband spectrum" of Q_E under flux modulation. Remembering that we are concerned with emission from the $|f\rangle$ state, for this calculation, we require the functional form of the qubit tuning curve $\omega_{ef}(\Phi)$, the static flux bias Φ_B, and the strength of the sinusoidal flux drive Φ_{AC}. We adopted the analytical form of the transmon tuning curve from ref [179] for accurate calculation of ω_{ef} as a function of Φ, as depicted in Fig. 3.S6a (gray solid line), from measurement of the highest qubit frequency, the lowest qubit frequency, and the anharmonicity η at the highest qubit frequency.

The sideband spectrum is calculated via the Fourier Transform of $e^{-i\phi(t)}$, with an example shown in Fig. 3.S6b, where the $s = 1$ sideband is highlighted in red. The spectrum yields the different ξ_s, as well as the average "DC shift" of the qubit frequency $\delta_{DC} \equiv \tilde{\omega}_Q - \omega_Q(\Phi_B)$ which depends on both Φ_B as well as Φ_{AC}. We can leverage this DC shift effect to obtain a mapping from AC flux amplitude at the qubit to input AC voltages to the fridge, as illustrated in Fig. 3.S6e. By inducing Q_E emission via flux modulation at various AC input voltages and measuring the carrier frequency of emitted photons, we observe the average DC shift of the qubit frequency via the changing carrier frequency of emitted photons. By comparing the change in photon carrier frequency to numerical predictions of δ_{DC}, we can obtain the scaling factor for converting input AC voltages to Φ_{AC} at the qubit. Meanwhile,

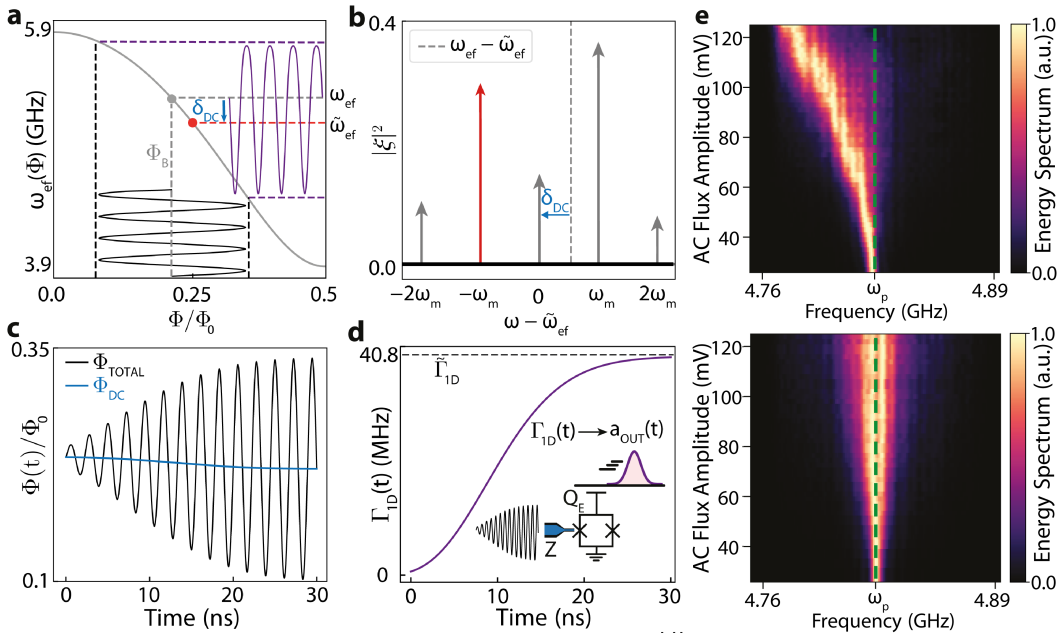

Figure 3.S6: **Pulse shaping via flux modulation of the emitter qubit a**, Illustration of flux modulation of the emitter qubit, when the qubit has a static flux bias $\Phi_B = 0.234\Phi_0$ and the AC flux amplitude $\Phi_{AC} = 0.152\Phi_0$, where Φ_0 is the magnetic flux quantum. The gray curve is the ω_{ef} emitter qubit tuning curve. The black line depicts typical flux modulation amplitudes in terms of flux quanta, while the purple curve depicts qubit frequency as a function of time under flux modulation. $\tilde{\omega}_{ef}$ corresponds to the average qubit frequency under flux modulation. **b**, Sideband spectrum of the emitter qubit under flux modulation. $|\xi|$ refers to sideband strength. The red colored arrow corresponds to the sideband used to effect emission into the SLWG in our experiment. **c**, Flux-modulation waveform used in experiment to generate high-bandwidth photons 2, 3, and 4. The blue curve corresponds to a dynamic DC correction that is used to maintain the emission frequency constant; see text for details. **d**, Effective $\Gamma_{1D}(t)$ obtained from the flux modulation waveform shown in **c**. **e**, Energy spectra of qubit emission for a constant flux modulation amplitude that is swept. Left: Energy spectra without DC shift compensation. Right: Energy spectra with DC shift compensation, where DC shifts are calculated theoretically assuming an specific insertion loss in the flux line for the used ω_{mod}.

note that we obtain a similar scaling factor for converting static DC bias voltages to Φ_B at the qubit via measurements of the qubit tuning curve (note that the two scaling factors are different due to differing DC and AC losses of the flux line).

Thus, we can achieve a desired time-dependent coupling between Q_E and the SLWG via flux modulation, by effecting a time-dependent $\xi(t)$ via some specific $\Phi_{AC}(t)$. However, a time-dependent $\Phi_{AC}(t)$ will also lead to a time-dependent $\delta_{DC}(t)$, which necessitates a "DC correction" signal to maintain the emission frequency constant. Therefore, we obtain the necessary flux drive $\Phi(t) = \Phi_{DC}(t) + \Phi_{AC}\sin(\omega_{\text{mod}}t)$ that achieves a desired $\xi(t)$ while maintaining a constant emission frequency. This is achieved by considering a suitable range of AC flux amplitudes, and obtaining associated Φ_{DC} correction flux biases for each flux amplitude such that for a given Φ_{AC}, overall static qubit bias Φ_B, and the flux amplitude dependent correction bias Φ_{DC}, the average qubit frequency $\tilde{\omega}_{ef}$ will be equal to $\omega_{ef}(\Phi_B)$; see Fig. 3.S6e (right) for demonstration of this DC correction procedure for various AC flux amplitudes. Then, the sideband amplitudes $\xi(\Phi_B, \Phi_{AC}, \Phi_{DC})$ are numerically calculated for each set of the aforementioned parameter values, with which a desired $\xi(t)$ can be mapped to the necessary $\Phi(t)$ signal; see Fig. 3.S6c,d for an example. Finally, we note that under the flux drive $\Phi(t)$, the time-dependent decay rate $\Gamma_{1D}^{ef}(t)$ of Q_E will be equal to $\Gamma_{1D}^{ef} \cdot |\xi(t)|^2$, where Γ_{1D}^{ef} is the intrinsic decay rate of the $|f\rangle$ state given by $\sim 4g_{uc}^2/J$.

As discussed in the main text, we sought to emit Gaussian shaped photons for our cluster state generation sequence, as illustrated in Fig. 2. We observed, both numerically and experimentally, that shaped photons with Gaussian spectra could be emitted by realizing the following sideband amplitude time dependence $\xi(t)$:

$$\begin{aligned} \xi(t) &= \xi_M \text{erf}^2\left(\frac{t}{t_R} + \delta\right) \\ \text{erf}(t) &\equiv \frac{2}{\sqrt{\pi}} \int_0^t e^{-t'^2} dt', \end{aligned} \tag{3.11}$$

where t_R scales the erf function with respect to time, ξ_M is the maximum attainable sideband amplitude at a given Φ_B, and the second line defines the erf function whose square increases from 0 and converges to 1 smoothly. The spectral bandwidth of the resultant Gaussian pulse is controlled by t_R, where slow (fast) increase of $\Gamma_{1D}(t)$ due to large (small) t_R leads to small (large) bandwidth. Moreover, the δ parameter shifts the entire function with respect to time, such that it reduces the time needed to reach the maximum sideband amplitude for a given emission time and t_R; this is

useful to further suppress residual $|f\rangle$ population after emission for short emission times. This parametrized time dependence is plotted in Fig. 3.S7a.

For the photonic pulses shown in Fig. 4c, photon 1 was generated by realizing the time-dependent sideband amplitude $\xi(t)$ of equation 3.11 with parameters $t_R = 50$ and $\delta = 0$, yielding a Gaussian pulse with 9.9 MHz bandwidth. However, for photons 2,3,4 we chose to utilize a finite δ in order to achieve a small $|f\rangle$ residual $|f\rangle$ population for the photons' short 30 ns emission time. In order to obtain the best δ, t_R combination, we modeled and measured experimentally this residual population after photon emission for a range of δ, t_R values, as depicted in Fig. 3.S7b,c (see App. 3.7.2 for modeling details). We found that the combination $t_R = 15$ ns, $\delta = 0.33$, suppresses residual $|f\rangle$ state population below 1% and constricts emitted photon pulses to a short time-bin measurement window, and we chose this parameter combination for emission of photons 2,3,4 depicted in Fig. 4c. We note that while higher δ values in general result in less residual $|f\rangle$ population, large δ values also lead to distortions in the emitted Gaussian pulse; thus the parameter choice $t_R = 15$ ns, $\delta = 0.33$ strikes a balance between minimizing residual $|f\rangle$ state population and maintaining the approximately Gaussian shape of the emitted pulse with 17.9 MHz bandwidth.

We also note that we realize fast unconditional reset using flux modulation, where the $|e\rangle$ and $|f\rangle$ state populations are emptied via induced photon emission. First, a constant flux modulation signal that induces emission of $|f\rangle$ to $|e\rangle$ is applied to Q_E. Next, another constant flux modulation signal that induces emission from $|e\rangle$ to $|g\rangle$ is applied to Q_E, bringing it to the ground state. Lastly, we wait approximately 3 μs after this reset before starting qubit control, in order to allow residual emitted fields trapped in the SLWG due to finite taper reflections to fully leave the waveguide. We note that this reset protocol effectively thermalizes Q_E to the SLWG temperature; indeed we confirm via separate measurements that the resultant $|e\rangle$ thermal population is $\sim 1\%$ (corresponding to an effective ~ 50 mK temperature). Using this unconditional reset protocol, we generate the 2D cluster state with a conservative repetition rate of 100 kHz.

3.7.4 Radiation field quantum state tomography

In order to characterize generated multipartite entangled photonic states, we utilize tomography methods for itinerant microwave photons that were pioneered in Circuit QED systems by Eichler et. al. [99, 180] with suitable modifications when appro-

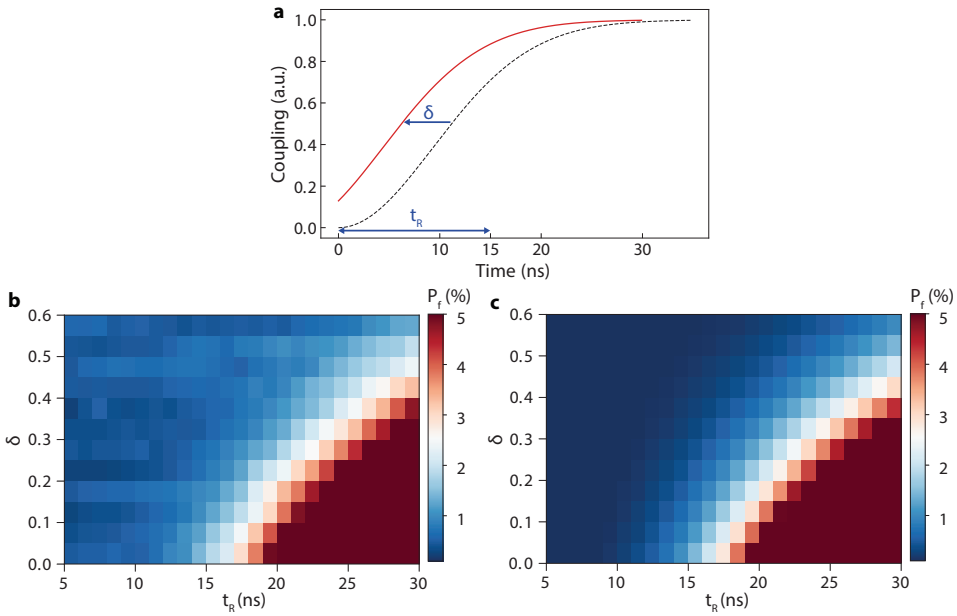

Figure 3.S7: **High bandwidth photon emission a**, Shape of time-dependent coupling effected by flux modulation, given by the square of the erf function: $\left|\frac{2}{\sqrt{\pi}}\int^{t/t_R+\delta} e^{-t'^2}dt'\right|^2$, where t_R and δ scale and shift the erf function with respect to time, respectively. **b** Residual $|f\rangle$ state population measurement after photon emission via flux modulation with various t_R and δ parameters. **c** Simulation of the experiment done in part **b**, using the model of equation 3.4.

priate for us. Below we present a detailed summary of our entire data analysis and tomography procedure. We conclude by presenting additional photonic quantum state preparation and tomography results not presented in the main text.

Measurement of $\langle a_{\mathbf{out}}(t)\rangle$ and $\left\langle a^{\dagger}{}_{\mathbf{out}}(t)a_{\mathbf{out}}(t)\right\rangle$

The average photon flux $\left\langle a^{\dagger}{}_{\mathrm{out}}(t)a_{\mathrm{out}}(t)\right\rangle$ and average field $\langle a_{\mathrm{out}}(t)\rangle$ of emitted photons are routinely measured in our experiment for the purposes of characterizing our shaped photon emission procedure, characterizing different aspects of our time-delayed feedback process, and obtaining mode matching functions $f(t)$ for the different photonic qubits in order to obtain time-independent statistics from their time-dependent fields (see rest of Supplementary text for further details). Measurement of both of these quantities for an emitted photon starts with heterodyne measurement of both quadratures, $I(t)$ and $Q(t)$, of its time-dependent microwave field, via the output chain described in Supplementary Section 3.7.1. Many measurements are performed and their results are averaged to compute the average field $\langle V(t)\rangle = \langle I(t) + iQ(t)\rangle$

and the the average photon flux $\langle V^2(t)\rangle = \left\langle |I(t)|^2 + |Q(t)|^2 \right\rangle$. Note that the calculation of $\langle V^2(t)\rangle$ results in a signal without any carrier frequency, but $\langle V(t)\rangle$ retains the carrier frequencies of $I(t)$ and $Q(t)$ which must be removed by digital demodulation.

Due to spurious DC shifts in the detection set-up, as well as imbalance and LO bleedthrough in the downconversion IQ mixer, the spectrum of $\langle V^2(t)\rangle$ and the demodulated $\langle V(t)\rangle$ will have spurious features outside of the baseband signal. In addition, these band-limited baseband signals will also have significant noise outside of their bandwidth. These undesirable features serve to obscure the time-dependent shape of the baseband signal that we wish to measure, and we remove them through digital low-pass filtering, with filter bandwidth set to be sufficiently high to capture all of the baseband signal. At this point, the resultant demodulated and filtered $\langle V(t)\rangle$ signal, followed by suitable normalization, can already be used as the mode-matching function $f(t)$, where the normalization is such that $\int |f(t)|^2 dt = 1$.

Further, with an absolute power calibration of our output chain that maps voltage measured at the ADC to field amplitude at the qubit (see subsequent subsection for details on how to obtain this calibration), the digitally processed $\langle V^2(t)\rangle$ and $\langle V(t)\rangle$ signals can be suitably scaled to yield the true $\left\langle {a^\dagger}_{\text{out}}(t) a_{\text{out}}(t)\right\rangle$ and $\langle a_{\text{out}}(t)\rangle$ in units of photon/s and $\sqrt{\text{photon/s}}$, respectively. However, for the purposes of plotting in this manuscript, we presented these quantities in terms of unitless, normalized values $\langle \tilde{a}_{\text{out}}\rangle = \langle a_{\text{out}}\rangle / \tilde{\Gamma}_{1D}^{-1/2}$ and $\left\langle \tilde{a}^\dagger_{\text{out}} \tilde{a}_{\text{out}}\right\rangle = \left\langle {a^\dagger}_{\text{out}} a_{\text{out}}\right\rangle / \tilde{\Gamma}_{1D}$, where $\tilde{\Gamma}_{1D}/2\pi = 40.8$ MHz is the maximum expected emission rate of the $|f\rangle \rightarrow |e\rangle$ transition under flux modulation induced emission (see Supplementary Section 3.7.3 for further details regarding $\tilde{\Gamma}_{1D}$). Thus, these normalized quantities express the time-dependent photon flux and field as a *fraction* of the maximum expected photon flux and field, respectively, for an excited qubit with emission rate $\tilde{\Gamma}_{1D}$ (as an illustrative example, note that for constant flux modulation with flux amplitude that yields $\Gamma_{1D}^{ef}(t) = \tilde{\Gamma}_{1D}$, $\left\langle \tilde{a}^\dagger_{\text{out}} \tilde{a}_{\text{out}}\right\rangle$ at $t = 0$ would be equal to 1).

Absolute power calibration

In order to perform quantum state tomography via heterodyne detection, we need an absolute power calibration that maps voltage measured at the ADC to field amplitude at the qubit's location on the device, given by some conversion factor G. This conversion factor G includes the following contributions: the scaling from the quantum field a to the physical voltage on the device, the gain of the output

chain from the first amplifier forward, and the detection efficiency η_{det}. We define η_{det} such that $(1 - \eta_{\text{det}})$ corresponds to the fraction of the itinerant photon's energy that is lost before it reaches the first amplifier (which in our case is a quantum-limited TWPA), either due to the loss or spurious reflections that are suffered by the photon (see Fig. 3.S2e for measurement of such reflections). Generically, G is obtained by measuring a signal at the ADC whose power at the qubit can be independently verified. In our work, we rely on measurement of the AC Stark shift of the qubit frequency induced by an input pulse on the SLWG as our method for power calibration.

The procedure for obtaining G via AC Stark shift measurements is the following. The qubit frequency ω_{ge} is detuned from ω_p by 740 MHz. A square pulse with carrier frequency ω_p is sent into the SLWG, for varying input powers. This square pulse induces an AC Stark shift Δ^{AC} on the qubit frequency whose magnitude is dependent on the SLWG input power; this Δ^{AC} is measured by determining the resonance excitation frequency of the qubit. The qubit's resonance frequency is measured by applying an excitation pulse to the qubit while the SLWG input pulse is off-resonantly driving the qubit; by sweeping the excitation pulse's frequency, measuring the qubit response, and fitting the resultant lineshape to a Gaussian, we obtain the resonance frequency via the Gaussian's mean. Repeating this procedure for all SLWG input powers, we experimentally obtain the dependence of Δ^{AC} on the power of the SLWG input pulse. Finally, the amplitude of the SLWG input pulse is measured at the ADC for all input powers used.

The power dependence of Δ^{AC} is then fit to the following transmon AC Stark shift model involving five transmon levels [181]:

$$\hat{H} = \sum_{j=0}^{N=4} \left(j\Delta + j(j-1)\eta\right) |j\rangle \langle j| + \frac{\Omega}{2}\left(\sqrt{j+1}\,|j+1\rangle \langle j| + \text{h.c.}\right), \tag{3.12}$$

where $\{j\}$ corresponds to the transmon levels, the SLWG drive frequency is ω_p, $\Delta = \omega_{ge} - \omega_p$, the transmon anharmonicity is $\eta/2\pi = -277$ MHz, and Ω is the Rabi frequency of the SLWG drive. Note that this Hamiltonian is obtained from the full Hamiltonian of a transmon interacting with a classical drive by simply going into the rotating frame of the drive (via the unitary transformation $U = \exp\left[it \sum_j j\, |j\rangle \langle j|\, \omega_p\right]$) and discarding counter-rotating terms. Also note that our model includes multiple transmon levels because the presence of multiple

transitions, along with their associated anharmonicities, quantitatively changes the theoretically predicted Δ^{AC}. We found that we needed up to five transmon levels for the theoretically predicted Δ^{AC} to converge for our experimental parameters, whereas beyond five levels changes in the predicted Δ^{AC} were negligible.

For a qubit coupled to a single-ended waveguide, the Rabi Frequency is given by $\Omega = |\alpha|\sqrt{4\Gamma_{1D}}$ [182], where $|\alpha|$ is the field amplitude of the SLWG drive *at the qubit*, and for our slow-light waveguide the qubit's emission rate into the waveguide (at the center of the passband) is given by $\Gamma_{1D} = 2g_{uc}^2/J$ [109]. The parameters g_{uc} and J of our device were obtained through device characterization experiments described in Supplementary Section 3.7.2, and were directly used in this model. From this model Hamiltonian, Δ^{AC} is numerically calculated in the following manner: first, the Hamiltonian is diagonalized to obtain its eigenenergies. Then, the difference between the energies of the "dressed" ground state and the "dressed" excited state is obtained, and by subtracting Δ from this difference Δ^{AC} is finally obtained.

The fit is performed simply by using $|\alpha| = V_{ADC} \cdot G$ in the model, where V_{ADC} is the amplitude of the SLWG input pulse measured at the ADC. By obtaining Δ^{AC} with G as a fit parameter, the fit of the model to the data is shown as the black curve in Fig. 3.S8c, showing excellent agreement to the data. The obtained fit parameter G was henceforth used to scale all radiation field voltages measured at the ADC. We note that by using a pulsed measurement, rather than a continuous wave (CW) SLWG input tone, the obtained G more accurately captures the contribution of spurious reflections to the overall η_{det} that is experienced by emitted pulses, and is significantly less sensitive to ripples in the output chain transfer function.

Measuring expectation values of radiation field moments

The time-independent quantum statistics of emitted photons can be extracted from single shot measurements of their (properly scaled) time-dependent fields by integration with a suitable mode-matching function $f(t)$. This integration $\int f(t)a_{out}(t)dt = I + iQ = S$ can be shown to yield single-shot measurements of the complex quantity $S = a + h^\dagger$, where a is the mode of interest, and h is the noise mode of the detection chain. By taking many single-shot measurements, one gains access to the statistics of $a + h^\dagger$, and similarly, one can also perform many single-shot "dark" measurements of the noise mode h to obtain its statistics. By calculating the expectation values of moments of $a + h^\dagger$ and h from their single shot measurements, the expectation values of moments of a can thus be obtained, which

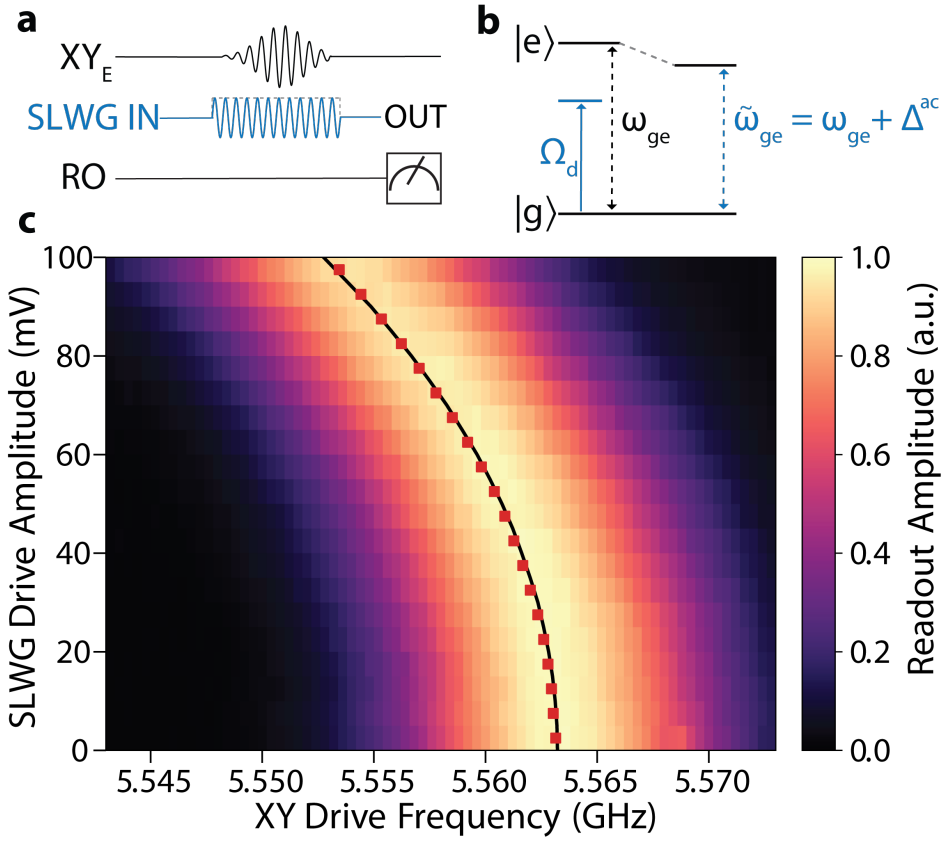

Figure 3.S8: **Absolute power calibration via AC Stark shift of emitter qubit**. **a**, Pulse sequence for the AC Stark Shift calibration experiment. An input square pulse with carrier frequency 740 MHz detuned from the qubit ω_{ge} is sent into slow-light waveguide (SLWG) and drives Q_E. Simultaneously, a qubit excitation pulse is sent into the XY_E line and arrives at the qubit at the same time the input SLWG pulse is driving the qubit, for the purposes of determining the resonance frequency of the AC Stark Shifted qubit. This experiment is repeated for multiple SLWG input pulse powers. **b**, Level diagram depicting the detuned drive on the qubit from the SLWG, and how that effects an AC Stark Shift of the qubit frequency. **c**, AC Stark Shift measurement data. The square markers are the measured qubit frequencies at different SLWG drive amplitudes, while the black line is fit to a model of the expected qubit frequency due to off-resonant driving. See the Supplementary text for more details.

is sufficient to reconstruct the density matrix of the mode of interest.

The procedure described above can be straightforwardly extended to multiple modes. For our experiment, the mode-matching function $f_i(t)$ for each photonic time-bin qubit is obtained by direct measurement of the average pulse shape $\langle a_{i,\text{out}}(t)\rangle$. This allows for single shot measurements of $S_i = a_i + h_i^\dagger$ for every photon, which are then processed into joint moments $\mathcal{S}$ of the form $\left\langle (S_1^\dagger)^{n_1} S_1^{m_1} (S_2^\dagger)^{n_2} S_2^{m_2} ... (S_N^\dagger)^{n_N} S_N^{m_N} \right\rangle$. Given that our emitter qubit is a single photon source, we take $n_i, m_i \in \{0, 1\}$ by assuming that the Hilbert Space of the photonic modes can be restricted to the single-photon manifold subspace. Note that we have experimentally verified the single photon character of our emitted photons (for each time-bin photonic qubit) via measurements of $\langle (a^\dagger)^2 a^2 \rangle$ for various prepared photonic states, which are plotted in Fig. 3.S9. The measured $\langle (a^\dagger)^2 a^2 \rangle$ moments are close to 0 for all prepared photonic states, corresponding to a vanishing second-order correlation function $g^{(2)}(0)$ at zero time delay.

In turn, the joint photon moments $\left\langle (a_1^\dagger)^{n_1} a_1^{m_1} (a_2^\dagger)^{n_2} a_2^{m_2} ... (a_N^\dagger)^{n_N} a_N^{m_N} \right\rangle \ \forall \ n_i, m_i \in \{0, 1\}$ can be calculated from algebraic formulas involving the measured joint moments $\mathcal{S}$ and the measured moments $\left\langle h_i^\dagger h_i \right\rangle$ under the following simplifying assumptions: the signal modes a_i are uncorrelated from the noise modes h_i, the noise modes h_i are not correlated to one another, and complex-valued moments of h_i are taken to be zero. These assumptions are appropriate when the noise modes h_i are in a thermal state, which is typically the case when the main added noise source of the output chain is amplifier noise (note that these assumptions were also verified experimentally). It can be shown that the expectation values of these joint photon moments is sufficient to uniquely reconstruct the density matrix of a multipartite state of N photonic qubits. While algebraic formulas relating the density matrix elements to the joint photon moments can be derived, we instead reconstruct the density matrix of generated photonic states via a maximum-likelihood estimation (MLE) algorithm that uses the obtained joint photon moments as input (for more details, see the next subsection).

MLE

We reconstruct the quantum state of the entangled microwave photons using a maximum-likelihood estimation (MLE) state tomography technique under the following assumptions: (1) the Fock spaces of the bosonic modes representing individual time-bin photonic qubits can be restricted to the single excitation manifold

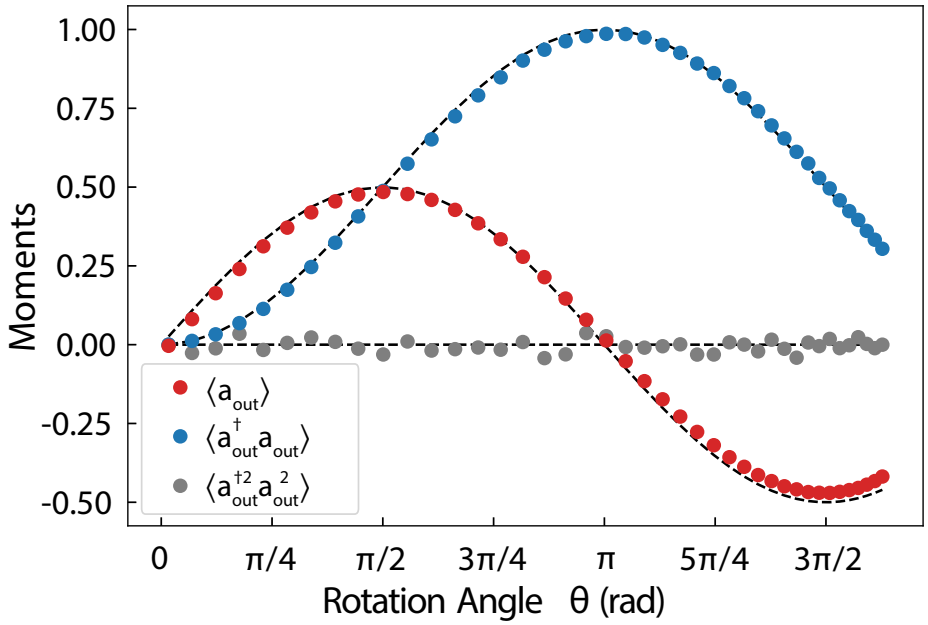

Figure 3.S9: **Measurement of radiation field moments**. Magnitude of measured moments $\langle a \rangle$ (red circles), $\langle a^\dagger a \rangle$ (blue circles), and $\langle (a^\dagger)^2 a^2 \rangle$ (gray circles), for emitted photon pulses from Q_E when it is prepared in state $|\psi\rangle_E = \cos(\theta/2)\,|e\rangle + \sin(\theta/2)\,|f\rangle$. Dashed black lines are ideal expected moments given a qubit rotation angle θ.

(i.e.: the Hilbert space spanned by Fock states $|0\rangle$ and $|1\rangle$), and (2) the distributions of the sample means of the moments of the measured photonic fields are well approximated by normal distributions in the case of many samples (i.e.: the statistical central limit theorem holds for the distributions of the means of these moments).

In statistics a likelihood functional $\mathcal{L}(D|H)$ is a function on a set D of observed statistical data sampled from a system which, assuming some underlying parameterization H of the system, returns a value proportional to the probability that the assumed parameterization would result in the observed data. Thus $\mathcal{L}$ encapsulates how 'likely' a set of observations is under certain assumptions on the system. Given a dataset of observations D, MLE techniques aim to explore the space of parameterizations of a system to find the one that maximizes a chosen likelihood functional. Our specified goal is to find the quantum state $\hat{\rho}$ of N photons that best approximates the actual photonic state we have prepared with our protocol. Thus to proceed with an MLE approach to this state tomography problem we must identify a dataset D we intend to collect and a likelihood functional $\mathcal{L}(D|\rho)$ over which we will optimize ρ.

To identify a sufficient dataset and associated likelihood functional for MLE state tomography of N entangled photons, note that for a single bosonic mode a constrained to the single excitation manifold, it suffices to know the expectation values $\langle a \rangle$, $\langle a^\dagger \rangle$, and $\langle a^\dagger a \rangle$ to uniquely reconstruct the quantum state of the mode. This is so because linear combinations of these operators along with the identity, when restricted to the Hilbert space of a two-level system, can reconstruct the single qubit operators σ_x, σ_y, and σ_z whose expectation values uniquely determine an arbitrary single qubit state. In a similar way, unique reconstruction of the state of a joint system of N bosonic modes each restricted to their single excitation manifold can be accomplished if all 2^{2N} expectations of the joint moments of the system of the form $\left\langle (a_1^\dagger)^{n_1} a_1^{m_1} (a_2^\dagger)^{n_2} a_2^{m_2} ... (a_N^\dagger)^{n_N} a_N^{m_N} \right\rangle \ \forall \ n_i, m_i \in \{0, 1\}$ are known.

Consider $A_j \in \{(a_1^\dagger)^{n_1} a_1^{m_1} (a_2^\dagger)^{n_2} a_2^{m_2} ... (a_N^\dagger)^{n_N} a_N^{m_N}\}$ to be one of the 2^{2N} moments of interest for such an N mode system. If we assume our system to be in the state ρ, then there will be an underlying distribution determined by ρ governing the statistics of measured values of A_j that will have some mean $\mu_j = \mathrm{Tr}\big(A_j \rho\big)$ and variance v_j. By the central limit theorem the sample mean of N measurements of A_j should, for large enough N, respect a normal distribution centered around $\mathrm{Tr}\big(A_j \rho\big)$ with variance v_j / N. This being the case, then the probability $p(\langle \bar{A}_j \rangle | \rho)$ of finding the sample mean of N measurements of A_j to be $\langle \bar{A}_j \rangle$ (we use the bar notation to emphasize that we are talking about a measured statistical value and not a calculated quantum mechanical expectation value), assuming a system state ρ, should obey [183]:

$$p(\langle \bar{A}_j \rangle | \rho) \propto e^{-|\langle \bar{A}_j \rangle - \mathrm{Tr}\left(A_j \rho\right)|^2 / (v_j / N)}. \tag{3.13}$$

Assuming the actual variance v_j of the moment is very well approximated by the measured sample variance $\bar{v}_j$, which it should be for large N by the law of large numbers, then v_j can be safely replaced by the measured variance $\bar{v}_j$ in this expression.

Consequently we find that we can define a likelihood functional inspired by (3.13) that takes the form [158]:

$$\mathcal{L}(D|\rho) = \prod_{j=1}^{j=2^{2N}} e^{-|\langle \bar{A}_j \rangle - \mathrm{Tr}\left(A_j \rho\right)|^2 / \bar{v}_j}. \tag{3.14}$$

This functional requires a dataset $D = \{(\langle \bar{A}_j \rangle, \ \bar{v}_j)\}_{j=1}^{j=2^{2N}}$ of measured sample means and variances of all the joint N photon moments considered above.

Because of the monotonically increasing nature of the logarithm, minimizing the negative log-likelihood is equivalent to maximizing the likelihood, and taking the negative of the logarithm of the likelihood yields

$$-\log \mathcal{L}(D|\rho) = \sum_{j=1}^{j=2^{2N}} |\langle \bar{A}_j \rangle - \mathrm{Tr}\big(A_j \rho\big)|^2 / \bar{v}_j. \tag{3.15}$$

Intuitively we see that minimizing this negative log-likelihood corresponds to finding the state ρ whose moments minimize the mean-squared error of the measured moments, discounting the error associated with higher variance measured moments more than the error associated with low variance measured moments. This optimization problem has the form of a quadratic programming problem subject to physicality constraints on the quantum state ρ (namely that ρ be trace-one and positive semidefinite):

$$\begin{aligned} \min_{\rho} \quad & -\log \mathcal{L}(D|\rho) \\ \text{s.t.} \quad & \mathrm{Tr}(\rho) = 1 \\ & \rho \succ 0. \end{aligned} \tag{3.16}$$

To perform this optimization over valid states ρ of an N mode system we use the CVXPY python library [184].

Quantum state tomography results

In addition to the quantum state tomography results of Fig. 4, we present in Fig. 3.S10 and 3.S11 reconstructed density matrices for other generated multipartite entangled photonic states (along with their associated fidelities), in order to illustrate the flexibility of our photonic state generation method. The 97% fidelity of the density matrix shown in Fig. 3.S10a of a prepared single photon Fock state constitutes the quantum efficiency of our Q_E single photon source (measurement errors notwithstanding). In addition, the reconstructed density matrix reveals that our source's emission has negligible two-photon character.

Importantly, we emphasize the capability of our platform in generating a genuine multidimensional cluster state by presenting the generated five photon pentagon cluster state illustrated in Fig. 3.S11a, along with its reconstructed density matrix in Fig. 3.S11b. As mentioned in the main text, this state is not equivalent to any

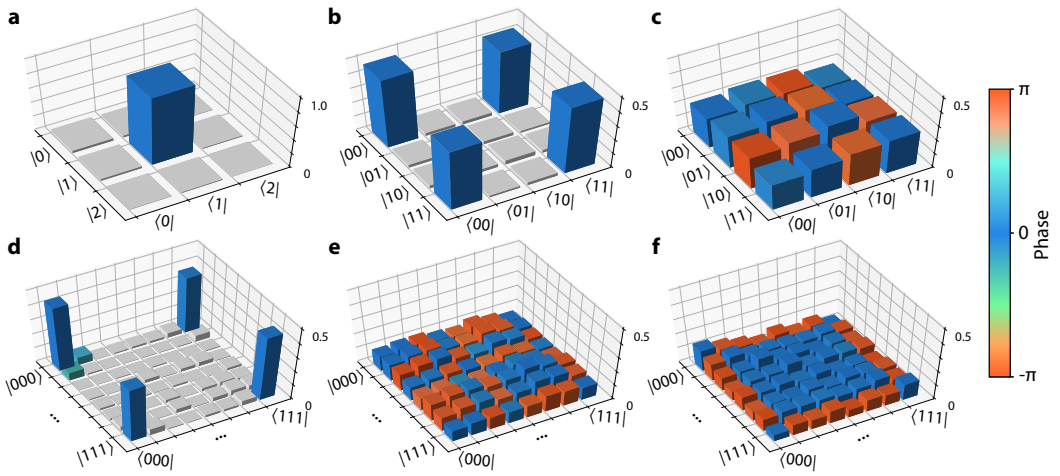

Figure 3.S10: **Reconstructed density matrices of various photonic states. a**, Reconstructed density matrix of a prepared single photon Fock state $|1\rangle$. (F = 97%). Only here, the Hilbert space includes the two-photon manifold for a single mode in order to demonstrate the single photon character of photon emission. **b-f**, Reconstructed density matrices of a two-photon GHZ state (F = 91%), a two-photon cluster state (F = 91%), a three-photon GHZ state (F = 83%), a three-photon 1D cluster state (F = 90%), and a three-photon triangular cluster state (where there is all-to-all entanglement connectivity, F = 73%). Note that time-delayed feedback was used to generate the three-photon triangular cluster state. The Hilbert space for each individual mode is truncated to the single-photon manifold. For each state, density matrix elements smaller than 10% of the expected largest density matrix element are colored gray for ease of visualization. Note that global offset phases associated with each photon are adjusted via software in order to arrive at the density matrices plotted here; this amounts to local-Z corrections on the states.

linear cluster state under local-Clifford gates. [159]. In the generation of this state, we utilized microwave photons with a higher bandwidth, emitted within 30 ns, for all the qubits participating in the cluster state. This choice was due to a stricter timing constraint imposed by the requirement of emitting four photons (rather than three photons, as was done for the four photon cluster state) during the round-trip of photon 1. It should be noted that the fidelity of the qubit-photon CZ gate and the mirror efficiency are lower when compared to that of the narrower bandwidth photon used in generating a four photon cluster state. Further discussion on the fidelity of the generated states can be found in more detail in Supplementary Section 3.7.6.

Furthermore, we bring particular attention to the five photon state illustrated in Fig. 3.S11c, with measured density matrix in Fig. 3.S11d. In order to generate this state, it was necessary to perform multiple CZ gate operations, including two CZ gate operations for photon 1. We note that in generating this state, both photon

1 and photon 2 (each of which have a length of approximately 70 ns) underwent two round-trips within the slow-light waveguide, accomplished by utilizing the switchable mirror qubit twice per photonic qubit. However, in the first round-trip of each photon we applied our CZ gate only between photon 1 and the emitter qubit (corresponding to the first dashed red rectangle in Fig. 3.S11c). We refrained from applying a CZ gate between photon 2 and the emitter during this first round trip by simply not implementing the required flux control on the emitter qubit, resulting in photon 2 merely scattering off of the terminated end of the slow-light waveguide, never interacting with the emitter qubit. During the second round-trips of photon 1 and photon 2, CZ gates were implemented between the emitter qubit and both photons, thus leading to the graph state connectivity shown in Fig. 3.S11c. Such use of *two* time-delayed feedback events for an emitted photon is the most fundamental prerequisite for extending our 2D cluster state generation scheme to generation of 3D cluster states [128, 139, 140]. Thus, generation of the 5 photon state illustrated in Fig. 3.S11, via multiple time-delayed feedback events, constitutes a preliminary demonstration of the adaptability of our platform for future generation of 3D cluster states of microwave photonic qubits.

We conclude this Supplementary Section by describing some technical details of our radiation field tomography measurements that may be of interest to the reader. Firstly, we note that when generating photonic states, lingering gate errors due to the AC Stark shifting of the $|e\rangle \rightarrow |f\rangle$ transition, as well as the use of flux modulation, will result in spurious phases gained by the qubit, which will be imparted onto the phase of emitted photons. This phase, however, is deterministic, and thus can be compensated in hardware by suitable qubit Z-control. For the density matrix presented in Fig. 4d, these spurious phases were compensated for by the use of Virtual Z-gates [185] when performing π_{ef} pulses before emission of every photon. Thus, we were able to generate the state whose ideal counterpart is shown in Fig. 3.S12b, and the 70% state fidelity quoted in the main text is calculated with respect to this state. We also note that while these spurious phases correspond to local Z-gates for every photon, which can be removed from the processed tomography data, in practice they could hinder use of such cluster states in quantum information applications. Thus, we chose to demonstrate this additional photon phase control in our generation process, and we stress that the data presented in Fig. 4d did not have any post-processing phase modification.

In addition, the measured $\left\langle h_i^\dagger h_i \right\rangle$ moments reveal an effective added noise photon

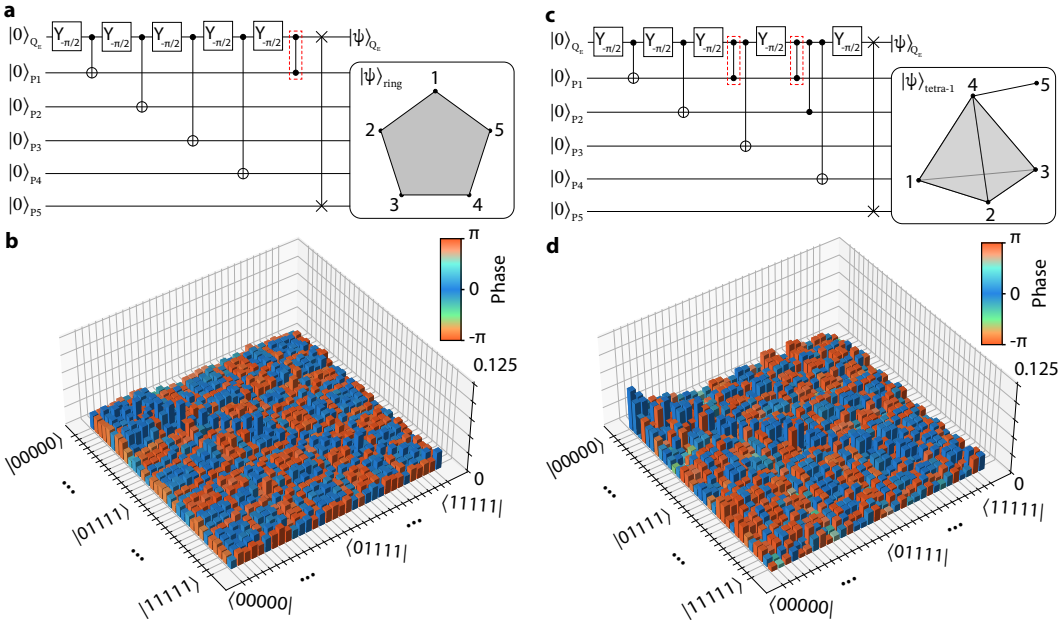

Figure 3.S11: **Five-Photon cluster state with multiple time-delayed feedback events. a**, Quantum circuit for the generation of the five-photon cluster state $|\psi_{\text{ring}}\rangle$. In this state, the entanglement structure forms a pentagon, as shown in the diagrams at the end of the quantum circuits. **b**, Reconstructed density matrix of the $|\psi_{\text{ring}}\rangle$ state. The fidelity of the generated state is $F = 61\%$. **c**, Quantum circuit for the generation of the five-photon cluster state $|\psi_{\text{tetra}-1}\rangle$. In this state, the entanglement structure of the first four photons (photon 1-4) forms a tetrahedron, and the photon 5 is entangled to photon 4, as shown in the diagram on the right. Two time-delayed feedback events on photon 1 (corresponding the the highlighted CZ gates) entangle photon 1 with both photon 3 and photon 4. **d**, Reconstructed density matrix of the $|\psi_{\text{tetra}-1}\rangle$ state. The fidelity of the generated state is $F = 50\%$. Global phases associated with each photon are adjusted via software in order to arrive at the plotted density matrices. We note that the data for these states was taken in a separate cooldown, and due to technical reasons, the absolute power calibration we used was acquired from the integrated flux of a prepared single photon state.

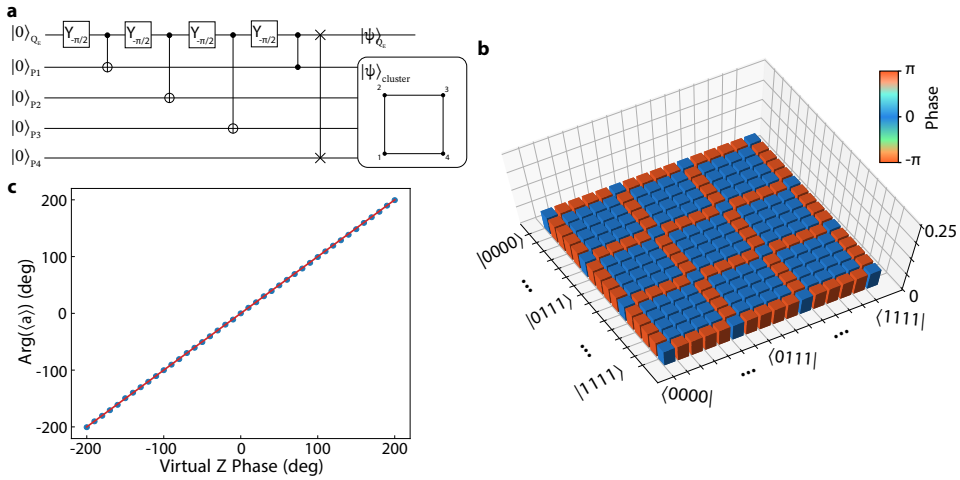

Figure 3.S12: **Phase control of cluster state a**, Quantum circuit of cluster state generation protocol, assuming Q_E and photonic states prepared in ground state. **b**, Ideal cluster state obtained from the quantum circuit of **(a)**. **c**, Measured phase of single photon moment $\langle a \rangle$ as a function of the phase of virtual-Z gates applied to Q_E during generation (blue circles). Red line shows ideal expected phase. Virtual-Z gates applied on Q_E are realized by adding an offset phase to π_{ef} pulses before photon emission.

number of $n_{\text{noise}} \approx 3.5$, corresponding to a quantum measurement efficiency of the output chain of $\eta_{\text{meas}} = (1+n_{\text{noise}})^{-1} \approx 0.22$. We note that for heterodyne detection, a finite detection efficiency η_{det} can be shown to be equivalent to added noise in the output chain, and we believe that the majority of n_{noise} can be attributed to losses and spurious reflections before the TWPA (where we estimate a total transmissivity for emitted photon pulses of -5.5dB).

Furthermore, we note that the scaling factor G will be slightly different for photons of different bandwidth. This is due in part to slight differences in the effective transmission coefficient of the tapered end of the SLWG for different bandwidth pulses (see Fig. 3.S2d). Moreover, higher bandwidth pulses will have slightly higher mode-matching inefficiency due to dispersion-induced distortion, which results in a small fraction of the pulse being situated outside of its measurement time-bin window. When generating photonic states we use up to two different bandwidths, and we quantify the difference in their respective G scaling factors by taking the ratio of their measured $\langle a^\dagger a \rangle$ moments when the qubit is fully excited to the $|f\rangle$ state before emission. We find a $\sim 5\%$ difference between the two G scaling factors, which we take into account for calculation of joint photon moments (we use the G obtained from Stark shift measurements for the lower bandwidth photon pulses).

Finally, for generation of the four photon 2D cluster state, the five photon tetrahedron-like cluster state in 3.S11c, and the five-photon pentagon cluster state in 3.S11a, we performed 500 million, 2 billion, and 5 billion single shot measurements, respectively, in order to have sufficient averaging for higher order joint photon moments; these numbers are consistent with the predicted number of single shot measurements required from the statistical analysis presented in ref. [186]. This corresponded to measurement times of 6 hours, 24 hours, and 60 hours, respectively; and due to the presence of slow qubit frequency drifts of ~ 0.5 MHz in our experimental setup, we recalibrated the qubit flux bias every hour during these long measurements. We expect that the use of GPU or FPGA based methods for data processing would significantly reduce these measurement times. Nevertheless, we note that full tomography of a photonic state of five itinerant microwave photons has hitherto never been demonstrated until now.

3.7.5 Process tomography of the time-delayed feedback operation

QPT experiment design

In order to characterize the qubit-photon CZ gate implemented with our time-delayed feedback protocol, we perform full quantum process tomography (QPT) of the qubit-photon interaction. We again limit the Hilbert space of the bosonic mode representing the itinerant photon to the single-excitation subspace, so the implemented CZ gate can be considered as a quantum process mapping the Hilbert space of an effective two qubit system to itself.

With this in mind, in characterizing our CZ implementation we are interested in the set of quantum processes that maps two-qubit states to two-qubit states. Such processes (outside of certain cases in which we are not concerned here, e.g.: projective measurements) are described by the set of completely-positive trace-preserving (CPTP) linear maps from two-qubit density matrices to two-qubit density matrices. [187]

Performing quantum process tomography requires identifying a complete set of 'fiducial' input states of the system and an 'informationally complete' set of measurement operators [187, 188]. A complete fiducial set of input states on a d-dimensional Hilbert space $\mathcal{H}$ is a set of d^2 states whose density matrices span the space of density matrices on $\mathcal{H}$. An informationally complete set of measurement operators $\{M_j\}$ is a set of $d^2 - 1$ operators on $\mathcal{H}$ whose expectation values given a state ρ, $\{\mathrm{Tr}(M_j\rho)\}$, uniquely determine ρ.

As our set of d^2 fiducial input states we select all 16 possible unentangled states of the form $|\psi_q\rangle \otimes |\phi_p\rangle$ where $|\psi_q\rangle \in \{|+z\rangle_q, |-z\rangle_q, |+x\rangle_q, |+y\rangle_q\}$ and $|\psi_p\rangle \in \{|+z\rangle_p, |-z\rangle_p, |+x\rangle_p, |-y\rangle_p\}$ (where we are using the conventional names for eigenstates of the Pauli spin operators σ_x, σ_y, σ_z). For our informationally complete set of measurement operators we select the 15 non-identity joint qubit-photon correlators of the form $\sigma_i \otimes a^{\dagger n} a^m$ (where $n, m \in \{0, 1\}$ and $\sigma_i \in \{\mathbb{I}, \sigma_x, \sigma_y, \sigma_z\}$). The expectations of these operators can be shown to uniquely specify any of the joint qubit-photon states we are considering in our effective two qubit Hilbert space [158]. To measure the expectations of these operators for a given prepared state, we perform single-shot heterodyne measurements of the microwave field in conjunction with single shot measurements of the qubit polarization (after rotation to the appropriate basis). This allows us, on a shot-by-shot basis, to compute the correlations between the microwave field moments and the qubit polarization operators.

The experimental sequence of our QPT implementation can be seen in Fig. 3.S13. We begin with Q_E and the photonic qubit in their respective ground states, after which we prepare the state of the photonic qubit by performing an X_π^{ge} pulse on Q_E, followed by one of an X_π^{ef} pulse, an $X_{\pi/2}^{ef}$ pulse, an $Y_{\pi/2}^{ef}$ pulse, or no pulse ($\mathbb{I}^{ef}$), following which we use a flux modulation tone to induce shaped emission of the photonic time-bin qubit from Q_E. This results in the initialized photonic time-bin qubit state to be conditioned on the choice of ef pulse, resulting in the states $|1\rangle$, $|-y\rangle$, $|+x\rangle$, or $|0\rangle$ respectively, while Q_E ends in state $|e\rangle$ after flux modulation.

Before the photonic qubit finishes its propagation through one round trip of the waveguide, we prepare Q_E in one of its four above specified cardinal states. When the photonic qubit finally returns to Q_E, both subsystems have been properly prepared and the CZ gate between the two proceeds by way of our time-delayed feedback interaction. After the CZ is completed the photonic time-bin qubit leaves the waveguide where it is amplified and its two independent I and Q quadratures are measured via heterodyne detection. The Q_E state is also measured along one of the three chosen polarization axes defining which qubit polarization operator σ_i we are measuring. Note that the emitter state preparation is deferred until immediately prior to the onset of time-delayed feedback, after the itinerant photon has travelled almost the entire round-trip length of the SLWG, in order to minimize the amount of dephasing suffered by Q_E before the CZ gate.

We perform the above control sequence for all 16×3 combinations of prepared states and possible values of σ_i. Note that, for example, while the experimental sequence

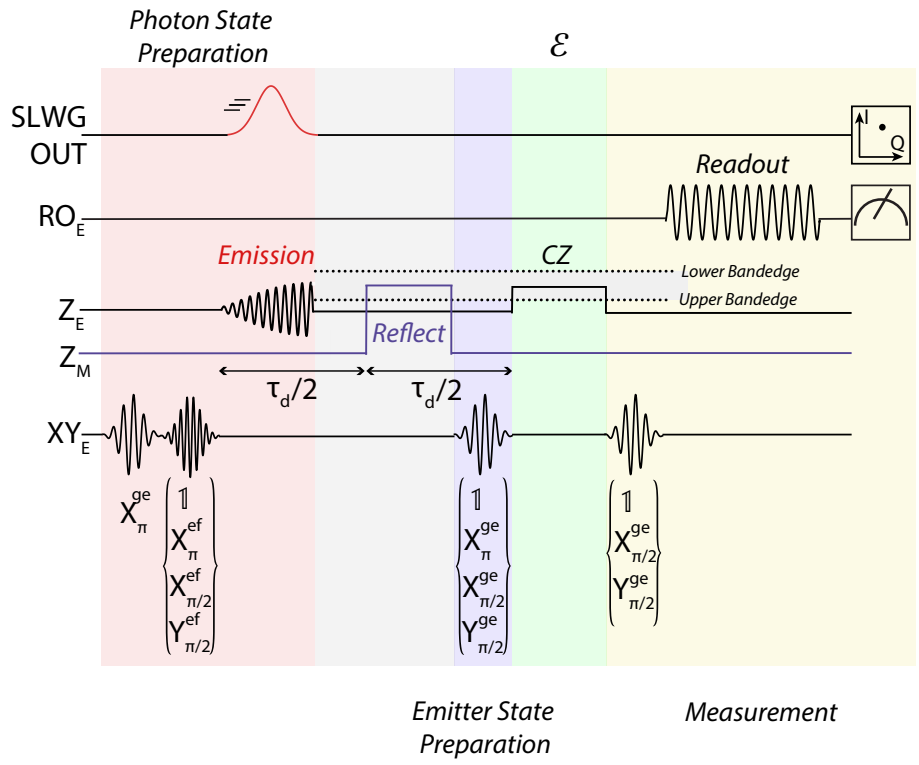

Figure 3.S13: **Experimental pulse sequence for QPT** A schematic for the pulse sequences that implement the QPT protocol for characterizing our CZ implementation. The shaded regions of different coloration represent different subsequences of the QPT protocol indicated by the italic text above or below the figure (the grey region is time during which the photonic qubit propagates through one round-trip of the waveguide). The bracketed lists of gates below the pulses on the $\mathrm{XY_E}$ line represent variable pulses corresponding to different photonic qubit state preparations (red region), Q_E state preparations (blue region), and Q_E measurement basis rotations (yellow region).

corresponding to measuring $\sigma_x a$ and $\sigma_y a$ require different qubit basis rotation pulses, the nature of heterodyne measurement of the microwave field means a single experiment can be used to measure all four quantities $\{\sigma_x, \sigma_x a, \sigma_x a^\dagger, \sigma_x a^\dagger a\}$. We thus perform 48 different experiments (each repeated many times) to compute the $16 \times 15 = 240$ different expectations of the form $\langle \sigma_i \otimes a^{\dagger n} a^m \rangle$ that uniquely specify each output state of the implemented CZ gate for each input state.

MLE

Once this data is collected, we perform a maximum-likelihood reconstruction of the time-delayed feedback operation to find the most likely quantum process ap-

proximating it. To do this we represent the quantum process $\mathcal{E}$ underlying the time-delayed feedback operation as its χ matrix in the Pauli Product basis of 2 qubits, whereby its action on a general input state is given by

$$\mathcal{E}(\rho) = \sum_{n,m} \chi_{n,m} P_n \rho P_m^\dagger. \tag{3.17}$$

The quantity χ is a 16×16 Hermitian, positive-semidefinite matrix, and $\{P_j\}$ is some enumeration of the 2 qubit Pauli group. With this representation of the time-delayed feedback process, we use the python library CVXPY [184] to minimize the negative log-likelihood functional of the dataset of qubit-photon correlator expectations given the CZ process $\mathcal{E}$:

$$-\log \mathcal{L}(D|\chi) = \sum_{i=1,j=1}^{i=15,j=16} |\langle \bar{M}_{ij} \rangle - \mathrm{Tr}\big(M_j \; \mathcal{E} \circ \mathcal{B}_i(\rho_0)\big)|^2 / v_{i,j}, \tag{3.18}$$

where $\rho_0 = |0\rangle\langle 0|_q \otimes |0\rangle\langle 0|_p$ is the initial state of the joint qubit-photon system, assumed to be the ground state of both systems, M_j is the j^{th} qubit-photon correlator, $\mathcal{B}_i$ is the i^{th} generalized state preparation superoperator (explained in more detail below), $\langle \bar{M}_{ij} \rangle$ is the measured sample mean of M_j given state preparation $\mathcal{B}_i$, and $\bar{v}_{i,j}$ is the sample variance of $\langle \bar{M}_{i,j} \rangle$. The free parameters available to the optimization are the elements of χ implicitly contained in the computation of $\mathcal{E} \circ \mathcal{B}_i(\rho_0)$ above.

The choice of this log-likelihood follows from exactly the same arguments as the state tomography log-likelihood functional equation (3.15) given in Supplementary Section 3.7.4, extended to the case of 16 simultaneous sets of state tomography data for the 16 states $\mathcal{E} \circ \mathcal{B}_i(\rho_0)$. Enforcing the CPTP physicality constraints on $\mathcal{E}$ defines the quadratic programming optimization problem for finding the most-likely Pauli-Product representation of $\mathcal{E}$, $\hat{\chi}$:

$$\begin{aligned} \min_{\chi} \quad & -\log \mathcal{L}(D|\chi) \\ \text{s.t.} \quad & \sum_{n,m} \chi_{n,m} P_m^\dagger P_n = \mathbb{I} \\ & \chi \succ 0. \end{aligned} \tag{3.19}$$

After the χ matrix representing our CZ implementation has been reconstructed we find the CZ gate that it most closely approximates modulo any simultaneous local Z operations on either Q_E or the photonic time-bin qubit. These local Z gates can be

removed in software and do not quantitatively alter the entangling nature of the CZ gate we are implementing, and thus have no impact on the $\mathrm{Tr}\left(\sqrt{\sqrt{\chi_{\mathrm{CZ}}}\chi_{\mathrm{ideal}}\sqrt{\chi_{\mathrm{CZ}}}}\right)^2$ figure of merit we use to characterize the gate.

Generalized state-preparation superoperator

It is well-documented that QPT can suffer significantly from so-called state preparation and measurement (SPAM) errors, wherein errors during preparation of the QPT input states and errors during measurement are interpreted by the tomographic reconstruction method as errors on the process itself. We find two sources of state-preparation error that we are able to correct for systematically by substituting idealized state preparation unitaries for more general state preparation superoperators. These sources of error are the initial thermal population of Q_E prior to the application of any state preparation control pulses, which by gate set tomography of Q_E (we use the python library pyGSTi [189] for this) we estimate to be $\sim 1\%$, and the round trip loss of $\sim 13\%$ that the itinerant microwave photon suffers between emission and reinteraction with Q_E.

To account for these errors we define the generalized state-preparation super operators $\{\mathcal{B}_i\}$, each of which we factorize as the composition of three different processes:

$$\mathcal{B}_i = \mathcal{R} \circ \mathcal{U}_i \circ \mathcal{P}. \tag{3.20}$$

The process $\mathcal{U}_i$ corresponds to the i^{th} **ideal** state preparation, the process $\mathcal{P}$ models the 1% initial thermal population of Q_E, and the process $\mathcal{R}$ models the 13% round trip loss of the itinerant microwave photon. $\mathcal{P}$ can be implemented by a pin map on the emitter qubit's Hilbert space: $\mathcal{P}(\rho_q) = 0.99\,|0\rangle\langle 0| + 0.01\,|1\rangle\langle 1|$ for all ρ_q. $\mathcal{R}$ can be modeled by a relaxation channel on the photonic qubit's Hilbert space with loss parameter $l = 0.13$. The preparation process $\mathcal{U}_i$ is given by the ideal processes implementing the pulse sequences in the red and blue shaded regions of Fig. 3.S13 (i.e., photonic qubit state preparation and Q_E state preparation).

Readout Error Correction

In the same way that it is possible to correct for certain characterized state preparation errors, it is also possible to correct for qubit readout measurement errors that obey certain assumptions. By computing the confusion matrix of the single-shot Q_E state measurement, we can correct for identifiable readout misclassification errors that give rise to erroneous values for qubit-photon correlator expectations.

Consider the quantity $\langle \sigma_z a \rangle$. This expectation can be computed from measured data in the following way:

$$\langle \sigma_z a \rangle = \tilde{p}(+1)\langle \tilde{a} \rangle|_{\sigma_z=+1} - \tilde{p}(-1)\langle \tilde{a} \rangle|_{\sigma_z=-1}, \tag{3.21}$$

where $\tilde{p}(+1)$ denotes the proportion of single-shot measurements for which the qubit polarization along the z quantization axis was found to be $+1$, and $\langle \tilde{a} \rangle|_{\sigma_z=+1}$ denotes the average value of the single shot field measurements in these same cases; with a similar computation for the -1 case.

Due to the fact that there are probabilities of mismeasurement of the qubit polarization, which we characterize in Supplementary Section 3.7.2, the quantity $\tilde{p}(+1)\langle \tilde{a} \rangle|_{\sigma_z=+1}$ itself should be written as

$$\begin{aligned} \tilde{p}(+1)\langle \tilde{a} \rangle|_{\sigma_z=+1} = {} & p(+1|+1)p(+1)\langle a \rangle|_{\sigma_z=+1} \\ & + p(+1|-1)p(-1)\langle a \rangle|_{\sigma_z=-1}, \end{aligned} \tag{3.22}$$

where $p(+1|+1)$ corresponds to the probability of measuring a qubit polarization of $+1$ when the polarization was in fact $+1$, $p(+1)$ is the actual probability that an ideal measurement would have yielded a polarization of $+1$, and $\langle a \rangle|_{\sigma_z=+1}$ is the actual expected value of the field conditioned on the qubit polarization along z being $+1$. There is a similar expression for $\tilde{p}(-1)\langle \tilde{a} \rangle|_{\sigma_z=-1}$:

$$\begin{aligned} \tilde{p}(-1)\langle \tilde{a} \rangle|_{\sigma_z=-1} = {} & p(-1|+1)p(+1)\langle a \rangle|_{\sigma_z=+1} \\ & + p(-1|-1)p(-1)\langle a \rangle|_{\sigma_z=-1}. \end{aligned} \tag{3.23}$$

These two expressions can be combined into a simple linear relationship between the measured quantities $\tilde{p}(+1)\langle \tilde{a} \rangle|_{\sigma_z=+1}$ and $\tilde{p}(-1)\langle \tilde{a} \rangle|_{\sigma_z=-1}$ and the 'premeasurement' undistorted quantities $p(+1)\langle a \rangle|_{\sigma_z=+1}$ and $p(-1)\langle a \rangle|_{\sigma_z=-1}$:

$$\begin{pmatrix} \tilde{p}(+1)\langle \tilde{a} \rangle|_{\sigma_z=+1} \\ \tilde{p}(-1)\langle \tilde{a} \rangle|_{\sigma_z=-1} \end{pmatrix} = C \begin{pmatrix} p(+1)\langle a \rangle|_{\sigma_z=+1} \\ p(-1)\langle a \rangle|_{\sigma_z=-1} \end{pmatrix}, \tag{3.24}$$

where C is given by the confusion matrix:

$$C = \begin{pmatrix} p(+1|+1) & p(+1|-1) \\ p(-1|+1) & p(-1|-1) \end{pmatrix}. \tag{3.25}$$

This confusion matrix can be measured under the assumption of perfect state preparation by preparing the qubit many times in the ground or excited state, performing

a single shot measurement of Q_E's state, and counting the relative proportions of ground and excited measurements given a particular state preparation. This matrix C can then be inverted and applied to the erroneous conditional photon moments to give the correct moments:

$$\begin{pmatrix} p(+1)\langle a\rangle|_{\sigma_z=+1} \\ p(-1)\langle a\rangle|_{\sigma_z=-1} \end{pmatrix} = C^{-1} \begin{pmatrix} \tilde{p}(+1)\langle \tilde{a}\rangle|_{\sigma_z=+1} \\ \tilde{p}(-1)\langle \tilde{a}\rangle|_{\sigma_z=-1} \end{pmatrix} \tag{3.26}$$

from which the correct qubit photon correlators can be computed.

State Fidelity Confidence Intervals

The 70% state reconstruction fidelity relative to an ideal target cluster state is quoted with a 95% confidence interval [69.1%, 70.4%] in the main text. We computed this confidence interval using a parametric bootstrapping protocol [190] that involved fitting the distributions of the measured photonic correlations and resampling the fit distributions to reconstruct 1,000 bootstrap states. Each distribution of a measured photonic correlation contains 5,000 points, where each point is computed from an average of 100,000 single shot field measurements. Thus corresponding to each moment was an approximately normal histogram of these 5,000 values. These histograms could be fit and resampled to reconstruct bootstrapped versions of the generated cluster state. We reconstructed 1,000 bootstrap copies this way, and for each copy we computed the fidelity relative to the target cluster state. Then we sorted these fidelities and approximated the 95% confidence interval by taking the 25^{th} element of this sorted list fidelity as the lower bound of the 95% confidence interval and the 975^{th} element as the upper bound.

3.7.6 Sources of infidelity and future improvements

Here we examine the main sources of infidelity in our experiment that limited the fidelity of the generated 2D cluster state and other photonic states. We discuss how this infidelity could be ameliorated, and comment on other possible design and hardware improvements to considerably increase the size of the cluster state.

Infidelity analysis

The main source of infidelity in this work was the poor decoherence rate $T_2^* = 561$ ns of Q_E. We ascribe this low T_2^* to excessive flux noise given our robust $T_1 = 34$ μs (and measured T_2^* of over 15 μs at its maximum frequency). The Ramsey decay time-dependence was strongly Gaussian, which suggests that our dephasing is limited by

$1/f$ noise [57, 191]. In order to properly model $1/f$ noise, typical Linbladian master-equation approaches, which assume a Markovian model of decoherence, do not suffice. We thus modeled the effect of $1/f$ noise in our cluster state generation sequence by simulating the state evolution of our joint system of Q_E (here a 3-level system) and photonic qubits under the influence of a $\delta(t)\hat{c}^\dagger\hat{c}$ term in the Hamiltonian, where $\hat{c}$ here is the annihilation operator of Q_E's anharmonic mode, and $\delta(t)$ is a random noise signal with noise power spectral density of $1/f$. The Hamiltonian for state evolution is thus composed of this $\delta(t)\hat{c}^\dagger\hat{c}$ term, and the time-dependent Hamiltonian that realizes the pulse sequence depicted in Fig. 4b.

Many different realizations of this noise are realized in the following manner: a random FFT spectrum is generated where each FFT bin is a normally distributed random complex value (and the spectrum is conjugate symmetric), the FFT bins are scaled according to a $1/f$ spectrum, and the inverse FFT is taken to arrive at a random noise signal. We ensure that the generated noise signals are long enough such that the center frequencies of FFT bins are as low as 50 Hz, in order for the resultant time signal to have significant power at very low frequencies. Consequently, we only use small portions of this long noisy time signal as the different realizations of $\delta(t)$ in our simulations (which are confirmed to have a $1/f$ power spectrum). We simulate state evolution of our system under different realizations of $\delta(t)$ and average the resultant states in order to obtain the "average" effect of $1/f$ noise induced dephasing on the system. We confirm that this simulation approach reproduces Gaussian shaped Ramsey decay as well as the "spin-echo" phenomenon; and with full simulation of our cluster state generation sequence of Fig. 4b under $1/f$ noise, we determine that our Q_E dephasing results in an infidelity of $\sim 15\%$ for the final 2D cluster state.

Secondly, the second most significant source of infidelity in our generation scheme is the round-trip loss of the slow-light waveguide. As seen in Fig. 3c, the round-trip loss of the slow-light waveguide corresponds to 13% energy loss for each photon undergoing a round-trip. Note that while a limited detection efficiency η_{det} is compensated for in heterodyne based state tomography via the scaling factor G, loss that occurs before the CZ gate, i.e. during state generation, is not considered part of η_{det} and directly contributes to infidelity. We find that our photon loss contributes to $\sim 5\%$ infidelity. Further, we estimate that control and preparation errors, including qubit thermal population (measured to be 1%), residual $|f\rangle$ state population after emission (measured to be 1%), and CZ gate infidelity contribute another total $\sim$ 4% infidelity. In total, we estimate a 76% fidelity limit for the generated state,

which does not take into account measurement errors or other state preparation errors. This is in good agreement of our measured fidelity of 70%. Finally, we note that while waveguide dispersion was not a serious impediment for the photonic state generation that we have presented, it would limit the use of higher bandwidth photons as compared to what we used.

In addition, the infidelity error budget of the five-photon pentagon cluster state shown in the Fig. 3.S11a, b is quantitatively different when compared to the infidelity breakdown of the four photon cluster state. For this state, the largest source of infidelity originates from using a higher bandwidth microwave photon for photon 1, which is a result of a stricter timing constraint in generating this state, as mentioned in the Supplementary Section 3.7.4. The ratio between the bandwidth of the photon and the linewidth of the mirror qubit is reduced in this experiment, which leads to a decrease in mirror efficiency, effectively increasing the round-trip loss [101]. From a separate measurement, we estimate the round-trip loss for this photon to be 24%, contributing to $\sim$ 12% of the infidelity. Additionally, the larger bandwidth of photon 1 reduces the fidelity of the qubit-photon CZ gate [138], accounting for $\sim$ 4% of the infidelity.

On the other hand, when generating this state, the decoherence rate of the emitter qubit was smaller, with $T_2^* \approx 1.7$ us (we note that the data corresponding to the generation of this state was taken in a separate cooldown). With this improved T_2^*, we estimate that the effect of decoherence on the fidelity of the generated state is only 7%. In total, we estimate a fidelity limit of 72% for the generated state, which includes the contribution of qubit thermal population (measured to be 1%) and the increase in residual $|f\rangle$ state population after emission (measured to be 4%) due to a smaller maximum achievable sideband (also a consequence of the reduced tuning range of the emitter qubit). These factors reasonably bound our measured fidelity of 61.3%. It should be noted that this 72% estimate does not include the state preparation error, long-term drifts in electronics, and additional measurement errors resulting from deleterious broadening and splitting effects caused by higher-order dispersion of the slow-light waveguide, which leads to unwanted temporal field overlap with adjacent photons and field leakage outside the measurement time-bin, to which photons with higher bandwidth are more susceptible.

Scaling the size of the cluster state

Although there were limiting technical issues in our experiment, we believe there is a straightforward path for mitigation of these issues, and realistic strategies for extending our generation scheme to synthesis of much larger cluster states. Firstly, we are confident that there is ample room to reduce the excessive flux noise in our setup to state-of-the-art values [192]. Additionally, while our reliance on flux modulation for tunable coupling between Q_E and the SLWG necessitates operation at "flux sensitive" qubit frequencies, the use of tunable couplers [47, 193] between Q_E and the SLWG would allow operation at Q_E's "sweet spot" frequencies, thereby increasing its resilience to flux noise. Given that $T_2^* \sim 100\mu$s has been reported for transmon qubits in the past, we expect that the deleterious effects of dephasing could be nearly fully dispensed with. If even more emitter coherence were to be required, the use of an error-corrected "logical qubit," with emission via an ancilla qubit, could be utilized to fully suppress emitter decoherence based errors.

Furthermore, the 0.46 dB round-trip loss of our waveguide is another serious limiting factor to our fidelity, and arises due to the limited Q of our unit cell resonators, which we estimate to be $69,000$. However, microwave superconducting resonators with $Q > 1,000,000$ have been fabricated in numerous previous works [194–196]. Thus, with fabrication or materials improvement that have already been demonstrated, the waveguide loss could realistically be substantially reduced. We note that while our current compact unit cell design has sharp corners that likely induce strong electric fields that couple to TLS, this effect could be mitigated with different geometrical design or material improvement.

Moreover, while the SLWG's dispersion hinders the use of higher bandwidth Gaussian photon pulses due to dispersion induced broadening, our tunable coupling capability or dispersion engineering allows for use of well-established [197, 198] or novel [199] dispersion mitigation techniques. By compensating for the dispersion through signal pre-distortion, or via dispersion cancelling elements post SLWG propagation, one could ensure that photon pulses arriving for re-scattering or for measurement are well-confined in time, thus alleviating the problem of overlapping broadened pulses. Such techniques would in principle enable even faster emission of photon pulses, and thus would allow for better utilization of limited round-trip delays.

Furthermore, achieving higher anharmonicity of Q_E would allow for realization of even larger Γ_{1D}, without compromising qubit coherence, than what was already

achieved in this work. Increasing Γ_{1D} would allow for even more rapid emission of shaped photon pulses, as well as less residual $|f\rangle$ population after emission, and a high fidelity CZ gate with high bandwidth photons. Analysis in ref. [138] shows that higher Γ_{1D} improves the fidelity of CZ gates, due to decreased "dispersion" of the Q_E induced reflection phase near Q_E's resonance frequency that is commensurate with the broadening of Q_E's lineshape. This reduced "dispersion" of the reflection phase results in the overall phase gained by the photon pulse during re-scattering to be closer to π, and reduces the distortion of the photon pulse imparted by the re-scattering process (which improves mode-matching efficiency). Limited anharmonicity η of Q_E is the main limiting factor to the magnitude of Γ_{1D}, as a Γ_{1D} significantly larger than η would lead to more substantial leakage of the $|e\rangle$ population into the SLWG. However, by using a different superconducting qubit design that has higher anharmonicity than the transmon [200–202], the magnitude of Γ_{1D} could be substantially increased without compromising other aspects of cluster state generation. Also, achieving higher anhamonicity would allow for a larger waveguide passband, which would lower higher-order dispersion (albeit at the cost of less delay per resonator).

Additionally, the round-trip delay could be substantially increased in several ways. One straightforward way is simply by increasing the number of unit cells of the SLWG. Although that would increase the size of the device, which could introduce spurious box modes to the sample, recent advances in microwave packaging techniques could ameliorate the impact of larger device size [173, 203]. Furthermore, the unit cell size could be reduced by leveraging compact high kinetic inductance superconducting resonators [160, 161], allowing for more delay per area. And looking forward even further, incorporation of an acoustic delay line into our system could allow for longer round-trip delays without additional dispersion or susceptibility to microwave packaging box modes [162–164], increasing the possible size of generated cluster states even further.

We stress that in addition to increasing cluster state size, cluster state dimensionality could be increased to 3D by coupling of another mirror qubit somewhere along the delay line rather than at the end, which would impart the ability to perform time-delayed feedback with two different delays. The ability to perform two time-delayed feedback events with two different delays is the pre-requisite to generating 3D cluster states via sequential photon emission and time-delayed feedback [139, 140], because it allows for sufficient non-nearest neighbor entanglement between photons of the

emitted pulse train such that the entanglement topology is that of a 3D cluster state. While this extension of our scheme would necessitate significantly larger delays, we believe achieving such delays is possible. Thus, we believe there is a viable path to measurement-based quantum computation with microwave photons via photonic resource state generation as we have described. We conclude by observing that, even if the size of generated photonic states were to hit some practical limitation, there are other measurement-based quantum computation schemes, such as fusion based quantum computation [204], that only require the repeated synthesis of smaller photonic resource states which are later "fused" into larger photonic states via linear optical elements. Our cluster state generation scheme would be well suited to be incorporated into such approaches, and could provide a "bridge" towards the goal of photonic resource state generation via linear optical elements.

Finally, we note that previous works [139, 140] have performed analysis of errors in cluster state generation in the context of fault-tolerant quantum computing. They find that for a gate error rate of $\sim 10^{-3}$ (where "gates" in this context includes Q_E single qubit gates, photon emission, and the qubit-photon CZ gate) and delay line losses of $\sim 3 \cdot 10^{-5}$ dB/ns, one can achieve a fault-tolerance "break-even" point where the logical error rate is lower than the gate error rate, and beyond which logical errors are exponentially suppressed as delay line loss is decreased. State-of-the-art single qubit gates can routinely achieve such gate error rates of 10^{-3}, while photon emission should in principle also achieve such error rates if there is enough time for full emission from the $|f\rangle$ state, and sufficient protection of the $|e\rangle$ state. Furthermore as mentioned in the main text, although our reported CZ gate fidelity was 90 %, we are able to ascribe most of that infidelity to SPAM errors via separate measurements. From separate simulations, we expected a 97 % fidelity for the CZ gate, and this fidelity could be increased further simply by increasing the Γ_{1D} of the emitter qubit. In addition, while necessary delay line losses are around ~ 100 times smaller than our current losses in our experiment, recent and future advances in superconducting circuit fabrication are expected to allow for 100 times (or more) lower losses in superconducting resonators [59]. Thus, we foresee that with realistic device and fabrication improvements, generating 3D cluster states for fault-tolerant measurement based quantum computation with negligible logical error rates should be feasible. Further, while single shot photon measurements along arbitrary basis would also be necessary for quantum computation with itinerant microwave photons, such single photon detection could be achieved with a "detector" qubit. With such a detector, an itinerant photon's state would be mapped to the detector qubit state's via

suitable time-dependent control of the detector qubit's coupling to the waveguide, as demonstrated in previous works [205, 206]; the "detector" qubit could then be measured in an arbitrary basis. Lastly, we also note that with different photonic qubit encodings, different generation and measurement protocols are also possible.

Chapter 4

FAST UNCONDITIONAL RESET AND LEAKAGE REDUCTION OF A TUNABLE SUPERCONDUCTING QUBIT VIA AN ENGINEERED DISSIPATIVE BATH

In Chapter 3, we show enhanced Purcell protection and demonstrate on-demand photon emission from a superconducting qubit using parametric flux modulation, where the dissipation is tailored by many modes. From another perspective, this process can be interpreted as on-demand qubit reset or leakage reduction. By further customizing the properties of the metamaterial waveguide, the same building blocks can be adapted for these operations. Here, we demonstrate simultaneous reset of multiple excited states and leakage reduction operation with state-of-the-art performance. This chapter is adapted from Ref. [92].

4.1 Introduction

Fast and high-fidelity reset of qubits into fiducial states is a necessary capability of quantum processors designed for demanding quantum information and computation tasks [21]. In the context of quantum error-correction, high-fidelity qubit reset minimizes faulty state preparation of auxiliary qubits, and rapid qubit reset reduces the idling error experienced by spectator qubits [207–212]. In addition, operations capable of resetting leakage states into the computational subspace provide the benefit of converting uncorrectable leakage errors into correctable errors [85, 105, 106, 213, 214]. More generally, fast and accurate qubit reset improves experimental repetition rates and state preparation fidelities, bringing the measurement times of higher-order statistics of noisy many-qubit devices within a feasible range.

In superconducting qubit systems, reset schemes that use projective single-shot measurement followed by conditional single-qubit control can realize reset within a few hundred nanoseconds [215–218]. However, measurement-based conditional reset is limited in speed by inevitable temporal overhead in post-processing, and limited in accuracy by readout infidelity, for example due to measurement-induced state transitions [68, 69].

More recently, state-of-the-art unconditional transmon qubit reset has been achieved by activating resonant exchange coupling between a transmon and a damped aux-

iliary mode such as a readout resonator, and allowing the system to decay to its collective ground state [44, 213, 219–223]. Such reset protocols prepare the ground state independent of the prior state of the qubit, and thus are not limited by readout time and fidelity. In addition, unconditional reset schemes help reduce the impact of state misclassification errors on fault-tolerant logical operations [212]. Still, the speed of these reset schemes is limited by the decay rate of the auxiliary mode, which is itself constrained by the need to suppress Purcell decay and, in the case where the mode belongs to the qubit's readout resonator, optimize readout fidelity [172, 213, 221, 224]. Furthermore, additional driving or complicated pulse shaping is required for each additional excited state to be reset due to the narrow-banded nature of the auxiliary modes.

In this work, we go beyond the state of the art by implementing fast, unconditional reset of the first two excited states of a frequency-tunable transmon qubit by coupling it to a broadband metamaterial waveguide (MMWG) strongly damped to a cold environment [107, 108, 117, 149, 225]. The MMWG provides stronger protection against Purcell decay compared to single-pole Purcell filters, thanks to the sharp extinction of its density of states (DOS) outside of its passband. This enables significantly faster reset than in previous works by alleviating the tradeoff between large achievable damping and idling qubit Purcell relaxation. The bandwidth of the MMWG can be made large relative to the transmon anharmonicity, allowing for simultaneous reset of multiple excited states. Additionally, band edges with roll-off that is steep relative to the transmon anharmonicity provide a means for implementing so-called leakage reduction units (LRUs) [214], which selectively reset the second excited state of the transmon without corrupting the information encoded in the computational subspace. Leveraging these capabilities of the MMWG combined with dynamical activation of the interaction via parametric flux modulation [153, 226, 227], we demonstrate simultaneous reset of a transmon's three lowest energy eigenstates and an LRU that selectively resets a transmon's second excited state.

4.2 Unconditional reset

We perform our measurements on a frequency-tunable transmon qubit (Q_1) on the same device used in Ref. [117], biased at its upper sweet-spot (USS) with a g-e transition frequency $\omega_{ge}/2\pi = 7.63$ GHz and an anharmonicity $\eta/2\pi \equiv (\omega_{ef} - \omega_{ge})/2\pi = -179$ MHz. The qubit has a dedicated microwave drive line for XY control and a flux line for slow and fast frequency control.

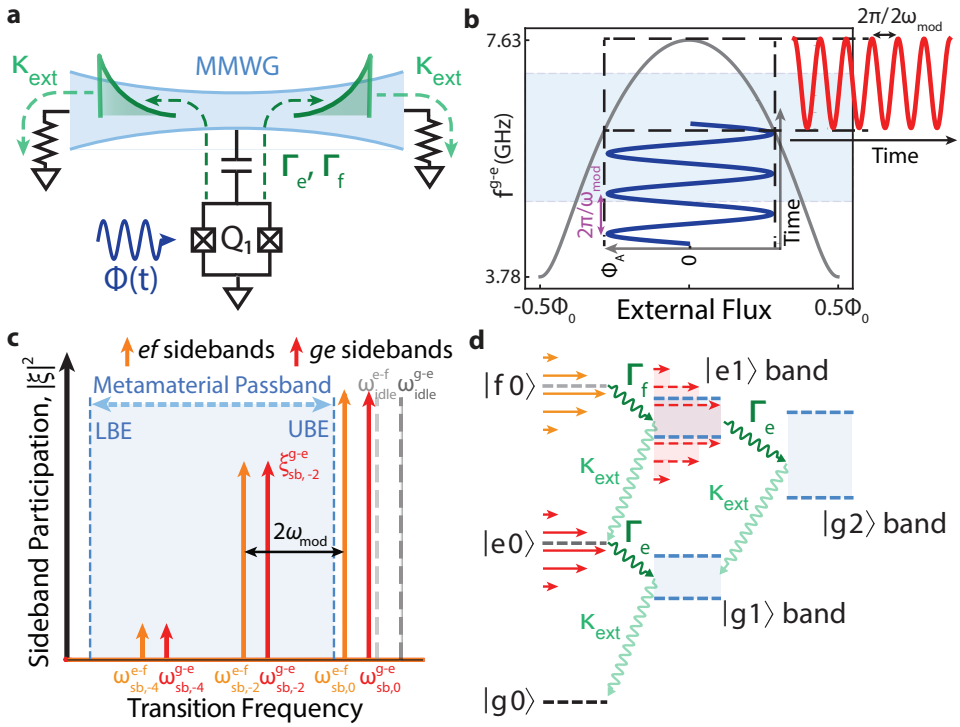

Figure 4.1: **Schematic of the reset protocol.** **a**, Illustration of reset of Q_1. External flux pulse $\Phi(t)$ applied to the SQUID loop of Q_1 causes bidirectional emission of excitation from Q_1 into the MMWG, which is damped to its external environment. **b**, Tuning curve of the flux-tunable transmon qubit. Φ_0 is the magnetic flux quantum. Parking the qubit at the upper sweet-spot, where the qubit is first-order insensitive to the external flux, a flux modulation tone of frequency ω_{mod} (dark blue curve) modulates the qubit frequency at a frequency $2\omega_{\mathrm{mod}}$ (red curve). The region shaded in pale blue denotes the extent of the MMWG passband. **c**, Sideband picture of the Q_1 during reset operation. Gray dashed lines represent idling g-e and e-f transition frequencies of Q_1, while colored lines indicate sideband frequencies with parametric modulation at ω_{mod} turned on. **d**, Energy level diagram showing flow of reset for different states. The notation $|s\, n\rangle$ is shorthand for Q_1 in state $|s\rangle$ and n photons being in the waveguide. Red and gold arrows denote modulation sidebands. Note that states of nonzero MMWG photon number live in a band of closely spaced energy levels, represented by the semi-opaque blue bands. The transition frequencies of the states in these bands can also be modulated when they include excitations in the qubit, as illustrated by the semi-opaque red rectangles representing the set of sidebands of the $|e\, 1\rangle$ band, because they depend on qubit frequency.

Q_1 is capacitively coupled to a single unit cell of a MMWG comprising a 1D coupled array of 52 lumped-element microwave resonators, as schematically shown in Fig. 4.1a. Such a structure can be modeled as a set of harmonic modes with a finite passband with sharp band edges, and allows rapid photon emission from coupled modes [109, 149, 150]. At either end of the MMWG is a tapering section consisting of four resonators that impedance-match the MMWG modes to 50 Ω transmission lines serving as input and outputs to the waveguide, providing strong damping to its environment across a wide and flat passband from approximately 5 GHz to 7 GHz. We measure Q_1 using standard dispersive readout techniques, with the MMWG serving as a Purcell filter waveguide for readout. Because of the need to estimate small residual excitation population for characterizing qubit reset on the order of the thermal population of the MMWG, achieving sufficiently high sensitivity in single-shot readout is crucial. More details of device parameters, readout, and thermal population of the MMWG can be found in Appendix 4.5.2 - 4.5.4.

Our qubit reset protocol is based on dynamically activating an exchange interaction between Q_1 and the MMWG modes. When Q_1 is idling, detuned above the MMWG passband, the rapid extinction of the MMWG DOS outside its band edges strongly protects Q_1 from Purcell decay through the 50 Ω ports of the MMWG. To turn on an exchange interaction, we apply a single-tone flux modulation pulse to Q_1's SQUID loop that activates a resonance condition between Q_1 and the MMWG passband and rapidly converts this Purcell decay protection into Purcell decay enhancement, inducing qubit reset. More information on relaxation times (T_1) as a function of qubit frequency can be found in Appendix 4.5.4 and Supplementary Material III of [117].

As illustrated in Fig. 4.1b, c, when Q_1 is biased at its USS, a flux modulation pulse of frequency ω_{mod} and amplitude Φ_m grows sidebands separated by even integer multiples ($\pm n2\omega_{\mathrm{mod}}$) from the time-averaged transition frequencies. Note that the negative convexity of the qubit's tuning curve at its bias point shifts the time-averaged transition frequencies of Q_1 downwards.

Sidebands of the transmon that fall within the passband of the MMWG are coupled to an effective continuum of modes and mediate radiative emission into the MMWG, as illustrated in the energy level diagram of Fig. 4.1c and d. The rate of emission of the transmon is roughly set by Fermi's golden rule involving the DOS of the MMWG and the transmon-MMWG coupling matrix element, which is determined

by the bare coupling between Q_1 and its unit cell, and the participation of the sidebands. Multiple excited states of the transmon can be simultaneously reset by the same mechanism, thanks to the large bandwidth of the MMWG as shown in Fig. 4.1c and d, where the emission processes for states up to the second-excited state are illustrated.

Emitted photons leave the waveguide at an effective damping rate κ_{ext} determined by the finite reflectivity of the MMWG tapers and a round trip time of ≈ 14 ns, estimated from the group velocity and the number of unit cells in the MMWG [149]. Note that full reset of both qubit and waveguide is important to avoid subsequent qubit control errors caused by photons remaining in the waveguide potentially inducing population revival or dephasing [149, 225].

We have chosen parametric modulation in order to avoid shelving and retrieval of excitation in and out of long-lived resonances whose frequencies collide with Q_1's frequency during flux tuning [228]. We find multiple such resonances, including two-level system defects (TLSs), and MMWG modes near the band edges that are not sufficiently damped to output lines, one of which we measure to have a relaxation time of ≈ 1.7 us. See Appendix 4.5.5 for details of reset with direct flux tuning and Landau-Zener-Stückelberg interference with long-lived resonances.

To calibrate a reset operation for at least the first two excited states of Q_1, we first define a flux pulse $\Phi(t; \Phi_A, \omega_{\text{mod}}, \tau_{\text{pulse}}) = \Phi_A \, \mathcal{E}(t; \tau_{\text{pulse}}) \sin(\omega_{\text{mod}} t)$ parameterized with Φ_A (modulation amplitude), ω_{mod} (modulation frequency), and τ_{pulse} (total flux pulse duration). The envelope function $\mathcal{E}(t; \tau_{\text{pulse}})$ is a square pulse of duration τ_{pulse} with zero-amplitude buffers $\tau_B = 2$ ns at the start and end filtered with a Gaussian kernel of width $\sigma = 1$ ns [106]. We perform a 3D sweep of the parameters Φ_A, ω_{mod}, and τ_{pulse} in order to characterize the reset at each point.

The pulse sequence for characterizing a reset operation is provided in Fig. 4.2a. We begin by pre-resetting Q_1 with a pre-calibrated reset pulse and heralding Q_1 in its ground state with high probability by using repeated rounds of projective measurement with a strict discrimination boundary [220]. Our ground state preparation has measured infidelity $1 - P_{g,\text{HERALD}} \approx 0.02\%$, which is significantly smaller than the thermal population $\approx 0.1\%$ of the MMWG. We then apply a combination of π_{ge} and π_{ef} pulses to prepare Q_1 in its $|g\rangle$, $|e\rangle$, or $|f\rangle$ state, after which we apply the appropriate reset pulse, followed by readout of the qubit. The measured state populations are inverted using the calibrated confusion matrix. We define the reset error (infidelity) $\equiv 1 - P_g$ to be the population not discriminated to be in the ground

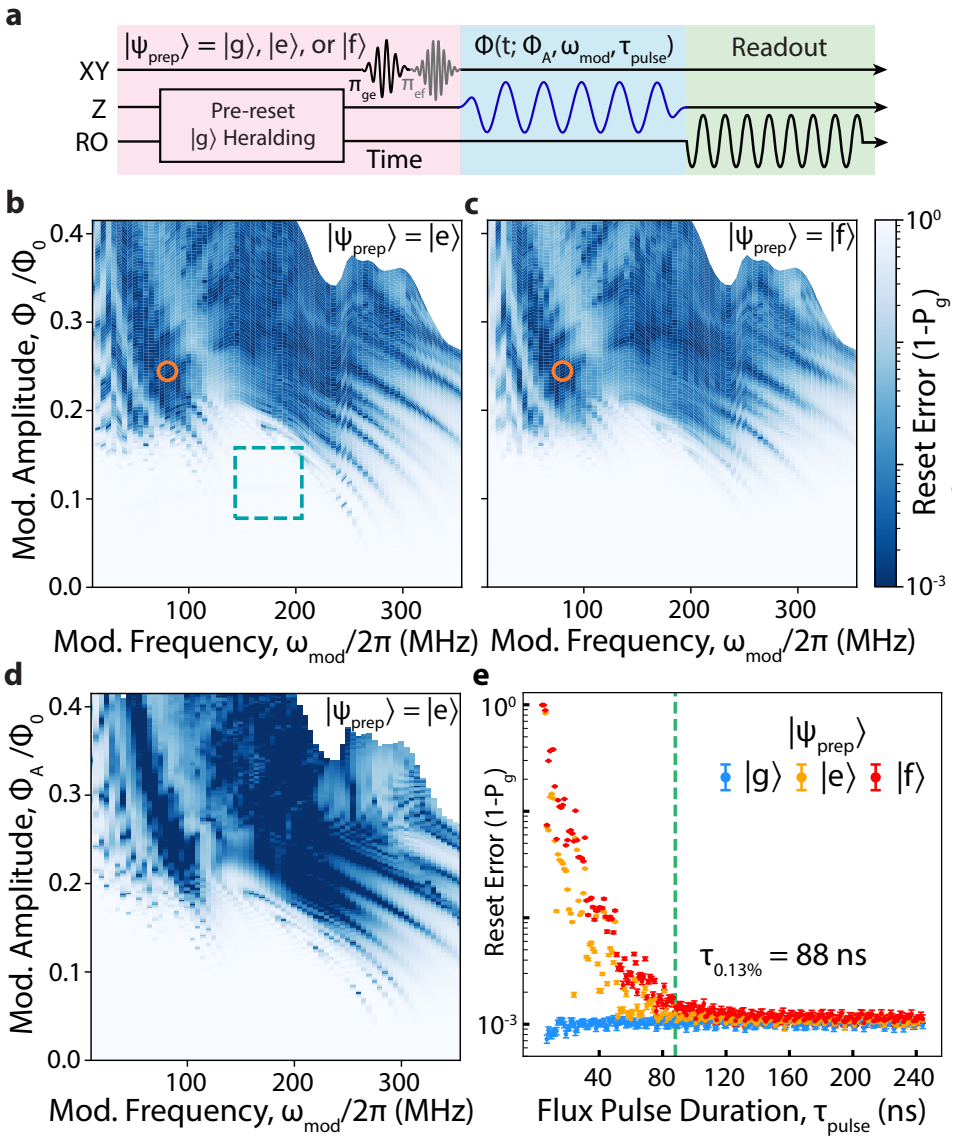

Figure 4.2: **Calibration and characterization of unconditional reset.** **a**, Pulse sequence for characterizing reset operation. **b, c**, Reset errors obtained from scan of reset pulse parameters ω_{mod} and Φ_{A}, for Q_1 prepared in $|e\rangle$ (**b**) and $|f\rangle$ (**c**). Dashed teal box indicates the scanned region for Fig. 4.3b. **d**, Simulation of the measurement of **b** up to single-excitation subspace. **e**, Reset errors obtained by sweeping τ_{pulse} with 1 ns resolution, for $\Phi_{\text{A}} = 0.244\Phi_0$ and $\omega_{\text{mod}} = 80$ MHz (orange hollow circles in **b** and **c**). Error bars indicate 95% confidence interval (t-test) with 30 samples, where each sample is obtained from 50,000 single-shot measurement.

state.

Fig. 4.2b and c shows the reset errors obtained from scanning the frequency and amplitude of a reset pulse of fixed length $\tau_{\text{pulse}} = 104$ ns, for prepared states $|e\rangle$ and $|f\rangle$. Thanks to the broadband nature of the MMWG, there are many frequency—amplitude pairs that could parameterize viable reset pulses with reset errors <1% for both prepared states. Simulation of the experiment of Fig. 4.2b agrees very well with experimental data, replicating most of the significant qualitative features of the data, as shown in Fig. 4.2d (see Appendix 4.5.6 for further details). Sets of curved features found in Fig. 4.2b-d show where sidebands are dominantly interacting with the longer-lived band edge modes of the MMWG passband. Additionally, the interference pattern found at the upper-leftmost region ($\omega_{\text{mod}}/2\pi < 40$ MHz and $\Phi_A > 0.17\Phi_0$) of 4.2b-d shows evidence of coherent dynamics due to the relatively slow tuning of the qubit at lower modulation frequencies through the more coherent band edge modes [228].

Fig. 4.2e shows reset quality at a fixed frequency and amplitude as τ_{pulse} is varied. For a given frequency and amplitude, we define the time τ_ϵ^i for reset of error ϵ such that for $\tau_{\text{pulse}} > \tau_\epsilon^i$, $1 - P_g < \epsilon$, for initial state $|i\rangle \in \{|g\rangle, |e\rangle, |f\rangle, ...\}$. We consider this definition to take into account time required for the depletion of photons in the MMWG after emission, which can re-excite the qubit upon spurious reflection from the MMWG taper. Fig. 4.2e shows a frequency-amplitude pair that gives one of the fastest resets as characterized by $\tau_{1\%}^e = 44$ ns, $\tau_{0.3\%}^e = 51$ ns, and $\tau_{0.13\%}^e = 88$ ns when prepared in $|e\rangle$, with a steady-state population $P_{\text{e}}^{\text{s.s.}} = 0.11\%(2)$ found from fit. This residual excitation population is close to the qubit excited state population when thermalized to the MMWG with its g-e transition frequency near the center of the passband. In addition, it is clearly demonstrated that the reset achieves simultaneous reset of multiple excited states, characterized by $\tau_{1\%}^f = 51$ ns, $\tau_{0.3\%}^f = 70$ ns, and $\tau_{0.16\%}^f = 88$ ns.

Similarly, rapid reset of multiple excited states with a small residual excited state population of $\approx 0.2\%$ within ≈ 97 ns is also achieved when the Q_1 is biased at its lower sweet-spot (LSS) with a g-e transition frequency $\omega_{ge}^{LSS}/2\pi \approx 3.78$ GHz. This demonstrates the flexibility in choosing the idling frequency relative to the strongly damped auxiliary modes used for unconditional reset, while maintaining the speed and the ability to reset multiple excited states simultaneously. For the results of unconditional reset from the lower sweet-spot, refer to Appendix 4.5.6.

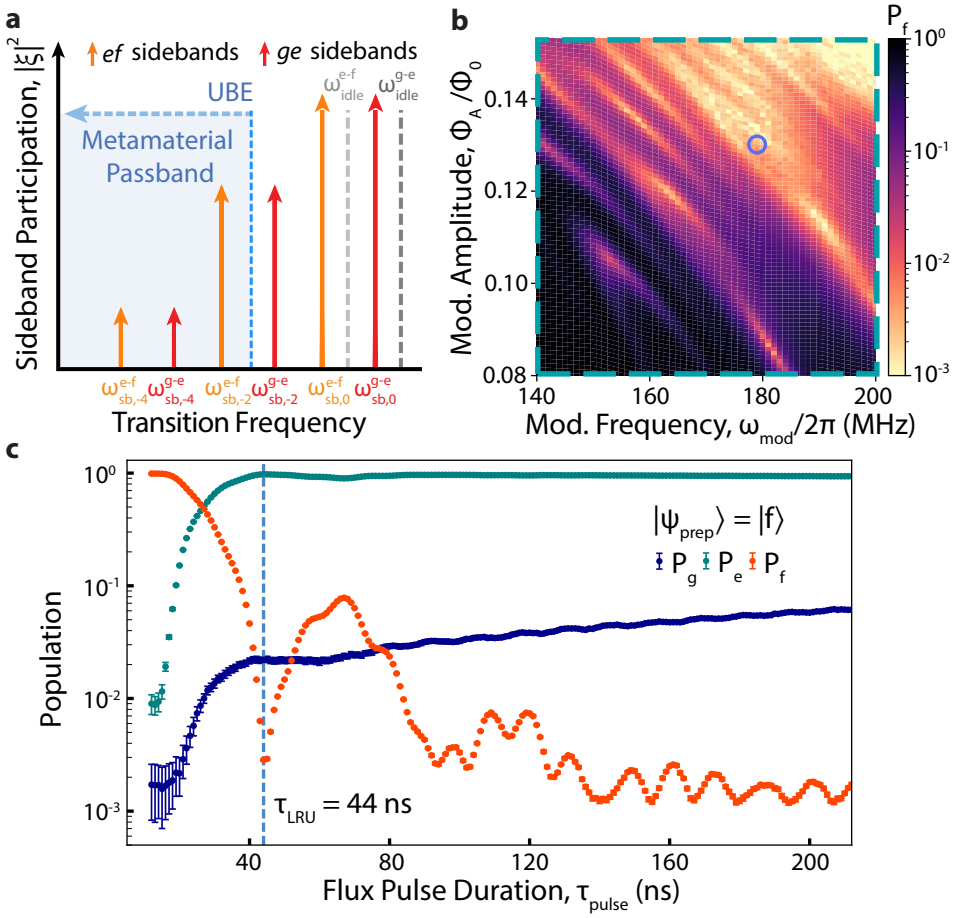

Figure 4.3: **Calibration and benchmarking of LRU operation.** **a**, Sideband picture of the parametric modulation of Q_1 during LRU. **b**, $|f\rangle$ population after applying LRU implemented by parametric flux modulation, with two-dimensional scan of pulse parameters over the region indicated in Fig. 4.2 b and c (dashed teal box). **c**, Resulting $|g\rangle$, $|e\rangle$, and $|f\rangle$ populations obtained after applying LRU to a qubit initially prepared in $|f\rangle$, where τ_{pulse} is swept with 1 ns resolution, for $\Phi_A = 0.13\Phi_0$ and $\omega_{\text{mod}}/2\pi = 179$ MHz (blue hollow circle in **b**). Error bars indicate 95% confidence interval (t-test) with 30 samples, where each sample is obtained from 100,000 single-shot measurements.

4.3 Leakage reduction unit

The sharp roll-off of the DOS at the upper band edge of the MMWG relative to the transmon anharmonicity enables implementation of leakage reduction units (LRUs), by selectively activating dissipation of $|f\rangle$ and higher excited states into the MMWG while maintaining the coherence of the g-e subspace. Fig. 4.3a shows the desired sideband configuration for implementing an LRU. An e-f sideband is placed within the passband of the MMWG, inducing radiative emission from $|f\rangle$ to $|e\rangle$, while the

corresponding g-e sideband, greater in frequency by the transmon anharmonicity, remains outside the passband.

It is desirable to minimize the time taken for the LRU so as to minimize the decoherence suffered by the g-e subspace due to relaxation and dephasing processes during leakage reset. This would generically require increasing the coupling of the e-f transition to the MMWG modes, which is accomplished in our parametric reset scheme by increasing the modulation amplitude for a given modulation frequency. However, depending on the amplitude of modulation, higher order sidebands of the g-e transition lying inside the MMWG passband may be of non-negligible participation, such as the fourth order sideband of the g-e transition as illustrated in Fig. 4.3a, and will limit the fidelity of LRU.

To determine viable parameter candidates for the LRU, we perform a more granular frequency—amplitude sweep with total flux pulse duration $\tau_{\text{pulse}} = 132$ ns. The explored parameter region is that indicated by the dashed teal box in Fig. 4.2b, where we observe insignificant $|e\rangle$ decay and we expect the second order e-f sideband to just be entering the passband of the MMWG. In this measurement, we chose a smoother Gaussian filter parameter $\sigma = 3$ ns and buffer duration $\tau_{\text{B}} = 6$ ns in order to suppress spectral broadening of the second order sideband of the g-e transition that can induce unwanted additional radiative decay of the $|e\rangle$ state [106]. The pulse sequence is identical to that of Fig. 4.2a. As can be seen in Fig. 4.3b, multiple prominent regions of $|f\rangle$ relaxation are visible, which we believe correspond to interaction of the e-f transition with different modes near the upper band edge of the MMWG.

The set of optimal LRU-parameters are found by trying to both maximize the $|f\rangle$ removal fraction and minimize the impact on remaining $|e\rangle$ population following LRU application (see Appendix 4.5.7 for further details in calibration of the LRU). For optimal modulation frequency $\omega_{\text{mod}}/2\pi = 179$ MHz and modulation amplitude $\Phi_{\text{A}} = 0.13\Phi_0$ (blue circle in Fig. 4.3b), we plot in Fig. 4.3c the measured final state g, e, and f probabilities as a function of LRU pulse length τ_{pulse} for an initial state of $|f\rangle$. We find the fastest LRU operation of 44 ns with a residual $|f\rangle$ population of 0.285(3)%. Note that we define the time needed for LRU to be the time to the first local minimum of the $|f\rangle$ population, in contrast to the definition of the unconditional reset time which included the time required for the depletion of MMWG, for the following reasons. First, leakage errors are expected to occur infrequently [85], and hence the vast majority of the time we expect no emitted photons after the LRU. Any

time spent waiting for waveguide ringdown in those cases serves no purpose and only incurs additional decoherence on spectator qubits. Second, in the event that leakage has occurred and the LRU has successfully returned the leaked population back to the computational subspace, a detected error in the next syndrome measurement is essentially inevitable. In this case, waiting for waveguide depletion to avoid additional computational errors is less valuable.

With the calibrated LRU, we study its efficacy in removing leakage errors over long sequences and its decoherence impacts on the g-e subspace by utilizing randomized benchmarking (RB). For this analysis we consider four different RB primitive sequences: reference, interleaved LRU ("LRU"), inject 3% leakage after each Clifford gate ("leakage injection"), and leakage injection followed by LRU ("leakage injection + LRU"), shown schematically in Fig. 4.4a [106, 231]. Figures 4.4b and 4.4c compare the measured ground-state survival population and leakage accumulation, respectively, for each of these RB sequences. The RB curves are fitted to the leakage accumulation and the survival population models provided in Ref. [229], which allows us to extract the steady-state leakage population of the RB sequences. When the leakage error rate per Clifford operation is significantly higher than the relaxation rates of the leakage states, the survived population P_g is expected to drop below 50% due to the buildup of a higher steady-state leakage population, as clearly observed in the case of "leakage injection", where P_f exceeds 20%. In contrast, we find that the use of the LRU effectively limits the accumulation of leakage significantly below that of the reference RB, resulting in a steady-state leakage population of $\approx 0.08\%$, which is close to the readout floor. Furthermore, the use of the LRU maintains a small steady-state leakage population of $\approx 0.09\%$, even when preceded by the injection of 3% leakage. These results clearly demonstrate that the LRU is sufficiently effective in suppressing typical leakage error rates for single- and two-qubit gates in transmon qubits.

Noting the sufficiently small leakage accumulation in both the "Reference" and "LRU" cases, we conduct a conventional interleaved RB (iRB) analysis [232], revealing a gate infidelity of 0.72(1)%. To better understand the sources of this infidelity, we quantify the impact of flux modulation on the g-e subspace by measuring coherence with the pulse sequence shown in Fig. 4.4d. We observed a reduced relaxation coherence time $T_1^{\mathrm{mod}} = 3.3\ \mu$s during the flux modulation with the same parameters as used in the LRU operation, as shown in Fig. 4.4e. Additionally, we observe a clear reduction in T_1^{mod} as the modulation amplitude is increased at a

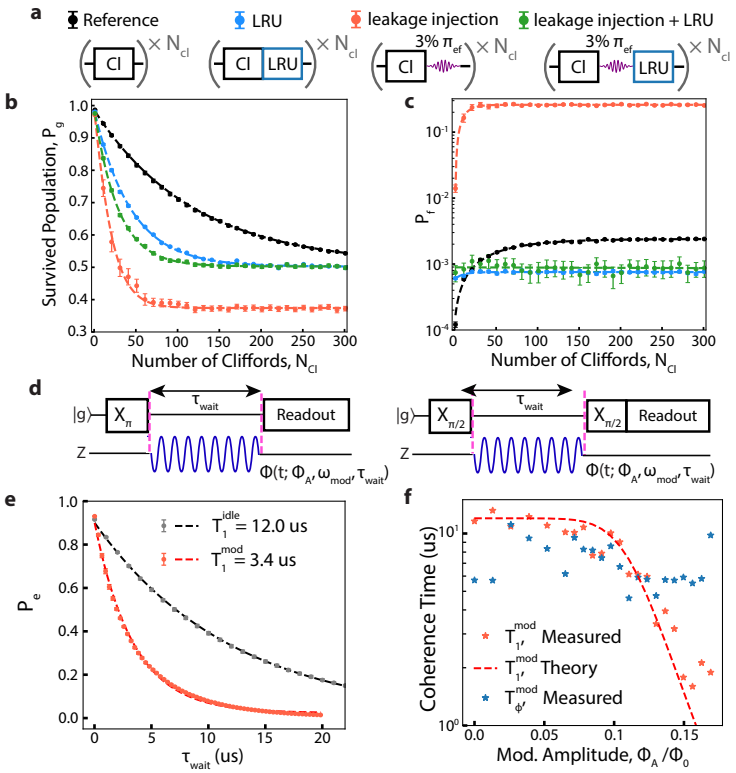

Figure 4.4: **Randomized benchmarking with LRU operation. a**, Primitive pulse sequences used for Randomized Benchmarking (RB) to assess the infidelity of the LRU as an idling gate (labelled "LRU") and the efficacy of the LRU against realistic leakage errors (labeled "leakage injection" and "leakage injection + LRU"). A reduced-amplitude π_{ef} pulse injects a leakage error of 3%. Every LRU operation is followed by a pre-calibrated virtual-Z operation that cancels the phase accumulated during the LRU. **b, c**, Survived population (**b**, P_g) and accumulated leakage (**c**, P_f) after applying RB sequences with different numbers of Clifford gates (N_{Cl}). Dashed lines indicate fits to the model from [229]. Error bars indicate 95% confidence interval (t-test) over 95 RB traces obtained over $\approx$ 25 hours. Each RB experiment is performed with 100 random Clifford sequences and averaged over 1,000 repetition. **d**, Pulse sequences used for measuring the relaxation coherence time, T_1^{mod} (left), and the Ramsey coherence time, $T_2^{*,\text{mod}}$ (right), under continuous flux modulation during the waiting times τ_{wait}. **e**, Comparison between relaxation coherence time without flux modulation (T_1^{idle}) and with flux modulation, using the parameters $\omega_{\text{mod}}/2\pi = 179$ MHz and $\Phi_{\text{A}} = 0.13\Phi_0$ as used in LRU. Dashed lines represent fits to an exponential decay profile. **f**, T_1^{mod} and pure dephasing coherence time T_ϕ^{mod} measured at different Φ_{A}, with $\omega_{\text{mod}}/2\pi = 179$ MHz. T_ϕ^{mod} is obtained from a relationship to Ramsey coherence time $(T_2^*)^{-1} = (2T_1)^{-1} + T_\phi^{-1}$ [230]. Red dashed curve shows the calculated T_1^{mod} (see Appendix 4.5.7).

fixed modulation frequency, as illustrated in Fig. 4.4f. We attribute such reduction in relaxation coherence time to the activation of higher-order g-e sidebands within the MMWG passband, which serves as an unintended channel for photon emission into the MMWG. This interpretation is supported by the strong agreement with the numerically estimated T_1^{mod} (red dashed curve), obtained from numerical calculation of sideband strengths and assuming constant emission rates within the MMWG passband. We also perform a Ramsey experiment with flux modulation activated to measure the decoherence time during the LRU operation and use this along with T_1^{mod} to estimate the pure dephasing rate during modulation, T_ϕ^{mod}. We find $T_\phi^{\text{mod}} = 3.7$ us, roughly uncorrelated with the modulation amplitude, as shown in Fig. 4.4f.

From these independent measurements, we estimate that such decay through unwanted sidebands contributes infidelity of $\approx 0.23\%$ for the pulse parameters used for LRU. Including contribution from background (idling) decoherence rates, we estimate infidelity of 0.72(1)% for the LRU restricted to the $g - e$ subspace, in good agreement with the measured infidelity. Further improvements in infidelity is expected for qubits with longer idling coherence time, since they allow for using a weaker modulation amplitude and longer pulse duration for LRU, suppressing decay through unwanted g-e sidebands. For further discussion on and analysis on LRU fidelity, refer to Appendix 4.5.7.

4.4 Summary and outlook

We have demonstrated simultaneous unconditional reset of a transmon with residual excitation population below 0.13% when prepared in $|e\rangle$ and below 0.16% when prepared in $|f\rangle$, in 88 ns. We additionally implement an LRU operation that resets a transmon's second excited state to 0.285(3)% residual excitation in 44 ns and has an overlap infidelity of 0.72(1)% with the identity operation in the computational subspace.

Although the reset and LRU operations presented here are remarkably fast, further avenues for improvement are clear. The qubit-waveguide coupling could be increased further, as the qubit relaxation times are not yet Purcell-limited ($T_1^{\text{Purcell-limit}} > 1$ s). Narrowing the passband of the waveguide would increase the emission rate by increasing the photonic DOS in the passband. Such a narrowing of the passband would also help suppress spurious reflections at the input and output ports by improving the achievable impedance matching, and provide

further Purcell protection during LRU by steepening the roll-off of the MMWG band edges. Further reduction in reset time could be achieved by cutting down on the number of unit cells of the MMWG. This would allow the MMWG to ring down more quickly by reducing the round trip time, compensating for the increased group delay from a narrower passband. State-of-the-art fabrication techniques and loss-optimized MMWG design choices can suppress relaxation at idle qubit frequency due to internal loss in the MMWG resonators, without compromising the reset rate. See Appendix 4.5.4 for more details. Regarding leakage reduction, use of a MMWG with a narrower passband could also prevent emission via higher-order g-e sidebands through the MMWG passband [225], providing better protection of the g-e subspace and yielding lower infidelity for the LRU. Further discussion and analysis of LRU performance is presented in Appendix 4.5.7.

The reported reset error level is understood to be limited by the thermal population of the MMWG. We believe the temperature of the MMWG ($\approx$ 45 mK) was elevated above the mixing plate temperature in our system due to an incidental overlap of one of our TWPA pumps with the MMWG passband, and insufficient isolation of our device from the pump tone. Ameliorating this systematic issue as well as improving the MMWG tapering to its environment could help better reduce the residual excitation population after reset. See Appendix 4.5.4 for further details.

While the unconditional nature of the reset obviates the need for the measurement of the transmon state, information, partial or otherwise, about the state of the transmon prior to reset can still be extracted by collecting the outgoing photonic field from any damped ends of the MMWG [225, 233, 234]. This could, in the most ideal case, allow for conversion of leakage errors into erasure errors by detecting when leakage events occur. It is also worth noting that the demonstrated unconditional reset and LRU in principle simultaneously reset a few higher excited states including the third ($|h\rangle$) and the fourth excited state of the transmon, as their transition sidebands are expected to reside within the broad passband of the MMWG. Although it has not been characterized in this work owing to lack of sufficient coherence in these states due to their spectral proximity to the MMWG passband, (bare ω_{fh} is expected to be $\approx$ 7.12 GHz, upper band edge $\approx$ 7.1 GHz) a device in which a MMWG possesses a lower frequency passband would allow for characterizing reset of such states.

Finally, the reset and leakage reduction method presented here can be extended to multi-qubit systems using a single MMWG, with a few technical considerations. To prevent unwanted excitation swapping between qubits instead of efficient resetting,

modulation parameters should be carefully chosen to ensure that qubit sidebands do not overlap. For extending leakage reduction to multi-qubit systems, it is important to address interactions mediated by the MMWG due to overlap between qubit-photon bound states [109, 117, 235]. One possible approach is to leverage these interactions to implement parametric multi-qubit gates or continuous multi-qubit interactions with built-in leakage reduction. This can be achieved by selecting modulation parameters that enable controlled interaction within the g-e subspace while placing higher-order sidebands of the transitions involving leakage states inside the MMWG passband. Alternatively, such interactions can be minimized by increasing the detuning from the MMWG band edge, which reduces localization lengths. In addition, since bound states exhibit an exponentially decaying wavefunction with distance, selectively spacing qubits by skipping a few resonators can further reduce unintended coupling.

4.5 Supplementary Information for Chapter IV

4.5.1 Measurement setup

Our fridge wiring is identical to that of Fig. S6 of the Supplementary Material of [117].

Our external control electronics wiring diagram can be seen in Fig. S1 here. It is similar to Fig. S5 of the Supplementary Material of [117], except we have removed the 10dB of attenuation on the fast flux lines of sub-figure a. to increase the dynamic range of our reset pulses, and the upconversion of our microwave XY signals is now handled by two Quantum Machines Octave units, obviating the need for some of the in-house filters, mixers, attenuators, amplifiers, and fast RF switches on those XY lines. Note that the readout upconversion and downconversion chain continue to use our previous in-house mixing configuration.

4.5.2 Device characterization

The circuit model of our device was identical to that of Supplementary Material section I of [117] including fit values for the inductances and capacitances, except that we also included the readout resonators of each qubit as lumped-element LC resonators with center frequencies ω_{ri} fit from spectroscopy data of the device, inductances $L_r = 4.5$ nH, and capacitances $C_{ri} = \frac{1}{\omega_{ri}^2 L_r}$. The readout resonators are capacitively coupled to each qubit with capacitance C_{qr} and the unit cell of the MMWG with capacitance C_{wr}. We did not include parasitics for the readout resonators.

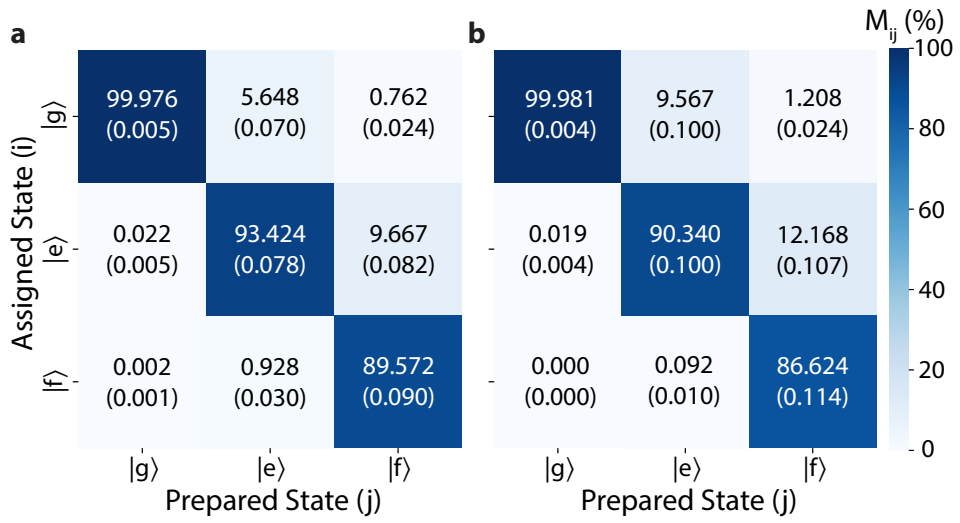

Figure 4.S1: **Estimated confusion matrix of single-shot readout.** Experimentally characterized readout confusion matrix M_{ij} used for estimating Q_1's population after applying the reset (**a**) and LRU operation (**b**), including the three lowest energy eigenstates of Q_1. The mean and standard error (in parentheses) of each matrix element are obtained over 100 repetitions, with each repetition consisting of 100,000 single-shot readouts.

4.5.3 Qubit readout calibration and characterization

We perform three-level state discrimination of Q_1 with the standard transmon dispersive readout technique [46, 57]. Our input and output signal paths and amplification chain for readout is identical to that of Fig. S5-6 of the Supplementary Material of [117].

In this work, we send readout input microwave pulse at around the frequency of R_1 (the readout resonator of Q_1), $\omega_{\text{drive}} \approx \omega_{R1}$, with a 248 ns-long square pulse envelope. We start the square envelope with a 20 ns kick with two times large amplitude for fast charging of readout resonator [236], and convolved the envelope with a Gaussian kernel of 10 ns standard deviation.

We measure temporal downconverted signals of both the microwave signals reflected (superscripted R) and transmitted (superscripted T) from the readout resonator and the MMWG Purcell filter using the OPX+, in order to improve SNR by ≈ 3 dB. For each single-shot measurement (subscripted k), we collect the signals for 348 ns, which is 100 ns longer than the input readout pulse, considering the transient response of R_1. The measured reflected and transmitted signals are then each mapped to a pair of real numbers (I_k^R, Q_k^R) and (I_k^T, Q_k^T) by integrating them with pre-calibrated sets of integration weights, whose definition is given in the Supplementary

Material of [210].

The four real numbers $u_{kj} \equiv (I_k^R, Q_k^R, I_k^T, Q_k^T)_j$ then characterizes the k-th single-shot readout of Q_1 prepared in state $|j\rangle$, $j \in \{g, e, f\}$. $\{u_{kj}\}$ yields three clusters of Gaussian distribution in a four-dimensional real space. Linear discrimination boundaries for real-time state discrimination are obtained by performing linear discriminant analysis (LDA) [237, 238]. We first collect in total 3×10^6 single-shot readout data (10^6 for each prepared states). Instead of directly feeding the measurement data into LDA, we cluster the data with Gaussian Mixture (GM) clustering method, an unsupervised clustering technique assuming mixtures of Gaussian distributions. During tihs process, we use the `GaussianMixture` API from the Python package scikit-learn [220, 238], and identify the corresponding state by selecting the state with the largest assignment probability. Next, we generate an artificially created ideal set of data $\{u_{kj,ideal}\}$, numerically drawn from the individual Gaussian distributions of each state. Finally, this ideal dataset is then fed into the LDA clustering algorithm by using `LinearDiscriminantAnalysis` API from scikit-learn, yielding linear discrimination boundaries. By using such artificially generated ideal samples instead of measured data, the process of determining the discrimination boundaries is significantly more resilient against various sources of errors including state preparation errors, T_1 relaxation, and measurement-induced state transitions.

We calibrate and characterize the readout by using readout confusion matrix $M \equiv \{M_{ij}\}$, where M_{ij} is the probability of assigning state $|i\rangle$ when Q_1 is prepared in state $|j\rangle$ giving the following relationship:

$$\mathbf{P}^{\mathrm{A}} = M\mathbf{P}, \tag{4.1}$$

where $\mathbf{P} = (P_g, P_e, P_f)^T$ is the column vector of the transmon state population and $\mathbf{P}^{\mathrm{A}} = (P_g^A, P_e^A, P_f^A)^T$ is the column vector of the assigned state population. The measured populations present in this work, unless otherwise noted, are obtained by multiplying the inverse of the confusion matrix in order to account for the measurement errors.

$$\mathbf{P} = M^{-1}\mathbf{P}^{\mathrm{A}}. \tag{4.2}$$

We aim at performing readout that is capable of accurately estimating residual excited state populations, while maintaining sufficiently large three-state assignment fidelity $F_{RO} \equiv (M_{11} + M_{22} + M_{33})/3$. We first run two-dimensional scan over readout pulse frequency and readout pulse amplitude and optimize for F_{RO}. Then, we increase

readout pulse amplitude until the probability of assigning $|e\rangle$ or $|f\rangle$ when a sample is drawn from ideal distribution of $|g\rangle$ is sufficiently small $\approx 10^{-4}$.

We start every measurement by heralding the $|g\rangle$ state using a stricter discrimination boundary with a target probability $P^{\text{target}}_{\text{g, HERALD}} = 0.9999$. This minimizes the effect of state preparation errors, and thus enables more accurate characterization of M. Note that negative populations that are often found in similar works may appear if the contribution from state preparation errors are not sufficiently excluded.

Fig. 4.S1a shows the readout confusion matrices used for characterizing unconditional reset operations. We achieve readout floor $1-M_{gg} \approx 2\times10^{-4} \approx 1-P_{\text{g, HERALD}}$ which is sufficiently small for estimating typical residual excited state population $\approx$ 0.1%, while maintaining high three-state readout fidelity of $F_{RO} \approx$ 94.3%. Fig. 4.S1b shows the readout confusion matrices used for characterizing LRU operations. For this readout, we use a different pulse with higher amplitude in order to better estimate residual population of $|f\rangle$ states as characterized by $M_{fe} \approx 0.09\%$, while compromising F_{RO} down to $\approx$ 92.3% and maintaining similar readout floor of $\approx 2 \times 10^{-4}$.

4.5.4 Characterization of metamaterial waveguide as a cold bath

Thermal population of the metamterial waveguide

The thermal population of the MMWG is responsible for residual excited state population observed after applying the unconditional reset operations. We estimate the thermal population of the MMWG by thermalizing Q_1 to the MMWG for a sufficiently long time and reading out the excited state population of Q_1. Fig. 4.S2a and b shows the pulse sequence used for this process. We first prepare Q_1 in its $|g\rangle$ or $|e\rangle$ state using an appropriate combination of heralding into $|g\rangle$ and a π_{ge}. Then, the g-e transition frequency of the Q_1 is tuned from 7.57 GHz to another frequency f^{g-e} by sending a 200 us-long square flux pulse. Finally, we record Q_1's residual excited state population via dispersive readout, as explained in the Appendix 4.5.3.

The measured residual excited state population P_e over different f^{g-e} at which Q_1 idles is shown in Fig. 4.S2. The residual populations are almost the same for the two prepared states over most of the range, suggesting that the Q_1 reached a steady-state at each point and the residual excited state population can be understood as the thermal population of the MMWG. The thermal population of $\approx$ 0.1% at 6 GHz corresponds to an effective temperature $T_{\text{eff}} \approx$ 43 mK, which is consistent with the values reported in various works. There is an unexpected peak at 6.684 GHz due to

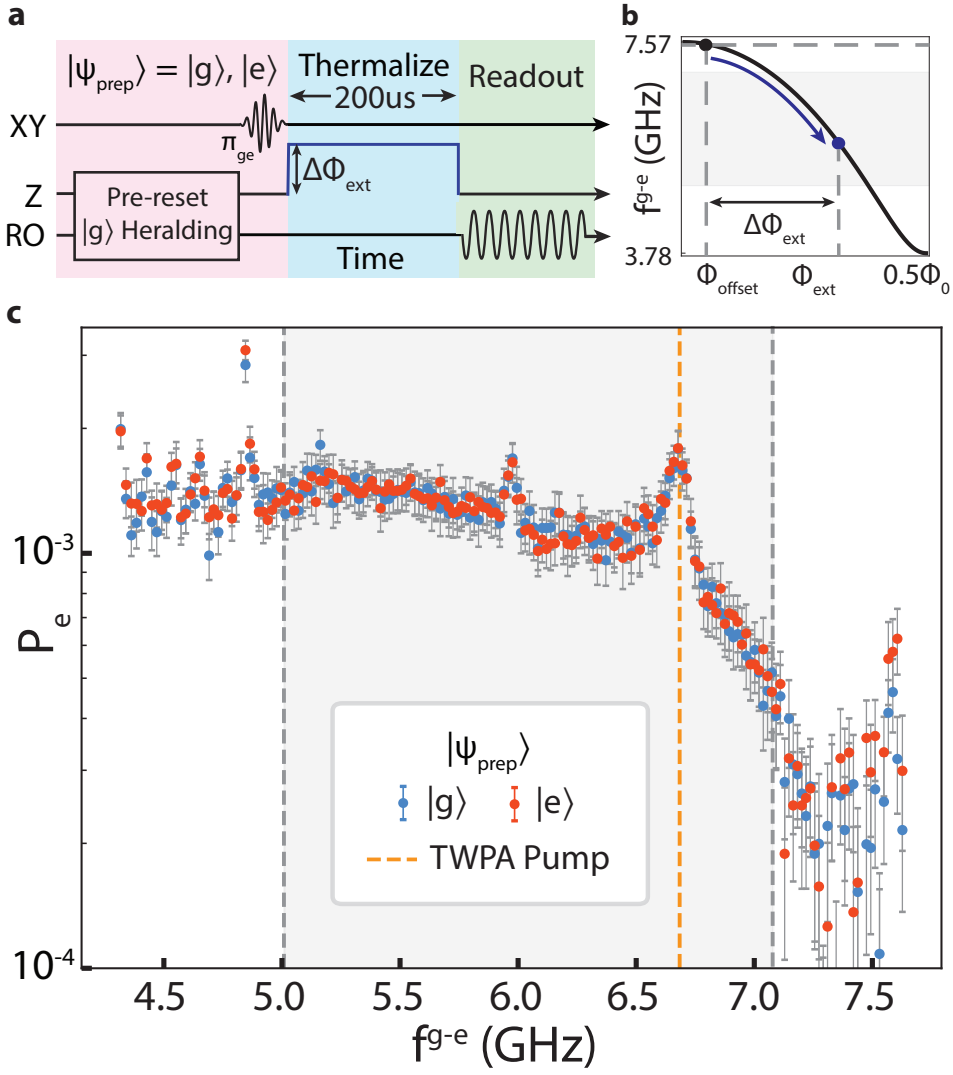

Figure 4.S2: **Characterization of the thermal excitation population at various g-e transition frequencies of Q_1. a, b**, Pulse sequence for characterizing thermal population. At each measurement, Q_1 is thermalized to its environment while a 200 us-long square flux pulse is applied, which brings g-e transition frequencies f^{g-e} to various points. **c**, Residual Q_1 excited state population P_e after thermalization, for prepared states $|g\rangle$ (blue) and $|e\rangle$ (red). The range over which f^{g-e} is swept includes the MMWG passband (gray shaded region) and USS frequency (rightmost point). The orange dashed line indicates the frequency of one the TWPA pumps (6.684 GHz) used for readout.

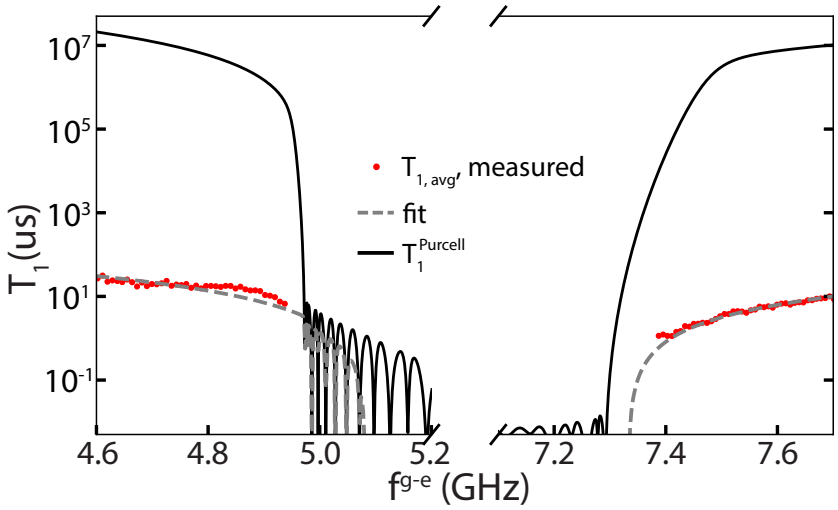

Figure 4.S3: T_1 **as a function of qubit frequency and comparison with the model.** Average relaxation time (T_1) of Q_1-Q_{10} as a function of operating frequency f^{g-e}. The T_1 values were measured in a separate cooldown. Data points are selected for frequency ranges where at least three qubits were measured. For better visualization, the frequency range [5.2 GHz, 7.1 GHz], where no measured data points are available has been omitted from the plot, indicated by diagonal break lines on the x-axis. Gray dashed line represents a fit to the modeled relaxation time T_1^{model} in eq.(4.3). Black solid line indicates the Purcell-limited relaxation time T_1^{Purcell}, as estimated in [117].

insufficient isolation of one of the TWPA pump driven at 6.684 GHz. This suggests that the thermal populations could be further reduced if we isolate the signals and noise flowing from the TWPA to the output line further (note that we use 40 dB isolator), or avoid overlap between the MMWG passband and the frequencies of the TWPA pumps.

Relaxation of qubits induced by metamaterial waveguide

To achieve effective reset and leakage reduction while maintaining coherence of the qubit when idle, it is necessary to ensure a high emission rate at the sideband frequencies and a sufficiently long relaxation rate (T_1) at the idle qubit frequency. This requires a sharp roll-off in the relaxation rate near the band edge of the MMWG. T_1 can be modeled as T_1^{model} in eq. (4.3), where the total relaxation rate is decomposed into background relaxation rate $1/T_1^{\text{background}}$ independent of the MMWG, Purcell-limited relaxation rate $1/T_1^{\text{Purcell}}$, and the internal-loss induced relaxation rate $1/T_1^{\text{internal}}$ from the MMWG resonators.

$$1/T_1^{\text{model}} = 1/T_1^{\text{background}} + 1/T_1^{\text{Purcell}} + 1/T_1^{\text{internal}} \tag{4.3}$$

T_1^{Purcell} is shown in Fig.4.S3, which is numerically calculated based on the admittance seen from the qubit node toward the MMWG output ports. Due to the multipole nature of the MMWG, T_1^{Purcell} changes rapidly near the band edge. For instance, T_1^{Purcell} decreases from over 1 ms at 7.2 GHz to below 10 ns at 7.0 GHz. For further details on the estimation of T_1^{Purcell}, refer to [117].

Another key factor determining the sharpness of the qubit relaxation rate is material loss in the lumped-element resonators in the MMWG. Due to strong qubit-resonator coupling and resulting hybridization, the qubit-like eigenstates inherit losses from the resonators that are not suppressed by the bandpass filter response of the MMWG. $1/T_1^{\text{internal}}$ of a qubit coupled to one of the MMWG resonators can be approximated as the following:

$$\begin{aligned} 1/T_1^{\text{internal}} &= \sum_k p_k \kappa_k^i \\ p_k &\approx \frac{g_k^2}{(\omega_q - \omega_k)^2}, \end{aligned} \tag{4.4}$$

where $k = 2\pi m/N$ (for integer m satisfying $k \in [-\pi, \pi]$) is the discrete wavevector of a MMWG mode with frequency ω_k, internal decay rate κ_k, and coupling g_k to the qubit. p_k represents the participation of mode k in the hybridized qubit-like eigenstate.

The dispersion relation of the MMWG and the coupling between the qubit and the MMWG modes can be approximated to the following [109, 149]:

$$\begin{aligned} \omega_k &= \omega_c - 2J\cos(k) \\ g_k &\approx \frac{g}{\sqrt{N}}, \end{aligned} \tag{4.5}$$

where ω_c is the center frequency of the MMWG, J is the hopping rate between adjacent resonators, and g is the coupling strength, and we assume a sufficiently long MMWG with N resonators and periodic boundary conditions.

In the continuum limit $N \to \infty$ where $\Delta k = 2\pi/N \to dk$, assuming all MMWG

modes have the same internal quality factor Q_i, T_1^{internal} simplifies to the following:

$$\begin{aligned} 1/T_1^{\text{interal}} &= \frac{g^2}{Q_i}\sum_k \frac{1}{N}\frac{\omega_c - 2J\cos(k)}{(\omega_q - \omega_c + 2J\cos(k))^2} \\ &\approx \frac{g^2}{2\pi Q_i}\int_{-\pi}^{\pi}\frac{\omega_c - 2J\cos(k)}{(\omega_q - \omega_c + 2J\cos(k))^2}dk \\ &= \frac{g^2}{Q_i}\frac{(\omega_q - \omega_c)\omega_c + 4J^2}{\left((\omega_q - \omega_c)^2 - 4J^2\right)^{3/2}}, \end{aligned}$$

where we use the relationship $\kappa_k = \omega_k/Q_i$.

By incorporating this analytical expression into eq.(4.3), we compare T_1^{model} with the measured T_1 values, as shown in Fig.4.S3. To mitigate site-specific variations such as resonances with two-level system (TLS) defects that could obscure the comparison, we use the average relaxation rate $T_{1,\,\text{avg}}$ of Q_1-Q_{10}. A fit to the data, which shows a good agreement as shown in Fig.4.S3, suggests an estimated Q_i of 2.3×10^4 for the lumped-element resonators in the MMWG.

This analysis suggests that decreasing qubit-MMWG coupling enhances T_1^{internal} by reducing overall hybridization. Still, the reset rate, primarily determined by the emission rate $\Gamma_{1D} = g^2/J$ at the center of the passband, can be preserved by reducing J proportionally to g^2. This implies that a device with a narrower MMWG passband and reduced qubit-MMWG coupling could achieve longer T_1^{internal} without compromising reset speed. For example, reducing the MMWG bandwidth from 2 GHz to 500 MHz while halving the coupling can improve T_1^{internal} by a factor of four without degrading reset performance.

Furthermore, significant improvements in quality factors are possible with recent advances in material engineering and choosing designs optimized for loss. State-of-the-art superconducting microwave resonators have demonstrated quality factors exceeding 10^6 for both lumped-element resonators and coplanar waveguide resonators [196, 239, 240]. Incorporating such high-quality resonators into the MMWG could further enhance T_1^{internal} while maintaining efficient reset and leakage reduction.

4.5.5 Reset with direct flux tuning and long lived band edge resonances

Theoretically, direct tuning of transmon's transition frequencies within the MMWG provides even larger emission rate $\Gamma_{1D} = \lambda_i^2 g_{\text{uc}}^2/J$ in the Markovian limit at the center of the passband [109, 150], where λ_i the relevant transition matrix element

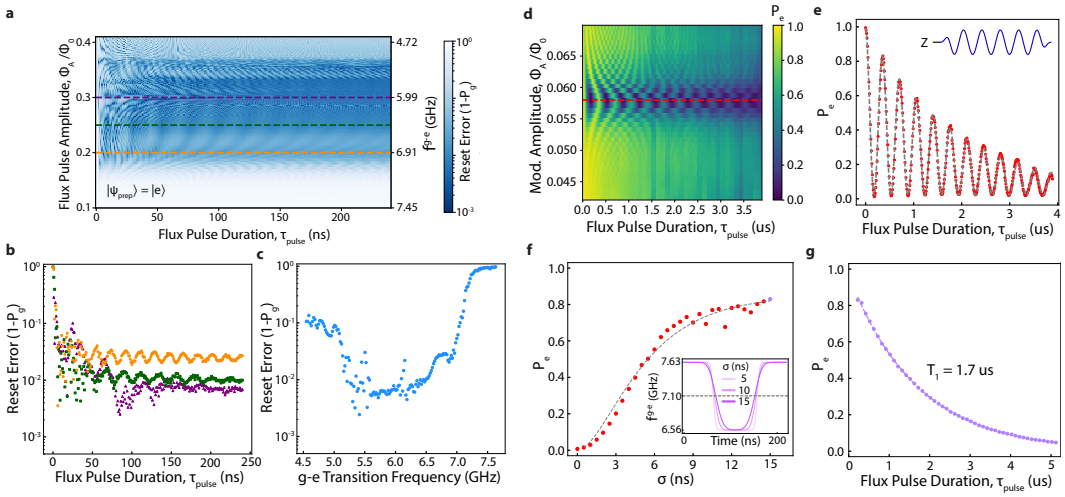

Figure 4.S4: **Reset with direct flux tuning, and probing presence and characterization of the long-lived resonances. a**, Quality of reset with direct flux tuning without AC modulation. Flux pulse amplitude Φ_A and flux pulse duration τ_{pulse} are swept. **b**, Cross-sectional view of a at various flux pulse amplitudes ($\Phi_A \approx 0.2\Phi_0$, $0.25\Phi_0$, $0.3\Phi_0$), showing the reset error over different pulse durations. **c**, Reset errors at $\tau_{\text{pulse}} = 240$ ns over different flux pulse amplitudes. (Cross-sectional view of **a** at $\tau_{\text{pulse}} = 240$ ns) **d**, Probing the presence of one of the long-lived modes by coherent swap-interaction. Q_1 is prepared in $|e\rangle$, followed by a weak parametric flux modulation with $\omega_{\text{mod}} = 250$ MHz. Flux pulse amplitude and flux pulse duration are swept. **e**, Cross-sectional view of **d** (red dashed line). The measured populations (red dots) are fitted with a damped Rabi oscillation model (gray dashed line) [241]. **f**, Characterization of the long-lived mode by Landau-Zener tunneling experiments. The tuning rate of f^{g-e} of the Q_1 when it crosses the frequency of the long-lived mode is varied by sweeping filter width σ of the Gaussian kernel used for filtering the square flux pulses. (inset) The measured residual excited state populations (red dots) are fitted to a model (gray dashed line). **g**, Measured residual excited state population (purple dots) obtained by sweeping τ_{pulse}, with $\sigma = 15$ ns. The fit (gray dashed line) characterizes the relaxation lifetime $T_1 = 1.7$ us of the long-lived mode. See appendix text for details of the Landau-Zener tunneling experiment.

for the i-th state in the transmon annihilation operator. Consequently, it is expected that Q_1 would achieve a reset error of 0.1% within 20 ns when prepared in $|e\rangle$, significantly faster that the reset demonstrated in the main text. However, as noted in the main text, we have chosen parametric flux modulation, in order to avoid adiabatic shelving of excitation into other modes that are coupled to the qubit which sets lower bound in achievable reset error and introduces non-Markovianity in the environment [242].

Fig. 4.S4a-c shows the quality of reset by direct flux tuning. Despite the rapid initial decay of excited states, the reset error stops decreasing and reveals coherent dynamics dominating at longer pulse durations, over a wide range of g-e transition frequency during the flux pulse including the entire MMWG passband.

Such phenomena can be understood by Landau-Zener-Stückelberg (LZS) interference with two passages; a fraction of excitation is transferred to long-lived resonances coupled Q_1 in the frequency collision during the rising edge of the flux pulse, and retrieved by the same mechanism during the falling edge of the flux pulse [228].

In order to test this hypothesis, we first probe the presence of a strongly-coupled long-lived resonance by activating a sufficient weak sideband of the g-e transition of Q_1 around the upper band edge of the MMWG. We indeed observe damped Rabi oscillation when there is a weak sideband at ≈ 7.1 GHz, which is a signature of two coupled coherent modes, evidenced by a chevron pattern and perfect fit to a model found in Fig. 4.S4d and e [241].

We then proceed to quantitative comparison with predictions from the theory of LZS interference. We perform two-passage experiment, in which the time-dependent g-e transition frequency $\omega_{ge}(t)$ of Q_1 prepared in $|e\rangle$ crosses the frequency of the long-lived resonance (7.1 GHz) twice, by applying a square flux pulse (without AC modulation). Here, the tuning rate of $\omega_{ge}(t)$ when it crosses 7.1 GHz is controlled by the filter width σ of the Gaussian kernel used for filtering the square flux pulse, as illustrated in the inset of Fig. 4.S4 f. The remaining $|e\rangle$ population P_R is measured over different σ from 0 ns (no filtering) to 15 ns, for a fixed duration of $\tau_{\text{pulse}} = 220$ ns, with buffers $\tau_{\text{B}} = 60$ ns at the start and the end. This choice of temporal parameters for flux pulses provides sufficient durations for the tested range of σ, during which Q_1 dumps most of its excitation into the MMWG when it is inside the MMWG passband, such that the P_R is dominated by the population retrieved from the long-lived resonance during the second passage. Therefore, theoretical prediction for this measurement is given by the following set of equations, rather than the equations

assuming maximum coherence for the resonances provided in [228]:

$$\begin{aligned} P_R &= P_0(1 - P_{\text{dia}})^2 \\ P_{\text{dia}} &= e^{-2\pi\Gamma} \\ \Gamma &= \frac{g^2_{\text{Q}_1\text{-M}}}{\mathrm{d}\omega_{ge}/\mathrm{d}t|_{\omega_{ge}=\omega_M}}, \end{aligned} \tag{4.6}$$

where P_0 is the revival population in the limit of an infinitely fast frequency tuning, M denotes the aforementioned long-lived resonance with a 0-1 transition frequency $\omega_M = 7.1$ GHz, and g_{Q_1-M} is coupling between Q_1 and M. We find an excellent agreement between the measured data and fit to eq.(4.6) with a strong coupling $g_{\text{Q}_1\text{-M}} \approx 23.6$ MHz, as shown in Fig. 4.S4f. In addition, we measure relaxation lifetime $T_1 = 1.7$ us for the resonance M, by sweeping the flux pulse duration with $\sigma = 15$ ns, as provided in Fig. 4.S4g.

It is worth noting that the rate of adiabatic exchange of population $P_{\text{adia}} = 1 - P_{\text{dia}}$ provided in eq.(4.6) is much greater for higher excited states of the transmons, due to their larger transition matrix elements. Consequently, this imposes challenges in resetting higher excited states with flux tuning with some adiabaticity that would be needed for unconditional reset of multiple excited states with narrow-banded auxiliary modes [213]. In order to overcome this issue, we have chosen parametric flux modulation which provides continuous dissipation through sidebands while interleaving multiple avoided crossing passages with long-lived resonances coupled to transmons, which does not require knowing the presence of or careful characterization of the relevant long-lived resonances.

4.5.6 Unconditional reset

Unconditional reset from the lower sweet-spot

In this appendix, we demonstrate the unconditional reset of a qubit when its idling frequency is below the passband of the MMWG. By positioning the MMWG passband above the qubit's idling frequency, we can achieve a lower residual population in the qubit after reset. This leverages the reduced thermal population at the higher frequency band of the MMWG, which is difficult to attain at the qubit's idling frequency [220, 221].

We begin by biasing Q_1 at its lower sweet-spot (LSS), where we measure a g-e transition frequency of $\omega_{ge}^{LSS} = 3.78$ GHz and relaxation coherence time of $T_1 \approx 30$ us. As with the unconditional reset demonstrated in the main text for Q_1 biased at its

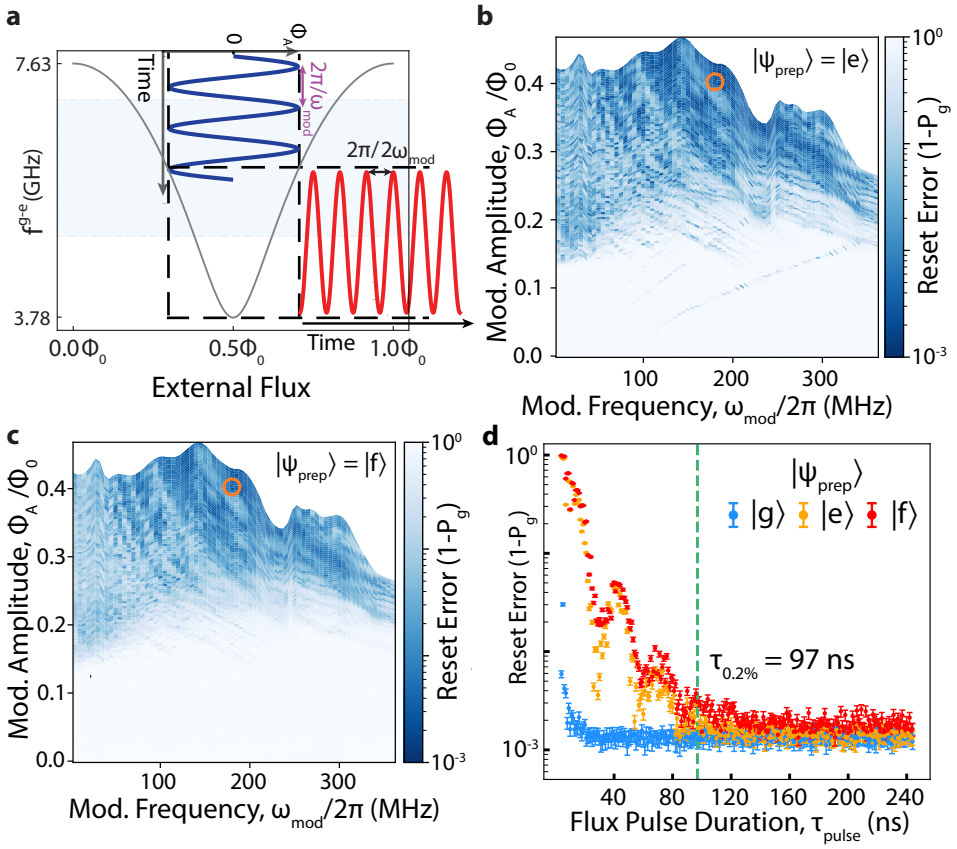

Figure 4.S5: **Unconditional reset from the lower sweet-spot (LSS) a**, Tuning curve of the flux-tunable transmon qubit centered at the LSS. Φ_0 is the magnetic flux quantum. Parking the qubit at the LSS, where the qubit is first-order insensitive to the external flux, a flux modulation tone of frequency ω_{mod} (dark blue curve) modulates the qubit frequency at a frequency $2\omega_{\mathrm{mod}}$ (red curve), similar to the case when the qubit is biased at its USS. The region shaded in pale blue denotes the extent of the MMWG passband. **b, c**, Reset errors obtained from scan of reset pulse parameters ω_{mod} and Φ_A, for Q_1 prepared in $|e\rangle$ (**b**) and $|f\rangle$ (**c**). **d**, Reset errors obtained by sweeping τ_{pulse} with 1 ns resolution, for $\Phi_{\mathrm{A}} = 0.4\Phi_0$ and $\omega_{\mathrm{mod}} = 180$ MHz (orange hollow circles in **b** and **c**). Error bars indicate 95% confidence interval obtained from bootstrapping.

upper sweet-spot, illustrated in Fig. 4.S5a, we apply a parameterized flux modulation pulse to activate sidebands within the passband of the MMWG. Fig. 4.S5b and c display the reset errors $(1 - P_g)$ as a function of the frequency (ω_{mod}) and amplitude (Φ_{A}) for a reset pulse with a fixed duration of $\tau_{\text{pulse}} = 104$ ns, for prepared states $|e\rangle$ and $|f\rangle$.

Similar to the reset achieved from the USS, we find numerous frequency-amplitude pairs that enable unconditional reset with errors below 1% for both prepared states. Fig. 4.S5d shows the reset errors obtained by varying the total pulse duration τ_{pulse} for the specific frequency-amplitude pair indicated by the orange circles in Fig. 4.S5b and c. Using the reset time definition from the main text, we find $\tau^{e}_{0.2\%} = 97$ ns and $\tau^{f}_{0.3\%} = 105$ ns, which are faster and as accurate as previously reported unconditional resets. This demonstrates the MMWG's capability for rapid and simultaneous reset of multiple excited states. Additionally, we observe a steady-state population of 0.15% from an exponential fit, corresponding to an effective temperature of ≈ 28 mK at the transition frequency of 3.78 GHz. This indicates that the MMWG effectively provides a cold bath for reset.

Note that the population estimates shown in Fig. 4.S5d are acquired differently from other results in this work due to limited ground state preparation fidelity, which compromised the accuracy of the confusion matrix estimation. Instead, we determined the state populations by fitting IQ points from 100,000 repeated measurements to a mixture of Gaussian distributions using the `GaussianMixture` API from the Python package scikit-learn. The confidence interval for the estimated reset error was calculated through bootstrapping with 1,000 resamples.

Simulation of reset dynamics

We performed a Lindblad master equation simulation of the reset dynamics using the QuTiP [243] python package to confirm the reset dynamics observed in measurement. Because of the overhead of quantifying the transfer function of our full flux lines for all the frequencies of interest in reset measurements, we did not attempt to use these simulations to obtain a quantitative fit of measured data, but only to verify that measured qualitative behaviour was expected in our best theoretical model of the device.

We performed a full dissipationless circuit quantization procedure using the capacitance and inductance matrices of the device to define its Hamiltonian. Our circuit model was identical to that of Supplementary Material section I of [117] including

fit values for the inductances and capacitances, except that we also included the readout resonators of each qubit as lumped-element LC resonators with center frequencies $\omega_{r\,i}$ fit from spectroscopy data of the device, inductances $L_r = 4.5$ nH, and capacitances $C_{r\,i} = \frac{1}{\omega_{r\,i}^2 L_r}$. The readout resonators are capacitively coupled to each qubit with capacitance C_{qr} and the unit cell of the MMWG with capacitance C_{wr}. We did not fit the parasitics for the readout resonators.

We modeled dissipation at either end of the MMWG by defining two collapse operators on the modes corresponding to the final taper cells at either end of the waveguide. The associated decay rates for these collapse operators were defined to be the decay rate of the charge on the taper cell capacitor found by modeling the last taper cells as independent (that is, not coupled to the rest of the MMWG) LC resonators coupled capacitively to a 50 Ω resistor standing in for the environment and solving the equations of motion for the charge. More accurate modeling would incorporate more unit cells of the metamaterial waveguide.

Because we were not considering any drive on the system, and because of the excitation number preserving nature of the Jaynes-Cummings Hamiltonian, and the fact that the defined collapse operators only remove excitations from the system, we could restrict the total number of excitations in our system to be less than some finite value N. We chose $N = 1$ because, given the total number of degrees of freedom in the MMWG-qubit-RO resonator system, $N = 2$ was prohibitively expensive to simulate.

We simulated reset of Q_1 for different flux pulses defined by different frequency-amplitude pairs with Q_1 beginning at its upper sweet-spot and a single excitation in the eigenstate of the full Hamiltonian with the largest overlap with the bare Q_1 eigenstate. Reset was simulated using a time-dependent term in the Hamiltonian that time-varied the frequency of Q_1 according to the frequency and amplitude of the flux pulse, assuming the same Gaussian $\sigma = 1$ ns filtering of the flux pulse in simulation as was used in actual measurement and reset pulses of total length 104 ns. Results of the simulation can be seen in Fig. 4.2d.

Evaluation of the demonstrated reset protocol

In Fig. 4.S6, we present a comparison of experimentally demonstrated reset protocols for superconducting qubits, evaluated by reset errors $(1 - P_g)$ and the time required to achieve these reset errors (T_{reset}) [44, 85, 213, 215, 218–223]. For conditional reset schemes, T_{reset} includes the time needed for readout and the application of

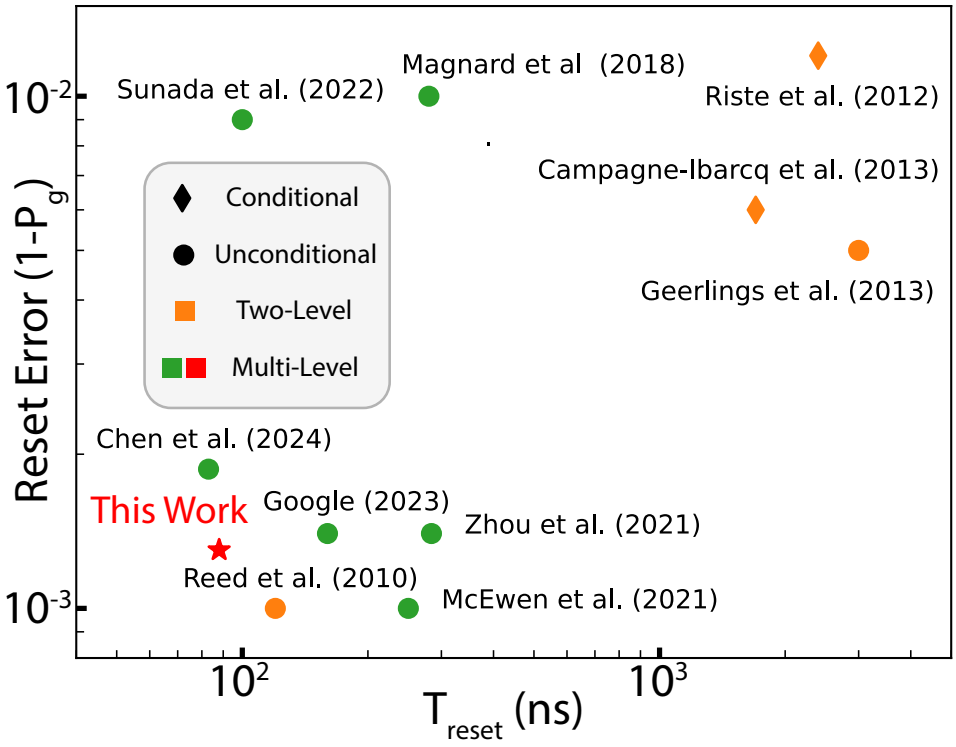

Figure 4.S6: **Comparison of experimentally demonstrated reset protocols.** Experimentally characterized reset errors (1-P_g) and the time to reach the quoted reset errors (T_{reset}) of various reset schemes reported in [44, 85, 213, 215, 218–222].

feedback on the qubits. For unconditional reset schemes, we quote T_{reset} as either the pulse duration after which reset errors stay below the quoted reset errors or the total reset time including depletion of auxiliary modes.

Protocol for resetting multiple qubits

The unconditional reset protocol can be extended to support the simultaneous reset of multiple qubits, such as illustrated in 4.S7a. Owing to the broad passband of the MMWG, multiple qubit transition sidebands can be accommodated within the passband while suppressing unwanted crosstalk and frequency crowding. A practical strategy is to space the sidebands of qubit transitions sufficiently far apart, as illustrated in 4.S7b. To minimize reset errors arising from formation of dark states between qubits or reabsorption of emitted excitations by other qubits in the MMWG, the sideband spacing should be sufficiently larger than the spectral linewidth of each sideband, as indicated by the green shaded regions around the arrows. Such spacing of transition sidebands can be realized by carefully choosing parametric modulation parameters.

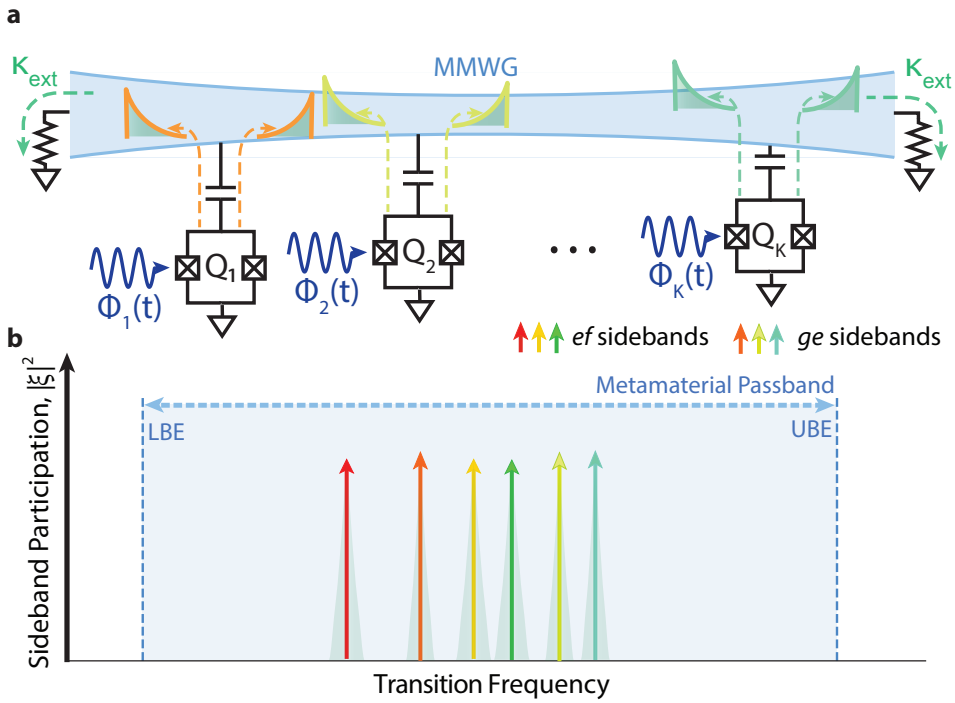

Figure 4.S7: **Schematic of the reset protocol for multiple qubits with a single MMWG a**, Illustration of reset of multiple qubits Q_1, Q_2, ..., Q_K. External flux pulses $\Phi_i(t)$, causes emission of excitation from Q_i into the MMWG, where $i \in \{1, 2, ...K\}$. **b**, Strategy for placing transition sidebands for simultaneous reset of multiple qubits. Green shaded regions around the arrows indicate the spectral lineshapes of the sidebands.

4.5.7 Leakage reduction units

Calibration of LRU parameters

To characterize LRUs at each combination of parameters, we conduct a three-dimensional sweep of Φ_A, ω_{mod}, and τ_{pulse}. For each frequency-amplitude pair, we determine the LRU duration $\tau_{LRU}(\omega_{mod}, \Phi_A)$ by identifying the point where the population P_f of Q_1, initially prepared in $|f\rangle$, reaches a local minimum, as shown in Fig. 4.S8a. This definition of LRU duration is the same as the definition provided in the main text. Fig. 4.S8b depicts the first excited state population P_e after applying the LRU with the calibrated τ_{LRU}, when Q_1 is initially prepared in $|e\rangle$. We find multiple LRU operation candidates, highlighted as the red triangles, where both a short τ_{LRU} and insignificant decay of P_e are simultaneously achieved. Finally, using the interleave randomized benchmarking (iRB) technique [232], we estimate the gate fidelity of the LRU operation, followed by virtual-Z correction, when acting as an idling gate acting on the g-e subspace of Q_1. We have only included the points

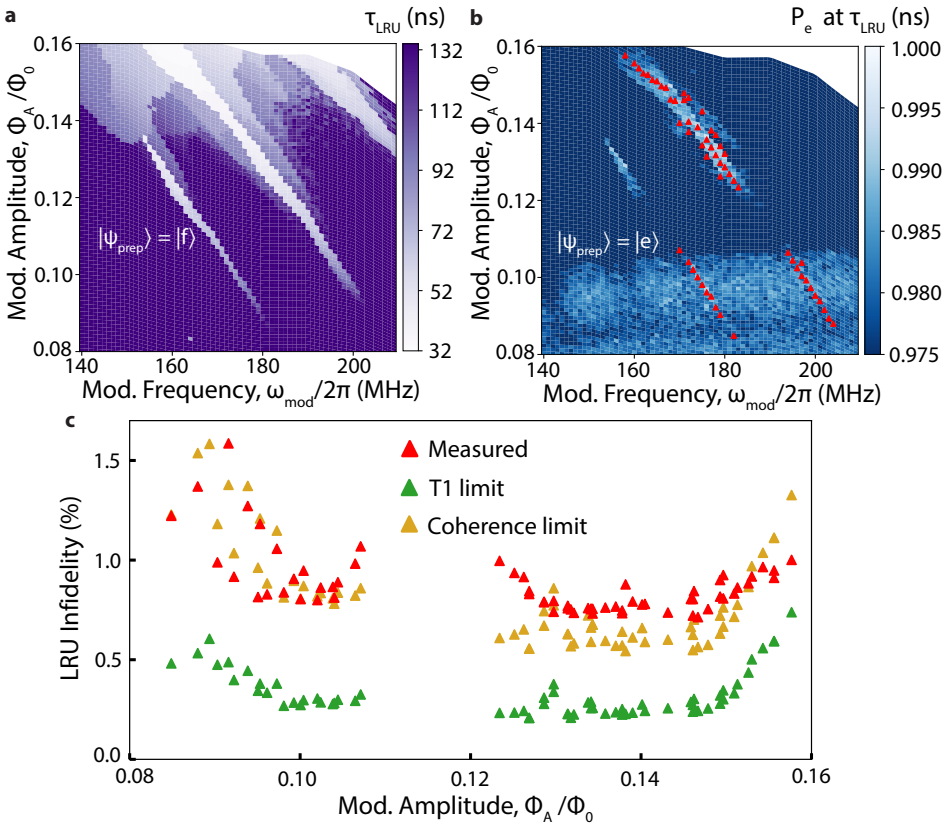

Figure 4.S8: **Calibration of LRU and impact of decoherence on infidelity in the g-e subspace. a**, τ_{LRU} over a range of (ω_{mod}, Φ_{A}) combination. τ_{LRU} is defined as the τ_{pulse} at which P_f reaches the first local minimum when Q_1 is initially prepared in $|f\rangle$, obtained from a 3-dimensional sweep of (ω_{mod}, Φ_{A}, τ_{pulse}). Note that the points without any local minimum are colored purple. **b**, Remaining P_e population with a flux pulse with duration τ_{LRU}, when Q_1 is initially prepared in $|e\rangle$. Red triangles indicate the parameter combinations for LRUs tested with iRB (**c**). **c**, Measured iRB infidelity of LRUs with different parameter combinations with T_1 and coherence limits. The coherence times (T_1 and T_2^*) are obtained from coherence measurements with the corresponding flux modulation tone applied continuously.

where leakage population ($P_f < 0.02$) is sufficiently low toensure effective leakage removal, and where the population revival after reaching the first minimum is less than 20%, excluding parameters where sufficient depletion of the MMWG modes is not achieved.

At each candidate parameters, coherence limits of the gate infidelities (IFs) are calculated using the following formula derived from [244]:

$$\mathrm{IF}(t_{\mathrm{gate}}, T_\phi, T_1) \equiv 1 - F_g \approx \frac{t_{\mathrm{gate}}}{3}\left(\frac{1}{T_\phi} + \frac{1}{T_1}\right), \tag{4.7}$$

where F_g represents the gate fidelity, and t_{gate} denotes the duration of the gate. In estimating infidelities, we approximate the LRU pulse as comprising two components: a buffer duration (12 ns) for the rising and falling edge of the envelope, during which the qubit is assumed to experience idling decoherence times ($T_1^{\mathrm{idle}} \approx 12$ us and $T_\phi^{\mathrm{idle}} \approx 7.3$ us), and the on-time ($\tau_{\mathrm{LRU}} - 12$ ns), during which we assume the qubit experiences enhanced decoherence time measured under continuous flux modulation tone, as detailed in the main text.

Fig. 4.S8c shows the distribution of LRU infidelities for the selected candidate parameters, along with calculated coherence limits and T_1 limits, which represent the contribution of T_1 to the overall coherence limit, as a function of modulation amplitude Φ_{A}. The LRU infidelities align well with the coherence limit, suggesting that no other error channels play a significant role. At low Φ_{A}, the LRU infidelities decrease as Φ_{A} increases, likely due to a reduced contribution from dephasing errors as τ_{LRU} shortens. However, at high Φ_{A}, despite the shortening of τ_{LRU}, the LRU fidelities begin to increase significantly due to increased T_1 decay rates during the sideband interaction. These two competing contributions result in a plateau of minimal infidelities in the range $\Phi_A \in [0.13\Phi_0, 0.15\Phi_0]$, from which we select the LRU parameters used in the LRU operation discussed in the main text. The absence of candidates in the region $\Phi_A \in [0.11\Phi_0, 0.12\Phi_0]$ is likely caused by a collision between the average qubit frequency of Q_1 (0^{th} sideband) and a nearby resonance, such as two-level system defects (TLSs). This hypothesis is supported by the observed enhanced decay of P_e across the entire modulation frequency ω_{mod}, which minimally contributes to the average qubit frequency.

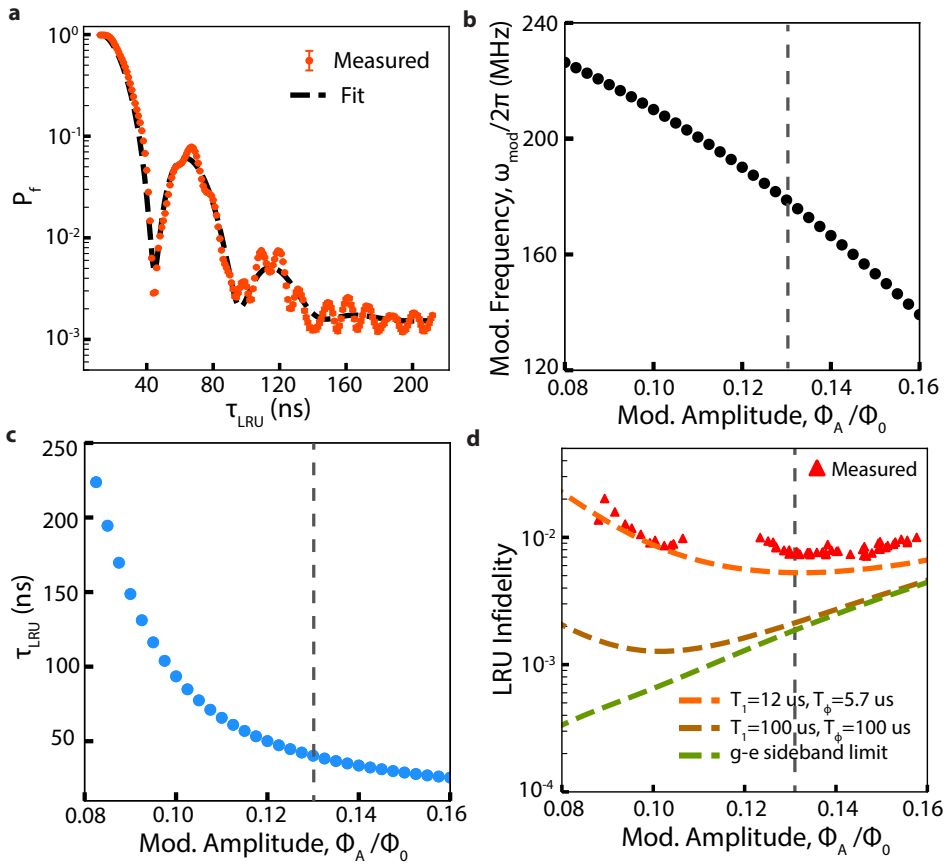

Figure 4.S9: **Approximation to single lossy-mode model and infidelity analysis for LRU operation a**, Resulting $|f\rangle$ population obtained after applying LRU, the same red curve in Fig. 4.3c. Black dashed line is the fit to the single lossy-mode model given by eq. (4.8), with $g_l/2\pi$ = 46.7 MHz, $\omega_l/2\pi$ = 6.93 GHz, $\kappa_l/2\pi$ = 17.6 MHz, and $P_{s.s.}$ = 0.15%. **b**, Modulation frequencies ω_{mod} needed for different Modulation amplitudes Φ_{A} to locate the second lower ($m = -2$) sideband frequency of the Q_1 at the lossy mode's frequency ω_l to induce resonant interaction. **c**, τ_{LRU}s estimated from the single lossy-mode model, at which P_fs (i.e., full-swap) reach their first local minima, for different modulation amplitudes Φ_{A}s with modulation frequency ω_{mod}s provided in **b**. **d**, Measured infidelities and infidelities estimated from eq. (4.10), over different Φ_{A}s. To understand the interplay between the optimal operating point of the LRU operation and the background decoherence rates of the qubits, we compare infidelity estimates with the measured decoherence rates (dashed red line), a case with improved coherence assuming T_1 = 100 us and T_ϕ = 100 us (dashed brown line), and the case without any background decoherence labeled g-e sideband limit (dashed green line). Dashed gray lines in **b**, **c**, and **d** indicate the modulation amplitude $\Phi_{\text{A}} = 0.13\Phi_0$ used for LRU operation shown in the main text, located at the plateau around the local minimum condition predicted by the model.

Infidelity analysis of the LRU operation and ideal MMWG design for LRU

During the flux modulation with amplitude Φ_{A} and modulation frequency ω_{mod}, the qubit-metamaterial interaction Hamiltonian can be written as the following, up to double-excitation subspace.

$$\hat{H}^{\mathrm{int}}_{\text{Q-MM}} \approx \sum_k \sum_{j\in 1,2} \sum_m \lambda_j g_k \xi_m e^{i(\omega_k - \omega_m^{j-1,j})t} \left|j-1\right\rangle \left\langle j\right| \hat{a}_k^\dagger + h.c.,$$

where $|0\rangle$, $|1\rangle$, and $|2\rangle$ indicates the transmon's three lowest energy eigenstates $|g\rangle$, $|e\rangle$, and $|f\rangle$, $\lambda_j \approx \sqrt{j}$ is the matrix element of the ladder operator for the transition between $|j-1\rangle$ and $|j\rangle$, $\omega_m^{j-1,j} = \overline{\omega^{j-1,j}(t)} + m\omega_{\mathrm{mod}}$ is the frequency of the m-th order sideband of the $|j-1\rangle$-$|j\rangle$ transition, ξ_m is the amplitude of the m-th sideband, k denotes MMWG mode index, ω_k and $\hat{a}_k$ are the corresponding frequency and ladder operator, and g_k is the coupling between the MMWG mode k and the qubit.

During an LRU operation, the coherent part of the dynamics of the e-f transition is dominated by the interaction with a single lossy waveguide mode located near the upper band edge of the MMWG. In Fig. 4.S9a, we show the dynamics of leakage population P_f with varied LRU duration τ_{LRU} that is accurately fitted to eq. (4.8) describing a qubit interacting with a lossy waveguide mode denoted with index l,

$$H_{\mathrm{eff}} = \begin{array}{c} \begin{matrix} |f0\rangle & |e1\rangle \end{matrix} \\ \begin{pmatrix} \Delta_{sb} - i\frac{\Gamma_{ef}}{2} & g_{sb} \\ g_{sb} & -i\frac{\kappa_l}{2} \end{pmatrix} \end{array} \begin{matrix} |f0\rangle \\ |e1\rangle \end{matrix}$$

$$P_f^{\mathrm{sol}}(t) = (1 - P_{s.s.}) \left| \frac{\alpha_- e^{\alpha_+ t} - \alpha_+ e^{\alpha_- t}}{\alpha_- - \alpha_+} \right|^2 + P_{s.s.} \tag{4.8}$$

$$\alpha_\pm = \frac{1}{2}\left(-b \pm \sqrt{b^2 - 4c}\right)$$

$$b = \frac{\kappa_l + \Gamma_{ef}}{2} + i\Delta_{sb},\ c = g_{sb}^2 + i\frac{\Delta_{sb}\Gamma_{ef}}{2} + \frac{\kappa_l \Gamma_{ef}}{4},$$

where H_{eff} is the effective Hamiltonian for the transmon-lossy MMWG mode's $\{|f0\rangle, |e1\rangle\}$ subspace via sideband interaction, $P_f^{\mathrm{sol}}(t)$ is the analytical solution for the Q_1's $|f\rangle$ state population during the sideband interaction with the initial condition $P_f^{\mathrm{sol}}(0) = 1$, $\Delta_{sb} \equiv \omega_{-2}^{1,2} - \omega_l$ is the detuning between the the lossy mode

l and the closest sideband ($m = -2$) of the e-f transition, $g_{sb} \equiv \sqrt{2} g_l \xi_{-2}$ is the effective coupling through the sideband, κ_l is the damping rate of the lossy mode, $\Gamma_{ef} = 1/T_1^{\mathrm{ef}}$ is the bare relaxation rate of the second excited state ($T_1^{ef} \approx 4.7 \mu$s), and $P_{s.s.}$ is the steady-state population.

On the other hand, the information encoded in g-e subspace is affected by added decoherence by activating sidebands inside the passband of the MMWG. The total relaxation rates of transmon's states, $\Gamma_{\mathrm{tot}}^{i-1,i}$, for the $|i-1\rangle - |i\rangle$ transition, can be approximated by summing the decay rates of each sidebands. Assuming a constant emission rate inside the MMWG passband, $\Gamma_{\mathrm{1D}}^{i-1,i}(\omega) \approx \frac{\lambda_i^2 g_{uc}^2}{J}$, and background relaxation rate, $\Gamma_0^{i-1,i} \equiv \frac{1}{T_1^{i-1,i}}$, outside the passband, we can use the following approximation:

$$\Gamma_{\mathrm{tot}}^{i-1,i} \approx \Gamma_0^{i-1,i} + \Gamma_{\mathrm{1D}}^{i-1,i} \left(\sum_{\omega_m^{i-1,i} \in \mathrm{Passband}} |\xi_m|^2 \right). \tag{4.9}$$

The dynamics and infidelity of LRU operations can be modeled using eq. (4.8) and eq. (4.9). Fig. 4.S9a shows a fit to the measured P_f for the model eq. (4.8), from which we obtain $g_l/2\pi = \frac{g_{sb}}{\sqrt{2}|\xi_{-2}|} = 46.7$ MHz, $\omega_l/2\pi = 6.93$ GHz, $\kappa_l/2\pi = 17.6$ MHz, and $P_{s.s.} = 0.15\%$. Based on this model, we find the LRU parameters ω_{mod} (Fig. 4.S9b) and τ_{LRU} (Fig. 4.S9c) at each modulation amplitude Φ_{A}, such that $\Delta_{sb} = 0$ during the flux modulation and $P_f < 0.02$ after the LRU operation.

With this model and using eq. (4.9) and eq. (4.7), we estimate infidelity of LRU operations for different flux modulation amplitudes by as shown in Fig. 4.S9d (dashed orange line), from which a good agreement with the measurement LRU infidelity (red triangle) is found. In addition, we find that the modulation amplitude used in the main text (dashed gray line) is close to the optimal condition predicted by the model.

Further, we analyze the interplay between the background coherence of the qubit and the optimal condition for LRU operation by comparing the infidelity estimates with different coherence times assumed: $T_1 = 12$ us, $T_\phi = 5.7$ us (this device, dashed orange line), $T_1 = 100$ us, $T_\phi = 100$ us (dashed brown line), and no background decoherence (dashed green line, labeled g-e sideband limit). As longer background coherence tolerates longer LRU operation, further improvements in infidelity is achieved by using weaker modulation which suppresses higher-order sidebands

inside the MMWG passband. Therefore, we expect LRU infidelity of $\approx 0.1\%$ is achievable for qubits with improved background coherence (≈ 100 us).

(4.10)

4.5.8 Microwave induced leakage reset

It is possible to perform leakage reset of a transmon dispersively coupled to a damped harmonic resonator by driving the transmon with a microwave charge drive at the difference frequency between the $|f\,0\rangle$ and $|g\,1\rangle$ states of the coupled system [154, 220]. This has the advantage of obviating the need for modulating the transmon frequency, thus avoiding the possibility of tuning the transmons through resonance with any other coupled modes in its spectrum (TLS, other qubits, etc.) and allowing leakage reset to even be performed on fixed frequency transmons.

Microwave leakage reset of a transmon capacitively coupled to a single harmonic mode is possible because the dispersive exchange coupling weakly dresses the bare $|f\,0\rangle$ and $|g\,1\rangle$ states in part with the $|e\,1\rangle$ and $|e\,0\rangle$ states respectively. The dressed states can then be coupled to one another via a charge drive on the transmon, as each dressed state contains some component of a state that differs from some component of the other only by a single excitation difference in the transmon part. If this driving is resonant with the energy splitting of the two states, the dressed $|f\,0\rangle$ and $|g,1\rangle$ states will strongly hybridize and undergo Rabi oscillations, and if the harmonic mode is strongly damped, the hybridized state will then decay to the global $|g\,0\rangle$ ground state of the system. Because such a drive will in general not be resonant with any transitions out of the $|g\,0\rangle$ or $|e\,0\rangle$ states, the reset will only occur for leakage population in the second excited state, and the logical subspace of the transmon will be preserved.

By replacing the single harmonic mode with a metamaterial waveguide, and coupling the transmon to a single unit cell of the waveguide, the qubit couples to the many different harmonic eigenmodes of the metamaterial and can be reset through any of

them. The Hamiltonian for such a system can be modeled as:

$$H = \omega_q a^\dagger a + \frac{\eta}{2} a^\dagger a^\dagger a a \tag{4.11}$$

$$+ \sum_{x=1}^{x=N} \omega_r b_x^\dagger b_x + J(b_x b_{x+1}^\dagger + b_x^\dagger b_{x+1}) \tag{4.12}$$

$$+ g(a^\dagger b_{x_0} + a b_{x_0}^\dagger) \tag{4.13}$$

$$+ \Omega \cos(\omega_d t)(a + a^\dagger), \tag{4.14}$$

where ω_q is the transmon frequency, η is the transmon anharmonicity; x indexes a periodic linear chain of N, identical nearest-neighbor coupled resonators, comprising the metamaterial waveguide, each with frequency ω_r and nearest-neighbor coupling J; g is the coupling between the transmon and the resonator indexed by x_0; and Ω is the strength of a drive at frequency ω_d on the transmon. The second line gives the bare metamaterial Hamiltonian, which can itself be diagonalized to give the bare eigenmodes of the waveguide in terms of the unit cell modes, and will also give the expression for b_{x_0} in terms of the eigenmodes. When the microwave drive frequency ω_d is resonant with energy splitting between the $|f\,0\rangle$ state and the $|g\,1\rangle$ state, where the 0 and 1 indices refer to the 0 and 1 photon states of the single unit cell to which the transmon is coupled, it will induce an effective resonant coupling between the states $\tilde{g} = \frac{1}{\sqrt{2}} \frac{\eta \Omega g}{\Delta(\Delta+\eta)}$ where $\Delta \equiv \omega_q - \omega_r$ [154, 220].

To give a simple example of microwave reset using such a waveguide, it is possible to design a waveguide in a regime where g/J is small while g is on the order of at least a few times the FSR of the metamaterial $\sim (4J/N)$. In this regime, a microwave drive resonant with the $|f\,0\rangle$ state and the waveguide passband will turn on a resonant exchange interaction between the transmon and a bath of multiple waveguide modes, and the transmon's second excited state will roughly undergo exponential decay via photon emission into the waveguide at a rate $\Gamma \sim \frac{\tilde{g}^2}{J}$ [109]. If the ends of the waveguide are well-damped to the environment, as with our tapered metamaterial waveguides, the photonic excitation will propagate away and the transmon-metamaterial system will decay to its global ground state. For $J/(2\pi) = 100$ MHz, $g/(2\pi) = 250$ MHz, $\eta/(2\pi) = -250$ MHz, $\Delta_{q-uc}/(2\pi) = -400$ MHz. With these parameters we get an FSR ~ 8 MHz, $\tilde{g}/(2\pi) \sim 25$ MHz, and $\Gamma_{1D}/(2\pi) \sim 6.5$ MHz. It is not necessary to operate in this particular regime, and the transmon leakage population should still be theoretically resettable even if the $|f\,0\rangle$ state is so weakly coupled that it sees well-defined modes of the waveguide, or so strongly coupled to individual modes that it undergoes non-exponential coherent dynamics with them

as coupled system decays.

Chapter 5

SIMULTANEOUS LONG-RANGE TUNABLE INTERACTION BETWEEN DUAL-RAIL TRANSMONS

As discussed in Chapter 2, achieving long-range, high-weight connectivity requires careful consideration of, or deliberate exploitation of, the multiple modes that inevitably arise between superconducting qubits. In this chapter, we discuss a novel long-range coupling architecture that leverages many coherent modes to realize all-to-all connectivity and simultaneous entangling operations, effectively implementing Mølmer-Sørensen interactions in superconducting quantum circuits.

Note that this chapter is based on ongoing collaborative research with external partners. Portions of the material will appear in manuscript Golan et al. (G. Kim among co-authors) currently in preparation [93]. Core concepts presented here have been publicly disclosed at APS Global Summit 2025 [94, 95]. G.K. contributed to the development of the realistic Hamiltonian and circuit design strategies, numerical analysis, and architectural extensions, and proposed the nearest-neighbor counterparts presented in this chapter.

5.1 Introduction

Fault-tolerant quantum computation requires protecting quantum information by implementing quantum error correcting (QEC) codes [30, 31]. Entanglement plays a key role in distributing logical quantum information across many physical qubits, enabling resilience against local errors and allowing recovery of coherence by syndrome extraction [32, 187].

In superconducting quantum processors, QEC implementations have largely followed architectures with nearest-neighbor connectivity and local syndrome measurements. Representative examples include repetition codes [30], surface codes [87], and heavy-hex codes [245]. These codes are well matched to planar superconducting hardware due to their strong local coupling and good local control and measurement of individual qubits [52, 53, 209, 210, 246]. However, such QEC codes exhibit encoding rates that decrease either linearly or quadratically with increasing code distance. This implies substantial physical qubit overhead for logical qubits at large code distances, presenting a major challenge in realizing utility-scale quantum

computation [76, 77].

Recent theoretical progress has demonstrated the existence of "good" quantum low-density parity check (qLDPC) codes, in which the encoding rate remains constant as the code distance increases [112]. These constructions require nonlocal connectivity and higher-weight stabilizer measurements. Among the most promising examples are bivariate bicycle (BB) codes [86], which achieve a constant encoding rate while requiring only moderate long-range connectivity on top of an underlying square-lattice architecture.

Implementing such codes in superconducting circuits presents substantial architectural challenges. Long-range connectivity over millimeter-to-centimeter scales has been demonstrated using dedicated interconnects and couplers [114, 115, 247, 248]. However, these approaches generally require adding one physical coupling resource per additional nonlocal edge, imposing considerable hardware overhead. Alternatively, all-to-all coupling architectures based on a shared bus mode, such as resonator-induced phase (RIP) gates [249, 250] or single-mode star architectures [251, 252], provide hardware-efficient multi-qubit connectivity. Nevertheless, these architectures typically allow only one entangling interaction at a time, which may increase circuit depth.

Our recent theoretical proposal [93–95] introduces a multi-mode all-to-all coupling architecture that enables simultaneous long-range entangling gates. The central element is a coupled resonator array bus (CRAB) [107, 108, 117, 149], whose delocalized eigenmodes mediate Mølmer-Sørensen interactions among spatially separated superconducting qubits [253]. The entangling interaction primitive is the cavity-mediated cross-cross-resonance (CCCR) interaction proposed in Gorshkov et al. [254]. To suppress parasitic cross-Kerr interactions between bus eigenmodes, we employ dual-rail transmons (DRTs) [255–257].

In this work, we develop realistic design strategies for implementing this long-range interaction scheme. Choosing a DRT gap frequency larger than the CRAB bandwidth mitigates spectral crowding during microwave control. Gate speeds across different qubit pairs are homogenized due to similar detunings from DRTs to CRAB eigenmodes. Direct and indirect static DRT-DRT interactions mediated by the CRAB are exponentially suppressed by inserting buffer resonators, at the cost of only a modest reduction in gate speed. An auxiliary transmon coupled to each unit-cell resonator enables *in situ* dispersion engineering and control and reset of CRAB eigenmodes. Finally, we propose a scalable extension of the long-range

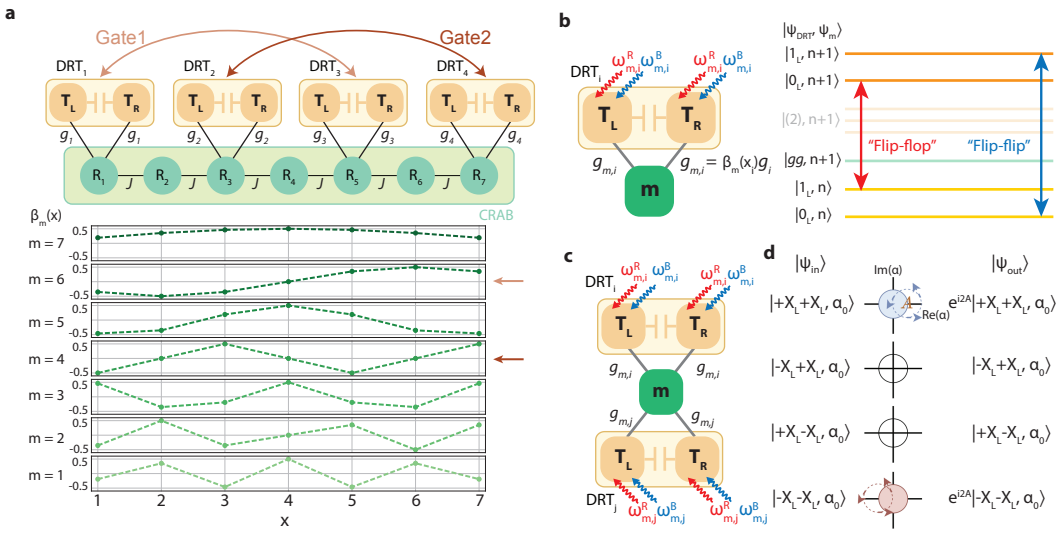

Figure 5.1: **Simultaneous long-range interaction mediated by coupled resonator arrays.** **a**, Simultaneous long-range interactions between dual-rail transmons (DRTs) enabled by a coupled resonator array bus (CRAB). $\beta_m(x)$ denotes mode amplitudes of an eigenmode m at location x. Multiple two-qubit gates between pairs of DRTs can be executed in parallel by selecting gates mediated by different orthogonal eigenmodes of the CRAB, as represented by light brown and dark brown arrows. **b**, Schematic illustration and energy-level diagram of $\mathrm{DRT_i}$ coupled to eigenmode m under cross-resonance drives. A wiggly red (blue) arrow denotes a red (blue) sideband microwave drive with frequency $\omega^R_{m,i}$ ($\omega^B_{m,j}$), activating a "flip-flop" ("flip-flip") interaction. **c**, Schematic illustration of $\mathrm{DRT_i}$ and $\mathrm{DRT_j}$ coupled to eigenmode m. **d**, XX-parity-dependent displacement of mode m arising from the cross-resonance interaction enabled by sideband drives, under sufficient detuning between red (blue) sideband drive frequency and the flip-flop (flip-flop) transition frequency.

connectivity using a row-and-column CRAB architecture.

5.2 Long-range interaction between DRTs mediated by a CRAB

In this section, we review the gate principle presented in Ref. [93], with the setup illustrated in Fig. 5.1. A CRAB consists of microwave resonators with identical resonance frequencies ω_r, coupled to their nearest neighbors with a uniform hopping rate J. DRTs are indexed by subscript i and placed at lattice site x_i. $\mathrm{DRT_i}$ is parked at the microwave operating frequency ω_i^{DRT} and has a dual-rail gap $\Omega^{DR}_{i,0} = 2g_i^{DRT}$, where g_i^{DRT} is the intra-qubit coupling. The two transmons in $\mathrm{DRT_i}$ couple symmetrically to the resonator at lattice site x_i with a rate g_i. The full system Hamiltonian, with the transmons approximated as Kerr harmonic oscillators, is given by

$$
\begin{aligned}
\hat{H}^{\text{total}} &= \hat{H}^{\text{CRAB}} + \sum_{i=1}^{N} \left(\hat{H}_i^{\text{DRT}} + \hat{H}_i^{\text{DRT-CRAB}} \right) \\
\hat{H}^{CRAB} &\equiv \omega_r \sum_{x=1}^{M} \hat{c}_x^\dagger \hat{c}_x - J \sum_{x=1}^{M-1} (\hat{c}_x - \hat{c}_x^\dagger)(\hat{c}_{x+1} - \hat{c}_{x+1}^\dagger) \\
\hat{H}_i^{DRT} &\equiv -\frac{\Omega_{i,0}^{DR}}{2} \left(\hat{a}_i - \hat{a}_i^\dagger \right) \left(\hat{b}_i - \hat{b}_i^\dagger \right) + \omega_i^{DRT} \left(\hat{a}_i^\dagger \hat{a}_i + \hat{b}_i^\dagger \hat{b}_i \right) + \hat{H}_i^{\text{quartic}} \\
\hat{H}_i^{\text{quartic}} &\equiv \frac{\eta_i}{2} \left(\hat{a}_i^\dagger \right)^2 (\hat{a}_i)^2 + \frac{\eta_i}{2} \left(\hat{b}_i^\dagger \right)^2 \left(\hat{b}_i \right)^2 \\
\hat{H}_i^{DRT-CRAB} &\equiv - g_i (\hat{a}_i - \hat{a}_i^\dagger)(\hat{c}_{x_i} - \hat{c}_{x_i}^\dagger) - g_i (\hat{b}_i - \hat{b}_i^\dagger)(\hat{c}_{x_i} - \hat{c}_{x_i}^\dagger),
\end{aligned} \tag{5.1}
$$

where $\hat{c}_x$ denotes the resonator mode at site x, M is the number of resonators in CRAB, N is the number of DRTs, $\hat{a}_i$ ($\hat{b}_i$) denotes the left (right) transmon in DRT_i, and η_i is the transmon anharmonicity.

For sufficiently large detuning $|\Delta_i| \gg |g_i|$, with $\Delta_i \equiv \omega_i^{DRT} - \omega_r$, the CRAB and DRT sectors can be diagonalized separately and treated perturbatively. The CRAB eigenmodes are spatially delocalized over the entire array, where eigenmode m has mode amplitude $\beta_m(x)$ at site x. Consequently, the transmons in DRT_i at site x_i couple to mode m with an effective rate $g_{m,i} = \beta_m(x_i) g_i$, proportional to local mode amplitude, as shown in Fig. 5.1b.

Under the rotating-wave approximation, the interaction between DRT_i and eigenmode m can be written as follows:

$$
\begin{aligned}
\hat{H}_i^{\text{DRT-m}} = &-\frac{\Omega_{i,0}^{DR}}{2} \hat{\sigma}_i^Z + \omega_i^{DRT} \left(\hat{a}_i^\dagger \hat{a}_i + \hat{b}_i^\dagger \hat{b}_i \right) \\
&+ \tilde{\omega}_m \hat{c}_m^\dagger \hat{c}_m + \sqrt{2} g_{m,i} \left((\hat{a}_i^+)^\dagger \hat{c}_m + h.c. \right) + \hat{H}_i^{\text{quartic}},
\end{aligned} \tag{5.2}
$$

where $\hat{c}_m$ is the CRAB eigenmode m with frequency ω_m, and $\hat{a}_i^\pm \equiv \left(\hat{a}_i \pm \hat{b}_i \right) / \sqrt{2}$ are the symmetric and anti-symmetric eigenmodes of DRT_i. The logical states are defined as $|1_L\rangle_i \equiv \left(\hat{a}_i^+ \right)^\dagger |vac\rangle_i$ and $|0_L\rangle_i \equiv \left(\hat{a}_i^- \right)^\dagger |vac\rangle_i$, and $\hat{\sigma}_i^k,\ k \in \{X, Y, Z\}$ are the Pauli operators of DRT_i.

As illustrated in Fig. 5.1b, two types of transitions arise: a "flip-flop" transition between $|1_L n\rangle$ and $|0_L(n+1)\rangle$ with a transition frequency close to $\omega_m - \Omega_{i,0}^{DR}$, and a "flip-flip" transition between $|1_L n\rangle_i$ and $|0_L(n+1)\rangle_i$ with a transition frequency close to $\omega_m + \Omega_{i,0}^{DR}$. Each ket denotes the tensor product of the qubit states of

$\mathrm{DRT_i}$ and the Fock state of mode m. These transitions correspond to entangling interactions of the form $\sigma_i^- \tilde{c}_m^\dagger + h.c.$ (flip-flop) and $\sigma_i^- \tilde{c}_m + h.c.$ (flip-flip). We therefore apply microwave drives at frequencies $\omega_{m,i}^R$ (red sideband) and $\omega_{m,i}^B$ (blue sideband), chosen close to the corresponding transition frequencies, with amplitudes $\Omega_{m,i}^R$ and $\Omega_{m,i}^B$ for two transmons with opposite phases:

$$\hat{H}_i^{\text{drive}} = \left(\Omega_{m,i}^R \cos\left(\omega_{m,i}^R t\right) + \Omega_{m,i}^B \cos\left(\omega_{m,i}^B t\right)\right)\left(\hat{a}_i - \hat{b}_i\right) + h.c.. \tag{5.3}$$

These microwave drives dress the transmon eigenstates and, in concert with the linear hybridization proportional to $g_{m,i}$, enable cross-resonant driving of the above transitions, realizing a cross-resonance interaction [258, 259]. Refer to [93] for details of the perturbative derivation. We denote by $\tilde{c}_m$ and $\tilde{\omega}_m$ the dressed CRAB eigenmode and eigenfrequency, and by Ω_i^{DR} the dressed dual-rail gap. We set $\omega_{m,i}^R = \epsilon_m + \tilde{\omega}_m - \Omega_i^{DR}$, $\omega_{m,i}^B = \epsilon_m + \tilde{\omega}_m + \Omega_i^{DR}$, enforce $\Omega_{m,i}^R/\Omega_{m,i}^B = \left(\Delta_{m,i} - g_i^{DRT}\right)^2 / \left(\Delta_{m,i} + g_i^{DRT}\right)^2$, and define $\Omega_{m,i} \equiv \Omega_{m,i}^B$ as the shared drive strength. Going into the frame rotating with $\tilde{\omega}_m \tilde{c}_m^\dagger \tilde{c}_m$ and $-\frac{\Omega_i^{DR}}{2}\hat{\sigma}_i^Z$, second-order perturbation theory yields, up to local phase rotations, the following effective Hamiltonian [93, 254]:

$$\hat{H}_{i,\text{eff}}^{\text{DRT-m}} = \epsilon_m \tilde{c}_m^\dagger \tilde{c}_m + g_{m,i}^{\text{CR}} \hat{\sigma}_i^X (\tilde{c}_m + \tilde{c}_m^\dagger), \tag{5.4}$$

where $g_{m,i}^{CR} \approx 2\frac{g_{m,i}\Omega_{m,i}}{\Delta_{m,i}^2}\eta_i$ is the cross-resonance drive rate. This corresponds to a longitudinal interaction between $\mathrm{DRT_i}$ and eigenmode m.

Finally, we introduce a second dual-rail transmon $\mathrm{DRT_j}$ as shown in Fig. 5.1c and apply consistently constructed red- and blue-sideband under sufficiently strong drives satisfying $g_{CR} \equiv g_{m,j}^{CR} = g_{m,i}^{CR}$, yielding the effective cavity-mediated cross-cross-resonance (CCCR) interaction:

$$\hat{H}_{i,j,\text{eff}}^{\text{DRT-m}} = \epsilon_m \tilde{c}_m^\dagger \tilde{c}_m + g_{CR}\left(\hat{\sigma}_i^X + \hat{\sigma}_j^X\right)(\tilde{c}_m + \tilde{c}_m^\dagger). \tag{5.5}$$

The resulting dynamics can be understood as conditional displacements of $\tilde{c}_m$ set by the $X_i + X_j$-parity of $\mathrm{DRT_i}$ and $\mathrm{DRT_j}$, as illustrated in Fig. 5.1d. If the two DRTs have opposite X-parities, the drive term cancels and no effective interaction occurs. If they have the same X-parities, the term $\tilde{c}_m + \tilde{c}_m^\dagger$ is driven with strength $\pm 2g_{CR}$, producing a displacement whose direction depends on the X-parities.

In particular, if ϵ_m is sufficiently large and the $g_{CR}(t)$ varies slowly enough for the dynamics to be adiabatic, the dressed eigenmode $\tilde{c}_m$ returns to its initial state, as illustrated in Fig. 5.1d, while the DRTs acquire a geometric phase ϕ proportional to the enclosed area in the phase space of $\tilde{c}_m$. Eq. (5.5) then implements an effective XX interaction between the two dual-rail transmons in the following form:

$$U_{i,j,m}^{XX} \approx e^{-i\phi(\hat{I}_i+\hat{\sigma}_i^X)(\hat{I}_j+\hat{\sigma}_j^X)}, \tag{5.6}$$

where choosing $\phi = \pi/4$ realizes a gate equivalent to a controlled-Z (CZ) gate up to single qubit rotations. For a square drive envelope, the shortest CZ gate time is given by $T_G \approx \pi/(2g_{CR})$ for $\epsilon_m = 4g_{CR}$.

CCCR two-qubit gates mediated by CRAB have several advantages. First, they provide long-range connectivity via delocalized CRAB eigenmodes, avoiding the need to decompose the operation into sequences of SWAPs. The gate speed is ultimately constrained by the CRAB free spectral range (FSR) to avoid populating spectator eigenmodes, with FSR $\approx 4J/M$. Second, they enable simultaneous two-qubit gates on multiple DRT pairs by using different eigenmodes, analogous to Mølmer-Sørensen interactions realized in trapped ion systems [253, 260]. This follows from the vanishing commutator $[\hat{H}_{i,j,\text{eff}}^{\text{DRT-m}}, \hat{H}_{x,y,\text{eff}}^{\text{DRT-n}}] = 0$ for $m \neq n$, due to the orthogonality of distinct CRAB eigenmodes. Additionally, the effective interaction strength scales linearly with the external drive, in contrast to schemes with quadratic or quartic power scaling requirements [249, 250]. Finally, the interaction scheme requires only a single additional physical connectivity to access all-to-all coupling, imposing minimal overhead.

It is crucial to suppress the zero cross-Kerr interaction term ($\hat{\sigma}^Z\hat{c}_m^\dagger\hat{c}_m$) between qubits and CRAB eigenmodes that originates from $\hat{H}_i^{\text{quartic}}$. For conventional transmons, the static dispersive coupling (cross-Kerr) modifies the mode frequency in a qubit-state dependent manner, thereby disrupting the intended interaction scheme and complicating dynamical decoupling protocols [254]. In our approach, this parasitic term is eliminated by employing dual-rail transmons and symmetrically coupling the two constituent qubits, a configuration shown to cancel the cross-Kerr interaction [255–257].

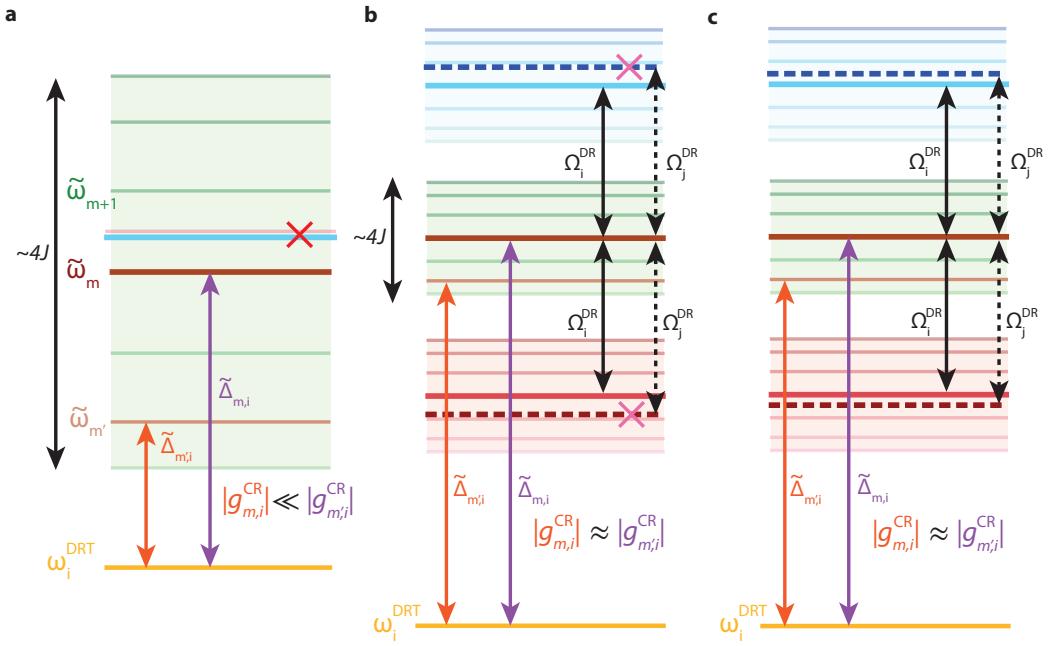

Figure 5.2: **Frequency allocation strategy for CRAB and DRT. a**, A CRAB with large FSR, leading to substantial variation in detuning relative to a DRT and possible spectral proximity between red- and blue-sidebands associated with different eigenmodes. **b**, A CRAB with narrow FSR, resulting in similar detunings to a DRT. DRT_i and DRT_j have dual-rail gaps that are too closely spaced. **c**, A CRAB with narrow FSRs, with similar detunings to a DRT. DRT_i and DRT_j have sufficiently separated dual-rail gaps.

5.3 CRAB and DRT design strategies

As a proof-of-concept demonstration for simultaneous operation of long-range two-qubit gates, we design a single CRAB system with four DRTs. In this section, we discuss realistic design considerations and strategies.

5.4 Frequency allocation

Because the interaction scheme relies on microwave drives placed close to the CRAB eigenmodes, and the achievable gate speed depends strongly on the detuning between the CRAB eigenmodes and DRTs, it is essential to avoid both frequency crowding and excessively large detuning. In this subsection, we discuss a frequency allocation strategy for a single CRAB.

Fig. 5.2 illustrates representative failure (a, b) and success (c) scenarios. As shown in Fig. 5.2a, if the FSR of the CRAB is too large, the detunings between a given DRT and different eigenmodes vary substantially. This leads to significant variation in

achievable gate times across different DRT pairs. Moreover, large FSR increases the likelihood of frequency collisions involving other eigenmodes and their associated red- and blue-sideband drives, unless the FSR is much larger than dual-rail gaps, which would require an extremely large hopping rate $J \gg 4M\Omega^{DR}$.

A practical solution is to employ a CRAB with a sufficiently narrow bandwidth (BW) compared to the gaps of the DRTs, so that all red- and blue-sideband drives lie outside the CRAB passband avoiding frequency collisions, as illustrated in Fig. 5.2b and c. We therefore choose Ω_i^{DR}s such that they satisfy $BW \approx 4J < \min\{\Omega_i^{DR}\}$. In this regime, the detunings to different eigenmodes are comparable, thereby reducing the variance of achievable cross-resonance interaction rates.

Finally, the dual-rail gaps must be sufficiently separated from one another. As shown in Fig. 5.2b, if two DRTs have similar dual-rail gaps, classical crosstalk from a drive applied to $\mathrm{DRT_i}$ can induce unintended sideband transitions in a spectator $\mathrm{DRT_j}$. In addition, parasitic static interactions between two DRTs are more likely to satisfy a resonance condition. Therefore, as shown in Fig. 5.2c, we allocate sufficiently distinct dual-rail gaps to suppress these frequency collisions. In summary, we allocate the frequencies according to the following relations:

$$4J < \min_i\{\Omega_i^{DR}\}, \quad \max_i\{g_{m,i}^{CR}\} < |\Omega_i^{DR} - \Omega_j^{DR}| < FSR \times 2\pi \approx \frac{4J}{M}. \tag{5.7}$$

The first condition ensures that the CRAB bandwidth remains smaller than the smallest dual-rail gap. The second condition constrains the separation between dual-rail gaps to exceed the maximum achievable cross-resonance interaction rate while remaining below the FSR. In our design, we choose $J/2\pi \approx 50$ MHz, $M = 7$, and $\Omega_i^{DR} \approx 220$ MHz. This yields $FSR \approx 30$ MHz, which is sufficient for supporting a two-qubit gate with a duration of approximately 300 ns.

5.5 Suppressing parasitic DRT-DRT interaction

The CRAB mediates linear coupling between distant qubit pairs due to the formation of bound states with long tails, as theoretically and experimentally shown in Refs [108, 109, 117, 149]. In the dispersive regime, where $|\Delta_i| \gg g_i$, the resulting indirect linear coupling rate $g_{ij}^{\mathrm{indirect}}$ decreases exponentially with spatial separation:

$$g_{ij}^{\mathrm{indirect}} \propto \left|\frac{J}{\Delta}\right|^{|x_i - x_j|}, \tag{5.8}$$

where Δ is the scale of detuning. In addition, because nearest-neighbor linear couplings are implemented by capacitive elements, the inverse capacitance matrix introduces a direct coupling rate between transmons g_{ij}^{direct}. This capacitance-network-mediated coupling likewise decays exponentially with distance when the coupling capacitances C_g are much smaller than the scale of bare transmon and resonator capacitances C_0, i.e.,

$$g_{ij}^{\text{direct}} \propto \left|\frac{C_g}{C_0}\right|^{|x_i - x_j|}. \tag{5.9}$$

Based on these considerations, we suppress the parasitic DRT-DRT linear coupling by inserting "buffer" resonators in every other cell, such that $M = 2N - 1$. This effectively reduces parasitic interactions by approximately an order of magnitude. As a result, the static ZZ interaction between DRTs is suppressed by approximately two orders of magnitude. The tradeoff is a reduction of the FSR, and consequently achievable gate speed, by a factor of two.

5.6 Disorder engineering

Because the long-range interaction relies on the spatial delocalization of the CRAB eigenmodes, it is important to suppress disorder in the resonator frequencies. In particular, since the lattice consists of two different types of resonators: resonators directly coupled to DRTs and buffer resonators, maintaining effective translational symmetry is critical. Moreover, as the DRTs operate within their logical subspace, it is necessary to properly account for Lamb and dispersive shifts induced by their coupling to the resonators.

To incorporate the effect of coupling to DRTs, we renormalize the bare frequencies of resonators connected to DRTs by including the Lamb and dispersive shifts. Specifically, we consider a single resonator at site x_i symmetrically coupled to a DRT_i, as shown in the schematic in Fig. 5.1c, where the CRAB eigenmode is replaced by a single resonator with couplings g_i. In this configuration, we estimate the resonator's average dressed eigenfrequency:

$$\bar{\omega}_{x_i} \equiv \frac{(\tilde{\omega}_{x_i}|_{|0_L\rangle} + \tilde{\omega}_{x_i}|_{|1_L\rangle})}{2}, \tag{5.10}$$

evaluated within the logical subspace of the DRT. We then use $\bar{\omega}_{x_i}$ as the effective resonance frequency relevant for determining the long-range properties and

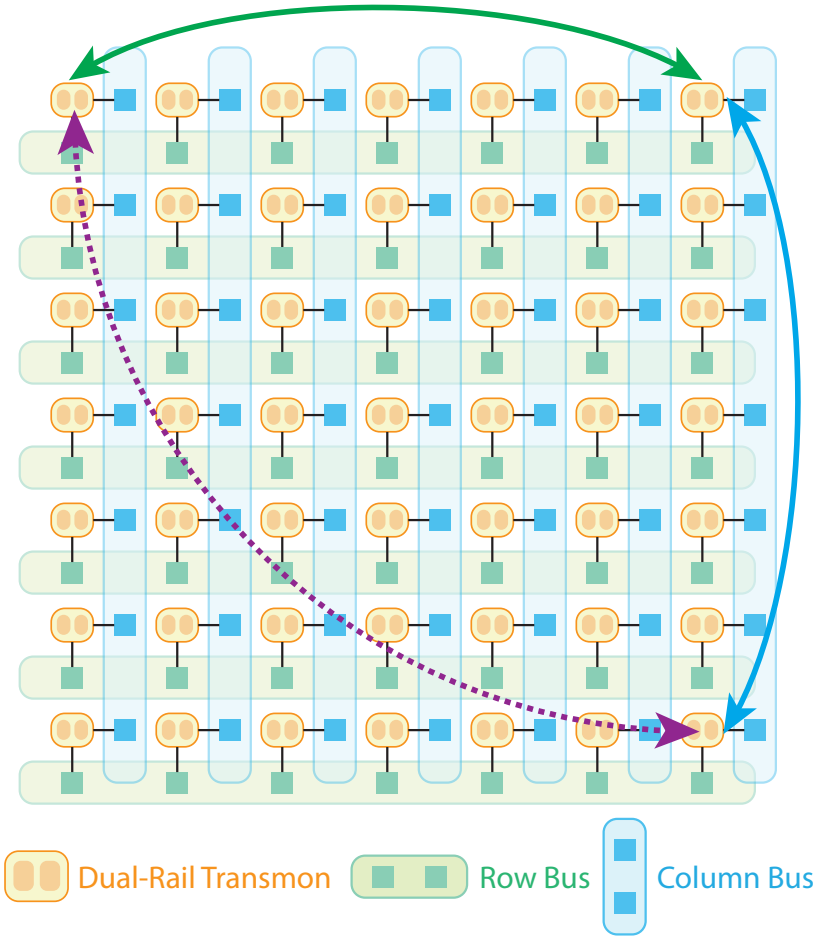

Figure 5.3: **Row-and-column CRAB architecture.** Envisioned two-dimensional array of CRABs hosting DRTs on a square lattice with long-range connectivity. Any long-range two-qubit gates (purple dashed line) can be decomposed into long-range gates within a row bus (green solid line) and a column bus (blue solid line).

dispersion of the CRAB eigenmodes. In addition, to enable *in situ* tuning of resonance frequencies and dispersion engineering, we couple an auxiliary flux-tunable transmon at each DRT-coupled resonator. By changing the frequency of the auxiliary transmons, the Lamb shift experienced by the resonators can be adjusted. These auxiliary transmons also serve as functional elements for tasks such as CRAB eigenmode tomography, photon number detection, and reset.

5.7 Scalable CRAB-based long-range architecture

In this section, we propose a strategy for scaling the CRAB-based long-range coupling scheme via a row-and-column bus architecture, as illustrated in Fig. 5.3. In this design, dual-rail transmons are arranged on a square lattice. Each row or col-

umn is equipped with a dedicated CRAB, which mediates long-range connectivity along that direction. The physical connectivity overhead per qubit is limited to two couplings to its row and column CRABs, and at most six if the underlying nearest-neighbor connectivity is also included.

This structure enables a constant-depth construction of arbitrary two-qubit gates between any pair of DRTs. As an example, consider implementing a two-qubit gate between $\mathrm{DRT}_{1,1}$ and $\mathrm{DRT}_{\mathrm{M,M}}$. The operation proceeds as follows: (1) a SWAP operation mediated by the first-row CRAB transfers the quantum state of $\mathrm{DRT}_{1,1}$ to $\mathrm{DRT}_{1,\mathrm{M}}$. (2) The M-th column CRAB performs the desired entangling operation between $\mathrm{DRT}_{1,\mathrm{M}}$ and $\mathrm{DRT}_{\mathrm{M,M}}$. (3) A final SWAP within the first-row CRAB returns the quantum state from $\mathrm{DRT}_{1,\mathrm{M}}$ back to $\mathrm{DRT}_{1,1}$. This sequence realizes an effective two-qubit gate between $\mathrm{DRT}_{1,1}$ and $\mathrm{DRT}_{\mathrm{M,M}}$.

The row-and-column CRAB architecture allows long-range connectivity without requiring extended sequences of nearest-neighbor SWAPs [261], thereby reducing compilation overhead and circuit depth. Moreover, the ability to perform parallel entangling operations within a CRAB makes certain transversal gate constructions more naturally aligned with the underlying physical system [262].

It is important to note that the side of CRAB need not be commensurate with the DRT lattice constant. Instead, the geometry can be chosen so that every L-th DRT couples to a given CRAB, allowing a single CRAB to mediate long-range connectivity over physical distances of order LM. This can be achieved either by miniaturizing the DRT footprint or by implementing the CRAB resonators as long physical structures, such as CPW resonators. In this architecture, one can place L interleaved CRABs within a row, each coupling to a different residue class modulo L. This yields connectivity over a range of order LM with $O(L)$ nearest-neighbor operations among different residue classes and $O(1)$ CRAB-mediated operations. An alternative hardware-efficient way to scaling the row-and-column CRAB architecture is to use two interleaved CRAB lattices and stagger them such that each CRAB in one lattice stitches together two CRABs in the other lattice. In such an architecture, the required physical connectivity per qubit is limited to at most four.

Finally, to maximize coupling range for a given circuit depth, one may organize CRABs in a tree-like hierarchy, enabling decomposition of a two-qubit gate between qubits separated by distance D into $O(\log_M D)$ CRAB-mediated operations. Such an architecture may be advantageous for quantum random-access memory

(QRAM) [263] and as a "router chip" for multi-chip integrated quantum processors [264].

5.8 Propagation of errors within a CRAB

As a trade-off for prodiving all-to-all coupling, a CRAB can also propagate errors on DRTs to other DRTs coupled to the bus. This occurs because the eigenmode frequencies of the CRAB shift significantly depending on whether a given DRT remains in the computational subspace or has lead into zero-excitation subspace through an erasure event. The resulting shift χ_{gg-L} between mode m and $\mathrm{DRT_i}$ is on the scale of the usual dispersive shift between a transmon and a harmonic resonator:

$$\chi_{gg-L} \approx \frac{2g_{m,i}^2}{\Delta_{mi}^2}\eta. \tag{5.11}$$

As a result, when an erasure error occurs on a spectator DRT, all eigenmodes can shift by a few megahertz. This significantly perturbs the cross-resonance interactions taking place elsewhere in the bus, effectively creating coherent errors on other qubits. Critically, such a spectator erasure can occur at any time during a CR interaction, making the resulting coherent dynamics stochastic rather than deterministic.

Understanding and mitigating this error propagation channel will be essential if CRAB-based architectures are to be used for quantum error correction. Its implication and handling strategy for different architectures, including those discussed in the previous section, should be carefully analyzed. Possible countermeasures should also be developed, such as reset protocols for the entire bus and all DRTs coupled to it, or pulse shapes engineered to be robust against such frequency shifts.

5.9 Conclusion and outlook

In this chapter, we develop a hardware-realistic framework and design strategy for simultaneous long-range entangling interactions in superconducting circuits based on a coupled resonator array bus (CRAB) and dual-rail transmons (DRTs). By activating cavity-mediated cross-cross-resonance interactions through sideband drives, delocalized CRAB eigenmodes mediate long-range XX interactions without dedicated couplers for each nonlocal edge. Symmetric dual-rail coupling suppresses parasitic static cross-Kerr terms, preserving clean geometric phase acquisition.

We outline practical design strategies, including frequency allocation to avoid spectral crowding, suppression of static DRT-DRT interactions via buffer resonators,

and disorder engineering by properly including frequency shifts due to coupling to DRTs and *in situ* tuning enabled by auxiliary tunable transmons. Combining these, we choose realistic conditions for design parameters for four DRTs and seven resonators for a CRAB.

Finally, we propose scalable extensions based on row-and-column CRAB architectures, enabling constant-depth long-range gates with limited connectivity overhead. This approach provides a viable pathway toward superconducting architectures with hardware-efficient long-range connectivity suitable for advanced quantum error-correcting codes.

Chapter 6

A TUNABLE, MODELESS, AND HYBRIDIZATION-FREE CROSS-KERR COUPLER FOR MINIATURIZED SUPERCONDUCTING QUBITS

Existing tunable coupling architectures rely on hybridization between qubits and couplers, where the nonlinear interaction inherits its nonlinearity from the qubits. Instead, engineering not only the tunability but also the source of nonlinearity in the coupling element itself can address several limitations present in existing tunable coupling architectures. In this chapter, I propose a novel coupling architecture using a SQUID coupler that provides tunable, modeless, and hybridization-free cross-Kerr coupling between transmons. This chapter is adapted from Ref. [96].

6.1 Introduction

Superconducting quantum processors utilize capacitors to realize linear couplings between circuit elements such as qubits, tunable couplers, and readout resonators [41, 47, 57, 84, 265, 266]. However, the design of capacitances can be constrained due to other goals, such as suppressing dielectric loss [60, 113, 267], maintaining large qubit anharmonicity [41, 57], and optimizing the form-factor and size of qubits [76]. Furthermore, tunable coupling schemes that utilize linear coupling elements rely on temporal variations in mode hybridization, which can introduce leakage errors through non-adiabatic transitions, thereby limiting gate speed and fidelity [47, 110, 268].

Merged-element transmons (mergemons) [269–271] provide a representative example of the challenges associated with using linear capacitive coupling. The concept behind the mergemon qubit is to localize the qubit capacitance to the small volume of the Josephson junction, limiting the (spectral) density of two-level system defects (TLSs) [60, 113, 267] that can decohere the qubit. Additional geometric capacitance in the circuit, for example to implement coupling between qubits and coupling to resonators for qubit read-out, increases the number of interacting TLS. Reducing the strength of qubit-TLS interactions can be accomplished by enlarging the capacitor volume and diluting the electric field intensity, however this leads to larger and less confined qubits that are more prone to parasitic crosstalk with other circuit elements [40, 41].

To overcome the bulkiness and mode hybridization of standard capacitive coupling architectures, we propose using SQUID (superconducting quantum interference device) couplers for dynamic coupling of elements. This approach is similar to other recent junction-based coupler proposals [71, 78, 119, 120, 265, 266, 272–276], with the distinct difference being that we focus on SQUIDs composed of Josephson junctions with relatively small tunneling energies to preserve a desired hierarchy of interactions and to limit the effects of junction non-idealities and noise. A primary benefit of a junction-based coupling scheme is that it need not introduce any additional modes to the system, modes that can serve as a channel for leakage errors when implementing qubit gate operations [85, 213]. In conventional approaches using linear coupling elements, entangling interactions arise indirectly from nonlinearities of the qubits themselves [45, 47, 84, 110, 266, 274]. In contrast, the SQUID coupler directly introduces intrinsic cross-Kerr interactions that can be switched on or off using external magnetic flux. As the cross-Kerr interaction does not rely on hybridization of the interacting elements, mixing between qubits can be independently engineered and suppressed [120]. In addition, the removal of geometric coupling capacitors relaxes the trade-off between dielectric loss and qubit size.

Along with the potential benefits of the SQUID coupler, there are several technical challenges that must also be considered. In particular, the effect of fabrication-induced junction asymmetries and the presence of extraneous SQUID loops formed via ground connections of the coupler can limit the coupler performance [276, 277]. Junction asymmetry in the SQUID coupler can lead to a reduced on-off extinction ratio, crosstalk with spectator qubits, and in conjunction with the extraneous SQUID loops, an increased sensitivity to magnetic flux noise. SQUID couplers used with floating transmons eliminate the presence of extraneous outer SQUID loops [272]; however, such a design introduces sloshing modes that can mediate parasitic interaction and leakage errors. In this work we take a different approach, and show that SQUID couplers formed from junctions with relatively small Josephson tunneling frequencies ($\lesssim$ 1 GHz) compared to the transition frequencies of the elements being coupled together ($\sim$ 5 GHz), and for junction asymmetries up to 20%, can achieve cross-Kerr interaction rates of a few tens of MHz with high extinction ratio and low parasitic crosstalk to neighboring elements, while maintaining low infidelity due to typical flux noise levels.

An outline of our analysis of the proposed SQUID coupler is as follows. We begin in Sec. 6.2 with a review of the Hamiltonian and external flux control parameters for a

SQUID coupler mediating coupling between two detuned transmon qubits, and show through numerical simulation of a quantized circuit model of a system with relatively small coupler junction energies, that a high-fidelity and fast controlled-Z (CZ) gate can be implemented with minimal adiabaticity overhead. In Sec. 6.3 we study both perturbatively and numerically the robustness of the CZ gate performance to coupler junction asymmetry, for small Josephson energies and relatively high qubit frequencies. We show that coherent errors remain below 5×10^{-7} for gate times of 22 ns over the entire range of junction asymmetry. A sensitivity analysis to flux noise is then presented in Sec. 6.4, indicating that for small Josephson energies the entangling phase of the CZ gate is robust to typical levels of flux noise in superconducting circuits. In Sec. 6.5 we identify two novel forms of crosstalk that can be mediated by the SQUID couplers, and show that both forms of crosstalk remain sufficiently small for realistic circuit parameters. Finally, in Sec. 6.6 we present a scalable mergemon architecture where all interactions are mediated by junction-based SQUID couplers, highlighting the potential for realizing a fully miniaturized quantum processor.

6.2 Tunable cross-Kerr Interaction via SQUID coupler

In order to elucidate the core aspects of the proposed coupling scheme we begin with an analysis of the circuit illustrated in Fig. 6.1a, comprising two transmon qubits coupled by a SQUID coupler. $E_{J,i}$, $E_{C,i}$, and C_i are the Josephson energy, the charging energy, and the capacitance to ground of the transmon $i \in \{1, 2\}$, respectively, $E_{J,C1}, E_{J,C2} \ll E_{J,1}, E_{J,2}$ and $C_{C1}, C_{C2} \ll C_1, C_2$ are the Josephson energies and the capacitances of the junctions in the SQUID coupler. $\Phi_{e,1}$ and $\Phi_{e,2}$ are external fluxes that thread the inner SQUID loop within the SQUID coupler and the outer SQUID loop formed along the ground connection, respectively.

The Hamiltonian describing the circuit is given by

$$\hat{H}_{\text{tot}} = \hat{H}_1 + \hat{H}_2 + \hat{H}_{\text{int}}, \tag{6.1}$$

$$\hat{H}_i = 4E_{C,i}\hat{n}_i^2 - E_{J,i}\cos\hat{\varphi}_i \;\; (i \in \{1, 2\}), \tag{6.2}$$

$$\begin{aligned}\hat{H}_{\text{int}} = &-E_{J,C1}\cos\left(\hat{\varphi}_2 - \hat{\varphi}_1 + \varphi_{e,1} + \varphi_{e,2}\right) \\ &-E_{J,C2}\cos\left(\hat{\varphi}_2 - \hat{\varphi}_1 + \varphi_{e,2}\right) + g\hat{n}_1\hat{n}_2,\end{aligned} \tag{6.3}$$

where $\hat{\varphi}_1$, $\hat{\varphi}_2$, $\hat{n}_1$, and $\hat{n}_2$ are phase and charge operators, $g = 4e^2C_C/C^2$ denotes the charge coupling rate due to the capacitances of the coupler junctions where

$C_C \equiv C_{C1} + C_{C2}$, $C^2 \equiv C_1C_2 + C_CC_1 + C_CC_2$, and $\varphi_{e,k} \equiv 2\pi\Phi_{e,k}/\Phi_0$ ($k \in \{1, 2\}$) are the reduced external fluxes. Details of the circuit quantization are provided in Appendix 6.9.1.

We introduce the flux "operating condition", $\varphi_{e,1} + 2\varphi_{e,2} = 0$, which ensures that the even-parity interactions, such as excitation hopping and cross-Kerr interaction, dominate over odd-parity interactions, such as longitudinal and two-photon exchange interactions. Under this constraint, the interaction Hamiltonian can be rewritten using trigonometric relations as follows:

$$\begin{aligned}\hat{H}_{\text{int}}|_{\varphi_{e,1}+2\varphi_{e,2}=0} = &-\Sigma E_{J,C} \cos\left(\frac{\varphi_{e,1}}{2}\right) \cos\left(\hat{\varphi}_2 - \hat{\varphi}_1\right) \\ &+ \Delta E_{J,C} \sin\left(\frac{\varphi_{e,1}}{2}\right) \sin\left(\hat{\varphi}_2 - \hat{\varphi}_1\right) + g\hat{n}_1\hat{n}_2, \end{aligned} \tag{6.4}$$

where $\Sigma E_{J,C} \equiv E_{J,C1} + E_{J,C2}$ and $\Delta E_{J,C} \equiv E_{J,C1} - E_{J,C2}$ are the total and differential Josephson energies. The cosine term proportional to $\Sigma E_{J,C}$ provides even-parity interactions, whereas the sine term with $\Delta E_{J,C} \ll \Sigma E_{J,C}$ provides odd-parity interactions. We first focus on symmetric SQUID couplers ($\Delta E_{J,C} = 0$), which leave only the even-parity terms. The effects of junction asymmetry are discussed in the following sections.

As $E_{J,C}$s are small, perturbation theory can be used to calculate the effective linear coupling rate, $g_{\text{eff}} \equiv \langle 10|\hat{H}_{\text{int}}|01\rangle$, and the first- and second- order corrections, $\zeta^{(1)}$ and $\zeta_c^{(2)}$, from the excitation-number-conserving matrix elements to the ZZ interaction rate, $\zeta \equiv \omega_{|0\tilde{0}\rangle} - \omega_{|0\tilde{1}\rangle} - \omega_{|1\tilde{0}\rangle} + \omega_{|1\tilde{1}\rangle}$:

$$g_{\text{eff}} = -\Sigma E'_{J,C} \cos\left(\frac{\varphi_{e,1}}{2}\right)\varphi_1^{zpf}\varphi_2^{zpf} + gn_1^{zpf}n_2^{zpf}, \tag{6.5}$$

$$\zeta^{(1)} = -\Sigma E'_{J,C} \cos\left(\frac{\varphi_{e,1}}{2}\right)(\varphi_1^{zpf})^2(\varphi_2^{zpf})^2, \tag{6.6}$$

$$\zeta_c^{(2)} = \frac{|\langle 02|H_{\text{int}}|11\rangle|^2}{\omega_{|11\rangle} - \omega_{|02\rangle}} + \frac{|\langle 20|H_{\text{int}}|11\rangle|^2}{\omega_{|11\rangle} - \omega_{|20\rangle}} \approx \frac{4g_{\text{eff}}^2\eta}{\Delta^2 - \eta^2}. \tag{6.7}$$

Here $\Sigma E'_{J,C} \equiv \Sigma E_{J,C} e^{-\frac{(\varphi_1^{zpf})^2}{2}} e^{-\frac{(\varphi_2^{zpf})^2}{2}}$ captures the byproduct of normal ordering, $\eta_1, \eta_2 \approx \eta$ are bare transmon anharmonicities, ω_1, ω_2 are bare transmon ground-to-first-excited state transition frequencies, and $\Delta \equiv \omega_1 - \omega_2$ is the transmon qubit detuning. $|ij\rangle$, $i, j \in \{0, 1\}$ represents the bare eigenstate, where the first (second)

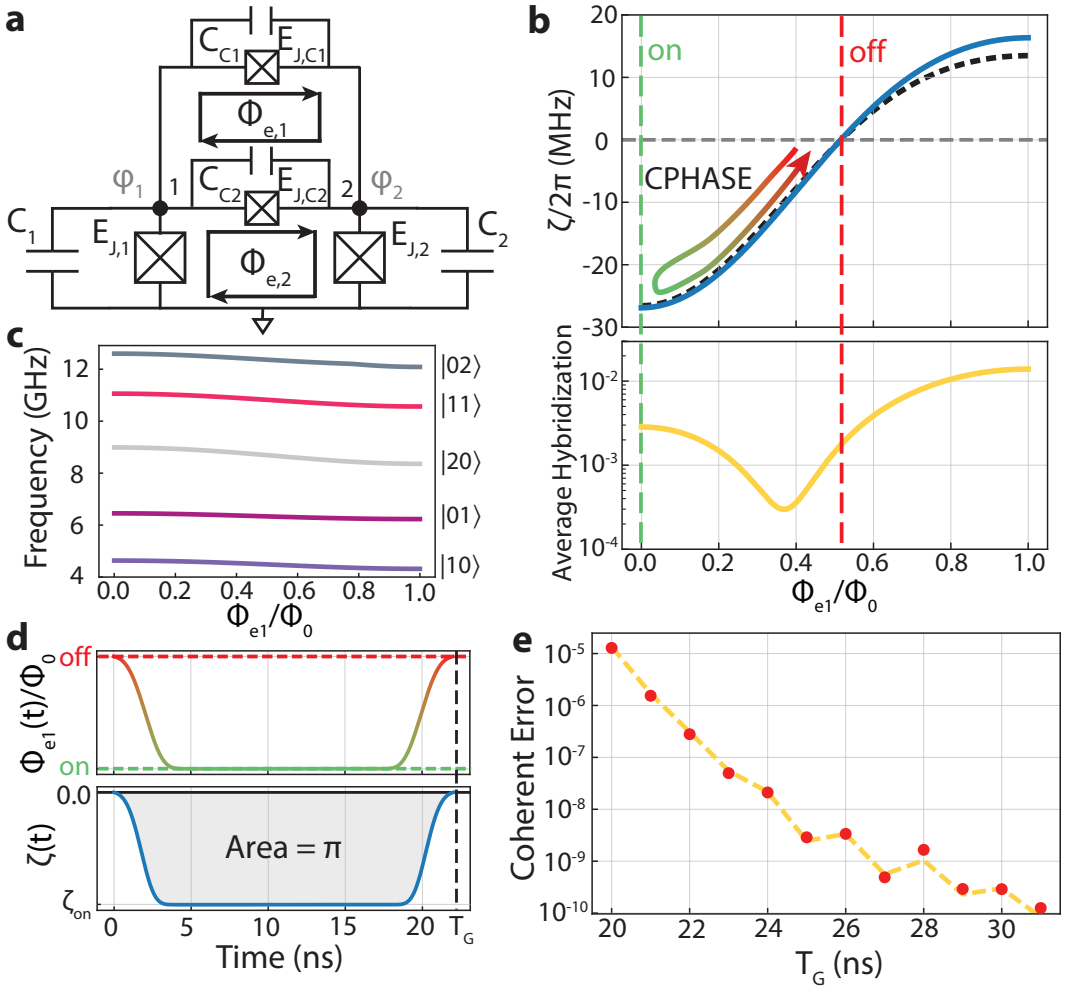

Figure 6.1: **Tunable cross-Kerr coupling and CZ gate via a SQUID coupler. a**, Circuit schematic of two transmons coupled via a SQUID coupler. **b**, ZZ interaction rate ζ and average hybridization as functions of $\Phi_{e,1}$. Red (green) dashed line indicates where ζ is zero (maximal). Black dashed line represents ζ calculated from perturbation theory. **c**, Eigenfrequencies of the first 5 excited states as functions of $\Phi_{e,1}$ under the operating condition $\Phi_{e,2} = -\Phi_{e,1}/2$. **d**, Flux waveform $\Phi_{e,1}(t)$ and the corresponding $\zeta(t)$, used for a 22 ns-long CZ gate. **e**, Coherent error of CZ gate for various gate durations T_G (red circles). Yellow dashed line represents the contribution from non-adiabatic state transitions.

$E_{J,1}/2\pi$	11.5 GHz	$E_{J,2}/2\pi$	20.0 GHz
C_1	77.5 fF	C_2	69.2 fF
$E_{J,C1}/2\pi$	0.40 GHz	$E_{J,C2}/2\pi$	0.40 GHz
C_{C1}	0.78 fF	C_{C2}	0.78 fF
$\omega_1/2\pi$	4.49 GHz	$\omega_2/2\pi$	6.33 GHz
$\eta_1/2\pi$	-0.284 GHz	$\eta_2/2\pi$	-0.306 GHz
Φ_{off}	0.516 Φ_0	$\zeta_{\text{on}}/2\pi$	-26.9 MHz

Table 6.1: Parameters used for numerical analysis. Parameters indicating energies are normalized by the reduced Planck constant $\hbar$.

index refers to transmon 1 (transmon 2) excitation number. Bare eigenstates and eigenfrequencies are obtained from $\hat{H}_1$ and $\hat{H}_2$. $\omega_{|i\tilde{j}\rangle}$ are the corresponding dressed eigenstate and eigenfrequency. Cosinusoidal terms are expanded in terms of creation ($\hat{a}_i^\dagger$) and annihilation operators ($\hat{a}_i$), with corresponding phase and charge operators $\hat{\varphi}_i = \varphi_i^{zpf}(\hat{a}_i + \hat{a}_i^\dagger)$ and $\hat{n}_i = in_i^{zpf}(\hat{a}_i - \hat{a}_i^\dagger)$, where φ_i^{zpf} and n_i^{zpf} are zero-point fluctuations. See Appendix 6.9.2 for further details.

The first-order correction $\zeta^{(1)}$ originates from diagonal perturbation terms, reaching a maximum at $\Phi_{e,1} = 0$ ("on") and zero at $\Phi_{e,1} = 0.5\Phi_0$ ("off"). Unlike ZZ interactions arising from hybridization, $\zeta^{(1)}$ depends only weakly on the detuning, allowing strong ZZ interaction rates even with a large detuning. The effective linear coupling g_{eff} can be reduced and can even be canceled out in the range $\Phi_{e,1} \in [0.0\Phi_0, 0.5\Phi_0)$ with appropriate choices of C_C due to the relative signs of the terms in eq. (6.5) [120, 265, 272]. With sufficiently small g_{eff} and large detuning, hybridization-induced ZZ interactions such as $\zeta_c^{(2)}$ can be suppressed in a substantial range of $\Phi_{e,1}$. Under such conditions, $\zeta^{(1)}$ dominates the ZZ interaction rate, and there is at least one idle external flux Φ_{off} at which the ZZ interaction can be turned off $\zeta(\Phi_{\text{off}}) = 0$ and the two transmons can idle.

In Fig. 6.1 we present a specific numerical example of the tunable cross-Kerr coupling between two far-detuned transmon qubits for a set of coupler and qubit parameters listed in Table 6.1. Note that junction tunneling energies and capacitances in this table are chosen to be consistent with experimentally achievable junction parameters [24, 56, 269–271, 278, 279]. Here we directly simulate the full Hamiltonian in eq. (6.1) by quantizing the circuit model and without applying rotating-wave approximations [243, 280, 281]. Fig. 6.1b shows ζ as a function of $\Phi_{e,1}$. An idle external flux $\Phi_{\text{off}} = 0.516\Phi_0$ and a large ZZ interaction rate $\zeta_{\text{on}}/2\pi = -26.9$ MHz

at $\Phi_{\text{on}} = 0$ are found. Although ζ varies appreciably, the change in eigenfrequencies remains less than 320 MHz throughout the tuning range for both qubits, as shown in Fig. 6.1c, minimizing susceptibility to flux noise [41, 57, 191, 282]. We chose capacitances $C_C/2 = C_{C1} = C_{C2}$ of the coupler that minimizes hybridization with other states in the relevant tuning range $[0, \Phi_{\text{off}}]$. To quantify this, the average hybridization with other states $\sum_{mn}(1 - P_{|mn\rangle})/4$ is used, where $P_{|mn\rangle} = |\langle mn|\tilde{mn}\rangle|^2$ is the overlap between bare ($|mn\rangle$) and dressed ($|\tilde{mn}\rangle$) eigenstates. As shown in Fig. 6.1b, the average hybridization is below 0.3% throughout the range $[0, \Phi_{\text{off}}]$.

A controlled phase (CPHASE) can be implemented by dynamically tuning the external flux from the idle bias point Φ_{off} to Φ_{on}, and back to Φ_{off}, as illustrated in Fig. 6.1d. To implement a CZ gate we aim for the accumulated controlled phase to be equal to π, i.e., $-\int_0^{T_G} \zeta(t)dt = \pi \pmod{2\pi}$, where T_G is the total gate duration and $\zeta(t)$ is the instantaneous ZZ interaction rate. We use a simplified adiabatic control technique similar to that employed in Refs. [268, 283] by treating $|11\rangle$ and $|02\rangle$ as a two-level system, in which the rate of change in hybridization (mixing-angle) between the two states is tailored. A target mixing-angle waveform is first generated by convolving a square pulse with a duration of βT_G and a Slepian-like pulse with a duration of $(1 - \beta)T_G$, in which β controls the adiabaticity while keeping T_G fixed. The flux waveform is then obtained by mapping the mixing-angles to external flux, and subsequently low-pass filtered by convolving with a Gaussian kernel of $\sigma = 0.5$ ns to account for realistic flux signal conditioning [106, 284]. An example waveform $\Phi_{e,1}(t)$ and the corresponding $\zeta(t)$ are shown in Fig. 6.1d.

The coherent error of the CZ gate as a function of T_G is shown in Fig. 6.1e. For each T_G, β is calibrated solely to achieve the target entangling phase. Under such calibration, non-adiabatic state transitions between states that are relatively close in frequency, such as $|\tilde{10}\rangle \leftrightarrow |\tilde{01}\rangle$ and $|\tilde{11}\rangle \rightarrow |\tilde{20}\rangle, |\tilde{02}\rangle$, are dominant sources of errors, which can be reduced by increasing T_G. We find that it is possible to implement a CZ gate with coherent errors below 3×10^{-7} in 22 ns, showing a minimal adiabaticity overhead of approximately 3.4 ns compared to the minimum gate time $\min T_G = \pi/|\zeta_{\text{on}}| \approx 18.6$ ns. This overhead may be further reduced through more advanced adiabatic control techniques [283] and less strict filtering. Note that the simulation uses the full Hamiltonian without employing the rotating-wave approximation. The gate is also simulated in the presence of T_1 relaxation errors, where a coherence-limited infidelity $1 - F$ of approximately $1.8 \times 10^{-5} \approx 0.8T_G/T_1$ is found when assuming $T_1 = 1$ ms for both transmons [244] (see Appendix 6.9.4).

6.3 Robustness against junction asymmetry

The odd-parity interaction is proportional to $\Delta E_{J,C} \sin(\varphi_{e,1}/2)$, reaching its strongest value near the idle point of $\Phi_{\text{off}} \approx 0.5\Phi_0$. This term includes longitudinal ($\hat{a}_i^\dagger \hat{a}_i(\hat{a}_j^\dagger + \hat{a}_j)$) and two-photon exchange ($(\hat{a}_i^\dagger)^2\hat{a}_j + h.c.$) interactions. The contribution to the ZZ interaction rate from the odd-parity interaction, $\zeta_{\text{odd}}^{(2)}$, scales inversely with odd-parity combinations of qubit frequencies and proportionally to higher-orders of phase zero-point fluctuations,

$$\zeta_{\text{odd}}^{(2)} \sim O\left(\frac{\Delta E_{J,C}^2 (\varphi^{zpf})^6}{m\omega_1 + n\omega_2}\right) + O\left(\frac{\Delta E_{J,C}^2 (\varphi^{zpf})^4}{\omega^2}\eta\right),$$

where $(m, n) \in \{(1,0), (0,1), (2,-1), (2,-1)\}$. A detailed calculation is provided in Appendix 6.9.2. Note that $(\varphi^{zpf})^6 \approx (2E_C/E_J)^{3/2}$ is less than 0.02 for a typical transmon where $E_J/E_C > 30$. Thus, for a SQUID coupler with junction tunneling energies ($E_{J,C}$) much less than the qubit frequencies, and for transmon qubits with relatively small φ^{zpf}, we expect that contributions to the ZZ interaction from the odd-parity interaction will be strongly suppressed, preserving the existence of an idle point, Φ_{off}.

In Fig. 6.2 we study the effects of junction asymmetry in the SQUID coupler for the nominal circuit parameters of Table 6.1. Using circuit quantization, ζ is estimated as a function of junction asymmetry $\Delta E_{J,C}/\Sigma E_{J,C}$ while $\Sigma E_{J,C}$ is kept constant, as shown in Fig. 6.2a. Josephson energy asymmetries and junction capacitance asymmetries are assumed to be the same. As expected from the analysis above, we find that the ZZ interaction rate does not depend significantly on junction asymmetry, and an idle external flux exists over the entire range of $\Delta E_{J,C}$. Estimates of Φ_{off} from first- and second-order perturbation theory considering up to a single excitation difference in the total excitation number (black dashed line) shows good correspondence with the full numerical computation from circuit quantization (red triangles). The effect of junction asymmetry is further tested by estimating the effect on the CZ gate coherent error, as shown in Fig. 6.2b. For the 22 ns-long CZ gate, coherent errors remain below 5×10^{-7} for the entire range of possible junction asymmetry (100% asymmetry corresponding to a single junction coupler as in Ref. [265, 266]). See Appendix 6.9.5 for further details.

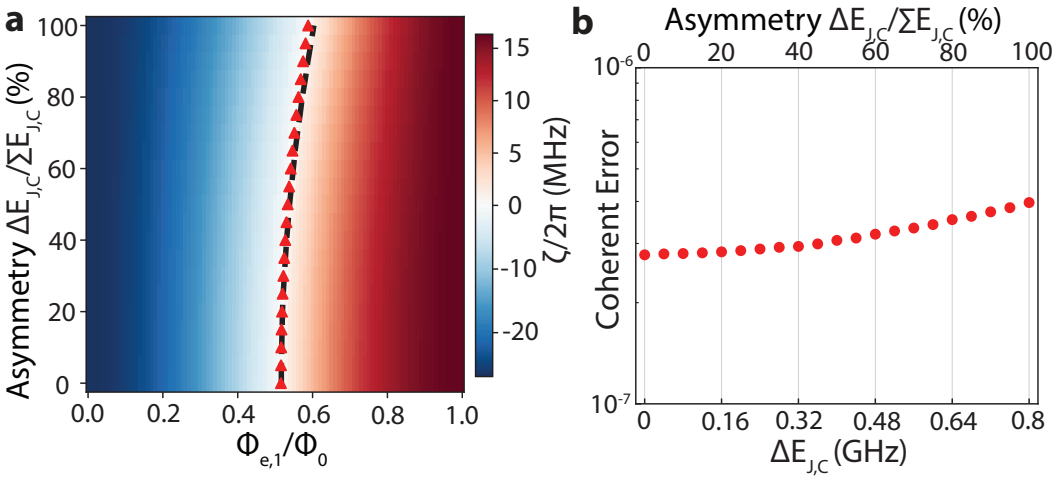

Figure 6.2: **Robustness against junction asymmetry.** **a**, ZZ interaction rate as a function of $\Phi_{e,1}$ and junction asymmetry. Junction capacitance asymmetry is set to be the same as the Josephson energy asymmetry. Red triangles indicate Φ_{off} obtained from circuit quantization, and black dashed line shows Φ_{off} estimated from perturbation theory. **b**, Coherent error of the 22 ns-long CZ gate as a function of junction asymmetry.

6.4 Sensitivity to flux noise

In order to accurately assess the sensitivity of the proposed junction coupler architecture to magnetic flux noise, the mapping from physical external fluxes to circuit flux variables $\Phi_{e,1}$ and $\Phi_{e,2}$ must account for the inductance in galvanic ground connections [285–287]. This is particularly important when considering the tiling of qubits and SQUID couplers on a two-dimensional lattice (see Sec. 6.6), where the multiple pathways to ground lead to additional extraneous SQUID loops. For such an analysis we therefore consider the SQUID coupler circuit illustrated in Fig. 6.3a with inductances L and L' much smaller than Josephson inductances of the junctions, modeling realistic ground connections in a square lattice tiling. Accounting for these ground connections we see that the resultant circuit has an inner SQUID loop threaded by external flux $\Phi_{e,i}$ and two outer SQUID loops threaded by external fluxes $\Phi_{e,o}$ and $\Phi'_{e,o}$, with associated reduced external flux variables $\varphi_{e,i}$, $\varphi_{e,o}$, and $\varphi'_{e,o}$. Refer to Appendix 6.9.1 for more details.

At $L = L'$, the circuit Hamiltonian depends only on $\Phi_{e,i}$ and the differential outer external flux $\Delta\Phi_{e,o} \equiv \Phi_{e,o} - \Phi'_{e,o}$, resulting in what is called a "gradiometric SQUID coupler". The mapping between the flux parameterization of the original SQUID coupler circuit of Fig. 6.1 and the gradiometric SQUID coupler is given by $\Phi_{e,1} = \Phi_{e,i}$ and $\Phi_{e,2} = (\Delta\Phi_{e,o} - \Phi_{e,i})/2$, with the original operating condition $\Phi_{e,1} +$

$2\Phi_{e,2} = 0$ being equivalent to $\Delta\Phi_{e,o} = 0$. Sensitivities of the qubit eigenfrequencies to external fluxes at the operating condition in the gradiometric SQUID coupler are given by

$$\frac{\partial\omega_{|\tilde{ij}\rangle}}{\partial\varphi_{e,i}}|_{\Delta\Phi_{e,o}=0} = \frac{1}{2}\Sigma E_{J,C}\sin\left(\frac{\varphi_{e,1}}{2}\right)\langle\cos\left(\hat{\varphi}_2 - \hat{\varphi}_1\right)\rangle, \tag{6.8}$$

$$\frac{\partial\omega_{|\tilde{ij}\rangle}}{\partial\varphi_{e,o}}|_{\Delta\Phi_{e,o}=0} = \frac{1}{2}\Delta E_{J,C}\sin\left(\frac{\varphi_{e,1}}{2}\right)\langle\cos\left(\hat{\varphi}_2 - \hat{\varphi}_1\right)\rangle, \tag{6.9}$$

$$\frac{\partial\omega_{|\tilde{ij}\rangle}}{\partial\varphi'_{e,o}}|_{\Delta\Phi_{e,o}=0} = -\frac{1}{2}\Delta E_{J,C}\sin\left(\frac{\varphi_{e,1}}{2}\right)\langle\cos\left(\hat{\varphi}_2 - \hat{\varphi}_1\right)\rangle, \tag{6.10}$$

where we have used the approximation $\langle\sin\left(\varphi_2 - \varphi_1\right)\rangle \approx 0$. As can be seen from eqs. (6.8-6.10), the sensitivity to inner SQUID flux noise scales with $\Sigma E_{J,C}$, while the sensitivity to flux noise in the outer SQUID loops scales with asymmetry in the coupler junctions, $\Delta E_{J,C}$.

We begin with an assessment of the impact of noise in the outer SQUID loops. As the loop area and perimeter of these outer loops can be relatively large they can host a significant amount of flux noise [277]. In Fig. 6.3b we provide an estimate of the echo dephasing times in the qubit states $|\tilde{10}\rangle$ and $|\tilde{01}\rangle$ in the presence of flux noise as a function of $\Delta E_{J,C}$. In this analysis we consider the coupler to be biased at the operational point, ($\Phi_{e,1} = \Phi_{\text{off}}$), and we assume an external flux noise model consisting of $1/f$ noise with amplitude $A_{\Phi_{e,i}} = 10^{-6}\Phi_0$ for the smaller inner SQUID loop and $A_{\Phi_{e,o}} = A_{\Phi'_{e,o}} = 5\times10^{-6}\Phi_0$ for the larger outer SQUID loops, consistent with typically measured flux noise in superconducting circuits [277] and for a circuit layout similar to that proposed below in Sec. 6.6. The echo dephasing time is calculated as per Ref. [191]:

$$\frac{1}{T^{1/f,|ij\rangle}_{\phi,\text{echo}}} = \sqrt{\ln 2}\sqrt{A^2_{\Phi_{e,i}}\left|\frac{\partial\omega_{|\tilde{ij}\rangle}}{\partial\Phi_{e,i}}\right|^2 + A^2_{\Phi_{e,o}}\left|\frac{\partial\omega_{|\tilde{ij}\rangle}}{\partial\Phi_{e,o}} - \frac{\partial\omega_{|\tilde{ij}\rangle}}{\partial\Phi'_{e,o}}\right|^2}, \tag{6.11}$$

where we take the inner and outer SQUID flux noises to be uncorrelated, but assume a worst-case correlation $\delta\Phi'_{e,o} = -\delta\Phi_{e,o}$ between the noise in the outer SQUID fluxes. This analysis shows that even for junction asymmetries of $\Delta E_{J,C}/2\pi = 160$ MHz (20%) we find coherence times $T_{\phi,\text{echo}} > 160$ μs, indicating that for realistic noise and experimentally achievable junction fabrication and circuit layouts we don't anticipate substantial degradation in qubit coherence.

Having examined the leading contribution to qubit dephasing associated with junction asymmetry, we now set $\Delta E_{J,C} = 0$ and discuss the contribution to dephasing

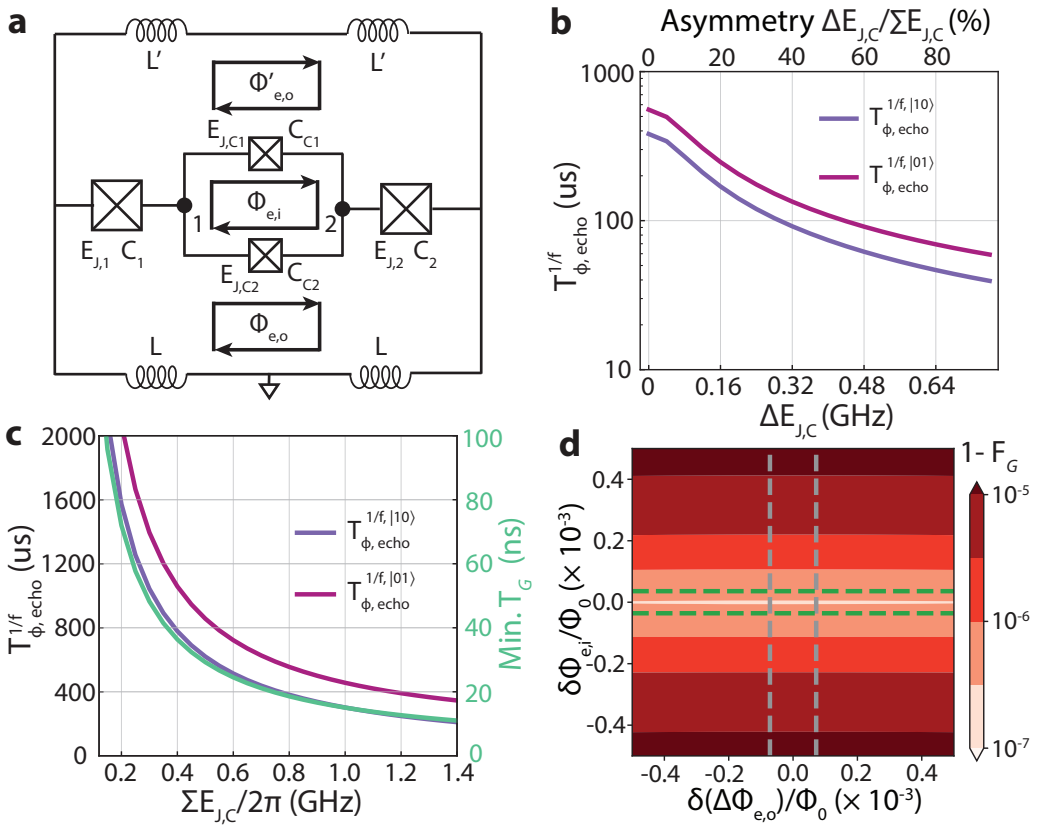

Figure 6.3: **Sensitivity to flux noise.** **a**, SQUID coupler circuit with physical external fluxes and realistic inductive network. Capacitors are omitted for brevity. **b**, Echo dephasing times $T_{\phi,\text{echo}}^{1/f,|10\rangle}$ and $T_{\phi,\text{echo}}^{1/f,|01\rangle}$ calculated for $1/f$ flux noise with amplitudes $A_{\Phi_{e,i}} = 10^{-6}\Phi_0$ and $A_{\Phi_{e,o}} = A_{\Phi'_{e,o}} = 5 \times 10^{-6}\Phi_0$. Here we assume worst-case scenario in which the outer SQUID flux noises are anti-correlated. **c**, Calculated echo dephasing time and minimum achievable gate time (π/ζ_{on}) as a function of $\Sigma E_{J,C}$ for $1/f$ flux noise with the same flux noise amplitudes as in **b**. **d**, Coherent error of the 22 ns-long CZ gate as a function of external flux offsets, $\delta\Phi_{e,1}$ and $\delta\Phi_{e,2}$. Green and gray dashed lines represent the range of flux offsets corresponding to the RMS deviation over a 1 hr drift period for $1/f$ flux noise with amplitudes $A_{\Phi_{e,i}} = A_{\Phi_{e,o}} = A_{\Phi'_{e,o}} = 5 \times 10^{-6}\Phi_0$, assuming an anti-correlation in the outer SQUID flux noises.

arising from $\Sigma E_{J,C}$. In this case, since the cross-Kerr interaction rate and flux sensitivity originate from the same diagonal term proportional to $\Sigma E_{J,C}$, and Φ_{off} remains nearly unaffected, a clear trade-off exists between flux-noise-induced dephasing and gate speed. We analyze this trade-off by comparing the echo dephasing times and the minimum achievable gate time, $\min T_G = \pi/|\zeta_{\text{on}}|$.

We use the method presented in Ref. [288] to simulate the impact of flux noise on the CZ gate error. As the maximum ZZ interaction occurs at the sweet spot, $\Phi_{e,i} = \Delta\Phi_{e,o} = 0$, we expect the entangling phase of the CZ gate to be robust against flux noise. Figure 6.3d shows the estimated coherent error of the 22 ns-long CZ gate as a function of static offsets $\delta\Phi_{e,i}$ and $\delta(\Delta\Phi_{e,o})$ added to the flux waveform. In this analysis we use local $\hat{Z}$ phases found from the zero offsets to simulate drifts in local phases due to flux noise. The green and gray dashed curves calibrate the zero offsets to root-mean-square (RMS) flux deviations in a 1-hour drift period for $1/f$ flux noise of amplitudes of $A_{\Phi_{e,i}} = A_{\Phi_{e,o}} = 5 \times 10^{-6}\Phi_0$ and an anti-correlation between the two outer SQUID flux noises. From this analysis we find that the CZ gate maintains a small coherent error below the 10^{-6} level over a 1-hour drift period.

6.5 Unconventional crosstalk

In an array of coupled qubits, we find that junction asymmetries in the SQUID coupler can induce crosstalk between next-nearest-neighbor pairs of qubits, as illustrated in Fig. 6.4a. This crosstalk results from odd-parity interactions, given by $\hat{H}_{\text{asym-asym}}$

$$\begin{aligned}\hat{H}_{\text{asym-asym}} = \Delta E_{J,C}^{12} \sin\left(\frac{\varphi_{e12}}{2}\right) \sin\left(\hat{\varphi}_2 - \hat{\varphi}_1\right) \\ + \Delta E_{J,C}^{23} \sin\left(\frac{\varphi_{e23}}{2}\right) \sin\left(\hat{\varphi}_3 - \hat{\varphi}_2\right),\end{aligned} \tag{6.12}$$

where $\Delta E_{J,C}^{12}$ and $\Delta E_{J,C}^{23}$ are differential Josephson energies due to junction asymmetry within the SQUID couplers which directly connect the nearest-neighbor pair of qubits and the next-nearest-neighbor pair of qubits, respectively, and φ_{e12} and φ_{e23} are are the corresponding external fluxes threading the SQUID couplers.

Expansion of eq. (6.12) to the third order reveals longitudinal interaction:

$$\hat{H}_{\text{longitudinal}} \approx \left(J_{12}\hat{a}_1^\dagger\hat{a}_1 + J_{23}\hat{a}_3^\dagger\hat{a}_3\right)\left(\hat{a}_2 + \hat{a}_2^\dagger\right), \tag{6.13}$$

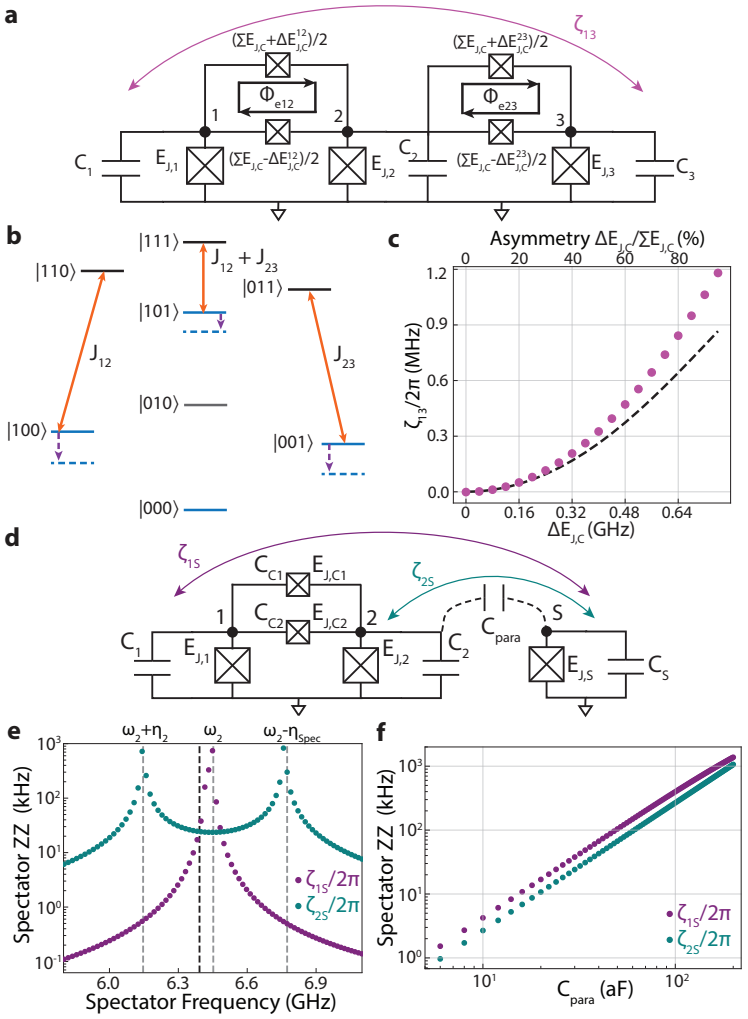

Figure 6.4: **Unconventional crosstalk mediated by SQUID couplers.** **a**, Circuit schematic of a chain of three transmons with nearest-neighbor connection via SQUID couplers. Coupler capacitances are omitted for brevity. **b**, Energy level diagram of **a** with transition matrix elements (solid orange lines) due to longitudinal interaction provided in eq. (6.13). **c**, ZZ interaction rate ζ_{13} calculated from circuit quantization numerically as a function of $\Delta E_{J,C}$ (purple circles). Black dashed line indicates ζ_{13} obtained from perturbation theory. **d**, Circuit schematic of two transmons coupled via a SQUID coupler and a spectator transmon coupled to transmon 2 over a parasitic capacitance C_{para}. **e**, Spectator ZZ interaction rates ζ_{1S} and ζ_{2S} as functions of spectator 0-1 transition frequency ω_S, with $C_{\text{para}} = 30$ aF. **f**, ζ_{1S} and ζ_{2S} as functions of C_{para}, estimated at $\omega_S/2\pi = \omega_2/2\pi - 60$ MHz (black dashed line in **e**).

where $J_{12} \approx \Delta E_{J,C}^{12'}(\varphi_1^{zpf})^2\varphi_2^{zpf} \sin\left(\frac{\varphi_{e12}}{2}\right)$ and $J_{23} \approx -\Delta E_{J,C}^{23'}(\varphi_3^{zpf})^2\varphi_2^{zpf} \sin\left(\frac{\varphi_{e23}}{2}\right)$. This is equivalent to a Z_1Z_3-parity-dependent driving of transmon 2, which for detuned qubits realizes an effective ZZ interaction between transmon 1 and 3, similar to the gate scheme described in Ref. [254]. The relevant transitions are illustrated in Fig. 6.4b. The ZZ interaction rate ζ_{13} obtained from second-order perturbation theory is given by:

$$\zeta_{13} \approx \frac{(J_{12} + J_{23})^2}{-\omega_2} - \frac{J_{12}^2}{-\omega_2} - \frac{J_{23}^2}{-\omega_2} = \frac{-2J_{12}J_{23}}{\omega_2}. \tag{6.14}$$

Using circuit quantization, ζ_{13} is calculated numerically as a function of $\Delta E_{J,C}^{12} = \Delta E_{J,C}^{23} = \Delta E_{J,C}$, and plotted in Fig. 6.4c. At each $\Delta E_{J,C}$, the junction capacitances are updated to maintain plasma frequencies and ζ_{13} is estimated under the idle conditions $\zeta_{12} = \zeta_{23} = 0$. The perturbative prediction of eq. (6.14) is in good agreement with the numerical circuit quantization result, indicating that most of ζ_{13} originates from the longitudinal interaction. Note that for $\Sigma E_{J,C}/2\pi = 0.8$ GHz, a junction asymmetry less than 20% is sufficient to suppress $\zeta_{13}/2\pi$ below 60 kHz.

Due to the weak dependence of the cross-Kerr interaction mediated by junction couplers, one can not rely on qubit frequency dispersion to suppress unwanted interactions within an array of coupled qubits. As such, crosstalk in the context of interactions with spectator qubits is a potential limitation of any SQUID-coupler-based architecture [118, 289, 290]. As illustrated in the circuit shown in Fig. 6.4d, SQUID couplers can propagate cross-Kerr interaction from a qubit that is not directly coupled to a spectator qubit. In this circuit, transmon 1 and 2 are directly connected via a SQUID coupler, and a spectator transmon of frequency ω_S (subscripted "S") couples to transmon 2 with a rate g_{para} through a parasitic capacitance C_{para}. This coupling hybridizes transmon 2 and the spectator qubit: $\hat{a}_2 \rightarrow \sqrt{1-|\gamma|^2}\hat{a}_2 + \gamma\hat{a}_S$, where $\gamma \approx g_{\text{para}}/(\omega_2 - \omega_S)$. Following eq. (6.4), this parasitic hybridization is translated into ZZ interaction ζ_{1S} between transmon 1 and the spectator as follows:

$$\zeta_{1S} \approx -\Sigma E'_{J,C} \cos\left(\frac{\varphi_{e,1}}{2}\right)(\varphi_1^{zpf})^2(\varphi_2^{zpf})^2|\gamma|^2 \approx \zeta^{(1)}|\gamma|^2. \tag{6.15}$$

This "indirect" ZZ crosstalk is maximized when the two transmons 1 and 2 exhibit maximal ZZ interaction, i.e., during CZ gate operations. As shown in Fig. 6.4e, we calculate ζ_{1S} as a function of ω_S at $\varphi_{e,1} = 0$, for parameters listed in Table. 6.1, $C_S = 69.2$ fF, and $C_{\text{para}} = 30$ aF. ω_S is varied by changing $E_{J,S}$. We also provide a comparison with conventional "direct" ZZ crosstalk ζ_{2S}. The indirect ZZ crosstalk is

maximized near the resonance condition $\omega_S \approx \omega_2$ and can even be stronger than ζ_{2S}, as illustrated in Fig. 6.4e and f. This adds emphasis to avoiding resonant frequency collision $\omega_S \approx \omega_2$ when allocating qubit frequencies [89, 291], and motivates the suppression of stray capacitances to levels at or below tens of aF (see Fig. 6.4f).

6.6 Fully miniaturized mergemon architecture

In this section we present a qubit tiling strategy towards a fully miniaturized superconducting quantum processor based on mergemon qubits coupled together with SQUID couplers. A schematic illustration of the proposed circuit is shown in Fig. 6.5. In this architecture all qubits and coupling elements are implemented using Josephson junctions, and free from bulky capacitor elements, greatly increasing the possible density of qubits within the array. It is envisioned that the same oxide barrier thickness for SQUID couplers and high-frequency mergemons can be employed, maintaining high CZ gate performance and reducing the complexity of the circuit fabrication (see Appendix 6.9.5). Note that the same tiling strategy can also be used for transmon qubits with dedicated shunt capacitors, simply by enlarging the extended leads to serve as capacitor pads.

For the circuit layout proposed in Fig. 6.5 there is a common ground (blue) connected to all of the low-voltage-side bottom junction electrodes (purple) of each mergemon qubit. The high-voltage-side top junction electrodes (orange and yellow) of the mergemon qubits have four lead extensions that connect each mergemon qubit to each of its four nearest-neighbors via a SQUID coupler. The low-voltage-side junction electrodes of the mergemon qubits, being galvanically connected to the common ground layer, give rise to the outer SQUID loops discussed in previous sections. The two junction electrode layers of each SQUID coupler separate the mergemon qubits in the square lattice into alternating "high" (H) and "low" (L) groupings, where the mergemon qubits labelled Q_L (colored orange) have their top junction electrodes coupled to the upper metalization layer of each junction-based coupler, and the mergemon qubits labelled Q_H (colored yellow) have their top junction electrodes connected to the lower junction electrode of the couplers.

This separation of metallization layers avoids hop-over wiring elements and limits the extraneous superconducting loops in the lattice of qubits. The regular square lattice layout also gives rise to a gradiometric design that makes the circuit insensitive to homogeneous magnetic flux [285–287, 292]. For maximal control, two flux delivery lines per SQUID coupler are required (control lines not shown). An

alternative is to use a flux delivery line that satisfies the operating condition $\Delta\Phi_{e,o} = 0$.

In this architecture, qubit frequencies can be dispersed over a relatively large range thanks to the strong cross-Kerr coupling provided by the SQUID coupler even under large qubit detunings. For instance, data qubits can be assigned to a low frequency band around 4.5 GHz and auxiliary qubits can be assigned to a high frequency band around 6.3 GHz. This mitigates frequency collision between nearest-neighbor pairs, enables the use of fixed-frequency qubits, and maximizes adiabaticity in CZ gates. To avoid accidental collision with strongly-coupled TLS defects, flux-tunable transmons may also be used [269–271].

As illustrated in Fig. 6.5, the top junction electrode of each mergemon qubit is galvanically connected to a lumped-element read-out resonator via a Josephson junction for qubit state read-out. This junction-based readout technique not only eliminates coupling capacitors for readout but can also simplify the read-out circuit by obviating the need for an additional Purcell filter [71, 120]. Moreover, the SQUIDs introduced by junction readout can provide tunability in nonlinear interactions and effective linear coupling, as demonstrated in Ref. [71]. We anticipate that this tunability can be used for unconditional qubit reset or leakage reduction by activating hybridization to readout resonators [44, 71, 105, 106, 213, 220, 221, 293].

The use of lumped-element readout resonators with compact footprints [72, 294–297] further enables the miniaturized tiling of the qubit lattice. In addition, by using a flip-chip architecture [298, 299], charge drive lines, flux delivery lines, and readout feedlines can be placed on an opposing "wiring" chip without consuming space on the qubit chip. Combining these features together, we estimate that a miniaturized mergemon processor with a qubit lattice constant of 100 um is achievable, enabling the packing of up to 10^6 qubits in an area of 10 cm $\times$ 10 cm that could be fabricated on a single 6-inch wafer [76].

Looking forward, there are myriad other fabrication and layout considerations that one can consider in such a mergemon-qubit architecture. One particularly appealing opportunity afforded by an all-junction architecture is the utilization of acoustic bandgap structures to engineer the phonon bath environment of the circuit elements. As proposed [300, 301] and recently demonstrated [279, 302], by shutting off the primary phonon bath decoherence channel of two-level-system (TLS) defects one can dramatically improve the coherence properties of TLS, and correspondingly

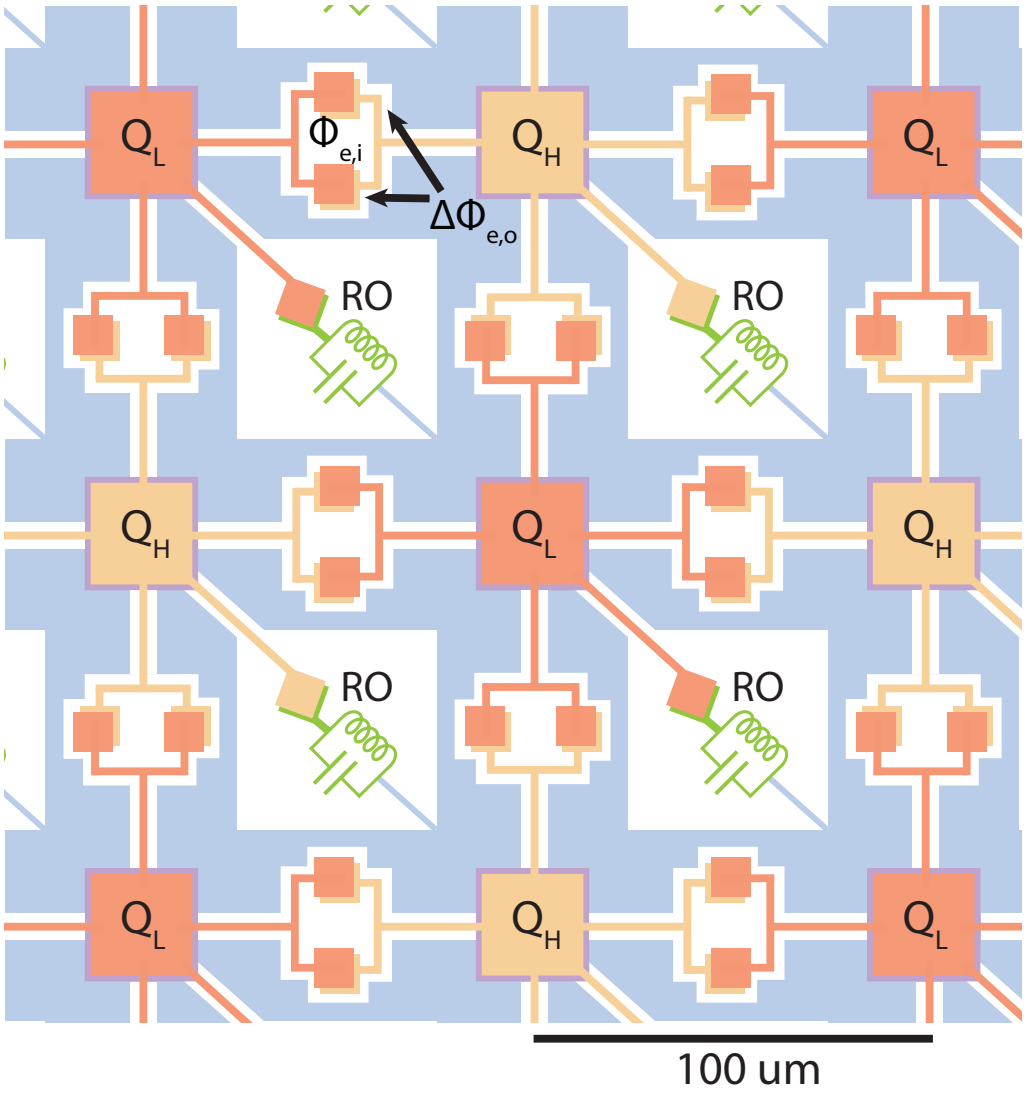

Figure 6.5: **Mergemons on a square lattice for a miniaturized quantum processor.** Orange (yellow) shape corresponds to high voltage side metalization for low frequency (high frequency) qubits, where an overlap with low voltage side metalization (purple) forms a mergemon. High voltage side metalization of each mergemon extends to their nearest-neighbors, forming SQUID couplers. Low voltage side metalization is connected galvanically to ground metalization (blue), forming the outer SQUID loops. Each mergemon is connected galvanically to its lumped-element readout resonator (green) via a Josephson junction for junction readout. For convenience in illustration, elements including Josephson junctions are intentionally displayed bigger than their realistic relative length scales. Scale bar represents the anticipated lattice constant provided in the main text.

the coherence properties of electrical or acoustic elements that couple to the TLS. This effect is particularly dramatic for elements that have a small surface area such that only a discrete set of two-level-system (TLS) are spectrally nearby, such as in a Josephson junction. Other considerations, such as minimizing the energy participation in the wiring leads of the tiled mergemon qubits and reducing parasitic capacitance to spectator qubits, are described in Appendices 6.9.6 and 6.9.7.

6.7 Other uses of the SQUID coupler

In this section we consider a few alternative uses of a SQUID coupler with similar hierarchy of coupler junction energy to operation frequency as proposed for transmon or mergemon qubit architectures. One such interesting application is to the engineering of two-photon exchange interactions used to dissipatively stabilize cat qubits [53, 74, 303, 304]. Under the SQUID coupler operating condition $\varphi_{e,1} + 2\varphi_{e,2} = \pi$, the odd-parity interaction $\hat{H}_{\text{sine}}$ is obtained:

$$\hat{H}_{\text{sine}} = \Sigma E_{J,C} \cos\left(\frac{\varphi_{e,1}}{2}\right) \sin\left(\hat{\varphi}_2 - \hat{\varphi}_1\right). \tag{6.16}$$

By introducing a time-dependent drive to the SQUID loop flux, $\varphi_{e,1}(t) = \pi + \epsilon_d \cos(\omega_d t)$, with $\omega_d \approx 2\omega_1 - \omega_2$ on $\varphi_{e,1}$, this yields under rotating-wave approximation a two-photon exchange interaction $\hat{H}_{\text{two-photon}}$ analogous to the result of Ref. [273]:

$$\hat{H}_{\text{two-photon}} \approx g_2 \hat{a}_1^2 \hat{a}_2^\dagger + h.c., \tag{6.17}$$

where $g_2 \equiv \frac{1}{8}\epsilon_d \Sigma E'_{J,C} (\varphi_1^{zpf})^2 (\varphi_2^{zpf})$. In the dissipatively-stabilized cat qubit system, mode 1 would be a harmonic oscillator storage mode and mode 2 could be a transmon qubit, for instance, used for "buffering" the storage mode. Remarkably, the g_2 coupling rate is directly proportional to the bare zero-point fluctuations of the two modes rather than their hybridized values. This separates the strength of the two-photon dissipation from that of the self- and/or cross-Kerr induced on the storage mode by the nonlinear buffer circuit due to mode hybridization [305, 306]. It also allows for more flexibility in allocating storage and buffer mode frequencies than in the conventional capacitively-coupled situation, where much larger detunings between elements may be employed.

Another potential use of the proposed SQUID coupler lies in engineering next-nearest-neighbor qubit interactions. For the three-transmon circuit illustrated in Fig. 6.4c, we obtain odd-parity interactions for the operating condition $\varphi_{e,1}+2\varphi_{e,2} = \pi$:

$$\begin{aligned}\hat{H}_{\text{sine-sine}} = \Sigma E_{J,C}^{12} \cos\left(\frac{\varphi_{e12}}{2}\right) \sin\left(\hat{\varphi}_2 - \hat{\varphi}_1\right) \\ + \Sigma E_{J,C}^{23} \cos\left(\frac{\varphi_{e23}}{2}\right) \sin\left(\hat{\varphi}_3 - \hat{\varphi}_2\right).\end{aligned} \tag{6.18}$$

This interaction renders the same longitudinal interaction and ZZ interaction rate ζ_{13} between the next-nearest-neighbor pair provided in eq. (6.13-6.14). Notably, $\zeta_{13}/2\pi$ can be larger than 1 MHz for $\Sigma E_{J,C}/2\pi = 0.8$ GHz as shown in Fig. 6.4f, and can be strengthened quadratically by increasing $\Sigma E_{J,C}$s.

Finally, the SQUID coupler can provide tunable XX interactions that can be used for the implementation of an adiabatic $\sqrt{\text{iSWAP}}$ gate between dual-rail transmons [255, 307]. This is derived from the fact that a single transmon Pauli-Z ($\hat{Z}$) operator is equivalent to a Pauli-X ($\hat{X}_{DR}$) operator of a dual-rail transmon that contains the transmon up to a global phase, as follows:

$$(\hat{I}_1\hat{Z}_2)(\hat{Z}_3\hat{I}_4) = -\hat{X}_{DR,a}\hat{X}_{DR,b}, \tag{6.19}$$

where subscript $i \in \{1, 2, 3, 4\}$ denotes transmon i, and dual-rail transmon a (b) consists of transmons 1, 2 (3, 4). Thus, if the SQUID coupler provides a tunable ZZ interaction in the form of $(\zeta/4)\hat{Z}_2\hat{Z}_3$ between transmons 2 and 3, this is equivalent to a tunable XX interaction $(-\zeta/4)\hat{X}_{DR,a}\hat{X}_{DR,b}$ for the dual-rail transmons a and b. This allows for the implementation of a $\sqrt{\text{iSWAP}}$ gate with duration $T_G^{\min} = \pi/|\zeta|$ plus an adiabaticity overhead [255], which is as short as a CZ gate between transmons. In the context of dual-rail qubits and erasure detection, the SQUID coupler preserves the error hierarchy by not introducing additional channels for leakage errors [255, 307, 308]. Furthermore, the impact of frequency noise is suppressed by operation at the artificial sweet-spot [255, 307]. See Appendix 6.9.8 for the tiling of dual-rail transmons.

6.8 Conclusion

The SQUID coupler provides modeless and tunable cross-Kerr coupling, which realizes a fast and high-fidelity CZ gate between transmons with minimal adiabaticity overhead. Sensitivities to junction asymmetry and flux noise are suppressed

by choosing high qubit frequencies and relatively small junction energies. Unconventional crosstalk due to parasitic hybridization to spectator qubits and junction asymmetry are also shown to be sufficiently small for realistic circuit parameters. SQUID couplers are particularly interesting in the context of a mergemon qubit architecture, where junctions with small Josephson energies and reduced SQUID loop sizes due to the absence of bulky shunt capacitors are anticipated. Using the junction-based coupling schemes, we propose a scalable tiling strategy towards a fully miniaturized superconducting quantum processor.

6.9 Supplementary Information for Chapter VI

6.9.1 Circuit quantization

The SQUID coupler circuit is analyzed following the standard circuit quantization procedure [309–311]. We define external flux drops $\Phi_{e,\text{top}}$ ($\Phi_{e,\text{bot}}$) as the external flux drop across the top (bottom) Josephson junction of the SQUID coupler, indicated by the blue (red) arrow, and $\Phi_{e,Ji}$s as the external flux drop across the transmon junctions. The branch fluxes Φ_{J1}, Φ_{J2} across Josephson junctions of transmon 1 and 2, and Φ_{top} and Φ_{bot} across the top and bottom Josephson junctions of the SQUID coupler are represented as follows:

$$\begin{aligned}
&\Phi_{J1} = \phi_1 + \Phi_{e,J1},\ \Phi_{J2} = -\phi_2 + \Phi_{e,J2},\\
&\Phi_{\text{bot}} = \phi_2 - \phi_1 + \Phi_{e,\text{bot}},\ \Phi_{\text{top}} = \phi_2 - \phi_1 + \Phi_{e,\text{top}},\\
&\Phi_{e,2} = \Phi_{e,J1} + \Phi_{e,\text{bot}} + \Phi_{e,J2},\\
&\Phi_{e,1} = \Phi_{e,\text{top}} - \Phi_{e,\text{bot}},
\end{aligned} \tag{6.20}$$

where ϕ_1, ϕ_2 are node variables of the two transmons.

The Lagrangian of the circuit is given by

$$\begin{aligned}
\mathcal{L} = &\frac{1}{2}C_1(\dot{\phi}_1 + \dot{\Phi}_{e,J1})^2 + \frac{1}{2}C_2(\dot{\phi}_2 - \dot{\Phi}_{e,J2})^2\\
&+ \frac{1}{2}C_{C1}(\dot{\phi}_2 - \dot{\phi}_1 + \dot{\Phi}_{e,\text{top}})^2 + \frac{1}{2}C_{C2}(\dot{\phi}_2 - \dot{\phi}_1 + \dot{\Phi}_{e,\text{bot}})^2\\
&+E_{J,1}\cos\left(2\pi\frac{(\phi_1 + \Phi_{e,J1})}{\Phi_0}\right) + E_{J,2}\cos\left(2\pi\frac{(\phi_2 - \Phi_{e,J2})}{\Phi_0}\right)\\
&+ E_{J,C1}\cos\left(2\pi\frac{(\phi_2 - \phi_1 + \Phi_{e,\text{top}})}{\Phi_0}\right)\\
&+ E_{J,C2}\cos\left(2\pi\frac{(\phi_2 - \phi_1 + \Phi_{e,\text{bot}})}{\Phi_0}\right),
\end{aligned} \tag{6.21}$$

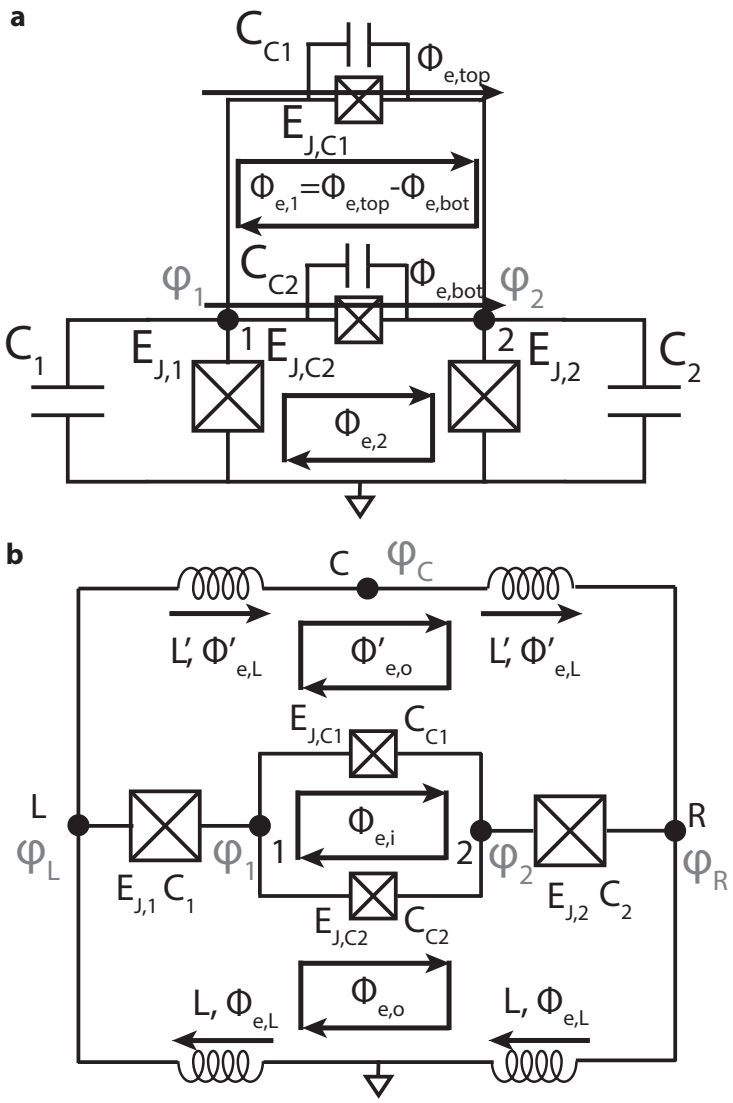

Figure 6.S1: **SQUID coupler with two transmons. a**, Single-sided SQUID coupler with two transmons. **b**, SQUID coupler with small inductances around ground connection, defining physical SQUID loops.

and the Legendre transformation:

$$
\begin{aligned}
Q_1 &= \frac{\partial \mathcal{L}}{\partial \dot{\phi}_1} = C_1(\dot{\phi}_1 + \dot{\Phi}_{e,J1}) + C_C(\dot{\phi}_1 - \dot{\phi}_2 - \dot{\Phi}_{\mathrm{e},12}), \\
Q_2 &= \frac{\partial \mathcal{L}}{\partial \dot{\phi}_2} = C_2(\dot{\phi}_2 - \dot{\Phi}_{e,J2}) + C_C(\dot{\phi}_2 - \dot{\phi}_1 + \dot{\Phi}_{\mathrm{e},12}),
\end{aligned} \tag{6.22}
$$

provides the Hamiltonian

$$
\begin{aligned}
H &= Q_1\dot{\phi}_1 + Q_2\dot{\phi}_2 - \mathcal{L} \\
&= \frac{C_2 + C_C}{2C^2}Q_1^2 + \frac{C_1 + C_C}{2C^2}Q_2^2 + \frac{C_C}{C^2}Q_1Q_2 \\
&+ Q_1\left(\frac{C_2C_C\dot{\Phi}_{\mathrm{e},12} - C_1(C_2 + C_C)\dot{\Phi}_{e,J1} + C_2C_C\dot{\Phi}_{e,J2}}{C^2}\right) \\
&+ Q_2\left(\frac{-C_1C_C\dot{\Phi}_{\mathrm{e},12} - C_1C_C\dot{\Phi}_{e,J1} + C_2(C_1 + C_C)\dot{\Phi}_{e,J2}}{C^2}\right) \\
&- E_{J,1}\cos\left(2\pi\frac{(\phi_1 + \Phi_{e,J1})}{\Phi_0}\right) - E_{J,2}\cos\left(2\pi\frac{(\phi_2 - \Phi_{e,J2})}{\Phi_0}\right) \\
&- E_{J,C1}\cos\left(2\pi\frac{(\phi_2 - \phi_1 + \Phi_{e,\mathrm{top}})}{\Phi_0}\right) \\
&- E_{J,C2}\cos\left(2\pi\frac{(\phi_2 - \phi_1 + \Phi_{e,\mathrm{bot}})}{\Phi_0}\right),
\end{aligned} \tag{6.23}
$$

where we have introduced the following definitions for a succinct description:

$$
\begin{aligned}
C_C &\equiv C_{C1} + C_{C2}, \\
\Phi_{e,12} &\equiv \frac{C_{C1}}{C_C}\Phi_{e,\mathrm{top}} + \frac{C_{C2}}{C_C}\Phi_{e,\mathrm{bot}}, \\
C^2 &\equiv C_1C_2 + C_1C_C + C_2C_C.
\end{aligned} \tag{6.24}
$$

The irrotational constraint can be found by eliminating the terms containing time-derivatives of the external fluxes:

$$
\begin{aligned}
C_2C_C\dot{\Phi}_{\mathrm{e},12} - C_1(C_2 + C_C)\dot{\Phi}_{e,J1} + C_2C_C\dot{\Phi}_{e,J2} &= 0, \\
-C_1C_C\dot{\Phi}_{\mathrm{e},12} - C_1C_C\dot{\Phi}_{e,J1} + C_2(C_1 + C_C)\dot{\Phi}_{e,J2} &= 0,
\end{aligned} \tag{6.25}
$$

which is satisfied with the following voltage-divider parameterization:

$$
C_1\dot{\Phi}_{e,J1} = C_2\dot{\Phi}_{e,J2} = C_C\dot{\Phi}_{e,12}. \tag{6.26}
$$

This reveals the relationship between the branch external flux drops and external fluxes by solving the linear equations and integrating over time:

$$\begin{aligned}
\Phi_{\text{e, top}} &= \Phi_{e,12} + \frac{1 - d_C}{2}\Phi_{e,1}, \\
\Phi_{\text{e, bot}} &= \Phi_{e,12} - \frac{d_C + 1}{2}\Phi_{e,1}, \\
\Phi_{e,2} &= \Phi_{e,J1} + \Phi_{e,J2} + \Phi_{e,\text{bot}}, \\
&= C_C \left(\frac{1}{C_1} + \frac{1}{C_2} + \frac{1}{C_C}\right)\Phi_{e,12} - \frac{d_C + 1}{2}\Phi_{e,1},
\end{aligned} \tag{6.27}$$

$$\begin{aligned}
\Phi_{e,12} &= \frac{C_1 C_2}{2C^2}\left((d_C + 1)\Phi_{e,1} + 2\Phi_{e,2}\right), \\
\Phi_{e,J1} &= \frac{C_2 C_C}{2C^2}\left((d_C + 1)\Phi_{e,1} + 2\Phi_{e,2}\right), \\
\Phi_{e,J2} &= \frac{C_1 C_C}{2C^2}\left((d_C + 1)\Phi_{e,1} + 2\Phi_{e,2}\right), \\
\Phi_{e,\text{top}} &= \Phi_{e,\text{bot}} + \Phi_{e,1}, \\
\Phi_{e,\text{bot}} &= \left(\frac{C_1 C_2}{C^2} - 1\right)\frac{(d_C + 1)}{2}\Phi_{e,1} + \frac{C_1 C_2}{C^2}\Phi_{e,2},
\end{aligned} \tag{6.28}$$

where $d_C \equiv (C_{C1} - C_{C2})/C_C$ is the junction capacitance asymmetry in the SQUID coupler. Note that if both junction capacitances and the Josephson energies are mostly proportional to the junction area, it is reasonable to assume that the Josephson energy asymmetry and the capacitance asymmetry are the same.

We can examine the consistency of the solution by considering the extreme cases. At $C_{C2} \to \infty$ (the bottom junction is replaced with a short), we find $\Phi_{e,\text{bot}} \to 0$ and $\Phi_{e,\text{top}} \to \Phi_{e,1}$, consistent with a shorted single junction. At $C_1 \to 0$ (transmon 1's junction is replaced with a pure inductor or open), we find $\Phi_{e,\text{bot}} \to -C_{C1}\Phi_{e,1}/C_C$, $\Phi_{e,\text{top}} \to C_{C2}\Phi_{e,1}/C_C$, and $\Phi_{e,J1} \to \Phi_{e,2}$, consistent with the DC SQUID and the fluxonium example provided in You et al. [310]. Finally, if we remove the top junction in the SQUID coupler, $C_{C1} \to 0$, we recover the solution found in Appendix A of Campbell et al. [265].

The complete expression for the Hamiltonian is as follows:

$$\begin{aligned}\hat{H} = &\\ &4E_{C,1}\hat{n}_1^2 - E_{J,1}\cos\left(\hat{\varphi}_1 + \frac{C_2C_C}{2C^2}((d_C+1)\varphi_{e,1} + 2\varphi_{e,2})\right)\\ &4E_{C,2}\hat{n}_2^2 - E_{J,2}\cos\left(\hat{\varphi}_2 - \frac{C_1C_C}{2C^2}((d_C+1)\varphi_{e,1} + 2\varphi_{e,2})\right)\\ &- E_{J,C1}\cos\left(\hat{\varphi}_2 - \hat{\varphi}_1 + \varphi_{e,\text{top}}\right)\\ &- E_{J,C2}\cos\left(\hat{\varphi}_2 - \hat{\varphi}_1 + \varphi_{e,\text{bot}}\right) + g\hat{n}_1\hat{n}_2, \end{aligned} \tag{6.29}$$

where node variables are replaced by operators (variables with hats). $\hat{\varphi}_i \equiv \frac{2\pi}{\Phi_0}\hat{\phi}_i$s are reduced flux operators, and $\hat{n}_i \equiv \frac{\hat{Q}_i}{2e}$ are reduced charge operators. $E_{C,1} \equiv e^2(C_2+C_C)/2C^2, E_{C,2} \equiv e^2(C_1+C_C)/2C^2$ are the charging energy of the two modes, and $g \equiv 4e^2C_C/C^2$ is the charge coupling rate. External fluxes are normalized to $\varphi_{e,k} \equiv 2\pi\Phi_{e,k}/\Phi_0$ ($k \in \{1,2\}$).

Under the symmetric SQUID approximation $d_C \approx 0$ and small junction approximation $C_C \ll C_1, C_2$ (note that the derivations up to eq. (6.29) are exact), φ_{top} and φ_{bot} approach $\varphi_{e,2}$ and $\varphi_{e,1} + \varphi_{e,2}$, and we eliminate the external fluxes from the transmon junction potentials. As a result, we obtain the Hamiltonian provided in the main text:

$$\begin{aligned}\hat{H} \approx &\, 4E_{C,1}\hat{n}_1^2 - E_{J,1}\cos\left(\hat{\varphi}_1\right) + 4E_{C,2}\hat{n}_2^2 - E_{J,2}\cos\left(\hat{\varphi}_2\right)\\ &- E_{J,C1}\cos\left(\hat{\varphi}_2 - \hat{\varphi}_1 + \varphi_{e,1} + \varphi_{e,2}\right)\\ &- E_{J,C2}\cos\left(\hat{\varphi}_2 - \hat{\varphi}_1 + \varphi_{e,2}\right) + g\hat{n}_1\hat{n}_2. \end{aligned} \tag{6.30}$$

Bringing back the asymmetry and the C_C terms, the ideal external flux constraint $\varphi_{e,1} = -2\varphi_{e,2}$ produces the following full-circuit Hamiltonian without the approximations:

$$\begin{aligned}\hat{H}|_{\varphi_{e,2}=-\varphi_{e,1}/2} = &\\ &4E_{C,1}\hat{n}_1^2 - E_{J,1}\cos\left(\hat{\varphi}_1 - \frac{C_2C_C}{2C^2}d_C\varphi_{e,1}\right)\\ &4E_{C,2}\hat{n}_2^2 - E_{J,2}\cos\left(\hat{\varphi}_2 + \frac{C_1C_C}{2C^2}d_C\varphi_{e,1}\right) + g\hat{n}_1\hat{n}_2\\ &- \Sigma E_{J,C}\cos\left(\frac{\varphi_{e1}}{2}\right)\cos\left(\hat{\varphi}_2 - \hat{\varphi}_1 + \frac{(C_1+C_2)C_C}{2C^2}d_C\varphi_{e,1}\right)\\ &+ \Delta E_{J,C}\sin\left(\frac{\varphi_{e1}}{2}\right)\sin\left(\hat{\varphi}_2 - \hat{\varphi}_1 + \frac{(C_1+C_2)C_C}{2C^2}d_C\varphi_{e,1}\right). \end{aligned} \tag{6.31}$$

where $\Sigma E_{J,C} \equiv E_{J,C1} + E_{J,C2}$, $\Delta E_{J,C} \equiv E_{J,C1} - E_{J,C2} \approx d_C \Sigma E_{J,C}$, and trigonometric relations are used to group cosine and sine terms. Within the cosinusoidal terms that contain the node variables, the external flux terms are suppressed to the scale of $d_C C_C/C_1$ and $d_C C_C/C_2$, which are approximately 0.002 assuming a modest asymmetry of $d_C \approx 0.2$ and C_C used in this work. This validates the perturbative analysis without including these terms.

For the SQUID coupler shown in Fig. 6.S1b, which reflects the realistic circuit shown in the tiling schematic Fig. 6.5, circuit quantization should be aided by properly considering the equilibrium node phases set by the small inductances around the low-impedance outer loops. Nodes L (left), R (right), and C (center), and the corresponding node fluxes ϕ_L, ϕ_R, and ϕ_C, are introduced by the inductor network consisting of 4 inductors with inductances $L, L' \ll L_J$, where L_J is the inductance of the Josephson junctions. In this circuit, we introduce three external fluxes $\Phi_{e,i}$, $\Phi_{e,o}$, and $\Phi'_{e,o}$ threading the three distinct SQUID loops.

Defining external flux drops at the inductors as $\Phi_{e,L}$ and $\Phi'_{e,L}$, the following set of equations is obtained due to fluxoid quantization:

$$\begin{aligned} 2\Phi'_{e,L} - (\Phi_{e,J1} + \Phi_{e,\text{top}} + \Phi_{e,J2}) &= \Phi'_{e,o}, \\ 2\Phi_{e,L} + (\Phi_{e,J1} + \Phi_{e,\text{bot}} + \Phi_{e,J2}) &= \Phi_{e,o}, \\ \Phi_{e,\text{top}} - \Phi_{e,\text{bot}} &= \Phi_{e,i}, \\ \rightarrow 2\Phi_{e,L} + 2\Phi'_{e,L} &= \Phi_{e,i} + \Phi_{e,o} + \Phi'_{e,o} \equiv \Sigma\Phi_e. \end{aligned} \tag{6.32}$$

As it is assumed that L and L' are small, the node phases ϕ_L, ϕ_R, and ϕ_b are localized around the equilibrium points ϕ_{L0}, ϕ_{R0}, and ϕ_{C0}. The inductive energy is given by

$$\begin{aligned} E_{\text{ind}} = &\frac{1}{2}E_L(\phi_L + \Phi_{e,L})^2 + \frac{1}{2}E_L(-\phi_R + \Phi_{e,L})^2 \\ &+ \frac{1}{2}E'_L(\phi_C - \phi_L + \Phi'_{e,L})^2 + \frac{1}{2}E'_L(\phi_R - \phi_C + \Phi'_{e,L})^2, \end{aligned} \tag{6.33}$$

where $E_L \equiv (\Phi_0/2\pi)^2/L$ and $E_L \equiv (\Phi_0/2\pi)^2/L'$ are inductive energies of the inductors. The equilibrium points are found by minimizing eq. (6.33) through solving the following set of equations:

$$\begin{aligned}
\frac{\partial E_{\text{ind}}}{\partial \phi_C} &= E'_L(\phi_C - \phi_L + \Phi'_{e,L}) - E'_L(\phi_R - \phi_C + \Phi'_{e,L}),\\
\frac{\partial E_{\text{ind}}}{\partial \phi_L} &= E_L(\phi_L + \Phi_{e,L}) - E'_L(\phi_C - \phi_L + \Phi'_{e,L}),\\
\frac{\partial E_{\text{ind}}}{\partial \phi_R} &= -E_L(-\phi_R + \Phi_{e,L}) + E'_L(\phi_R - \phi_C + \Phi'_{e,L}),\\
\rightarrow \phi_{L0} = -\phi_{R0} &= \frac{E'_L\Phi'_{e,L} - E_L\Phi_{e,L}}{E_L + E'_L},\ \phi_{C0} = 0.
\end{aligned} \tag{6.34}$$

The role of ϕ_{L0} and ϕ_{R0}, compared to the single-sided SQUID coupler, is to shift the external flux drops on qubit 1 and 2 by $\Phi_{e,J1} \rightarrow \Phi_{e,J1} - \phi_{L0}$ and $\Phi_{e,J2} \rightarrow \Phi_{e,J2} + \phi_{R0}$. Thus, the irrotational constraint and the subsequent algebra yields

$$\begin{aligned}
C_1\dot{\tilde{\Phi}}_{e,J1} = C_2\dot{\tilde{\Phi}}_{e,J2} &= C_C\dot{\Phi}_{e,12},\\
\tilde{\Phi}_{e,J1} \equiv \Phi_{e,J1} - \phi_{L0},\ \tilde{\Phi}_{e,J2} &\equiv \Phi_{e,J2} + \phi_{R0},
\end{aligned} \tag{6.35}$$

$$\begin{aligned}
\Phi_{e,o} &= (\Phi_{e,J1} - \phi_{L0}) + (\Phi_{e,J2} + \phi_{R0}) + \Phi_{e,\text{bot}}\\
&\quad + 2\Phi_{e,L} + \phi_{L0} - \phi_{R0}\\
&= \tilde{\Phi}_{e,J1} + \tilde{\Phi}_{e,J2} + \Phi_{e,\text{bot}} + \frac{E'_L(2\Phi_{e,L} + 2\Phi'_{e,L})}{E_L + E'_L},\\
\rightarrow &\tilde{\Phi}_{e,J1} + \tilde{\Phi}_{e,J2} + \Phi_{e,\text{bot}} = \Phi_{e,o} - \frac{E'_L}{E_L + E'_L}\Sigma\Phi_e.
\end{aligned} \tag{6.36}$$

The last line in eq. (6.36) indicates that the solutions found for the single-sided SQUID coupler can be used as follows:

$$
\begin{aligned}
\Phi_{e,1} \equiv &\Phi_{e,i}, \quad \Phi_{e,2} \equiv \Phi_{e,o} - \frac{E'_L}{E_L + E'_L}\Sigma\Phi_e, \\
\Phi_{e,12} &= \frac{C_1 C_2}{2C^2}\left((d_C+1)\Phi_{e,i} + 2\Phi_{e,2}\right), \\
\tilde{\Phi}_{e,J1} &= \frac{C_2 C_C}{2C^2}\left((d_C+1)\Phi_{e,1} + 2\Phi_{e,2}\right), \\
\tilde{\Phi}_{e,J2} &= \frac{C_1 C_C}{2C^2}\left((d_C+1)\Phi_{e,1} + 2\Phi_{e,2}\right), \\
\Phi_{e,\text{top}} &= \Phi_{e,\text{bot}} + \Phi_{e,1}, \\
\Phi_{e,\text{bot}} &= \left(\frac{C_1 C_2}{C^2} - 1\right)\frac{(d_C+1)}{2}\Phi_{e,1} + \frac{C_1 C_2}{C^2}\Phi_{e,2}.
\end{aligned} \tag{6.37}
$$

$\Phi_{e,2}$ converges to $\Phi_{e,o}$ as the ratio of the outer loop inductances approaches 0 $L/L' \to 0$ ($E'_L/E_L \to 0$), consistent with the single-sided SQUID coupler. A special case emerges at the symmetric inductances $L = L' \to \Phi_{e,2} = (\Delta\Phi_{e,o} - \Phi_{e,i})/2$, at which the circuit is sensitive only to the differential of the outer external fluxes $\Delta\Phi_{e,o} \equiv \Phi_{e,o} - \Phi'_{e.o}$, thus called a "gradiometric SQUID coupler", and the inner external flux.

Finally, the operating condition $\Phi_{e,1} + 2\Phi_{e,2} = 0$ can be re-expressed as follows, for the general case and the gradiometric case:

$$
\begin{aligned}
(1 - \frac{E'_L}{E_L})\Phi_{e,i} + 2(\Phi_{e,o} - \frac{E'_L}{E_L}\Phi'_{e,o}) &= 0, \\
\xrightarrow{L=L'} \Delta\Phi_{e,o} &= 0.
\end{aligned} \tag{6.38}
$$

6.9.2 Perturbation theory

Normal-ordered expansion of cosinuosidal operators

To expand the cosinusoidal terms with phase variables $\hat{\varphi}_i$ using annihilation ($\hat{a}_i$) and creation ($\hat{a}_i^\dagger$) operators, the terms can be rewritten with displacement operators $\mathcal{D}_i(\alpha) \equiv e^{\alpha\hat{a}_i^\dagger - \alpha^*\hat{a}_i}$ with the corresponding amplitudes $\alpha = \pm i\varphi_i^{zpf}$ as follows:

$$
\begin{aligned}
\cos\hat{\varphi}_i &= \cos\left(\varphi_i^{zpf}(\hat{a}_i + \hat{a}_i^\dagger)\right) \\
&= \frac{1}{2}\left(e^{i\varphi_i^{zpf}(\hat{a}_i+\hat{a}_i^\dagger)} + e^{-i\varphi_i^{zpf}(\hat{a}_i+\hat{a}_i^\dagger)}\right) \\
&= \frac{1}{2}\left(\mathcal{D}(i\varphi_i^{zpf}) + \mathcal{D}(-i\varphi_i^{zpf})\right),
\end{aligned} \tag{6.39}
$$

$$\begin{aligned}\sin\hat{\varphi}_i &= \sin\left(\varphi_i^{zpf}(\hat{a}_i+\hat{a}_i^\dagger)\right)\\ &= \frac{1}{2i}\left(e^{i\varphi_i^{zpf}(\hat{a}_i+\hat{a}_i^\dagger)} - e^{-i\varphi_i^{zpf}(\hat{a}_i+\hat{a}_i^\dagger)}\right)\\ &= \frac{1}{2i}\left(\mathcal{D}_i(i\varphi_i^{zpf}) - \mathcal{D}_i(-i\varphi_i^{zpf})\right).\end{aligned} \tag{6.40}$$

Using the normal-ordered representation obtained from the Baker-Campbell-Hausdorff formula $\mathcal{D}_i(\alpha) = e^{-\frac{|\alpha|^2}{2}} e^{\alpha\hat{a}_i^\dagger} e^{-\alpha^*\hat{a}_i}$ [312], we obtain the following normal-ordered expansions:

$$\begin{aligned}&\cos\hat{\varphi}_i\\ &= \frac{e^{-\frac{(\varphi_i^{zpf})^2}{2}}}{2}\left(e^{i\varphi_i^{zpf}\hat{a}_i^\dagger}e^{i\varphi_i^{zpf}\hat{a}_i} + e^{-i\varphi_i^{zpf}\hat{a}_i^\dagger}e^{-i\varphi_i^{zpf}\hat{a}_i}\right)\\ &= e^{-\frac{(\varphi_i^{zpf})^2}{2}}\sum_n\sum_{k=0}^{2n}\frac{(-1)^n(\varphi_i^{zpf})^{2n}}{k!(2n-k)!}(\hat{a}_i^\dagger)^k(\hat{a}_i)^{2n-k},\end{aligned} \tag{6.41}$$

$$\begin{aligned}&\sin\hat{\varphi}_i\\ &= \frac{e^{-\frac{(\varphi_i^{zpf})^2}{2}}}{2i}\left(e^{i\varphi_i^{zpf}\hat{a}_i^\dagger}e^{i\varphi_i^{zpf}\hat{a}_i} - e^{-i\varphi_i^{zpf}\hat{a}_i^\dagger}e^{-i\varphi_i^{zpf}\hat{a}_i}\right)\\ &= e^{-\frac{(\varphi_i^{zpf})^2}{2}}\sum_n\sum_{k=0}^{2n+1}\frac{(-1)^n(\varphi_i^{zpf})^{2n+1}}{k!(2n+1-k)!}(\hat{a}_i^\dagger)^k(\hat{a}_i)^{2n+1-k},\end{aligned} \tag{6.42}$$

which are used for calculating matrix elements and perturbative analyses provided in the main text.

Estimating zero-point fluctuations

Expanding the cosine potential in the bare transmon Hamiltonians $\hat{H}_i$ produces the following expression up to the second order:

$$\begin{aligned}\hat{H}_i \approx &\left(8E_{C,i}(n_i^{zpf})^2 - E_{J,i}e^{-\frac{(\varphi_i^{zpf})^2}{2}}(\varphi_i^{zpf})^2\right)\hat{a}_i^\dagger\hat{a}_i\\ &+\left(-4E_{C,i}(n_i^{zpf})^2 + \frac{1}{2}E_{J,i}e^{-\frac{(\varphi_i^{zpf})^2}{2}}(\varphi_i^{zpf})^2\right)(\hat{a}_i^2+(\hat{a}_i^\dagger)^2).\end{aligned} \tag{6.43}$$

The condition to eliminate the $\hat{a}_i^2 + (\hat{a}_i^\dagger)^2$ term and the normalization condition $n_i^{zpf}\varphi_i^{zpf} = 1/2$ yield the following equation that enables calculating φ_i^{zpf} numeri-

cally:

$$(\varphi_i^{zpf})^4 e^{-\frac{(\varphi_i^{zpf})^2}{2}} = \frac{2E_{C,i}}{E_{J,i}}. \tag{6.44}$$

ZZ interaction rate

ZZ interaction rate obtained from perturbation theory ζ_{pert} is calculated up to the second-order and single excitation number differences that are considered to provide the leading contributions to the ZZ interaction rate, with the following breakdown:

$$\zeta_{\text{pert}} \approx \zeta^{(1)} + \zeta_c^{(2)} + \zeta_{\text{odd}}^{(2)}, \tag{6.45}$$

where the even-parity interaction is responsible for the first-order contribution $\zeta^{(1)}$ and the second-order contribution $\zeta_c^{(2)}$ due to excitation-number-conserving transitions up to a single-excitation hopping, and the odd-parity interaction due to junction asymmetry accounts for the second-order contribution $\zeta_{\text{odd}}^{(2)}$ due to single-excitation-number differences.

The $\zeta_{\text{odd}}^{(2)}$ is calculated as follows:

$$\begin{aligned}
g_{ijkl} &\equiv \langle ij|\,\hat{H}_{\text{int}}|kl\rangle, \quad \omega_{ij} \equiv \langle ij|\,\hat{H}_0\,|ij\rangle\,, \\
E_{J,C}^{\sin} &\equiv \Delta E_{J,C} e^{-\frac{(\varphi_1^{zpf})^2+(\varphi_2^{zpf})^2}{2}} \sin\left(\frac{\varphi_{e,1}}{2}\right), \\
g_{0100} &= E_{J,C}^{\sin}\varphi_2^{zpf}, \quad g_{1000} = -E_{J,C}^{\sin}\varphi_1^{zpf}, \\
g_{0201} &= \sqrt{2}E_{J,C}^{\sin}\left(\varphi_2^{zpf} - \frac{1}{2}(\varphi_2^{zpf})^3\right), \\
g_{2010} &= -\sqrt{2}E_{J,C}^{\sin}\left(\varphi_1^{zpf} - \frac{1}{2}(\varphi_1^{zpf})^3\right), \\
g_{1110} &= E_{J,C}^{\sin}\varphi_2^{zpf}\left(1 - (\varphi_1^{zpf})^2\right), \\
g_{1101} &= -E_{J,C}^{\sin}\varphi_1^{zpf}\left(1 - (\varphi_2^{zpf})^2\right),
\end{aligned}$$

$$
\begin{aligned}
g_{1211} &= \sqrt{2}E_{J,C}^{\sin}\left(1-(\varphi_1^{zpf})^2\right)\left(\varphi_2^{zpf}-\frac{1}{2}(\varphi_2^{zpf})^3\right),\\
g_{2111} &= -\sqrt{2}E_{J,C}^{\sin}\left(1-(\varphi_2^{zpf})^2\right)\left(\varphi_1^{zpf}-\frac{1}{2}(\varphi_1^{zpf})^3\right),\\
g_{2001} &= E_{J,C}^{\sin}\varphi_2^{zpf}\left(-\frac{\sqrt{2}}{2}(\varphi_1^{zpf})^2\right),\\
g_{0210} &= -E_{J,C}^{\sin}\varphi_1^{zpf}\left(-\frac{\sqrt{2}}{2}(\varphi_2^{zpf})^2\right),\\
g_{3011} &= E_{J,C}^{\sin}\varphi_2^{zpf}\left(-\frac{\sqrt{6}}{2}(\varphi_1^{zpf})^2+\frac{\sqrt{6}}{6}(\varphi_1^{zpf})^4\right),\\
g_{0311} &= -E_{J,C}^{\sin}\varphi_1^{zpf}\left(-\frac{\sqrt{6}}{2}(\varphi_2^{zpf})^2+\frac{\sqrt{6}}{6}(\varphi_2^{zpf})^4\right),
\end{aligned}
\tag{6.46}
$$

$$
\begin{aligned}
\zeta_{\text{odd}}^{(2)} &= \sum_{ij}(-1)^{i+j}E_{ij,\text{odd}}^{(2)}\\
&= \frac{g_{3011}^2}{\omega_{11}-\omega_{30}}+\frac{g_{0311}^2}{\omega_{11}-\omega_{03}}-\frac{g_{0210}^2}{\omega_{10}-\omega_{02}}-\frac{g_{2001}^2}{\omega_{01}-\omega_{20}}\\
&+\frac{g_{2111}^2}{\omega_{11}-\omega_{21}}+\frac{g_{1211}^2}{\omega_{11}-\omega_{12}}+\frac{2g_{1110}^2}{\omega_{11}-\omega_{10}}+\frac{2g_{1101}^2}{\omega_{11}-\omega_{01}}\\
&-\frac{g_{2010}^2}{\omega_{10}-\omega_{20}}-\frac{g_{0201}^2}{\omega_{01}-\omega_{02}}-\frac{2g_{1000}^2}{\omega_{10}-\omega_{00}}-\frac{2g_{0100}^2}{\omega_{01}-\omega_{00}}\\
&\approx -(E_{J,C}^{\sin}\varphi_1^{zpf}\varphi_2^{zpf})^2\times\left(\frac{(\varphi_1^{zpf})^2}{2\omega_1-\omega_2}+\frac{(\varphi_2^{zpf})^2}{2\omega_2-\omega_1}\right.\\
&\left.+\frac{4(\varphi_1^{zpf})^2}{\omega_1}+\frac{4(\varphi_2^{zpf})^2}{\omega_2}+\frac{4\eta_1}{\omega_1^2}+\frac{4\eta_2}{\omega_2^2}\right)\\
&\sim O\left(\frac{\Delta E_{J,C}^2(\varphi^{zpf})^6}{m\omega_1+n\omega_2}\right)+O\left(\frac{\Delta E_{J,C}^2(\varphi^{zpf})^4\eta}{\omega^2}\right),
\end{aligned}
\tag{6.47}
$$

where ω_1 and ω_2 are the bare 0-1 transition frequencies of the two qubits, $(m,n)\in\{(1,0),(0,1),(2,-1),(-1,2)\}$, and the approximations $(\varphi^{zpf})^2\ll 1$ and $|\eta_1|,|\eta_2|\ll m\omega_1+n\omega_2$ are used.

6.9.3 Simulation methods

Numerical simulation tools

`Python` packages `scQubits` [280] and `QuTiP` [243] are used for numerical circuit quantization, diagonalization, and time-domain simulation.

Computational subspace

ZZ turn-off point Φ_{off} is found by sweeping $\Phi_{e,1}$ under the constraint $\Phi_{e,2} = -\Phi_{e,1}/2$. At this point, we perform numerical diagonalization to identify computational eigenstates. The mapping between the dressed eigenstates and the bare eigenstates is found by the hierarchical diagonalization procedure [313, 314].

Gate fidelity

The coherent error $(1 - F_G)$ of the CZ gates is estimated using the standard average gate fidelity [244]:

$$F_G(\hat{U}) = \frac{\text{Tr}(\hat{U}_{proj}^{\dagger}\hat{U}_{proj}) + |\text{Tr}(\hat{U}_{CZ}^{\dagger}\hat{U}_{proj})|^2}{20}, \tag{6.48}$$

where $\hat{U}_{proj} \equiv \hat{P}\hat{U}\hat{P}^{\dagger}$ is the simulated unitary propagator projected onto the computational subspace with the projector $\hat{P}$, and $\hat{U}_{CZ}$ is the ideal unitary for a CZ gate, represented with computational eigenstates.

For gate infidelities $(1 - F)$ including incoherent processes, we use the standard gate fidelity involving Kraus operators [244]:

$$F(\hat{U}) = \frac{\text{Tr}(\sum_k \hat{M}_k^{\dagger}\hat{M}_k) + \sum_k |\text{Tr}(\hat{M}_k)|^2}{20}, \tag{6.49}$$

where $\hat{M}_k \equiv \hat{P}U_{CZ}\hat{G}_k\hat{P}^{\dagger}$, and $\hat{G}_k$s are the Kraus operators.

By solving the following optimization problem, we report the coherent error and gate infidelity after eliminating the effect of local phases that can be canceled out by virtual-Z operations [315]:

$$\min_{\phi_1,\phi_2} \left(1 - F_G(\hat{U}e^{-i\phi_1\hat{Z}_1}e^{-i\phi_2\hat{Z}_2})\right), \tag{6.50}$$

$$\min_{\phi_1,\phi_2} \left(1 - F(\hat{U}e^{-i\phi_1\hat{Z}_1}e^{-i\phi_2\hat{Z}_2})\right), \tag{6.51}$$

where $\hat{Z}_1$ and $\hat{Z}_2$ are Pauli-Z operators of the qubits.

Hilbert space truncation

In order to run time-domain simulations within a feasible computation time, the Hilbert space is truncated to include up to the 40 lowest energy eigenstates. To examine the effect of Hilbert space truncation, we sweep the Hilbert space dimension $dim(\mathcal{H})$ and estimate the coherent error of the 22 ns-long CZ gate shown in the

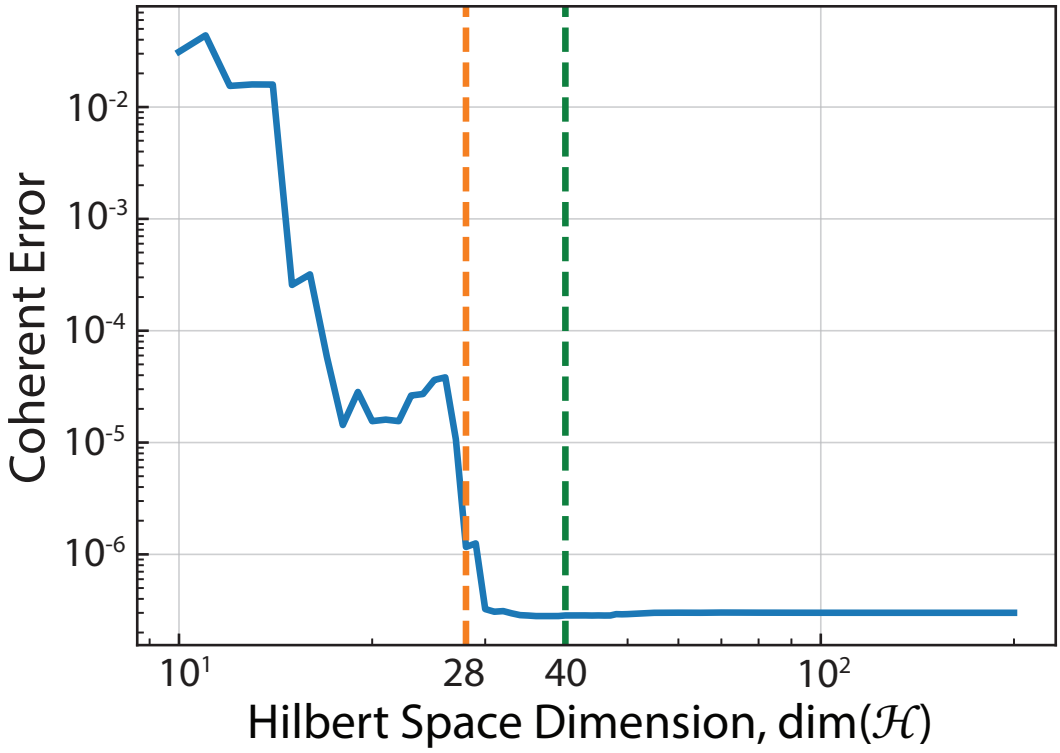

Figure 6.S2: **Effect of Hilbert space truncation.** Coherent error of the simulated 22 ns-long CZ gate as a function of Hilbert space dimension $dim(\mathcal{H})$ (blue solid line). $dim(\mathcal{H}) = 40$ (green dashed line) is used for the time-domain simulations reported in the main text, and $dim(\mathcal{H}) = 28$ (orange dashed line) is used for CZ gate simulation with relaxation process.

main text, as shown in Fig. 6.S2. For $dim(\mathcal{H}) \geq 40$, the change in the coherent error is less than 2×10^{-8}, which is sufficiently small to estimate the coherent errors of 3×10^{-7} reported in the main text. For incoherent simulations in Appendix 6.9.4, we use $dim(\mathcal{H}) = 28$ to reduce computation time, while maintaining the numerical errors from Hilbert space truncation below 10^{-6}.

6.9.4 Gate fidelity in the presence of relaxation error

By simulating the Lindblad master equation, the performance of the CZ gate is examined in the presence of Markovian relaxation, as shown in Fig. 6.S3. We model the relaxation process by adding bare transmon's annihilation operators as jump operators $\sqrt{1/T_1}\hat{a}_i$, where T_1 is the bare relaxation time of the transmons. We use the same T_1s for both qubits. To construct the bare annihilation operators, we use the hierarchically diagonalization procedure [313, 314].

The gate infidelity is fitted to a linear model shown in eq. (6.52):

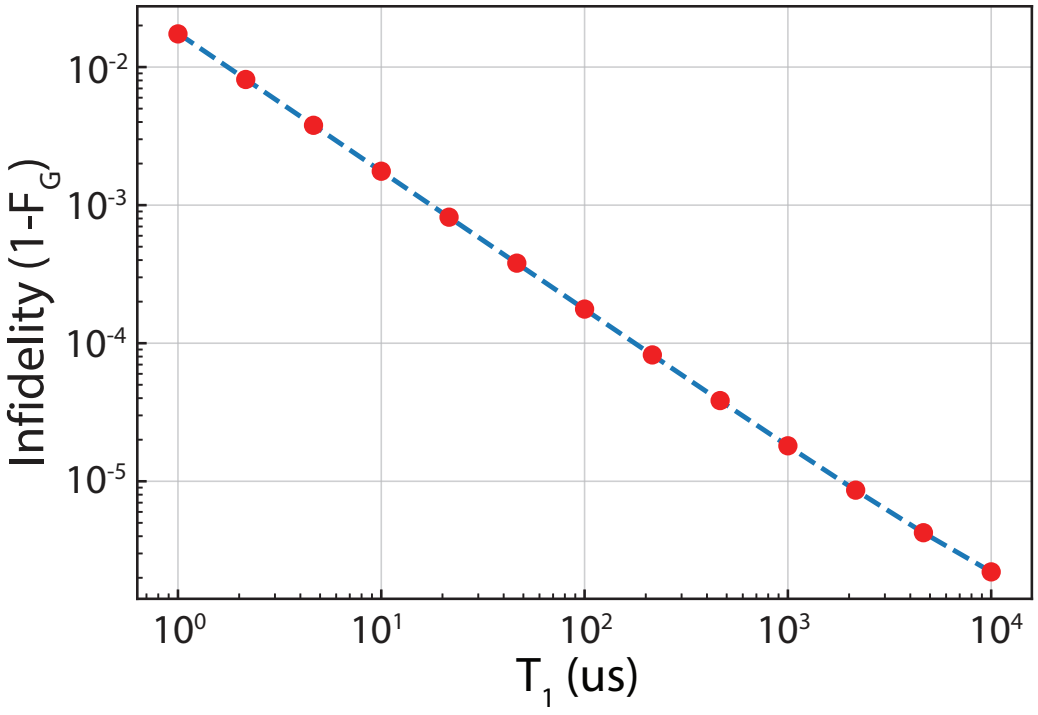

Figure 6.S3: **Gate fidelity in the presence of Markovian relaxation.** Infidelity of the simulated 22 ns-long CZ gate as a function of relaxation time (T_1) of the two transmons (red dots). Blue dashed line is a fit to eq. (6.52).

$$1 - F \approx a\frac{T_G}{T_1} + b, \tag{6.52}$$

recovering $a = 0.799$ and $b = 4.5 \times 10^{-7}$, which is consistent with the prediction $a = 0.8$ based on the analysis in Ref. [244].

6.9.5 SQUID couplers with various circuit parameters

Circuit parameters available for idle operation and robustness against capacitance targeting

The existence of at least one idle operating point Φ_{off} at which the ZZ interaction rate is turned off $\zeta(\Phi_{\text{off}}) = 0$ is crucial. This condition can be found approximately by investigating the following expression obtained from the second-order perturbation theory:

$$\zeta_{\text{pert}}(\varphi_{e,1}) = -\Sigma E'_{J,C} \cos\left(\frac{\varphi_{e,1}}{2}\right)(\varphi_1^{zpf})^2(\varphi_2^{zpf})^2 + \frac{4g_{\text{eff}}^2\eta}{\Delta^2 - \eta^2}, \tag{6.53}$$

$$g_{\text{eff}} = -\Sigma E'_{J,C} \cos\left(\frac{\varphi_{e,1}}{2}\right)\varphi_1^{zpf}\varphi_2^{zpf} + g n_1^{zpf} n_2^{zpf}. \tag{6.54}$$

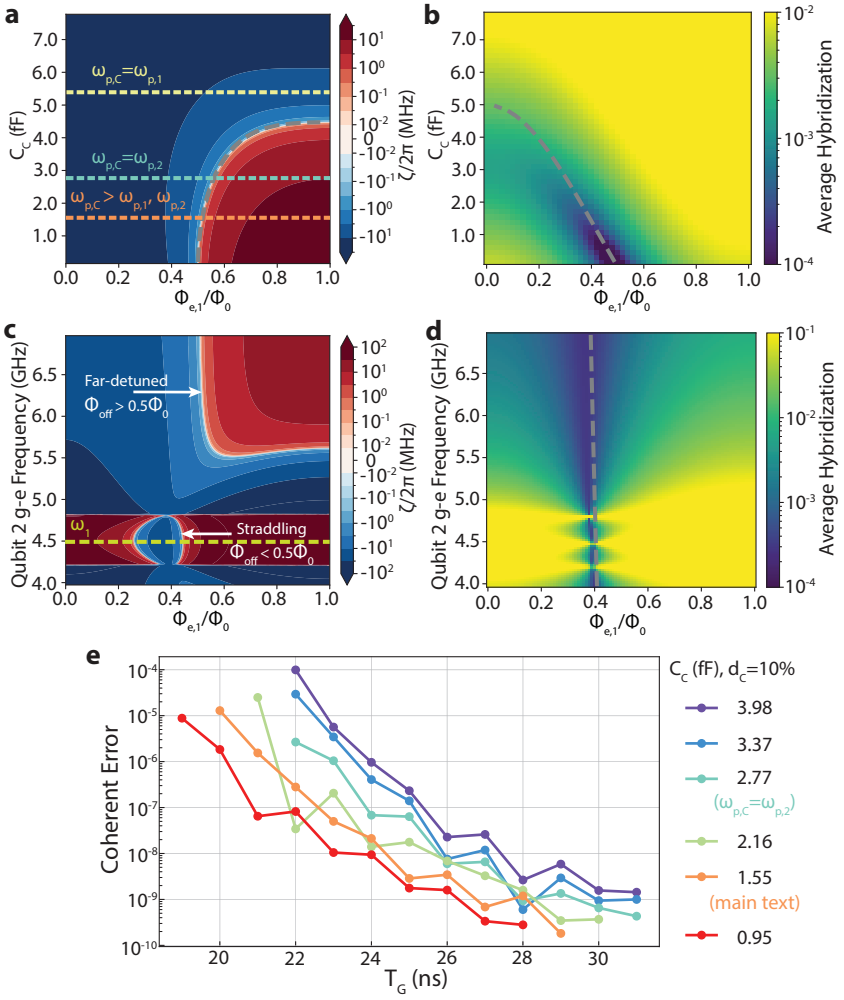

Figure 6.S4: **ZZ interaction rates and hybridization.** **a**, ZZ interaction rate obtained from circuit quantization, as a function of total SQUID coupler capacitance C_C and external flux $\Phi_{e,1}$, while other parameters are the same as the Table. 1 in the main text. Yellow (light blue) dashed line line corresponds to the case where the coupler junctions have the same plasma frequency as transmon 1 (transmon 2). Orange dashed line indicates the capacitance used in the analysis presented in the main text. Gray dashed curve shows the Φ_{off} predicted from perturbative analysis. **b**, Average hybridization $\sum_{mn}(1 - P_{|ij\rangle})/4$ as a function of C_C and $\Phi_{e,1}$. **c**, ZZ interaction rate as a function of qubit 2 frequency ω_2 and $\Phi_{e,1}$, with other parameters are the same as the Table. 1 in the main text. ω_2 is varied by changing $E_{J,2}$. Yellow dashed line represents qubit 1 frequency ω_1. **d**, Average hybridization as a function of ω_2 and $\Phi_{e,1}$. In **b** and **d**, Gray dashed lines indicate the biases $\Phi_{e,1}$ where the effective linear coupling is canceled $g_{\text{eff}}(\Phi_{e,1}) = 0$, predicted from the perturbation theory. **e**, Coherent errors of the simulated CZ gates as functions of gate duration T_G, for different C_C.

When the two qubits are far-detuned, $|\Delta| \gg |\eta|$, the sign of the second term in ζ_{pert} is negative, as transmon anharmonicities are negative. Thus, the ZZ interaction rate can be turned off only at $\varphi_{e,1} > \pi$ at which the first term becomes positive. As $\zeta_{\text{pert}}(0) > 0$ is always satisfied, the following condition guarantees the existence of an idling external flux due to the intermediate value theorem:

$$0 \leq \zeta_{\text{pert}}(2\pi) = \Sigma E'_{J,C}(\varphi_1^{zpf})^2(\varphi_2^{zpf})^2 + \frac{4(\Sigma E'_{J,C}\varphi_1^{zpf}\varphi_2^{zpf} + g n_1^{zpf} n_2^{zpf})^2 \eta}{\Delta^2 - \eta^2}. \tag{6.55}$$

As the first term is always positive, the second term originating from the hybridization, which is negative, should be suppressed. This is achieved by reducing the charge coupling rate g and increasing the absolute value of qubit-qubit detuning $|\Delta|$.

In contrast, when the two transmons are in the straddling regime $\omega_{02}, \omega_{20} < \omega_{11}$ or $|\Delta| < |\eta|$, the second term in eq. (6.54) becomes positive and the idle operating point would be located at $\varphi_{e,1} < \pi$, if it exists.

Fig. 6.S4a shows the ZZ interaction rates as functions of external flux calculated using circuit quantization and numerical diagonalization, as C_C is swept. We find that at sufficiently small C_Cs, the idle operating point exists. Comparison of the plasma frequency $\omega_{p,C}$ of the coupler junctions to the plasma frequencies of the qubit junctions' $\omega_{p,1}$ and $\omega_{p,2}$ shows that an idle operating point can exist without requiring extreme oxidation conditions to lower $\omega_{p,C}$ further. The existence of an idle operating point at $\omega_{p,C} = \omega_{p,2}$ and its robustness against C_C implies that the same junction oxidation condition used in one of the qubits can be used for junctions in SQUID couplers. The average hybridization can be suppressed to or below 1% for a similar range of C_Cs that provides an idle bias point, as found in Fig. 6.S4b. In addition, such junction processes with thick oxide barriers ease junction area targeting due to their smaller tunneling energy per area.

Fig. 6.S4c shows the ZZ interaction rates as the qubit 2's g-e transition frequency is swept, by varying $E_{J,2}$. Qubit 1's g-e frequency is approximately at 4.49 GHz. As expected, $\Phi_{\text{off}} > 0.5\Phi_0$ ($\varphi_{e,1} > \pi$) exists for sufficiently large detuning, and $\Phi_{\text{off}} < 0.5\Phi_0$ ($\varphi_{e,1} < \pi$) in the straddling regime.

To examine the tolerance of SQUID coupler operation against circuit parameter targeting inaccuracy and to explore available junction plasma frequencies for the

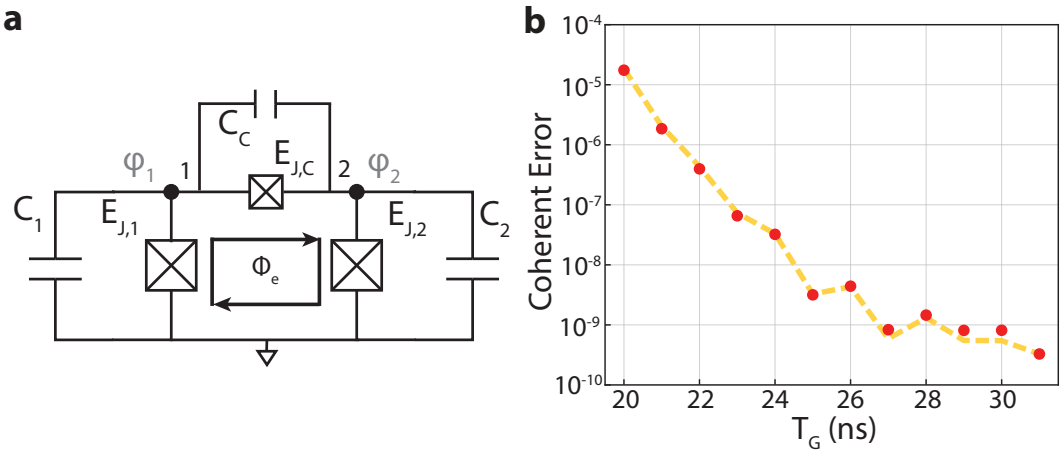

Figure 6.S5: **CZ gate with junction coupler.** **a**, Circuit diagram of the junction coupler. **b**, Coherent error of the CZ gate as a function of gate duration T_G, implemented by the junction coupler. Dashed yellow line represents the contribution from the non-adiabatic state transitions.

junctions in the SQUID coupler, we estimate the coherent errors of the CZ gates for different C_C for the 10 shortest gate durations, as shown in Fig. 6.S4e. We assume an asymmetry $d_C = \Delta E_{J,C}/\Sigma E_{J,C} = (C_{C,1} - C_{C,2})/C_C = 10$ % for the two junctions in the SQUID couplers, in which we correlate the asymmetry in the junction energies and the capacitance. We find that all C_Cs in the wide range of [0.95, 3.98] fF provide fast and high-fidelity CZ gates with small adiabaticity overheads, showing the robustness of the gate scheme against coupler capacitance targeting. Note that the difference in the minimum CZ gate time is due to the change in the hybridization-induced ZZ interaction rate $\zeta^{(2)}$ originating from charge coupling.

Junction coupler

The limit in which the asymmetry is 100 percent or -100 percent corresponds to the case in which one of the junctions in the SQUID coupler is eliminated, as shown in Fig. 6.S5a. The interaction Hamiltonian is thus provided as follows:

$$\begin{aligned}\hat{H}_{\text{int}} &\approx -E_{J,C}\cos\left(\hat{\varphi}_2 - \hat{\varphi}_1 + \varphi_e\right) + g\hat{n}_1\hat{n}_2 \\ &= -E_{J,C}\cos\left(\varphi_e\right)(\hat{\varphi}_2 - \hat{\varphi}_1) \\ &+ E_{J,C}\sin\left(\varphi_e\right)(\hat{\varphi}_2 - \hat{\varphi}_1) + g\hat{n}_1\hat{n}_2, \end{aligned} \tag{6.56}$$

where $\varphi_e \equiv 2\pi\Phi_e/\Phi_0$. The SQUID coupler interaction Hamiltonian is mapped to the junction coupler interaction Hamiltonian under $\Sigma E_{J,C}, \Delta E_{J,C} \rightarrow E_{J,C}$ and

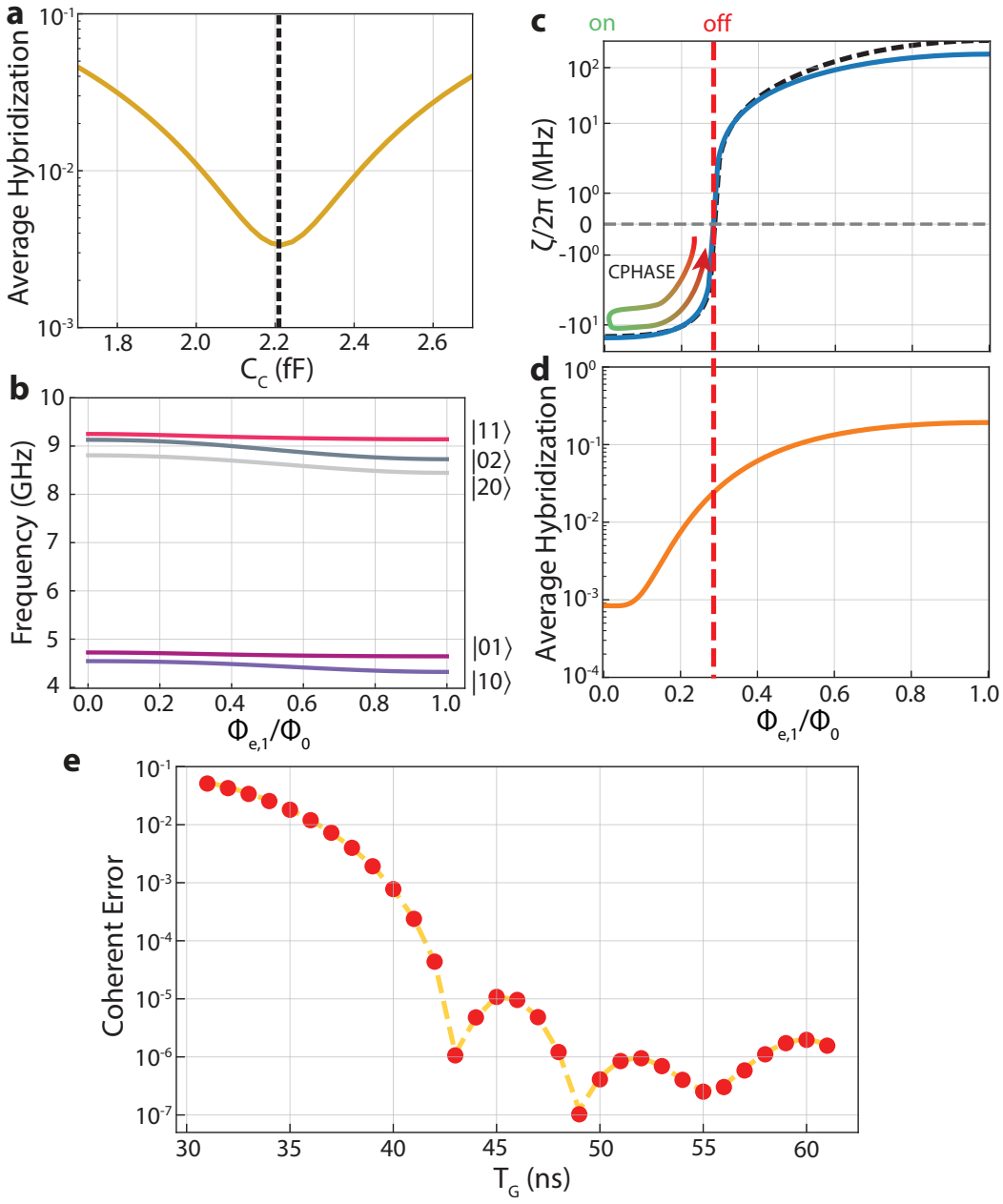

Figure 6.S6: **Two transmons in straddling regime coupled via a SQUID coupler.** **a**, Average hybridization as a function of total coupler junction capacitance C_C, at $\Phi_{e,1} = 0$. Dashed black line denotes the C_C that provides the minimum hybridization. **b**, Eigenfrequencies of the five lowest eigenstates as functions of external flux $\Phi_{e,1}$. **c, d** ZZ interaction rate and average hybridization as functions of $\Phi_{e,1}$. Dashed red line represents the ZZ interaction turn-off point Φ_{off}. **e**, Coherent error of the CZ gate implemented with the straddling regime parameter.

$\Phi_{e,1} + \Phi_{e,2} \rightarrow \Phi_e$. Defining $\Phi_{e,1} \equiv -2\Phi_e$, we can compare the junction coupler with the SQUID coupler in a consistent way.

The junction coupler is an extreme example that shows the robustness of the SQUID coupler against the junction asymmetry. The junction coupler still yields an idle external flux and allows the implementation of a high-fidelity adiabatic CZ gate as efficient as the symmetric SQUID coupler, whose coherent error is presented in Fig. 6.S5b. However, they induce longitudinal interactions that act as the crosstalk channel when chained with more couplers and qubits, as discussed in the main text.

CZ gate in straddling regime

The SQUID coupler can be used for implementing a CZ gate between two transmons in a stradling regime. In this example, the transmon 2 frequency ω_2 is brought close to ω_1 to satisfy the straddling condition $\omega_{|20\rangle}, \omega_{|02\rangle} < \omega_{|11\rangle}$, as shown in Fig. 6.S6b. In this parameter regime, it is crucial to suppress linear coupling, due to their relatively large contribution to the ZZ interaction rate. We choose C_C that minimizes the average hybridization at $\Phi_e = 0$, as found in Fig. 6.S6a.

As discussed earlier, the idle external flux Φ_{off} is less than $0.5\Phi_0$ in the straddling regime, as shown in Fig. 6.S6c. Similarly to the pair of transmons that are far-detuned, a CZ gate can be implemented by dynamically tuning the external flux. We find that a 43 ns-long CZ gate with coherent error of 10^{-6} can be implemented as illustrated in Fig. 6.S6e, showing the utility of the SQUID coupler in the straddling regime.

6.9.6 Calculation of losses from interfacial dielectric layers

As the SQUID coupler does not require capacitive coupling from the planar capacitance, the capacitance to ground from the lead for galvanic connection can be suppressed. This allows us to use narrower metalizations and gaps to the ground while keeping the losses from contaminated interfacial dielectric layers small. The interfacial loss due to the geometry presented in Fig. 6.S7a is modeled by approximating the leads to coplanar waveguides (CPWs) of a uniform geometry, with the lead width W and the gap to ground G being the CPW parameters.

The capacitance of a single mergemon to ground can be broken down into junction capacitance C_J and lead capacitance C_{Lead}, as illustrated in the circuit diagram provided in Fig. 6.S7b. Thus, the contribution of the leads to the quality factor Q_{Lead} can be modeled as the following:

$$\frac{1}{Q_{Lead}} = \frac{U_{Lead}}{U_{tot}} \sum_{i\in\{MS,SA,MA\}} \frac{U_i}{U_{Lead}} \tan\delta_i$$
$$\approx \frac{C_{Lead}}{C_\Sigma} \sum_{i\in\{MS,SA,MA\}} p_{i,CPW} \tan(\delta_i), \tag{6.57}$$

where U_{Lead} and U_{tot} are the energy stored in leads and the total energy, respectively, and U_i is the energy stored in the interfacial layer i, $p_{i,CPW}$ is the surface participation for interfacial layer i calculated by approximating the lead geometry as a CPW assuming that the entire energy is stored in the leads (i.e., the denominator is U_{Lead}), $\tan\delta_i$ is the corresponding loss tangent, and $C_\Sigma = C_J + C_{Lead}$ is the total capacitance of the mergemon. We consider the three interfacial layers: metal-to-substrate (MS), substrate-to-air (SA), and metal-to-air (MA).

We provide the analytically calculated C_{Lead} in Fig. 6.S7b and c as a function of two parameters: the lattice constant (a) and the lead width W, following the formula provided in Ref. [317], for silicon substrate with $\epsilon_{si} = 11.47$ and gap to ground $G = 8$ um. In this model, C_{Lead} is directly proportional to the total length of the leads, which we assume to be 2.5×lattice constant, considering the four connections to the nearest-neighbor qubits and the connection to the readout resonator, as illustrated in Fig. 6.S7a. To reduce C_{Lead}, we consider the trenching of the substrate and assume a filling factor of 10%. The following analysis assumes a lattice constant of 100 um.

Surface participation as a function of lead width is calculated by approximating the lead geometry as a CPW and using the analytical model provided in Refs. [316], as shown in Fig. 6.S7. We assume a uniform thickness of 2 nm for the contaminated dielectric for all interfacial layers. MS, SA, and MA relative permittivities of 11.4, 10, and 4, respectively, are used to consistently cite the loss tangents provided in Ref. [318]. To account for the effect of substrate trenching that reduces MS and SA participations and increases MA participation [239, 319], the MS, SA, and MA participations are multiplied by 1/4, 1/3, and 4, respectively.

Finally, the contributions to the quality factor are calculated using eq. (6.57), assuming C_Σ of 80 fF, shown in Fig. 6.S7. The MS and SA loss tangents are obtained from [318]. Considering using Tantalum films for the leads, which are known to provide one of the cleanest MA surfaces [240, 320–323], we use the MA loss tangent provided in Ref. [321] with consistent scaling considering the interfacial layer thickness and the relative permittivity as suggested by Ref. [239]. As expected, the

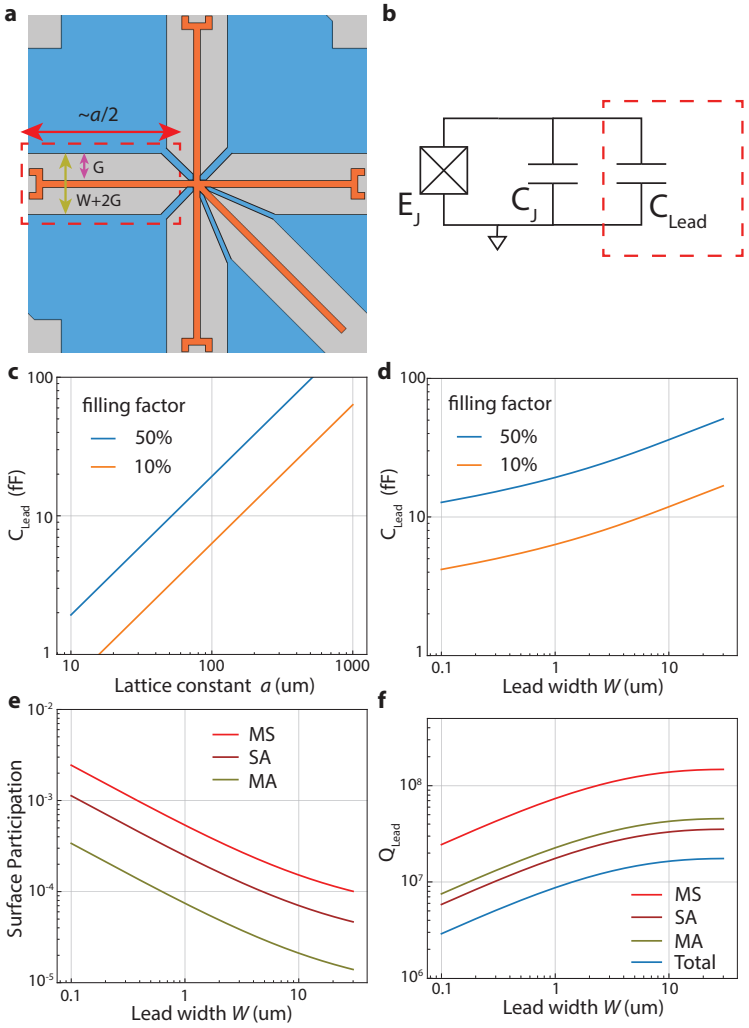

Figure 6.S7: **Calculation of the losses from the interfacial dielectric layers. a**, A single mergemon modeled as a cross-shaped metalization (orange), where the mergemon junction is located at the center and the other parts of the metalization is considered "leads". Ground metalization (blue) is connected to the low voltage side metalization of the mergemon at the center (hidden). **b**, Circuit schematic of the mergemon. C_J denotes the contribution from the junction, and C_{Lead} indicates the contribution from the leads. **c**, Analytically calculated C_{Lead} as a function of the lattice constant. A gap to ground G of 8 um and a lead width W of 1 um are used. **d**, Analytically calculated C_{Lead} as a function of the lead width. A gap to ground G of 8 um and a lattice constant of 100 um are used. **e**, Analytically calculated surface participation as a function of the lead width using the formula provided in Ref. [316]. Trenching factors of 1/4, 1/3, and 4 are multiplied to MS, SA, and MA interfaces, respectively. **f**, Analytically calculated Q_{Lead} and the contributions to Q_{Lead} from each interfacial layers as functions of the lead width.

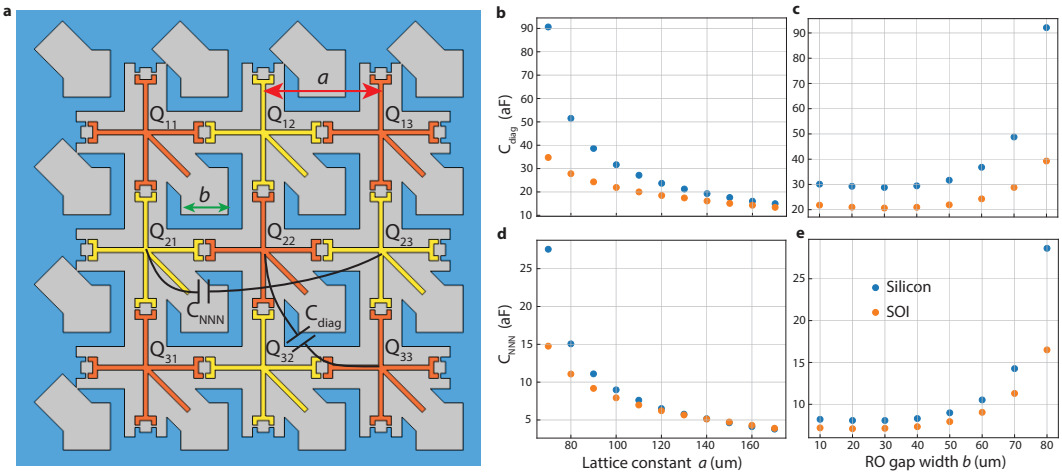

Figure 6.S8: **Parasitic capacitance estimation.** **a**, Geometry for electrostatics simulation. Lattice constant (a), RO gap width (b), parasitic capacitances C_{diag} and C_{NNN} are denoted. **b, d**, C_{diag} and C_{NNN} as functions of lattice constant, for RO gap width = 50 um. **c, e**, C_{diag} and C_{NNN} as functions of RO gap width, for lattice constant = 100 um. Simulations are conducted with two different substrate material settings: silicon and SOI.

quality factor improves as the lead widens due to the decrease in surface participation, which stagnates at $G \ll W$ as the increase in C_{Lead} catches up. For a lead width of 1 um, we find $Q_{Lead} \approx 8.7 \times 10^6$, whose contribution to the relaxation time is $T_1^{Lead} = 1/(\omega Q_{Lead}) \approx 309$ us for a $\omega/2\pi = 4.5$ GHz qubit.

6.9.7 Parasitic capacitance

The parasitic capacitances in the proposed tiling scheme is estimated by finite-element method (FEM), using the COMSOL electrostatic simulation module. We model the metalizations in the mergemon processor as shown in Fig. 6.S8a. Each colored cross (orange, yellow) with a label Q_{ij} represents the high voltage side metalization of the mergemon at (i, j) location, including the elongated leads for galvanic connection to the SQUID couplers. We assume lead thicknesses of 1um. The placeholders for SQUIDs are modeled as capacitors between nearest-neighbor qubits, with footprints of 5 um × 5 um and gaps between high voltage side leads of 1um. The distance between the leads and the ground metalization (blue) is 8um. We consider two different substrates: 1) a 500 um-thick silicon substrate with relative permittivity of $\epsilon_r = 11.47$, and 2) silicon-on-insulator (SOI) substrate with a 220 nm-thick suspended silicon layer, a 3 um-thick vacuum gap layer, and a 725 um-thick silicon handle layer [167]. For both substrates, the layer above the metalizations is

set to vacuum.

In this model, the elongated leads for realizing the galvanic connection are expected to determine the bulk of the capacitance. We identify two crucial dimensions that contribute to parasitic capacitances. First, the lattice constant (a) determines the proximity among the leads and the perimeter of the leads. Second, the width of the gapped regions to locate the lumpled element readout resonators (RO gap width, b) determines the amount of ground metalization around each lattice site for a given lattice constant, which screens the electric field. Note that the leads extended from the low voltage metalization of the mergemons are omitted to reduce computation overhead, omission of which would likely lead to overestimation of the parasitic capacitances.

Fig. 6.S8b-e show the estimated parasitic capacitances as functions of the aforementioned parameters. We plot the two largest parasitic capacitances: the diagonal parasitic capacitance C_{diag} between the lattice sites (i, j) and $(i + 1, j + 1)$ and the next-nearest-neighbor parasitic capacitance C_{NNN} between lattice sites (i, j) and $(i + 2, j)$ or between lattice sites (i, j) and $(i, j + 2)$, as illustrated in Fig. 6.S8a.

We find that increasing the lattice constant reduces parasitic capacitances, for the same RO gap width. This indicates that the reduction in the parasitic capacitances, due to the increase in the ground metalization area, is faster than the increase in the parasitic capacitance originating from the longer lead lengths. The increase in the RO gap width significantly strengthens the parasitic capacitances by reducing the ground metalization area. For the combination of parameters that yields a sufficient amount of ground metalization (large a, small b), the parasitic capacitances of the two different substrates become closer in value. This implies that the bulk of the parasitic capacitances are mediated by the stray capacitances in the vacuum layer above the metalizations in such parameter regimes. We find that for the lattice constant of 100 um and the RO gap widths of 50 um, parasitic capacitances are approximately 30 aF or lower for both substrate materials. As mentioned in the main text, simulations including substrate trenching and galvanic connection elements to an opposing chip are expected to estimate smaller stray capacitances by reducing substrate filling factors and adding more ground metalizations that screen electric fields.

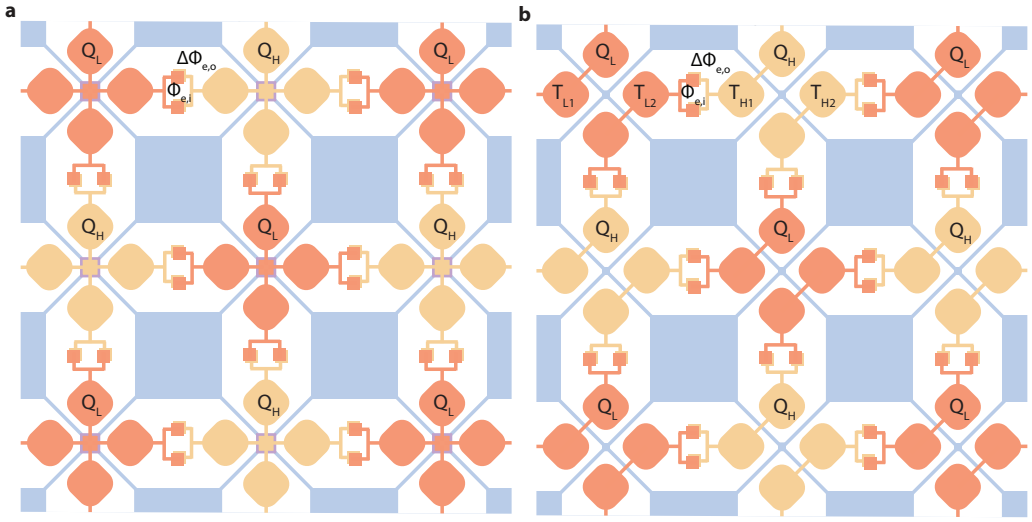

Figure 6.S9: **Tiling transmons with shunt capacitors and dual-rail transmons on a square lattice. a**, Transmons tiled on a square lattice. High voltage metalization (yellow, orange) provides the shunt capacitor needed for transmon. Josephson junctions are located at the center of each unit cell, illustrated as the overlap between the high voltage metalization and the low voltage metalization (purple) that are each galvanically connected to the four extended leads. **b**, Dual-rail transmons tiled on a square lattice. Each unit cell consists of two transmons, which are coupled capacitively. The overlap between the high voltage leads (yellow, orange) and the ground metalization (blue) represents a single Josephson junction needed for implementing a fixed-frequency transmon or two Josephson junctions forming a SQUID loop needed for implementing a frequency-tunable transmon.

6.9.8 Tiling transmons with shunt capacitors and dual-rail transmons

The tiling strategy for conventional transmons with planar shunt capacitance can be obtained simply by widening the leads and gaps to ground starting from the mergemon tiling scheme, as illustrated in Fig. 6.S9a. The presence of shunt capacitors requires the outer SQUID loops to be enlarged, which poses a trade-off between dephasing due to flux noise in the outer SQUID loops and the dielectric loss from the contaminated interfacial layers on capacitor pads. The bulky capacitor pads may also mediate larger stray capacitance, which can lead to more spectator ZZ interactions.

In contrast, the use of dual rail transmons suppresses the effect of flux noise, due to the protection against frequency noise provided by their operation at artificial sweet-spots [255, 307]. We provide a tiling example with dual-rail transmons in Fig. 6.S9b, where each unit cell consists of two capacitively coupled transmons.

Chapter 7

OUTLOOK AND FUTURE DIRECTIONS

Taken together, the results reported in this thesis suggest that the number and nature of mediating modes constitute an important design degree of freedom for superconducting quantum processors. In this chapter, we outline several directions for extending the experimental platforms and circuit architectures developed here, and discuss potential applications of these ideas. Direct extensions of the work presented in individual chapters are discussed within those chapters and the corresponding supplementary information.

7.1 Novel platform for microwave quantum optics

In Chapter 3, we demonstrate deterministic generation of multidimensional microwave photonic cluster states. The on-demand single-photon emitter and the slow-light waveguide developed for this work have numerous potential applications in microwave quantum optics. In this section, we discuss two possible extensions of this experimental platform.

7.1.1 Dual-rail encoded microwave optics platform

The ability to detect losses in itinerant photons is helpful for establishing fault-tolerance in measurement-based quantum information processing with flying qubits [139, 324]. Dual-rail encoding of microwave photons allows detection of loss events [307, 308, 325, 326], by encoding a qubit in the manifold with a fixed excitation number. Such dual-rail encodings can be implemented with a slow-light waveguide system in several ways. The sharp and flat passband enables frequency-bin dual-rail encoding [326] with minimal higher-order dispersion, the slow group velocity enables time-bin dual-rail encoding [156, 327], and using two slow-light waveguides with two coupled emitters enables spatial dual-rail encoding.

7.1.2 Single photon absorption

Being able to completely absorb a single photon with a qubit allows full control of quantum information, including readout in an arbitrary basis, which is crucial for measurement-based quantum computation [97]. Photon absorption using time-reversed shaped coupling has been demonstrated with high-efficiency in the

microwave domain [205, 328, 329]. The slow-light waveguide provides precise control over photon propagation and arrival time while offering dynamically tunable strong emitter-waveguide coupling, making the platform naturally suitable for high-efficiency photon absorption. In a preliminary measurement using the device from Chapter 3, we recover approximately 87.6% of the initial population upon re-absorption of an emitted photon with the same emitter, accounting for photon loss, mirror efficiency, and the readout confusion matrix.

7.2 Dissipation engineering

We propose a "bright-dark" double-band metamaterial in which each unit cell consists of two resonators in resonance that form hybridized symmetric and anti-symmetric eigenmodes. Under sufficiently small inter-unit-cell coupling, the symmetric and anti-symmetric eigenmodes form disjoint passbands. At the end of the metamaterial where the waveguide couples to the output, if the last two resonators (the last unit cell) are coupled symmetrically to the output, only the symmetric eigenmodes couple strongly to the environment, making the corresponding passband "bright". In contrast, the anti-symmetric eigenmode passband remains coherent, which we refer to as the "dark" band. Such a metamaterial waveguide provides a Purcell filter with a sharp band edge necessary for fast qubit readout and reset via the bright band [91, 92, 117], while the dark band can be used for coherent long-range interactions between superconducting qubits or for information storage. This architecture provides a hardware-efficient route to color the dissipation while preserving coherence in protected bands.

7.3 Engineering intrinsic nonlinearities

In Chapter 6, we propose SQUID couplers with perturbatively small Josephson energies for controllable nonlinear interactions. Here we discuss several additional directions for engineering intrinsic nonlinearities in superconducting quantum circuits that remain relatively unexplored.

7.3.1 Galvanic nonlinear coupling architecture

Engineering purely nonlinear coupling, such as Quarton couplers [119], junction-based readout schemes [71, 120], and SQUID couplers, has largely focused on cross-Kerr interactions with transmons. However, the broader design space of galvanically coupled nonlinear circuits remains only partially explored. In particular, the parameter regimes that favor such architectures, their compatibility with other

nonlinear interaction mechanisms such as longitudinal coupling and multi-photon processes, and their interaction with different qubit and resonator archetypes are still open questions. Because galvanic coupling can provide strong and direct nonlinear interactions, small and conceptually simple circuit architectures may prove useful.

7.3.2 Slightly tunable superconducting qubits

Flux-tunable qubits are often challenged by the excessively large tunability of their transition frequency, which exposes the qubit to flux noise and leads to dephasing. This typically arises from the relatively large accessible Josephson energies in a SQUID loop, limited by lithographic constraints. The use of thick oxide barriers, as suggested in Chapter 6, would release this constraint by enabling junctions with substantially smaller critical currents for the same area. This approach would make it feasible to realize transmons with only minute tunability.

7.3.3 Junction readout with small E_J

Junction readout techniques have been proposed and demonstrated to provide high-performance readout of superconducting qubits and robustness against measurement-induced state transitions [71, 120]. In these approaches, suppressing the self-Kerr of the readout resonator requires reducing zero-point fluctuations of phase. This typically necessitates making the readout resonator highly capacitive, which increases its physical footprint or otherwise introduces additional dielectric loss. Moreover, an additional coupling capacitor is often required to cancel hybridization between the qubit and the readout resonator, further increasing complexity and footprint.

An alternative approach is to employ junctions with sufficiently small Josephson energy realized using thick oxide barriers. Such junctions suppress self-Kerr nonlinearities, allow the use of less capacitive, more compact readout resonators, and eliminate the need for a separate capacitor for hybridization cancelation.

BIBLIOGRAPHY

[1] M. Planck. *The theory of heat radiation*. Blakiston, 1914 (cit. on p. 1).

[2] A. Einstein. "On a heuristic viewpoint concerning the emission and transformation of light". In: *Annalen der Physik* 17.6 (1905), pp. 132–148 (cit. on p. 1).

[3] A. Einstein. "On the quantum theory of radiation". In: *Physikalische Zeitschrift* 18.121 (1917), pp. 167–83 (cit. on p. 1).

[4] W. Heisenberg. "On the quantum-theoretical reinterpretation of kinematical and mechanical relationships". In: *Z. Physik* 33 (1925), pp. 879–893 (cit. on p. 1).

[5] E. Schrödinger. "An undulatory theory of the mechanics of atoms and molecules". In: *Physical review* 28.6 (1926), p. 1049 (cit. on p. 1).

[6] P. A. M. Dirac. "The quantum theory of the emission and absorption of radiation". In: *Proceedings of the Royal Society of London. Series A, Containing Papers of a Mathematical and Physical Character* 114.767 (1927), pp. 243–265. DOI: 10.1098/rspa.1927.0039 (cit. on pp. 1, 35, 39).

[7] R. J. Glauber. "The quantum theory of optical coherence". In: *Physical Review* 130.6 (1963), p. 2529 (cit. on p. 1).

[8] A. Einstein, B. Podolsky, and N. Rosen. "Can quantum-mechanical description of physical reality be considered complete?" In: *Physical review* 47.10 (1935), p. 777 (cit. on p. 1).

[9] J. S. Bell. "On the einstein podolsky rosen paradox". In: *Physics Physique Fizika* 1.3 (1964), p. 195 (cit. on p. 1).

[10] G. Weihs, T. Jennewein, C. Simon, H. Weinfurter, and A. Zeilinger. "Violation of Bell's inequality under strict Einstein locality conditions". In: *Physical Review Letters* 81.23 (1998), p. 5039. DOI: 10.1103/PhysRevLett.81.5039 (cit. on p. 1).

[11] R. P. Feynman. "Simulating physics with computers". In: *International Journal of Theoretical Physics* 21.6 (1982), pp. 467–488 (cit. on p. 1).

[12] D. Deutsch. "Quantum theory, the Church–Turing principle and the universal quantum computer". In: *Proceedings of the Royal Society of London. A. Mathematical and Physical Sciences* 400.1818 (1985), pp. 97–117 (cit. on p. 1).

[13] S. Lloyd. "Universal quantum simulators". In: *Science* 273.5278 (1996), pp. 1073–1078. DOI: 10.1126/science.273.5278.1073 (cit. on p. 1).

[14] P. W. Shor. "Algorithms for quantum computation: discrete logarithms and factoring". In: *Proceedings 35th annual symposium on foundations of computer science*. Ieee. 1994, pp. 124–134 (cit. on p. 1).

[15] L. K. Grover. "A fast quantum mechanical algorithm for database search". In: *Proceedings of the twenty-eighth annual ACM symposium on Theory of computing*. 1996, pp. 212–219 (cit. on p. 1).

[16] A. W. Harrow, A. Hassidim, and S. Lloyd. "Quantum Algorithm for Linear Systems of Equations". In: *Phys. Rev. Lett.* 103 (15 Oct. 2009), p. 150502. DOI: 10.1103/PhysRevLett.103.150502 (cit. on p. 1).

[17] M. Greiner, O. Mandel, T. Esslinger, T. W. Hänsch, and I. Bloch. "Quantum phase transition from a superfluid to a Mott insulator in a gas of ultracold atoms". In: *nature* 415.6867 (2002), pp. 39–44. DOI: 10.1038/415039a (cit. on p. 1).

[18] I. Bloch, J. Dalibard, and S. Nascimbene. "Quantum simulations with ultracold quantum gases". In: *Nature Physics* 8.4 (2012), pp. 267–276. DOI: 10.1038/nphys2259 (cit. on p. 1).

[19] J. I. Cirac and P. Zoller. "Quantum Computations with Cold Trapped Ions". In: *Phys. Rev. Lett.* 74 (20 May 1995), pp. 4091–4094. DOI: 10.1103/PhysRevLett.74.4091 (cit. on p. 1).

[20] C. Monroe, D. M. Meekhof, B. E. King, W. M. Itano, and D. J. Wineland. "Demonstration of a Fundamental Quantum Logic Gate". In: *Phys. Rev. Lett.* 75 (25 Dec. 1995), pp. 4714–4717. DOI: 10.1103/PhysRevLett.75.4714 (cit. on p. 1).

[21] D. P. DiVincenzo. "The physical implementation of quantum computation". In: *Fortschritte der Physik: Progress of Physics* 48.9-11 (2000), pp. 771–783. DOI: https://doi.org/10.1002/1521-3978(200009)48:9/11<771::AID-PROP771>3.0.CO;2-E (cit. on pp. 1, 2, 78).

[22] J. R. Petta, A. C. Johnson, J. M. Taylor, E. A. Laird, A. Yacoby, M. D. Lukin, et al. “Coherent manipulation of coupled electron spins in semiconductor quantum dots”. In: *Science* 309.5744 (2005), pp. 2180–2184. DOI: 10.1126/science.1116955 (cit. on p. 1).

[23] M. Endres, H. Bernien, A. Keesling, H. Levine, E. R. Anschuetz, A. Krajenbrink, et al. “Atom-by-atom assembly of defect-free one-dimensional cold atom arrays”. In: *Science* 354.6315 (2016), pp. 1024–1027. DOI: 10.1126/science.aah3752 (cit. on p. 1).

[24] B. Josephson. “Possible new effects in superconductive tunnelling”. In: *Physics Letters* 1.7 (1962), pp. 251–253. DOI: 10.1016/0031-9163(62)91369-0 (cit. on pp. 1, 2, 133).

[25] J. M. Martinis, M. H. Devoret, and J. Clarke. “Experimental tests for the quantum behavior of a macroscopic degree of freedom: The phase difference across a Josephson junction”. In: *Phys. Rev. B* 35 (10 Apr. 1987), pp. 4682–4698. DOI: 10.1103/PhysRevB.35.4682 (cit. on p. 1).

[26] Y. Nakamura, Y. A. Pashkin, and J. S. Tsai. “Coherent control of macroscopic quantum states in a single-Cooper-pair box”. In: *Nature* 398.6730 (1999), pp. 786–788. DOI: 10.1038/19718 (cit. on pp. 1, 2).

[27] C. E. Shannon. “A mathematical theory of communication”. In: *The Bell system technical journal* 27.3 (1948), pp. 379–423 (cit. on p. 1).

[28] J. Von Neumann. “Probabilistic logics and the synthesis of reliable organisms from unreliable components”. In: *Automata studies* 34.34 (1956), pp. 43–98 (cit. on p. 1).

[29] I. L. Chuang, R. Laflamme, P. W. Shor, and W. H. Zurek. “Quantum Computers, Factoring, and Decoherence”. In: *Science* 270.5242 (1995), pp. 1633–1635. DOI: 10.1126/science.270.5242.1633 (cit. on p. 1).

[30] P. W. Shor. “Scheme for reducing decoherence in quantum computer memory”. In: *Phys. Rev. A* 52 (4 Oct. 1995), R2493–R2496. DOI: 10.1103/PhysRevA.52.R2493 (cit. on pp. 1, 115).

[31] P. Shor. “Fault-tolerant quantum computation”. In: *Proceedings of 37th Conference on Foundations of Computer Science*. 1996, pp. 56–65. DOI: 10.1109/SFCS.1996.548464 (cit. on pp. 1, 115).

[32] A. Y. Kitaev. “Quantum computations: algorithms and error correction”. In: *Russian Mathematical Surveys* 52.6 (Dec. 1997), pp. 1191–1249. DOI: 10.1070/RM1997v052n06ABEH002155 (cit. on pp. 1, 115).

[33] E. Dennis, A. Kitaev, A. Landahl, and J. Preskill. “Topological quantum memory”. In: *Journal of Mathematical Physics* 43.9 (Sept. 2002), pp. 4452–4505. DOI: 10.1063/1.1499754 (cit. on p. 1).

[34] C. Alexander. *Notes on the Synthesis of Form*. Vol. 5. Harvard University Press, 1964 (cit. on p. 1).

[35] H. A. Simon. *The Sciences of the Artificial*. MIT press, 1970 (cit. on p. 1).

[36] D. L. Parnas. “On the criteria to be used in decomposing systems into modules”. In: *Communications of the ACM* 15.12 (1972), pp. 1053–1058 (cit. on p. 1).

[37] C. Y. Baldwin and K. B. Clark. *Design rules, Volume 1: The power of modularity*. MIT press, 2000 (cit. on p. 1).

[38] C. Mead and L. Conway. *Introduction to VLSI systems*. 1980 (cit. on p. 1).

[39] N. H. Weste and D. Harris. *CMOS VLSI design: a circuits and systems perspective*. Pearson Education India, 2015 (cit. on p. 1).

[40] A. Blais, R.-S. Huang, A. Wallraff, S. M. Girvin, and R. J. Schoelkopf. “Cavity quantum electrodynamics for superconducting electrical circuits: An architecture for quantum computation”. In: *Phys. Rev. A* 69.6 (2004), p. 062320. DOI: 10.1103/PhysRevA.69.062320 (cit. on pp. 2, 19, 128).

[41] J. Koch, T. M. Yu, J. Gambetta, A. A. Houck, D. I. Schuster, J. Majer, et al. “Charge-insensitive qubit design derived from the Cooper pair box”. In: *Phys. Rev. A* 76 (4 Oct. 2007), p. 042319. DOI: 10.1103/PhysRevA.76.042319 (cit. on pp. 2, 7, 128, 134).

[42] A. A. Houck, J. A. Schreier, B. R. Johnson, J. M. Chow, J. Koch, J. M. Gambetta, et al. “Controlling the Spontaneous Emission of a Superconducting Transmon Qubit”. In: *Phys. Rev. Lett.* 101 (8 Aug. 2008), p. 080502. DOI: 10.1103/PhysRevLett.101.080502 (cit. on pp. 2, 3, 6).

[43] A. Blais, A. M. van den Brink, and A. M. Zagoskin. “Tunable Coupling of Superconducting Qubits”. In: *Phys. Rev. Lett.* 90 (12 Mar. 2003), p. 127901. DOI: 10.1103/PhysRevLett.90.127901 (cit. on pp. 2, 14).

[44] M. D. Reed, B. R. Johnson, A. A. Houck, L. DiCarlo, J. M. Chow, D. I. Schuster, et al. “Fast reset and suppressing spontaneous emission of a superconducting qubit”. In: *Appl. Phys. Lett.* 96.20 (May 2010), p. 203110. DOI: 10.1063/1.3435463 (cit. on pp. 2, 3, 79, 104, 105, 143).

[45] Y. Chen, C. Neill, P. Roushan, N. Leung, M. Fang, R. Barends, et al. “Qubit Architecture with High Coherence and Fast Tunable Coupling”. In: *Phys. Rev. Lett.* 113 (22 Nov. 2014), p. 220502. DOI: 10.1103/PhysRevLett.113.220502 (cit. on pp. 2, 129).

[46] E. Jeffrey, D. Sank, J. Y. Mutus, T. C. White, J. Kelly, R. Barends, et al. “Fast Accurate State Measurement with Superconducting Qubits”. In: *Phys. Rev. Lett.* 112 (19 May 2014), p. 190504. DOI: 10.1103/PhysRevLett.112.190504 (cit. on pp. 2, 92).

[47] F. Yan, P. Krantz, Y. Sung, M. Kjaergaard, D. L. Campbell, T. P. Orlando, et al. “Tunable coupling scheme for implementing high-fidelity two-qubit gates”. In: *Phys. Rev. Appl.* 10.5 (2018), p. 054062. DOI: 10.1103/PhysRevApplied.10.054062 (cit. on pp. 2, 3, 14, 74, 128, 129).

[48] A. A. Houck, H. E. Türeci, and J. Koch. “On-chip quantum simulation with superconducting circuits”. In: *Nature Physics* 8.4 (Apr. 2012), pp. 292–299. DOI: 10.1038/nphys2251 (cit. on p. 2).

[49] R. Barends, L. Lamata, J. Kelly, L. García-Álvarez, A. G. Fowler, A. Megrant, et al. “Digital quantum simulation of fermionic models with a superconducting circuit”. In: *Nature Communications* 6.1 (July 2015), p. 7654. DOI: 10.1038/ncomms8654 (cit. on p. 2).

[50] D. Castelvecchi. “IBM releases first-ever 1,000-qubit quantum chip”. In: *Nature* 624.7991 (2023), pp. 238–238. DOI: 10.1038/d41586-023-03854-1 (cit. on p. 2).

[51] F. Arute, K. Arya, R. Babbush, D. Bacon, J. C. Bardin, R. Barends, et al. “Quantum supremacy using a programmable superconducting processor”. In: *Nature* 574.7779 (2019), pp. 505–510. DOI: 10.1038/s41586-019-1666-5 (cit. on p. 2).

[52] G. Q. AI and Collaborators. “Quantum error correction below the surface code threshold”. In: *Nature* 638.8052 (2025), pp. 920–926. DOI: 10.1038/s41586-024-08449-y (cit. on pp. 2, 14, 115).

[53] H. Putterman, K. Noh, C. T. Hann, G. S. MacCabe, S. Aghaeimeibodi, R. N. Patel, et al. “Hardware-efficient quantum error correction via concatenated bosonic qubits”. In: *Nature* 638.8052 (2025), pp. 927–934. DOI: 10.1038/s41586-025-08642-7 (cit. on pp. 2, 115, 145).

[54] H. Kamerlingh Onnes. “Further experiments with Liquid Helium. D. On the change of Electrical Resistance of Pure Metals at very low Temperatures, etc. V. The Disappearance of the resistance of mercury”. In: *Koninklijke Nederlandse Akademie van Wetenschappen Proceedings Series B Physical Sciences* 14 (1911), pp. 113–115 (cit. on p. 2).

[55] J. Bardeen, L. N. Cooper, and J. R. Schrieffer. “Theory of Superconductivity”. In: *Phys. Rev.* 108 (5 Dec. 1957), pp. 1175–1204. DOI: 10.1103/PhysRev.108.1175 (cit. on p. 2).

[56] D. E. McCumber. “Effect of ac Impedance on dc Voltage-Current Characteristics of Superconductor Weak-Link Junctions”. In: *Journal of Applied Physics* 39.7 (June 1968), pp. 3113–3118. DOI: 10.1063/1.1656743 (cit. on pp. 2, 133).

[57] P. Krantz, M. Kjaergaard, F. Yan, T. P. Orlando, S. Gustavsson, and W. D. Oliver. “A quantum engineer’s guide to superconducting qubits”. In: *Appl. Phys. Rev.* 6.2 (2019), p. 021318. DOI: 10.1063/1.5089550 (cit. on pp. 2, 72, 92, 128, 134).

[58] V. E. Manucharyan, J. Koch, L. I. Glazman, and M. H. Devoret. “Fluxonium: Single Cooper-Pair Circuit Free of Charge Offsets”. In: *Science* 326.5949 (2009), pp. 113–116. DOI: 10.1126/science.1175552 (cit. on p. 2).

[59] A. P. Place, L. V. Rodgers, P. Mundada, B. M. Smitham, M. Fitzpatrick, Z. Leng, et al. “New material platform for superconducting transmon qubits with coherence times exceeding 0.3 milliseconds”. In: *Nature Comm.* 12.1 (2021), pp. 1–6. DOI: 10.1103/PhysRevA.98.042318 (cit. on pp. 2, 76).

[60] C. E. Murray. “Material matters in superconducting qubits”. In: *Materials Science and Engineering: R: Reports* 146 (2021), p. 100646. DOI: 10.1016/j.mser.2021.100646 (cit. on pp. 2, 3, 15, 128).

[61] A. Somoroff, Q. Ficheux, R. A. Mencia, H. Xiong, R. Kuzmin, and V. E. Manucharyan. “Millisecond Coherence in a Superconducting Qubit”. In: *Phys. Rev. Lett.* 130 (26 June 2023), p. 267001. DOI: 10.1103/PhysRevLett.130.267001 (cit. on p. 2).

[62] S. Ganjam, Y. Wang, Y. Lu, A. Banerjee, C. U. Lei, L. Krayzman, et al. “Surpassing millisecond coherence in on chip superconducting quantum memories by optimizing materials and circuit design”. In: *Nature Communications* 15.1 (2024), p. 3687. DOI: 10.1038/s41467-024-47857-6 (cit. on p. 2).

[63] M. McEwen, K. C. Miao, J. Atalaya, A. Bilmes, A. Crook, J. Bovaird, et al. "Resisting High-Energy Impact Events through Gap Engineering in Superconducting Qubit Arrays". In: *Phys. Rev. Lett.* 133 (24 Dec. 2024), p. 240601. DOI: 10.1103/PhysRevLett.133.240601 (cit. on p. 2).

[64] M. P. Bland, F. Bahrami, J. G. Martinez, P. H. Prestegaard, B. M. Smitham, A. Joshi, et al. "Millisecond lifetimes and coherence times in 2D transmon qubits". In: *Nature* (2025), pp. 1–6. DOI: 10.1038/s41586-025-09687-4 (cit. on p. 2).

[65] A. Dane, K. Balakrishnan, B. Wacaser, L.-W. Hung, H. Mamin, D. Rugar, et al. "Performance stabilization of high-coherence superconducting qubits". In: *arXiv preprint arXiv:2503.12514* (2025). DOI: 10.48550/arXiv.2503.12514 (cit. on p. 2).

[66] Z. Li, P. Liu, P. Zhao, Z. Mi, H. Xu, X. Liang, et al. "Error per single-qubit gate below 10- 4 in a superconducting qubit". In: *npj Quantum Information* 9.1 (2023), p. 111. DOI: 10.1038/s41534-023-00781-x (cit. on p. 2).

[67] D. A. Rower, L. Ding, H. Zhang, M. Hays, J. An, P. M. Harrington, et al. "Suppressing Counter-Rotating Errors for Fast Single-Qubit Gates with Fluxonium". In: *PRX Quantum* 5 (4 Dec. 2024), p. 040342. DOI: 10.1103/PRXQuantum.5.040342 (cit. on p. 2).

[68] D. Sank, Z. Chen, M. Khezri, J. Kelly, R. Barends, B. Campbell, et al. "Measurement-Induced State Transitions in a Superconducting Qubit: Beyond the Rotating Wave Approximation". In: *Phys. Rev. Lett.* 117 (19 Nov. 2016), p. 190503. DOI: 10.1103/PhysRevLett.117.190503 (cit. on pp. 2, 78).

[69] M. Khezri, A. Opremcak, Z. Chen, K. C. Miao, M. McEwen, A. Bengtsson, et al. "Measurement-induced state transitions in a superconducting qubit: Within the rotating-wave approximation". In: *Phys. Rev. Appl.* 20 (5 Nov. 2023), p. 054008. DOI: 10.1103/PhysRevApplied.20.054008 (cit. on pp. 2, 78).

[70] M. F. Dumas, B. Groleau-Paré, A. McDonald, M. H. Muñoz-Arias, C. Lledó, B. D'Anjou, et al. "Measurement-Induced Transmon Ionization". In: *Phys. Rev. X* 14 (4 Oct. 2024), p. 041023. DOI: 10.1103/PhysRevX.14.041023 (cit. on p. 2).

[71] C. Wang, F.-M. Liu, H. Chen, Y.-F. Du, C. Ying, J.-W. Wang, et al. "Longitudinal and Nonlinear Coupling for High-Fidelity Readout of a Superconducting Qubit". In: *Phys. Rev. Lett.* 135 (6 Aug. 2025), p. 060803. DOI: 10.1103/98n9-13y4 (cit. on pp. 2, 17, 129, 143, 172, 173).

[72] L. B. Nguyen, Y.-H. Lin, A. Somoroff, R. Mencia, N. Grabon, and V. E. Manucharyan. "High-Coherence Fluxonium Qubit". In: *Phys. Rev. X* 9 (4 Nov. 2019), p. 041041. DOI: 10.1103/PhysRevX.9.041041 (cit. on pp. 2, 143).

[73] L. Ding, M. Hays, Y. Sung, B. Kannan, J. An, A. Di Paolo, et al. "High-Fidelity, Frequency-Flexible Two-Qubit Fluxonium Gates with a Transmon Coupler". In: *Phys. Rev. X* 13 (3 Sept. 2023), p. 031035. DOI: 10.1103/PhysRevX.13.031035 (cit. on p. 2).

[74] M. Mirrahimi, Z. Leghtas, V. V. Albert, S. Touzard, R. J. Schoelkopf, L. Jiang, et al. "Dynamically protected cat-qubits: a new paradigm for universal quantum computation". In: *New Journal of Physics* 16.4 (Apr. 2014), p. 045014. DOI: 10.1088/1367-2630/16/4/045014 (cit. on pp. 2, 145).

[75] B. L. Brock, S. Singh, A. Eickbusch, V. V. Sivak, A. Z. Ding, L. Frunzio, et al. "Quantum error correction of qudits beyond break-even". In: *Nature* 641.8063 (May 2025), pp. 612–618. DOI: 10.1038/s41586-025-08899-y (cit. on p. 2).

[76] C. Gidney. *How to factor 2048 bit RSA integers with less than a million noisy qubits*. 2025 (cit. on pp. 3, 116, 128, 143).

[77] J. Eisert and J. Preskill. "Mind the gaps: The fraught road to quantum advantage". In: *arXiv preprint arXiv:2510.19928* (2025). DOI: 10.48550/arXiv.2510.19928 (cit. on pp. 3, 116).

[78] P. Brooks, A. Kitaev, and J. Preskill. "Protected gates for superconducting qubits". In: *Phys. Rev. A* 87 (5 May 2013), p. 052306. DOI: 10.1103/PhysRevA.87.052306 (cit. on pp. 3, 129).

[79] A. Gyenis, A. Di Paolo, J. Koch, A. Blais, A. A. Houck, and D. I. Schuster. "Moving beyond the Transmon: Noise-Protected Superconducting Quantum Circuits". In: *PRX Quantum* 2 (3 Sept. 2021), p. 030101. DOI: 10.1103/PRXQuantum.2.030101 (cit. on p. 3).

[80] S. Puri, L. St-Jean, J. A. Gross, A. Grimm, N. E. Frattini, P. S. Iyer, et al. "Bias-preserving gates with stabilized cat qubits". In: *Science Advances* 6.34 (2020), eaay5901. DOI: 10.1126/sciadv.aay5901 (cit. on p. 3).

[81] C. Wang, C. Axline, Y. Y. Gao, T. Brecht, Y. Chu, L. Frunzio, et al. “Surface participation and dielectric loss in superconducting qubits”. In: *Applied Physics Letters* 107.16 (Oct. 2015), p. 162601. DOI: 10.1063/1.4934486 (cit. on p. 3).

[82] S. Ashhab, A. O. Niskanen, K. Harrabi, Y. Nakamura, T. Picot, P. C. de Groot, et al. “Interqubit coupling mediated by a high-excitation-energy quantum object”. In: *Phys. Rev. B* 77 (1 Jan. 2008), p. 014510. DOI: 10.1103/PhysRevB.77.014510 (cit. on p. 3).

[83] R. A. Pinto, A. N. Korotkov, M. R. Geller, V. S. Shumeiko, and J. M. Martinis. “Analysis of a tunable coupler for superconducting phase qubits”. In: *Phys. Rev. B* 82 (10 Sept. 2010), p. 104522. DOI: 10.1103/PhysRevB.82.104522 (cit. on p. 3).

[84] J. Stehlik, D. M. Zajac, D. L. Underwood, T. Phung, J. Blair, S. Carnevale, et al. “Tunable Coupling Architecture for Fixed-Frequency Transmon Superconducting Qubits”. In: *Phys. Rev. Lett.* 127 (8 Aug. 2021), p. 080505. DOI: 10.1103/PhysRevLett.127.080505 (cit. on pp. 3, 14, 128, 129).

[85] K. C. Miao, M. McEwen, J. Atalaya, D. Kafri, L. P. Pryadko, A. Bengtsson, et al. “Overcoming leakage in quantum error correction”. In: *Nat. Phys.* 19.12 (2023), pp. 1780–1786. DOI: 10.1038/s41567-023-02226-w (cit. on pp. 3, 9, 16, 78, 86, 104, 105, 129).

[86] S. Bravyi, A. W. Cross, J. M. Gambetta, D. Maslov, P. Rall, and T. J. Yoder. “High-threshold and low-overhead fault-tolerant quantum memory”. In: *Nature* 627.8005 (2024), pp. 778–782. DOI: 10.1038/s41586-024-07107-7 (cit. on pp. 3, 15, 116).

[87] A. G. Fowler, M. Mariantoni, J. M. Martinis, and A. N. Cleland. “Surface codes: Towards practical large-scale quantum computation”. In: *Phys. Rev. A* 86 (3 Sept. 2012), p. 032324. DOI: 10.1103/PhysRevA.86.032324 (cit. on pp. 3, 115).

[88] P. Mundada, G. Zhang, T. Hazard, and A. Houck. “Suppression of Qubit Crosstalk in a Tunable Coupling Superconducting Circuit”. In: *Phys. Rev. Appl.* 12 (5 Nov. 2019), p. 054023. DOI: 10.1103/PhysRevApplied.12.054023 (cit. on pp. 3, 16).

[89] M. Brink, J. M. Chow, J. Hertzberg, E. Magesan, and S. Rosenblatt. “Device challenges for near term superconducting quantum processors: frequency collisions”. In: *2018 IEEE International Electron Devices Meeting (IEDM)*. 2018, pp. 6.1.1–6.1.3. DOI: 10.1109/IEDM.2018.8614500 (cit. on pp. 3, 142).

[90] P. A. Spring, S. Cao, T. Tsunoda, G. Campanaro, S. Fasciati, J. Wills, et al. “High coherence and low cross-talk in a tileable 3D integrated superconducting circuit architecture”. In: *Science Advances* 8.16 (2022), eabl6698. DOI: 10.1126/sciadv.abl6698 (cit. on p. 3).

[91] V. S. Ferreira, G. Kim, A. Butler, H. Pichler, and O. Painter. “Deterministic generation of multidimensional photonic cluster states with a single quantum emitter”. In: *Nat. Phys.* 20.5 (2024), pp. 865–870. DOI: 10.1038/s41567-024-02408-0. (Cit. on pp. 4, 18, 172).

[92] G. Kim, A. Butler, V. S. Ferreira, X. Zhang, A. Hadley, E. Kim, and O. Painter. “Fast unconditional reset and leakage reduction of a tunable superconducting qubit via an engineered dissipative bath”. In: *Phys. Rev. Appl.* 24 (1 July 2025), p. 014013. DOI: 10.1103/6wc6-78y3. (Cit. on pp. 4, 78, 172).

[93] O. Golan, A. V. Gorshkov, A. Butler, G. Kim, F. G. Brandao, O. Painter, et al. “All-to-All Connectivity in Superconducting Qubits via Metamaterial-Mediated Interactions”. In: *in preparation* (2026) (cit. on pp. 4, 115–117, 119).

[94] O. Golan, A. Retzker, A. V. Gorshkov, A. Butler, G. Kim, S. Aghaeimeibodi, et al. “Long-Range Gates in Superconducting Dual-Rail Qubits (Part 1-Theory)”. In: *SMT 2025*. APS. 2025 (cit. on pp. 4, 115, 116).

[95] A. Butler, G. Kim, O. Golan, A. V. Gorshkov, M. Matheny, A. Retzker, et al. “Long-Range Gates in Superconducting Dual-Rail Qubits (Part2-Design)”. In: *SMT 2025*. APS. 2025 (cit. on pp. 4, 115, 116).

[96] G. Kim, A. Butler, and O. Painter. “A Tunable, Modeless, and Hybridization-free Cross-Kerr Coupler for Miniaturized Superconducting Qubits”. In: *arXiv preprint* (2026). DOI: 10.48550/arXiv.2602.03186. (Cit. on pp. 4, 128).

[97] R. Raussendorf and H. J. Briegel. “A one-way quantum computer”. In: *Phys. Rev. Lett.* 86.22 (2001), p. 5188. DOI: 10.1103/PhysRevLett.86.5188 (cit. on pp. 5, 18, 171).

[98] N. Gisin and R. Thew. “Quantum communication”. In: *Nat. Phot.* 1.3 (2007), pp. 165–171. DOI: 10.1038/nphoton.2007.22 (cit. on pp. 5, 18).

[99] C. Eichler, D. Bozyigit, C. Lang, L. Steffen, J. Fink, and A. Wallraff. "Experimental state tomography of itinerant single microwave photons". In: *Phys. Rev. Lett.* 106.22 (2011), p. 220503. DOI: 10.1103/PhysRevLett.106.220503 (cit. on pp. 5, 19, 51).

[100] I.-C. Hoi, T. Palomaki, J. Lindkvist, G. Johansson, P. Delsing, and C. Wilson. "Generation of nonclassical microwave states using an artificial atom in 1D open space". In: *Phys. Rev. Lett.* 108.26 (2012), p. 263601. DOI: 10.1103/PhysRevLett.108.263601 (cit. on pp. 5, 19).

[101] J.-T. Shen and S. Fan. "Coherent single photon transport in a one-dimensional waveguide coupled with superconducting quantum bits". In: *Phys. Rev. Lett.* 95.21 (2005), p. 213001. DOI: 10.1103/PhysRevLett.95.213001 (cit. on pp. 5, 21, 73).

[102] D. Roy, C. M. Wilson, and O. Firstenberg. "Colloquium: Strongly interacting photons in one-dimensional continuum". In: *Rev. Mod. Phys.* 89 (2 May 2017), p. 021001. DOI: 10.1103/RevModPhys.89.021001 (cit. on p. 5).

[103] A. F. Kockum, G. Johansson, and F. Nori. "Decoherence-Free Interaction between Giant Atoms in Waveguide Quantum Electrodynamics". In: *Phys. Rev. Lett.* 120 (14 Apr. 2018), p. 140404. DOI: 10.1103/PhysRevLett.120.140404 (cit. on p. 5).

[104] M. Arcari, I. Söllner, A. Javadi, S. Lindskov Hansen, S. Mahmoodian, J. Liu, et al. "Near-Unity Coupling Efficiency of a Quantum Emitter to a Photonic Crystal Waveguide". In: *Phys. Rev. Lett.* 113 (9 Aug. 2014), p. 093603. DOI: 10.1103/PhysRevLett.113.093603 (cit. on p. 8).

[105] J. F. Marques, H. Ali, B. M. Varbanov, M. Finkel, H. M. Veen, S. L. M. van der Meer, et al. "All-Microwave Leakage Reduction Units for Quantum Error Correction with Superconducting Transmon Qubits". In: *Phys. Rev. Lett.* 130 (25 June 2023), p. 250602. DOI: 10.1103/PhysRevLett.130.250602 (cit. on pp. 9, 78, 143).

[106] N. Lacroix, L. Hofele, A. Remm, O. Benhayoune-Khadraoui, A. McDonald, R. Shillito, et al. "Fast Flux-Activated Leakage Reduction for Superconducting Quantum Circuits". In: *Phys. Rev. Lett.* 134 (12 Mar. 2025), p. 120601. DOI: 10.1103/PhysRevLett.134.120601 (cit. on pp. 9, 78, 82, 86, 87, 134, 143).

[107] M. Mirhosseini, E. Kim, V. S. Ferreira, M. Kalaee, A. Sipahigil, A. J. Keller, et al. "Superconducting metamaterials for waveguide quantum electrodynamics". In: *Nat. Commun.* 9.1 (2018), p. 3706. DOI: 10.1038/s41467-018-06142-z (cit. on pp. 10, 79, 116).

[108] E. Kim, X. Zhang, V. S. Ferreira, J. Banker, J. K. Iverson, A. Sipahigil, et al. "Quantum Electrodynamics in a Topological Waveguide". In: *Phys. Rev. X* 11 (1 Jan. 2021), p. 011015. DOI: 10.1103/PhysRevX.11.011015 (cit. on pp. 10, 79, 116, 122).

[109] G. Calajó, F. Ciccarello, D. Chang, and P. Rabl. "Atom-field dressed states in slow-light waveguide QED". In: *Phys. Rev. A* 93.3 (2016), p. 033833. DOI: 10.1103/PhysRevA.93.033833 (cit. on pp. 10, 21, 35, 39, 47, 55, 81, 91, 97, 98, 113, 122).

[110] Y. Sung, L. Ding, J. Braumüller, A. Vepsäläinen, B. Kannan, M. Kjaergaard, et al. "Realization of High-Fidelity CZ and ZZ-Free iSWAP Gates with a Tunable Coupler". In: *Phys. Rev. X* 11 (2 June 2021), p. 021058. DOI: 10.1103/PhysRevX.11.021058 (cit. on pp. 14, 128, 129).

[111] F. Marxer, J. Mrożek, J. Andersson, L. Abdurakhimov, J. Adam, V. Bergholm, et al. "Above 99.9% fidelity single-qubit gates, two-qubit gates, and readout in a single superconducting quantum device". In: *arXiv preprint arXiv:2508.16437* (2025) (cit. on p. 14).

[112] N. P. Breuckmann and J. N. Eberhardt. "Quantum Low-Density Parity-Check Codes". In: *PRX Quantum* 2 (4 Oct. 2021), p. 040101. DOI: 10.1103/PRXQuantum.2.040101 (cit. on pp. 15, 116).

[113] J. M. Martinis, K. B. Cooper, R. McDermott, M. Steffen, M. Ansmann, K. D. Osborn, et al. "Decoherence in Josephson Qubits from Dielectric Loss". In: *Phys. Rev. Lett.* 95 (21 Nov. 2005), p. 210503. DOI: 10.1103/PhysRevLett.95.210503 (cit. on pp. 15, 128).

[114] J. Niu, L. Zhang, Y. Liu, J. Qiu, W. Huang, J. Huang, et al. "Low-loss interconnects for modular superconducting quantum processors". In: *Nature Electronics* 6.3 (2023), pp. 235–241. DOI: 10.1038/s41928-023-00925-z (cit. on pp. 15, 116).

[115] M. Mollenhauer, A. Irfan, X. Cao, S. Mandal, and W. Pfaff. "A high-efficiency elementary network of interchangeable superconducting qubit devices". In: *Nature Electronics* 8.7 (2025), pp. 610–619. DOI: 10.1038/s41928-025-01404-3 (cit. on pp. 15, 116).

[116] D. C. McKay, R. Naik, P. Reinhold, L. S. Bishop, and D. I. Schuster. "High-Contrast Qubit Interactions Using Multimode Cavity QED". In: *Phys. Rev. Lett.* 114 (8 Feb. 2015), p. 080501. DOI: 10.1103/PhysRevLett.114.080501 (cit. on p. 16).

[117] X. Zhang, E. Kim, D. K. Mark, S. Choi, and O. Painter. "A superconducting quantum simulator based on a photonic-bandgap metamaterial". In: *Science* 379.6629 (2023), pp. 278–283. DOI: DOI:10.1126/science.ade7651 (cit. on pp. 16, 79, 81, 91, 92, 96, 97, 103, 116, 122, 172).

[118] S. Krinner, S. Lazar, A. Remm, C. Andersen, N. Lacroix, G. Norris, et al. "Benchmarking Coherent Errors in Controlled-Phase Gates due to Spectator Qubits". In: *Phys. Rev. Appl.* 14 (2 Aug. 2020), p. 024042. DOI: 10.1103/PhysRevApplied.14.024042 (cit. on pp. 16, 141).

[119] Y. Ye, K. Peng, M. Naghiloo, G. Cunningham, and K. P. O'Brien. "Engineering Purely Nonlinear Coupling between Superconducting Qubits Using a Quarton". In: *Phys. Rev. Lett.* 127 (5 July 2021), p. 050502. DOI: 10.1103/PhysRevLett.127.050502 (cit. on pp. 16, 129, 172).

[120] A. A. Chapple, O. Benhayoune-Khadraoui, S. Richer, and A. Blais. "Balanced cross-Kerr coupling for superconducting qubit readout". In: *arXiv preprint arXiv:2501.09010* (2025) (cit. on pp. 17, 129, 133, 143, 172, 173).

[121] W. K. Wootters. "Quantum entanglement as a quantifiable resource". In: *Phil. Trans. R. Soc. A.* 356.1743 (1998), pp. 1717–1731. DOI: 10.1098/rsta.1998.0244 (cit. on p. 18).

[122] R. Horodecki, P. Horodecki, M. Horodecki, and K. Horodecki. "Quantum entanglement". In: *Rev. Mod. Phys.* 81.2 (2009), p. 865. DOI: 10.1103/RevModPhys.81.865 (cit. on p. 18).

[123] C. H. Bennett. "Quantum information". In: *Phys. Scr.* 1998.T76 (1998), p. 210. DOI: 10.1238/physica.topical.076a00210 (cit. on p. 18).

[124] H. J. Kimble. "The quantum internet". In: *Nature* 453.7198 (2008), pp. 1023–1030. DOI: 10.1038/nature07127 (cit. on p. 18).

[125] R. Jozsa. *Entanglement and quantum computation, appearing in Geometric issues in the foundations of science, Huggett S et. al., eds*. 1997. DOI: 10.48550/arXiv.quant-ph/9707034 (cit. on p. 18).

[126] J. Kempe. "Multiparticle entanglement and its applications to cryptography". In: *Phys. Rev. A* 60.2 (1999), p. 910. DOI: 10.1103/PhysRevA.60.910 (cit. on p. 18).

[127] R. Raussendorf, D. E. Browne, and H. J. Briegel. "Measurement-based quantum computation on cluster states". In: *Phys. Rev. A* 68.2 (2003), p. 022312. DOI: 10.1103/PhysRevA.68.022312 (cit. on p. 18).

[128] R. Raussendorf, J. Harrington, and K. Goyal. "Topological fault-tolerance in cluster state quantum computation". In: *New J. Phys.* 9.6 (2007), p. 199. DOI: 10.1088/1367-2630/9/6/199 (cit. on pp. 18, 28, 62).

[129] H. J. Briegel, D. E. Browne, W. Dür, R. Raussendorf, and M. Van den Nest. "Measurement-based quantum computation". In: *Nat. Phys.* 5.1 (2009), pp. 19–26. DOI: 10.1038/nphys1157 (cit. on p. 18).

[130] M. A. Nielsen. "Optical quantum computation using cluster states". In: *Phys. Rev. Lett.* 93.4 (2004), p. 040503. DOI: 10.1103/PhysRevLett.93.040503 (cit. on p. 18).

[131] D. E. Browne and T. Rudolph. "Resource-efficient linear optical quantum computation". In: *Phys. Rev. Lett.* 95.1 (2005), p. 010501. DOI: 10.1103/PhysRevLett.95.010501 (cit. on p. 18).

[132] P. Kok, W. J. Munro, K. Nemoto, T. C. Ralph, J. P. Dowling, and G. J. Milburn. "Linear optical quantum computing with photonic qubits". In: *Rev. Mod. Phys.* 79.1 (2007), p. 135. DOI: 10.1103/RevModPhys.79.135 (cit. on p. 18).

[133] C. Schön, E. Solano, F. Verstraete, J. I. Cirac, and M. M. Wolf. "Sequential generation of entangled multiqubit states". In: *Physical review letters* 95.11 (2005), p. 110503. DOI: 10.1103/PhysRevLett.95.110503 (cit. on p. 18).

[134] N. H. Lindner and T. Rudolph. "Proposal for pulsed on-demand sources of photonic cluster state strings". In: *Phys. Rev. Lett.* 103.11 (2009), p. 113602. DOI: 10.1103/PhysRevLett.103.113602 (cit. on pp. 18, 19).

[135] I. Schwartz, D. Cogan, E. R. Schmidgall, Y. Don, L. Gantz, O. Kenneth, et al. "Deterministic generation of a cluster state of entangled photons". In: *Science* 354.6311 (2016), pp. 434–437. DOI: 10.1126/science.aah4758 (cit. on pp. 18, 19).

[136] P. Thomas, L. Ruscio, O. Morin, and G. Rempe. "Efficient generation of entangled multi-photon graph states from a single atom". In: *Nature* 608.7924 (2022), pp. 677–681. DOI: 10.1038/s41586-022-04987-5 (cit. on p. 18).

[137] C. Liu, E. Barnes, and S. Economou. "Proposal for generating complex microwave graph states using superconducting circuits". In: *arXiv preprint arXiv:2201.00836* (2022). DOI: 10.48550/ARXIV.2201.00836 (cit. on p. 18).

[138] H. Pichler, S. Choi, P. Zoller, and M. D. Lukin. "Universal photonic quantum computation via time-delayed feedback". In: *PNAS* 114.43 (2017), pp. 11362–11367. DOI: 10.1073/pnas.1711003114 (cit. on pp. 19, 21, 22, 27, 32, 73, 75).

[139] K. Wan, S. Choi, I. H. Kim, N. Shutty, and P. Hayden. "Fault-tolerant qubit from a constant number of components". In: *PRX Quant.* 2.4 (2021), p. 040345. DOI: 10.1103/PRXQuantum.2.040345 (cit. on pp. 19, 28, 62, 75, 76, 171).

[140] Y. Shi and E. Waks. "Deterministic generation of multidimensional photonic cluster states using time-delay feedback". In: *Phys. Rev. A* 104.1 (2021), p. 013703. DOI: 10.1103/PhysRevA.104.013703 (cit. on pp. 19, 28, 62, 75, 76).

[141] Y. Zhan and S. Sun. "Deterministic generation of loss-tolerant photonic cluster states with a single quantum emitter". In: *Phys. Rev. Lett.* 125.22 (2020), p. 223601. DOI: 10.1103/PhysRevLett.125.223601 (cit. on p. 19).

[142] S. Xu and S. Fan. "Generate tensor network state by sequential single-photon scattering in waveguide QED systems". In: *APL Phot.* 3.11 (2018), p. 116102. DOI: 10.1063/1.5044248 (cit. on p. 19).

[143] A. Goban, C.-L. Hung, S.-P. Yu, J. Hood, J. Muniz, J. Lee, et al. "Atom–light interactions in photonic crystals". In: *Nat. Comm.* 5.1 (2014), pp. 1–9. DOI: 10.1038/ncomms4808 (cit. on p. 19).

[144] N. V. Corzo, J. Raskop, A. Chandra, A. S. Sheremet, B. Gouraud, and J. Laurat. "Waveguide-coupled single collective excitation of atomic arrays". In: *Nature* 566.7744 (2019), pp. 359–362. DOI: 10.1038/s41586-019-0902-3 (cit. on p. 19).

[145] C. Lang, C. Eichler, L. Steffen, J. Fink, M. J. Woolley, A. Blais, et al. "Correlations, indistinguishability and entanglement in Hong–Ou–Mandel experiments at microwave frequencies". In: *Nat. Phys.* 9.6 (2013), pp. 345–348. DOI: 10.1038/nphys2612 (cit. on p. 19).

[146] C. Eichler, J. Mlynek, J. Butscher, P. Kurpiers, K. Hammerer, T. J. Osborne, et al. "Exploring interacting quantum many-body systems by experimentally creating continuous matrix product states in superconducting circuits". In: *Phys. Rev. X* 5.4 (2015), p. 041044. DOI: 10.1103/PhysRevX.5.041044 (cit. on p. 19).

[147] B. Kannan, D. L. Campbell, F. Vasconcelos, R. Winik, D. Kim, M. Kjaergaard, et al. "Generating spatially entangled itinerant photons with waveguide quantum electrodynamics". In: *Science Advances* 6.41 (2020), eabb8780. DOI: 10.1126/sciadv.abb8780 (cit. on p. 19).

[148] J.-C. Besse, K. Reuer, M. C. Collodo, A. Wulff, L. Wernli, A. Copetudo, et al. "Realizing a Deterministic Source of Multipartite-Entangled Photonic Qubits". In: *Nat. Commun.* 11.4877 (2020). DOI: 10.1038/s41467-020-18635-x (cit. on p. 19).

[149] V. S. Ferreira, J. Banker, A. Sipahigil, M. H. Matheny, A. J. Keller, E. Kim, et al. "Collapse and Revival of an Artificial Atom Coupled to a Structured Photonic Reservoir". In: *Phys. Rev. X* 11.4 (2021), p. 041043. DOI: 10.1103/PhysRevX.11.041043 (cit. on pp. 21, 29, 31, 33, 38, 42, 79, 81, 82, 97, 116, 122).

[150] A. González-Tudela and J. I. Cirac. "Markovian and non-Markovian dynamics of quantum emitters coupled to two-dimensional structured reservoirs". In: *Phys. Rev. A* 96.4 (2017), p. 043811. DOI: 10.1103/PhysRevA.96.043811 (cit. on pp. 21, 39, 81, 98).

[151] F. Beaudoin, M. P. da Silva, Z. Dutton, and A. Blais. "First-order sidebands in circuit QED using qubit frequency modulation". In: *Phys. Rev. A* 86.2 (2012), p. 022305. DOI: 10.1103/PhysRevA.86.022305 (cit. on pp. 22, 46).

[152] J. Strand, M. Ware, F. Beaudoin, T. Ohki, B. Johnson, A. Blais, et al. "First-order sideband transitions with flux-driven asymmetric transmon qubits". In: *Physical Review B* 87.22 (2013), p. 220505. DOI: 10.1103/PhysRevB.87.220505 (cit. on pp. 22, 46).

[153] M. Silveri, J. Tuorila, E. Thuneberg, and G. Paraoanu. "Quantum systems under frequency modulation". In: *Reports on Progress in Physics* 80.5 (2017), p. 056002. DOI: 10.1088/1361-6633/aa5170 (cit. on pp. 22, 46, 79).

[154] M. Pechal, L. Huthmacher, C. Eichler, S. Zeytinoğlu, A. Abdumalikov Jr, S. Berger, et al. "Microwave-controlled generation of shaped single photons in circuit quantum electrodynamics". In: *Phys. Rev. X* 4.4 (2014), p. 041010. DOI: 10.1103/PhysRevX.4.041010 (cit. on pp. 24, 112, 113).

[155] P. Forn-Diaz, C. Warren, C. Chang, A. Vadiraj, and C. Wilson. "On-demand microwave generator of shaped single photons". In: *Phys. Rev. Appl.* 8.5 (2017), p. 054015. DOI: 10.1103/PhysRevApplied.8.054015 (cit. on p. 24).

[156] J. Ilves, S. Kono, Y. Sunada, S. Yamazaki, M. Kim, K. Koshino, et al. "On-demand generation and characterization of a microwave time-bin qubit". In: *npj Quantum Inf.* 6.1 (2020), pp. 1–7. DOI: 10.1038/s41534-020-0266-4 (cit. on pp. 24, 171).

[157] K. Reuer, J.-C. Besse, L. Wernli, P. Magnard, P. Kurpiers, G. J. Norris, et al. "Realization of a universal quantum gate set for itinerant microwave photons". In: *Phys. Rev. X* 12.1 (2022), p. 011008. DOI: 10.1103/PhysRevX.12.011008 (cit. on pp. 24, 25).

[158] C. Eichler, D. Bozyigit, and A. Wallraff. "Characterizing Quantum Microwave Radiation and its Entanglement with Superconducting Qubits using Linear Detectors". In: *Phys. Rev. A* 86 (2012), p. 032106. DOI: 10.1103/PhysRevA.86.032106 (cit. on pp. 25, 27, 59, 66).

[159] M. Hein, J. Eisert, and H. J. Briegel. "Multiparty entanglement in graph states". In: *Physical Review A* 69.6 (2004), p. 062311 (cit. on pp. 27, 61).

[160] A. Shearrow, G. Koolstra, S. J. Whiteley, N. Earnest, P. S. Barry, F. J. Heremans, et al. "Atomic layer deposition of titanium nitride for quantum circuits". In: *Appl. Phys. Lett.* 113.21 (2018), p. 212601. DOI: 10.1063/1.5053461 (cit. on pp. 28, 75).

[161] L. Grünhaupt, N. Maleeva, S. T. Skacel, M. Calvo, F. Levy-Bertrand, A. V. Ustinov, et al. "Loss mechanisms and quasiparticle dynamics in superconducting microwave resonators made of thin-film granular aluminum". In: *Phys. Rev. Lett.* 121.11 (2018), p. 117001. DOI: 10.1103/PhysRevLett.121.117001 (cit. on pp. 28, 75).

[162] A. Bienfait, K. J. Satzinger, Y. Zhong, H.-S. Chang, M.-H. Chou, C. R. Conner, et al. "Phonon-mediated quantum state transfer and remote qubit entanglement". In: *Science* 364.6438 (2019), pp. 368–371. DOI: 10.1126/science.aaw8415 (cit. on pp. 28, 75).

[163] G. Andersson, B. Suri, L. Guo, T. Aref, and P. Delsing. "Non-exponential decay of a giant artificial atom". In: *Nat. Phys.* 15.11 (2019), pp. 1123–1127. DOI: 10.1038/s41567-019-0605-6 (cit. on pp. 28, 75).

[164] É. Dumur, K. Satzinger, G. Peairs, M.-H. Chou, A. Bienfait, H.-S. Chang, et al. "Quantum communication with itinerant surface acoustic wave phonons". In: *npj Quantum Inf.* 7.1 (2021), pp. 1–5. DOI: 10.1038/s41534-021-00511-1 (cit. on pp. 28, 75).

[165] S. Barrett and T. Stace. "Fault Tolerant Quantum Computation with Very High Threshold". In: *Physical review letters* 105.20 (2010), p. 200502. DOI: 10.1103/PhysRevLett.105.200502 (cit. on p. 28).

[166] M. Mirhosseini, E. Kim, X. Zhang, A. Sipahigil, P. B. Dieterle, A. J. Keller, et al. "Cavity quantum electrodynamics with atom-like mirrors". In: *Nature* 569.7758 (2019), p. 692. DOI: 10.1038/s41586-019-1196-1 (cit. on pp. 29, 31).

[167] A. J. Keller, P. B. Dieterle, M. Fang, B. Berger, J. M. Fink, and O. Painter. "Al transmon qubits on silicon-on-insulator for quantum device integration". In: *Appl. Phys. Lett.* 111.4 (2017), p. 042603. DOI: 10.1063/1.4994661 (cit. on pp. 31, 168).

[168] S. Krinner, S. Storz, P. Kurpiers, P. Magnard, J. Heinsoo, R. Keller, et al. "Engineering cryogenic setups for 100-qubit scale superconducting circuit systems". In: *EPJ Quant. Tech.* 6.1 (2019), p. 2. DOI: 10.1140/epjqt/s40507-019-0072-0 (cit. on p. 31).

[169] C. Macklin, K. O'Brien, D. Hover, M. E. Schwartz, V. Bolkhovsky, X. Zhang, et al. "A near–quantum-limited Josephson traveling-wave parametric amplifier". In: *Science* 350 (6258 Oct. 2015), pp. 307–310. DOI: 10.1126/science.aaa8525 (cit. on p. 31).

[170] R. Engelen, Y. Sugimoto, Y. Watanabe, J. Korterik, N. Ikeda, N. van Hulst, et al. "The effect of higher-order dispersion on slow light propagation in photonic crystal waveguides". In: *Opt. Express* 14.4 (Feb. 2006), pp. 1658–1672. DOI: 10.1364/OE.14.001658 (cit. on p. 34).

[171] R. Barends, J. Kelly, A. Megrant, D. Sank, E. Jeffrey, Y. Chen, et al. "Coherent Josephson qubit suitable for scalable quantum integrated circuits". In: *Phys. Rev. Lett.* 111.8 (2013), p. 080502. DOI: 10.1103/PhysRevLett.111.080502 (cit. on p. 39).

[172] E. Jeffrey, D. Sank, J. Y. Mutus, T. C. White, J. Kelly, R. Barends, et al. "Fast Accurate State Measurement with Superconducting Qubits". In: *Phys. Rev. Lett.* 112 (19 May 2014), p. 190504. DOI: 10.1103/PhysRevLett.112.190504 (cit. on pp. 41, 79).

[173] N. T. Bronn, V. P. Adiga, S. B. Olivadese, X. Wu, J. M. Chow, and D. P. Pappas. "High coherence plane breaking packaging for superconducting qubits". In: *Quantum Sci. Technol.* 3.2 (2018), p. 024007. DOI: 10.1088/2058-9565/aaa645 (cit. on pp. 41, 75).

[174] E. A. Sete, J. M. Martinis, and A. N. Korotkov. "Quantum theory of a bandpass Purcell filter for qubit readout". In: *Phys. Rev. A* 92 (1 July 2015), p. 012325. DOI: 10.1103/PhysRevA.92.012325 (cit. on p. 41).

[175] A. Y. Cleland, M. Pechal, P.-J. C. Stas, C. J. Sarabalis, E. A. Wollack, and A. H. Safavi-Naeini. "Mechanical Purcell filters for microwave quantum machines". In: *Applied Physics Letters* 115.26 (2019), p. 263504. DOI: 10.1063/1.5111151 (cit. on p. 41).

[176] D. M. Pozar. *Microwave engineering; 3rd ed.* Hoboken, NJ: Wiley, 2005 (cit. on p. 41).

[177] M. A. Rol, L. Ciorciaro, F. K. Malinowski, B. M. Tarasinski, R. E. Sagastizabal, C. C. Bultink, et al. "Time-domain characterization and correction of on-chip distortion of control pulses in a quantum processor". In: *Appl. Phys. Lett.* 116.5 (2020), p. 054001. DOI: 10.1063/1.5133894 (cit. on pp. 45, 46).

[178] B. R. Johnson. *Controlling photons in superconducting electrical circuits*. Yale University, 2011 (cit. on p. 46).

[179] N. Didier, E. A. Sete, M. P. da Silva, and C. Rigetti. "Analytical modeling of parametrically modulated transmon qubits". In: *Phys. Rev. A* 97 (2 Feb. 2018), p. 022330. DOI: 10.1103/PhysRevA.97.022330 (cit. on pp. 47, 48).

[180] C. Eichler. "Experimental characterization of quantum microwave radiation and its entanglement with a superconducting qubit". PhD thesis. ETH Zurich, 2013. DOI: 10.3929/ethz-a-009771047 (cit. on p. 51).

[181] J. Koch, T. M. Yu, J. Gambetta, A. A. Houck, D. I. Schuster, J. Majer, et al. "Charge-insensitive qubit design derived from the Cooper pair box". In: *Phys. Rev. A* 76 (Oct. 2007), p. 042319. DOI: 10.1103/PhysRevA.76.042319 (cit. on p. 54).

[182] I.-C. Hoi. *Quantum optics with propagating microwaves in superconducting circuits*. Chalmers University of Technology, 2013 (cit. on p. 55).

[183] J. M. Chow, J. M. Gambetta, A. D. Córcoles, S. T. Merkel, J. A. Smolin, C. Rigetti, et al. "Universal Quantum Gate Set Approaching Fault-Tolerant Thresholds with Superconducting Qubits". In: *Phys. Rev. Lett.* 109.6 (2012), p. 060501. DOI: 10.1103/PhysRevLett.109.060501 (cit. on p. 59).

[184] S. Diamond and S. Boyd. "CVXPY: A Python-embedded modeling language for convex optimization". In: *Journal of Machine Learning Research* 17.83 (2016), pp. 1–5 (cit. on pp. 60, 68).

[185] D. C. McKay, C. J. Wood, S. Sheldon, J. M. Chow, and J. M. Gambetta. "Efficient Z gates for quantum computing". In: *Phys. Rev. A* 96.2 (2017), p. 022330. DOI: 10.1103/PhysRevA.96.022330 (cit. on p. 62).

[186] M. P. da Silva, D. Bozyigit, A. Wallraff, and A. Blais. "Schemes for the observation of photon correlation functions in circuit QED with linear detectors". In: *Phys.Rev. A* 82.4 (2010), p. 043804. DOI: 10.1103/PhysRevA.82.043804 (cit. on p. 65).

[187] M. Nielsen and I. L. Chuang. *Quantum Computation and Quantum Information*. Cambridge University Press, 2010. DOI: doi:10.1017/CBO9780511976667 (cit. on pp. 65, 115).

[188] E. Nielsen, J. K. Gamble, K. Rudin, T. Scholten, K. Young, and R. Blume-Kohout. "Gate Set Tomography". In: *Quantum* 5 (2021), p. 557. DOI: 10.22331/q-2021-10-05-557 (cit. on p. 65).

[189] E. Nielsen, R. Blume-Kohout, L. Saldyt, J. Gross, T. Scholten, K. Rudinger, et al. *PyGSTi version 0.9.9.1*. 2020. DOI: 10.5281/zenodo.3675466 (cit. on p. 69).

[190] A. C. Keith, C. H. Baldwin, S. Glancy, and E. Knill. "Joint quantum-state and measurement tomography with incomplete measurements". In: *Phys. Rev. A* 98 (4 Oct. 2018), p. 042318. DOI: 10.1103/PhysRevA.98.042318 (cit. on p. 71).

[191] J. Bylander, S. Gustavsson, F. Yan, F. Yoshihara, K. Harrabi, G. Fitch, et al. "Noise spectroscopy through dynamical decoupling with a superconducting flux qubit". In: *Nat. Phys.* 7.7 (2011), pp. 565–570. DOI: 10.1038/nphys1994 (cit. on pp. 72, 134, 137).

[192] M. Hutchings, J. B. Hertzberg, Y. Liu, N. T. Bronn, G. A. Keefe, M. Brink, et al. "Tunable superconducting qubits with flux-independent coherence". In: *Phys. Rev. Appl.* 8.4 (2017), p. 044003. DOI: 10.1103/PhysRevApplied.8.044003 (cit. on p. 74).

[193] Y. Chen, C. Neill, P. Roushan, N. Leung, M. Fang, R. Barends, et al. "Qubit architecture with high coherence and fast tunable coupling". In: *Phys. Rev. Lett.* 113.22 (2014), p. 220502. DOI: 10.1103/PhysRevLett.113.220502 (cit. on p. 74).

[194] A. Megrant, C. Neill, R. Barends, B. Chiaro, Y. Chen, L. Feigl, et al. "Planar superconducting resonators with internal quality factors above one million". In: *Appl. Phys. Lett.* 100.11 (2012), p. 113510. DOI: 10.1063/1.3693409 (cit. on p. 74).

[195] G. Calusine, A. Melville, W. Woods, R. Das, C. Stull, V. Bolkhovsky, et al. "Analysis and mitigation of interface losses in trenched superconducting coplanar waveguide resonators". In: *Appl. Phys. Lett.* 112.6 (2018), p. 062601. DOI: 10.1063/1.5006888 (cit. on p. 74).

[196] W. Woods, G. Calusine, A. Melville, A. Sevi, E. Golden, D. K. Kim, et al. "Determining interface dielectric losses in superconducting coplanar-waveguide resonators". In: *Phys. Rev. Appl.* 12.1 (2019), p. 014012. DOI: 10.1103/PhysRevApplied.12.014012 (cit. on pp. 74, 98).

[197] R. Killey, P. Watts, M. Glick, and P. Bayvel. "Electronic dispersion compensation by signal predistortion". In: *2006 Optical Fiber Communication Conference and the National Fiber Optic Engineers Conference*. IEEE. 2006, 3–pp. DOI: 10.1109/OFC.2006.215449 (cit. on p. 74).

[198] S. Ramachandran. *Fiber based dispersion compensation*. Vol. 5. Springer Science & Business Media, 2007. DOI: 10.1007/s10297-007-0084-x (cit. on p. 74).

[199] Z. Huang, A. Clerk, and I. Martin. "Nondispersing Wave Packets in Lattice Floquet Systems". In: *Physical Review Letters* 126.10 (2021), p. 100601. DOI: 10.1103/PhysRevLett.126.100601 (cit. on p. 74).

[200] L. B. Nguyen, Y.-H. Lin, A. Somoroff, R. Mencia, N. Grabon, and V. E. Manucharyan. "High-coherence fluxonium qubit". In: *Phys. Rev. X* 9.4 (2019), p. 041041. DOI: 10.1103/PhysRevX.9.041041 (cit. on p. 75).

[201] M. Yurtalan, J. Shi, G. Flatt, and A. Lupascu. "Characterization of Multilevel Dynamics and Decoherence in a High-Anharmonicity Capacitively Shunted Flux Circuit". In: *Phys. Rev. Appl.* 16.5 (2021), p. 054051. DOI: 10.1103/PhysRevApplied.16.054051 (cit. on p. 75).

[202] F. Yan, Y. Sung, P. Krantz, A. Kamal, D. K. Kim, J. L. Yoder, et al. "Engineering framework for optimizing superconducting qubit designs". In: *arXiv:2006.04130* (2020). DOI: 10.48550/ARXIV.2006.04130 (cit. on p. 75).

[203] S. Huang, B. Lienhard, G. Calusine, A. Vepsäläinen, J. Braumüller, D. K. Kim, et al. "Microwave package design for superconducting quantum processors". In: *PRX Quant.* 2.2 (2021), p. 020306. DOI: 10.1103/PRXQuantum.2.020306 (cit. on p. 75).

[204] S. Bartolucci, P. Birchall, H. Bombin, H. Cable, C. Dawson, M. Gimeno-Segovia, et al. "Fusion-based quantum computation". In: *arXiv:2101.09310* (2021). DOI: 10.48550/ARXIV.2101.09310 (cit. on p. 76).

[205] J. Wenner, Y. Yin, Y. Chen, R. Barends, B. Chiaro, E. Jeffrey, et al. "Catching time-reversed microwave coherent state photons with 99.4% absorption efficiency". In: *Phy. Rev. Lett.* 112.21 (2014), p. 210501. DOI: 10.1103/PhysRevLett.112.210501 (cit. on pp. 77, 172).

[206] P. Kurpiers, P. Magnard, T. Walter, B. Royer, M. Pechal, J. Heinsoo, et al. "Deterministic quantum state transfer and remote entanglement using microwave photons". In: *Nature* 558.7709 (2018), pp. 264–267. DOI: 10.1038/s41586-018-0195-y (cit. on p. 77).

[207] H. K. Ng, D. A. Lidar, and J. Preskill. "Combining dynamical decoupling with fault-tolerant quantum computation". In: *Phys. Rev. A* 84 (1 July 2011), p. 012305. DOI: 10.1103/PhysRevA.84.012305 (cit. on p. 78).

[208] M. D. Reed, L. DiCarlo, S. E. Nigg, L. Sun, L. Frunzio, S. M. Girvin, et al. "Realization of three-qubit quantum error correction with superconducting circuits". In: *Nature* 482.7385 (2012), pp. 382–385. DOI: 10.1038/nature10786 (cit. on p. 78).

[209] Z. Chen, K. J. Satzinger, J. Atalaya, A. N. Korotkov, A. Dunsworth, D. Sank, et al. "Exponential suppression of bit or phase errors with cyclic error correction". In: *Nature* 595.7867 (2021), pp. 383–387. DOI: 10.1038/s41586-021-03588-y (cit. on pp. 78, 115).

[210] S. Krinner, N. Lacroix, A. Remm, A. Di Paolo, E. Genois, C. Leroux, et al. "Realizing repeated quantum error correction in a distance-three surface code". In: *Nature* 605.7911 (2022), pp. 669–674. DOI: 10.1038/s41586-022-04566-8 (cit. on pp. 78, 93, 115).

[211] R. Acharya, I. Aleiner, R. Allen, T. I. Andersen, M. Ansmann, F. Arute, et al. "Suppressing quantum errors by scaling a surface code logical qubit". In: *Nature* 614.7949 (2023), pp. 676–681. DOI: 10.1038/s41586-022-05434-1 (cit. on p. 78).

[212] G. P. Gehér, M. Jastrzebski, E. T. Campbell, and O. Crawford. "To reset, or not to reset–that is the question". In: *arXiv preprint arXiv:2408.00758* (2024). DOI: 10.48550/arXiv.2408.00758 (cit. on pp. 78, 79).

[213] M. McEwen, D. Kafri, Z. Chen, J. Atalaya, K. J. Satzinger, C. Quintana, et al. "Removing leakage-induced correlated errors in superconducting quantum error correction". In: *Nat. Commun.* 12.1 (2021), p. 1761. DOI: 10.1038/s41467-021-21982-y (cit. on pp. 78, 79, 101, 104, 105, 129, 143).

[214] F. Battistel, B. Varbanov, and B. Terhal. "Hardware-Efficient Leakage-Reduction Scheme for Quantum Error Correction with Superconducting Transmon Qubits". In: *PRX Quantum* 2 (3 July 2021), p. 030314. DOI: 10.1103/PRXQuantum.2.030314 (cit. on pp. 78, 79).

[215] D. Ristè, J. G. van Leeuwen, H.-S. Ku, K. W. Lehnert, and L. DiCarlo. "Initialization by Measurement of a Superconducting Quantum Bit Circuit". In: *Phys. Rev. Lett.* 109 (5 Aug. 2012), p. 050507. DOI: 10.1103/PhysRevLett.109.050507 (cit. on pp. 78, 104, 105).

[216] D. Ristè, C. C. Bultink, K. W. Lehnert, and L. DiCarlo. "Feedback Control of a Solid-State Qubit Using High-Fidelity Projective Measurement". In: *Phys. Rev. Lett.* 109 (24 Dec. 2012), p. 240502. DOI: 10.1103/PhysRevLett.109.240502 (cit. on p. 78).

[217] J. E. Johnson, C. Macklin, D. H. Slichter, R. Vijay, E. B. Weingarten, J. Clarke, et al. "Heralded State Preparation in a Superconducting Qubit". In: *Phys. Rev. Lett.* 109 (5 Aug. 2012), p. 050506. DOI: 10.1103/PhysRevLett.109.050506 (cit. on p. 78).

[218] P. Campagne-Ibarcq, E. Flurin, N. Roch, D. Darson, P. Morfin, M. Mirrahimi, et al. "Persistent Control of a Superconducting Qubit by Stroboscopic Measurement Feedback". In: *Phys. Rev. X* 3 (2 May 2013), p. 021008. DOI: 10.1103/PhysRevX.3.021008 (cit. on pp. 78, 104, 105).

[219] K. Geerlings, Z. Leghtas, I. M. Pop, S. Shankar, L. Frunzio, R. J. Schoelkopf, et al. "Demonstrating a Driven Reset Protocol for a Superconducting Qubit". In: *Phys. Rev. Lett.* 110 (12 Mar. 2013), p. 120501. DOI: 10.1103/PhysRevLett.110.120501 (cit. on pp. 79, 104, 105).

[220] P. Magnard, P. Kurpiers, B. Royer, T. Walter, J.-C. Besse, S. Gasparinetti, et al. "Fast and Unconditional All-Microwave Reset of a Superconducting Qubit". In: *Phys. Rev. Lett.* 121 (6 Aug. 2018), p. 060502. DOI: 10.1103/PhysRevLett.121.060502 (cit. on pp. 79, 82, 93, 101, 104, 105, 112, 113, 143).

[221] Y. Zhou, Z. Zhang, Z. Yin, S. Huai, X. Gu, X. Xu, et al. "Rapid and unconditional parametric reset protocol for tunable superconducting qubits". In: *Nat. Commun.* 12.1 (2021), p. 5924. DOI: 10.1038/s41467-021-26205-y (cit. on pp. 79, 101, 104, 105, 143).

[222] Y. Sunada, S. Kono, J. Ilves, S. Tamate, T. Sugiyama, Y. Tabuchi, et al. "Fast Readout and Reset of a Superconducting Qubit Coupled to a Resonator with an Intrinsic Purcell Filter". In: *Phys. Rev. Appl.* 17 (4 Apr. 2022), p. 044016. DOI: 10.1103/PhysRevApplied.17.044016 (cit. on pp. 79, 104, 105).

[223] L. Chen, S. P. Fors, Z. Yan, A. Ali, T. Abad, A. Osman, et al. "Fast unconditional reset and leakage reduction in fixed-frequency transmon qubits". In: *arXiv preprint arXiv:2409.16748* (2024). DOI: 10.48550/arXiv.2409.16748 (cit. on pp. 79, 104).

[224] E. Purcell. "Spontaneous emission probabilities at radio frequency". In: *Phys. Pev.* 69 (1946), p. 681. DOI: 10.1007/978-1-4615-1963-8_40 (cit. on p. 79).

[225] V. S. Ferreira, G. Kim, A. Butler, H. Pichler, and O. Painter. "Deterministic generation of multidimensional photonic cluster states with a single quantum emitter". In: *Nat. Phys.* 20.5 (2024), pp. 865–870. DOI: 10.1038/s41567-024-02408-0 (cit. on pp. 79, 82, 90).

[226] F. Beaudoin, M. P. da Silva, Z. Dutton, and A. Blais. "First-order sidebands in circuit QED using qubit frequency modulation". In: *Phys. Rev. A* 86 (2 Aug. 2012), p. 022305. DOI: 10.1103/PhysRevA.86.022305 (cit. on p. 79).

[227] J. D. Strand, M. Ware, F. Beaudoin, T. A. Ohki, B. R. Johnson, A. Blais, et al. "First-order sideband transitions with flux-driven asymmetric transmon qubits". In: *Phys. Rev. B* 87 (22 June 2013), p. 220505. DOI: 10.1103/PhysRevB.87.220505 (cit. on p. 79).

[228] S. N. Shevchenko, S. Ashhab, and F. Nori. "Landau–zener–stückelberg interferometry". In: *Phys. Rep.* 492.1 (2010), pp. 1–30. DOI: 10.1016/j.physrep.2010.03.002 (cit. on pp. 82, 84, 100, 101).

[229] C. J. Wood and J. M. Gambetta. "Quantification and characterization of leakage errors". In: *Phys. Rev. A* 97 (3 Mar. 2018), p. 032306. DOI: 10.1103/PhysRevA.97.032306 (cit. on pp. 87, 88).

[230] G. Ithier, E. Collin, P. Joyez, P. J. Meeson, D. Vion, D. Esteve, et al. "Decoherence in a superconducting quantum bit circuit". In: *Phys. Rev. B* 72 (13 Oct. 2005), p. 134519. DOI: 10.1103/PhysRevB.72.134519 (cit. on p. 88).

[231] G. Huber, F. Roy, L. Koch, I. Tsitsilin, J. Schirk, N. Glaser, et al. "Parametric multi-element coupling architecture for coherent and dissipative control of superconducting qubits". In: *arXiv preprint arXiv:2403.02203* (2024). DOI: 10.48550/arXiv.2403.02203 (cit. on p. 87).

[232] E. Magesan, J. M. Gambetta, B. R. Johnson, C. A. Ryan, J. M. Chow, S. T. Merkel, et al. "Efficient Measurement of Quantum Gate Error by Interleaved Randomized Benchmarking". In: *Phys. Rev. Lett.* 109 (8 Aug. 2012), p. 080505. DOI: 10.1103/PhysRevLett.109.080505 (cit. on pp. 87, 106).

[233] J.-C. Besse, S. Gasparinetti, M. C. Collodo, T. Walter, P. Kurpiers, M. Pechal, et al. "Single-Shot Quantum Nondemolition Detection of Individual Itinerant Microwave Photons". In: *Phys. Rev. X* 8 (2 Apr. 2018), p. 021003. DOI: 10.1103/PhysRevX.8.021003 (cit. on p. 90).

[234] K. Reuer, J.-C. Besse, L. Wernli, P. Magnard, P. Kurpiers, G. J. Norris, et al. "Realization of a Universal Quantum Gate Set for Itinerant Microwave Photons". In: *Phys. Rev. X* 12 (1 Jan. 2022), p. 011008. DOI: 10.1103/PhysRevX.12.011008 (cit. on p. 90).

[235] N. M. Sundaresan, R. Lundgren, G. Zhu, A. V. Gorshkov, and A. A. Houck. "Interacting Qubit-Photon Bound States with Superconducting Circuits". In: *Phys. Rev. X* 9 (1 Feb. 2019), p. 011021. DOI: 10.1103/PhysRevX.9.011021 (cit. on p. 91).

[236] D. T. McClure, H. Paik, L. S. Bishop, M. Steffen, J. M. Chow, and J. M. Gambetta. "Rapid Driven Reset of a Qubit Readout Resonator". In: *Phys. Rev. Appl.* 5 (1 Jan. 2016), p. 011001. DOI: 10.1103/PhysRevApplied.5.011001 (cit. on p. 92).

[237] R. A. FISHER. "THE USE OF MULTIPLE MEASUREMENTS IN TAXONOMIC PROBLEMS". In: *Ann. Eugen.* 7.2 (1936), pp. 179–188. DOI: 10.1111/j.1469-1809.1936.tb02137.x (cit. on p. 93).

[238] F. Pedregosa, G. Varoquaux, A. Gramfort, V. Michel, B. Thirion, O. Grisel, et al. "Scikit-learn: Machine Learning in Python". In: *J. of Mach. Learn. Res.* 12 (2011), pp. 2825–2830 (cit. on p. 93).

[239] G. Calusine, A. Melville, W. Woods, R. Das, C. Stull, V. Bolkhovsky, et al. "Analysis and mitigation of interface losses in trenched superconducting coplanar waveguide resonators". In: *Appl. Phys. Lett.* 112.6 (Feb. 2018), p. 062601. DOI: 10.1063/1.5006888 (cit. on pp. 98, 166).

[240] L. Shi, T. Guo, R. Su, T. Chi, Y. Sheng, J. Jiang, et al. "Tantalum microwave resonators with ultra-high intrinsic quality factors". In: *Appl. Phys. Lett.* 121.24 (Dec. 2022), p. 242601. DOI: 10.1063/5.0124821 (cit. on pp. 98, 166).

[241] N. Kosugi, S. Matsuo, K. Konno, and N. Hatakenaka. "Theory of damped Rabi oscillations". In: *Phys. Rev. B* 72 (17 Nov. 2005), p. 172509. DOI: 10.1103/PhysRevB.72.172509 (cit. on pp. 99, 100).

[242] M. Spiecker, P. Paluch, N. Gosling, N. Drucker, S. Matityahu, D. Gusenkova, et al. "Two-level system hyperpolarization using a quantum Szilard engine". In: *Nat. Phys.* 19.9 (2023), pp. 1320–1325. DOI: 10.1038/s41567-023-02082-8 (cit. on p. 100).

[243] J. Johansson, P. Nation, and F. Nori. "QuTiP: An open-source Python framework for the dynamics of open quantum systems". In: *Comput. Phys. Commun.* 183.8 (2012), pp. 1760–1772. DOI: 10.1016/j.cpc.2012.02.021 (cit. on pp. 103, 133, 157).

[244] L. H. Pedersen, N. M. Møller, and K. Mølmer. "Fidelity of quantum operations". In: *Phys. Lett. A* 367.1 (2007), pp. 47–51. DOI: 10.1016/j.physleta.2007.02.069 (cit. on pp. 108, 134, 158, 160).

[245] C. Chamberland, G. Zhu, T. J. Yoder, J. B. Hertzberg, and A. W. Cross. "Topological and Subsystem Codes on Low-Degree Graphs with Flag Qubits". In: *Phys. Rev. X* 10 (1 Jan. 2020), p. 011022. DOI: 10.1103/PhysRevX.10.011022 (cit. on p. 115).

[246] B. Hetényi and J. R. Wootton. "Creating Entangled Logical Qubits in the Heavy-Hex Lattice with Topological Codes". In: *PRX Quantum* 5 (4 Dec. 2024), p. 040334. DOI: 10.1103/PRXQuantum.5.040334 (cit. on p. 115).

[247] F. Marxer, A. Vepsäläinen, S. W. Jolin, J. Tuorila, A. Landra, C. Ockeloen-Korppi, et al. "Long-Distance Transmon Coupler with cz-Gate Fidelity above 99.8%". In: *PRX Quantum* 4 (1 Feb. 2023), p. 010314. DOI: 10.1103/PRXQuantum.4.010314 (cit. on p. 116).

[248] M. Field, A. Q. Chen, B. Scharmann, E. A. Sete, F. Oruc, K. Vu, et al. "Modular superconducting-qubit architecture with a multichip tunable coupler". In: *Phys. Rev. Appl.* 21 (5 May 2024), p. 054063. DOI: 10.1103/PhysRevApplied.21.054063 (cit. on p. 116).

[249] H. Paik, A. Mezzacapo, M. Sandberg, D. T. McClure, B. Abdo, A. D. Córcoles, et al. "Experimental Demonstration of a Resonator-Induced Phase Gate in a Multiqubit Circuit-QED System". In: *Phys. Rev. Lett.* 117 (25 Dec. 2016), p. 250502. DOI: 10.1103/PhysRevLett.117.250502 (cit. on pp. 116, 120).

[250] M. Kumph, J. Raftery, A. Finck, J. Blair, A. Carniol, S. Carnevale, et al. "Demonstration of RIP gates in a quantum processor with negligible transverse coupling". In: *arXiv preprint arXiv:2406.11770* (2024). DOI: 10.48550/arXiv.2406.11770 (cit. on pp. 116, 120).

[251] F. Vigneau, S. Majumder, A. Rath, P. Parrado-Rodríguez, F. R. F. Pereira, H.-S. Ku, et al. "Quantum Error Detection in Qubit-Resonator Star Architecture". In: *PRX Quantum* 6 (4 Dec. 2025), p. 040369. DOI: 10.1103/8m33-wn4g (cit. on p. 116).

[252] M. Renger, J. Verjauw, N. Wurz, A. Hosseinkhani, C. Ockeloen-Korppi, W. Liu, et al. "Superconducting qubit-resonator quantum processor with effective all-to-all connectivity". In: *Phys. Rev. Res.* 8 (1 Feb. 2026), p. 013148. DOI: 10.1103/8x68-cx1w (cit. on p. 116).

[253] K. Mølmer and A. Sørensen. "Multiparticle Entanglement of Hot Trapped Ions". In: *Phys. Rev. Lett.* 82 (9 Mar. 1999), pp. 1835–1838. DOI: 10.1103/PhysRevLett.82.1835 (cit. on pp. 116, 120).

[254] A. V. Gorshkov, D. Cohen, A. Haim, A. Rotem, O. Golan, G. Kim, et al. *Cavity-mediated cross-cross-resonance gate*. 2025 (cit. on pp. 116, 119, 120, 141).

[255] A. Kubica, A. Haim, Y. Vaknin, H. Levine, F. Brandão, and A. Retzker. "Erasure Qubits: Overcoming the T_1 Limit in Superconducting Circuits". In: *Phys. Rev. X* 13 (4 Nov. 2023), p. 041022. DOI: 10.1103/PhysRevX.13.041022 (cit. on pp. 116, 120, 146, 170).

[256] A. Haim, J. S.-C. Hung, P. Arrangoiz-Arriola, F. G. Brandão, A. A. Clerk, A. Khalajhedayati, et al. "Erasure detection of transmon dual-rail qubit with symmetrically coupled readout (Part 1/2)". In: *SMT 2025*. APS. 2025 (cit. on pp. 116, 120).

[257] J. S.-C. Hung, A. Haim, P. Arrangoiz-Arriola, F. G. Brandão, A. A. Clerk, D. J. Hover, et al. "Erasure detection of transmon dual-rail qubit with symmetrically coupled readout (Part 2/2)". In: *SMT 2025*. APS. 2025 (cit. on pp. 116, 120).

[258] G. S. Paraoanu. "Microwave-induced coupling of superconducting qubits". In: *Phys. Rev. B* 74 (14 Oct. 2006), p. 140504. DOI: 10.1103/PhysRevB.74.140504 (cit. on p. 119).

[259] C. Rigetti and M. Devoret. "Fully microwave-tunable universal gates in superconducting qubits with linear couplings and fixed transition frequencies". In: *Phys. Rev. B* 81 (13 Apr. 2010), p. 134507. DOI: 10.1103/PhysRevB.81.134507 (cit. on p. 119).

[260] C. Figgatt, A. Ostrander, N. M. Linke, K. A. Landsman, D. Zhu, D. Maslov, et al. "Parallel entangling operations on a universal ion-trap quantum computer". In: *Nature* 572.7769 (2019), pp. 368–372. DOI: 10.1038/s41586-019-1427-5 (cit. on p. 120).

[261] A. Cowtan, S. Dilkes, R. Duncan, A. Krajenbrink, W. Simmons, and S. Sivarajah. "On the Qubit Routing Problem". In: *14th Conference on the Theory of Quantum Computation, Communication and Cryptography (TQC 2019)*. Ed. by W. van Dam and L. Mančinska. Vol. 135. Leibniz International Proceedings in Informatics (LIPIcs). Dagstuhl, Germany: Schloss Dagstuhl – Leibniz-Zentrum für Informatik, 2019, 5:1–5:32. DOI: 10.4230/LIPIcs.TQC.2019.5 (cit. on p. 125).

[262] B. Eastin and E. Knill. "Restrictions on Transversal Encoded Quantum Gate Sets". In: *Phys. Rev. Lett.* 102 (11 Mar. 2009), p. 110502. DOI: 10.1103/PhysRevLett.102.110502 (cit. on p. 125).

[263] V. Giovannetti, S. Lloyd, and L. Maccone. “Quantum Random Access Memory”. In: *Phys. Rev. Lett.* 100 (16 Apr. 2008), p. 160501. DOI: 10.1103/PhysRevLett.100.160501 (cit. on p. 126).

[264] Q. Xu, A. Seif, H. Yan, N. Mannucci, B. O. Sane, R. Van Meter, et al. “Distributed Quantum Error Correction for Chip-Level Catastrophic Errors”. In: *Phys. Rev. Lett.* 129 (24 Dec. 2022), p. 240502. DOI: 10.1103/PhysRevLett.129.240502 (cit. on p. 126).

[265] D. L. Campbell, A. Kamal, L. Ranzani, M. Senatore, and M. D. LaHaye. “Modular Tunable Coupler for Superconducting Circuits”. In: *Phys. Rev. Appl.* 19 (6 June 2023), p. 064043. DOI: 10.1103/PhysRevApplied.19.064043 (cit. on pp. 128, 129, 133, 135, 150).

[266] H. Goto. “Double-Transmon Coupler: Fast Two-Qubit Gate with No Residual Coupling for Highly Detuned Superconducting Qubits”. In: *Phys. Rev. Appl.* 18 (3 Sept. 2022), p. 034038. DOI: 10.1103/PhysRevApplied.18.034038 (cit. on pp. 128, 129, 135).

[267] J. Lisenfeld, A. Bilmes, A. Megrant, R. Barends, J. Kelly, P. Klimov, et al. “Electric field spectroscopy of material defects in transmon qubits”. In: *npj Quantum Information* 5.1 (2019), p. 105. DOI: 10.1038/s41534-019-0224-1 (cit. on p. 128).

[268] J. M. Martinis and M. R. Geller. “Fast adiabatic qubit gates using only σ_z control”. In: *Phys. Rev. A* 90 (2 Aug. 2014), p. 022307. DOI: 10.1103/PhysRevA.90.022307 (cit. on pp. 128, 134).

[269] R. Zhao, S. Park, T. Zhao, M. Bal, C. McRae, J. Long, et al. “Merged-Element Transmon”. In: *Phys. Rev. Appl.* 14 (6 Dec. 2020), p. 064006. DOI: 10.1103/PhysRevApplied.14.064006 (cit. on pp. 128, 133, 143).

[270] H. Mamin, E. Huang, S. Carnevale, C. Rettner, N. Arellano, M. Sherwood, et al. “Merged-Element Transmons: Design and Qubit Performance”. In: *Phys. Rev. Appl.* 16 (2 Aug. 2021), p. 024023. DOI: 10.1103/PhysRevApplied.16.024023 (cit. on pp. 128, 133, 143).

[271] E. Daum, B. Berlitz, S. Deck, A. V. Ustinov, and J. Lisenfeld. “Investigation of Parasitic Two-Level Systems in Merged-Element Transmon Qubits”. In: (2025). DOI: 10.48550/arXiv.2509.22593 (cit. on pp. 128, 133, 143).

[272] M. Kounalakis, C. Dickel, A. Bruno, N. K. Langford, and G. A. Steele. “Tuneable hopping and nonlinear cross-Kerr interactions in a high-coherence superconducting circuit”. In: *npj Quantum Information* 4.1 (2018), p. 38. DOI: 10.1038/s41534-018-0088-9 (cit. on pp. 129, 133).

[273] E. V. Stolyarov, V. L. Andriichuk, and A. M. Sokolov. “Two-photon coupling via Josephson element: Breaking the symmetry with magnetic fields”. In: *Phys. Rev. B* 111 (21 June 2025), p. 214517. DOI: 10.1103/w12t-92qg (cit. on pp. 129, 145).

[274] R. Li, K. Kubo, Y. Ho, Z. Yan, Y. Nakamura, and H. Goto. “Realization of High-Fidelity CZ Gate Based on a Double-Transmon Coupler”. In: *Phys. Rev. X* 14 (4 Nov. 2024), p. 041050. DOI: 10.1103/PhysRevX.14.041050 (cit. on p. 129).

[275] A. Chakraborty, B. Bhandari, D. D. Briseño-Colunga, N. Stevenson, Z. Pedramrazi, C.-H. Liu, et al. “Tunable Superconducting Quantum Interference Device Coupler for Fluxonium Qubits”. In: (2025). DOI: 10.48550/arXiv.2508.16907 (cit. on p. 129).

[276] M. Hays, J. Kim, and W. D. Oliver. “Nondegenerate Noise-Resilient Superconducting Qubit”. In: *PRX Quantum* 6 (4 Oct. 2025), p. 040321. DOI: 10.1103/dd96-gcb6 (cit. on p. 129).

[277] J. Braumüller, L. Ding, A. P. Vepsäläinen, Y. Sung, M. Kjaergaard, T. Menke, et al. “Characterizing and Optimizing Qubit Coherence Based on SQUID Geometry”. In: *Phys. Rev. Appl.* 13 (5 May 2020), p. 054079. DOI: 10.1103/PhysRevApplied.13.054079 (cit. on pp. 129, 137).

[278] W. C. Stewart. “CURRENT-VOLTAGE CHARACTERISTICS OF JOSEPHSON JUNCTIONS”. In: *Applied Physics Letters* 12.8 (Apr. 1968), pp. 277–280. DOI: 10.1063/1.1651991 (cit. on p. 133).

[279] M. Chen, J. C. Owens, H. Putterman, M. Schäfer, and O. Painter. “Phonon engineering of atomic-scale defects in superconducting quantum circuits”. In: *Science Advances* 10.37 (2024), eado6240. DOI: 10.1126/sciadv.ado6240 (cit. on pp. 133, 143).

[280] P. Groszkowski and J. Koch. “Scqubits: a Python package for superconducting qubits”. In: *Quantum* 5 (Nov. 2021), p. 583. DOI: 10.22331/q-2021-11-17-583 (cit. on pp. 133, 157).

[281] L. Allen and J. H. Eberly. *Optical resonance and two-level atoms*. Courier Corporation, 2012 (cit. on p. 133).

[282] J. M. Chávez-Garcia, F. Solgun, J. B. Hertzberg, O. Jinka, M. Brink, and B. Abdo. "Weakly Flux-Tunable Superconducting Qubit". In: *Phys. Rev. Appl.* 18 (3 Sept. 2022), p. 034057. DOI: 10.1103/PhysRevApplied.18.034057 (cit. on p. 134).

[283] A. Baksic, H. Ribeiro, and A. A. Clerk. "Speeding up Adiabatic Quantum State Transfer by Using Dressed States". In: *Phys. Rev. Lett.* 116 (23 June 2016), p. 230503. DOI: 10.1103/PhysRevLett.116.230503 (cit. on p. 134).

[284] C. Hellings, N. Lacroix, A. Remm, R. Boell, J. Herrmann, S. Laz ăr, et al. "Calibrating magnetic flux control in superconducting circuits by compensating distortions on timescales from nanoseconds up to tens of microseconds". In: *Phys. Rev. Res.* 7 (4 Nov. 2025), p. 043142. DOI: 10.1103/1qhb-r4fb (cit. on p. 134).

[285] M. J. Schwarz, J. Goetz, Z. Jiang, T. Niemczyk, F. Deppe, A. Marx, et al. "Gradiometric flux qubits with a tunable gap". In: *New Journal of Physics* 15.4 (Apr. 2013), p. 045001. DOI: 10.1088/1367-2630/15/4/045001 (cit. on pp. 136, 142).

[286] J. Braumüller, M. Sandberg, M. R. Vissers, A. Schneider, S. Schlör, L. Grünhaupt, et al. "Concentric transmon qubit featuring fast tunability and an anisotropic magnetic dipole moment". In: *Applied Physics Letters* 108.3 (Jan. 2016), p. 032601. DOI: 10.1063/1.4940230 (cit. on pp. 136, 142).

[287] Y. Ye, J. B. Kline, A. Yen, G. Cunningham, M. Tan, A. Zang, et al. "Near-ultrastrong nonlinear light-matter coupling in superconducting circuits". In: *Nature Communications* 16.1 (2025), p. 3799. DOI: 10.1038/s41467-025-59152-z (cit. on pp. 136, 142).

[288] E. L. Rosenfeld, C. T. Hann, D. I. Schuster, M. H. Matheny, and A. A. Clerk. "High-Fidelity Two-Qubit Gates between Fluxonium Qubits with a Resonator Coupler". In: *PRX Quantum* 5 (4 Nov. 2024), p. 040317. DOI: 10.1103/PRXQuantum.5.040317 (cit. on p. 139).

[289] T.-Q. Cai, X.-Y. Han, Y.-K. Wu, Y.-L. Ma, J.-H. Wang, Z.-L. Wang, et al. "Impact of Spectators on a Two-Qubit Gate in a Tunable Coupling Superconducting Circuit". In: *Phys. Rev. Lett.* 127 (6 Aug. 2021), p. 060505. DOI: 10.1103/PhysRevLett.127.060505 (cit. on p. 141).

[290] P. Jurcevic and L. C. G. Govia. "Effective qubit dephasing induced by spectator-qubit relaxation". In: *Quantum Science and Technology* 7.4 (Sept. 2022), p. 045033. DOI: 10.1088/2058-9565/ac8cad (cit. on p. 141).

[291] A. Morvan, L. Chen, J. M. Larson, D. I. Santiago, and I. Siddiqi. "Optimizing frequency allocation for fixed-frequency superconducting quantum processors". In: *Phys. Rev. Res.* 4 (2 Apr. 2022), p. 023079. DOI: 10.1103/PhysRevResearch.4.023079 (cit. on p. 142).

[292] E. Hyyppä, S. Kundu, C. F. Chan, A. Gunyhó, J. Hotari, D. Janzso, et al. "Unimon qubit". In: *Nature Communications* 13.1 (2022), p. 6895. DOI: 10.1038/s41467-022-34614-w (cit. on p. 142).

[293] G. Kim, A. Butler, V. S. Ferreira, X. (Zhang, A. Hadley, E. Kim, et al. "Fast unconditional reset and leakage reduction of a tunable superconducting qubit via an engineered dissipative bath". In: *Phys. Rev. Appl.* 24 (1 July 2025), p. 014013. DOI: 10.1103/6wc6-78y3 (cit. on p. 143).

[294] J. Zotova, R. Wang, A. Semenov, Y. Zhou, I. Khrapach, A. Tomonaga, et al. "Compact Superconducting Microwave Resonators Based on Al-AlO_x-Al Capacitors". In: *Phys. Rev. Appl.* 19 (4 Apr. 2023), p. 044067. DOI: 10.1103/PhysRevApplied.19.044067 (cit. on p. 143).

[295] M. T. Bell, I. A. Sadovskyy, L. B. Ioffe, A. Y. Kitaev, and M. E. Gershenson. "Quantum Superinductor with Tunable Nonlinearity". In: *Phys. Rev. Lett.* 109 (13 Sept. 2012), p. 137003. DOI: 10.1103/PhysRevLett.109.137003 (cit. on p. 143).

[296] I. V. Pechenezhskiy, R. A. Mencia, L. B. Nguyen, Y.-H. Lin, and V. E. Manucharyan. "The superconducting quasicharge qubit". In: *Nature* 585.7825 (2020), pp. 368–371. DOI: 10.1038/s41586-020-2687-9 (cit. on p. 143).

[297] C. Jünger, T. Chistolini, L. B. Nguyen, H. Kim, L. Chen, T. Ersevim, et al. "Implementation of scalable suspended superinductors". In: *Applied Physics Letters* 126.4 (Jan. 2025), p. 044003. DOI: 10.1063/5.0250341 (cit. on p. 143).

[298] C. R. Conner, A. Bienfait, H.-S. Chang, M.-H. Chou, É. Dumur, J. Grebel, et al. "Superconducting qubits in a flip-chip architecture". In: *Applied Physics Letters* 118.23 (June 2021), p. 232602. DOI: 10.1063/5.0050173 (cit. on p. 143).

[299] S. Kosen, H.-X. Li, M. Rommel, D. Shiri, C. Warren, L. Grönberg, et al. "Building blocks of a flip-chip integrated superconducting quantum processor". In: *Quantum Science and Technology* 7.3 (June 2022), p. 035018. DOI: 10.1088/2058-9565/ac734b (cit. on p. 143).

[300] R. O. Behunin, F. Intravaia, and P. T. Rakich. "Dimensional transformation of defect-induced noise, dissipation, and nonlinearity". In: *Phys. Rev. B* 93 (22 June 2016), p. 224110. DOI: 10.1103/PhysRevB.93.224110 (cit. on p. 143).

[301] G. S. MacCabe, H. Ren, J. Luo, J. D. Cohen, H. Zhou, A. Sipahigil, et al. "Nano-acoustic resonator with ultralong phonon lifetime". In: *Science* 370.6518 (2020), pp. 840–843. DOI: 10.1126/science.abc7312 (cit. on p. 143).

[302] M. Odeh, K. Godeneli, E. Li, R. Tangirala, H. Zhou, X. Zhang, et al. "Non-Markovian dynamics of a superconducting qubit in a phononic bandgap". In: *Nature Physics* 21.3 (2025), pp. 406–411. DOI: 10.1038/s41567-024-02740-5 (cit. on p. 143).

[303] Z. Leghtas, S. Touzard, I. M. Pop, A. Kou, B. Vlastakis, A. Petrenko, et al. "Confining the state of light to a quantum manifold by engineered two-photon loss". In: *Science* 347.6224 (2015), pp. 853–857. DOI: 10.1126/science.aaa2085 (cit. on p. 145).

[304] R. Lescanne, M. Villiers, T. Peronnin, A. Sarlette, M. Delbecq, B. Huard, et al. "Exponential suppression of bit-flips in a qubit encoded in an oscillator". In: *Nature Physics* 16.5 (2020), pp. 509–513. DOI: 10.1038/s41567-020-0824-x (cit. on p. 145).

[305] A. Marquet, A. Essig, J. Cohen, N. Cottet, A. Murani, E. Albertinale, et al. "Autoparametric Resonance Extending the Bit-Flip Time of a Cat Qubit up to 0.3 s". In: *Phys. Rev. X* 14 (2 Apr. 2024), p. 021019. DOI: 10.1103/PhysRevX.14.021019 (cit. on p. 145).

[306] H. Putterman, K. Noh, R. N. Patel, G. A. Peairs, G. S. MacCabe, M. Lee, et al. "Preserving Phase Coherence and Linearity in Cat Qubits with Exponential Bit-Flip Suppression". In: *Phys. Rev. X* 15 (1 Mar. 2025), p. 011070. DOI: 10.1103/PhysRevX.15.011070 (cit. on p. 145).

[307] H. Levine, A. Haim, J. S. C. Hung, N. Alidoust, M. Kalaee, L. DeLorenzo, et al. "Demonstrating a Long-Coherence Dual-Rail Erasure Qubit Using Tunable Transmons". In: *Phys. Rev. X* 14 (1 Mar. 2024), p. 011051. DOI: 10.1103/PhysRevX.14.011051 (cit. on pp. 146, 170, 171).

[308] K. S. Chou, T. Shemma, H. McCarrick, T.-C. Chien, J. D. Teoh, P. Winkel, et al. "A superconducting dual-rail cavity qubit with erasure-detected logical measurements". In: *Nature Physics* 20.9 (2024), pp. 1454–1460. DOI: 10.1038/s41567-024-02539-4 (cit. on pp. 146, 171).

[309] U. Vool and M. Devoret. "Introduction to quantum electromagnetic circuits". In: *International Journal of Circuit Theory and Applications* 45.7 (2017), pp. 897–934. DOI: 10.1002/cta.2359 (cit. on p. 147).

[310] X. You, J. A. Sauls, and J. Koch. "Circuit quantization in the presence of time-dependent external flux". In: *Phys. Rev. B* 99 (17 May 2019), p. 174512. DOI: 10.1103/PhysRevB.99.174512 (cit. on pp. 147, 150).

[311] R. .-. Riwar and D. P. DiVincenzo. "Circuit quantization with time-dependent magnetic fields for realistic geometries". In: *npj Quantum Information* 8.1 (2022), p. 36. DOI: 10.1038/s41534-022-00539-x (cit. on p. 147).

[312] W. McCrea. "Operational proofs of some identities". In: *The Mathematical Gazette* 17.222 (1933), pp. 43–45 (cit. on p. 155).

[313] A. J. Kerman. "Efficient numerical simulation of complex Josephson quantum circuits". In: (2020). DOI: 10.48550/arXiv.2010.14929 (cit. on pp. 158, 159).

[314] S. P. Chitta, T. Zhao, Z. Huang, I. Mondragon-Shem, and J. Koch. "Computer-aided quantization and numerical analysis of superconducting circuits". In: *New Journal of Physics* 24.10 (Nov. 2022), p. 103020. DOI: 10.1088/1367-2630/ac94f2 (cit. on pp. 158, 159).

[315] D. C. McKay, C. J. Wood, S. Sheldon, J. M. Chow, and J. M. Gambetta. "Efficient Z gates for quantum computing". In: *Phys. Rev. A* 96 (2 Aug. 2017), p. 022330. DOI: 10.1103/PhysRevA.96.022330 (cit. on p. 158).

[316] C. E. Murray, J. M. Gambetta, D. T. McClure, and M. Steffen. "Analytical Determination of Participation in Superconducting Coplanar Architectures". In: *IEEE Transactions on Microwave Theory and Techniques* 66.8 (2018), pp. 3724–3733. DOI: 10.1109/TMTT.2018.2841829 (cit. on pp. 166, 167).

[317] R. N. Simons. *Coplanar waveguide circuits, components, and systems*. John Wiley & Sons, 2004 (cit. on p. 166).

[318] A. Melville, G. Calusine, W. Woods, K. Serniak, E. Golden, B. M. Niedzielski, et al. “Comparison of dielectric loss in titanium nitride and aluminum superconducting resonators”. In: *Applied Physics Letters* 117.12 (Sept. 2020), p. 124004. DOI: 10.1063/5.0021950 (cit. on p. 166).

[319] C. E. Murray. “Analytical Modeling of Participation Reduction in Superconducting Coplanar Resonator and Qubit Designs Through Substrate Trenching”. In: *IEEE Transactions on Microwave Theory and Techniques* 68.8 (2020), pp. 3263–3270. DOI: 10.1109/TMTT.2020.2995894 (cit. on p. 166).

[320] A. P. M. Place, L. V. H. Rodgers, P. Mundada, B. M. Smitham, M. Fitzpatrick, Z. Leng, et al. “New material platform for superconducting transmon qubits with coherence times exceeding 0.3 milliseconds”. In: *Nature Communications* 12.1 (2021), p. 1779. DOI: 10.1038/s41467-021-22030-5 (cit. on p. 166).

[321] K. D. Crowley, R. A. McLellan, A. Dutta, N. Shumiya, A. P. M. Place, X. H. Le, et al. “Disentangling Losses in Tantalum Superconducting Circuits”. In: *Phys. Rev. X* 13 (4 Oct. 2023), p. 041005. DOI: 10.1103/PhysRevX.13.041005 (cit. on p. 166).

[322] G. Marcaud, D. Perello, C. Chen, E. Umbarkar, C. Weiland, J. Gao, et al. “Low-loss superconducting resonators fabricated from tantalum films grown at room temperature”. In: *Communications Materials* 6.1 (2025), p. 182. DOI: 10.1038/s43246-025-00897-x (cit. on p. 166).

[323] T. A. van Schijndel, A. P. McFadden, A. N. Engel, J. T. Dong, W. J. Yánez-Parreño, M. Parthasarathy, et al. “Cryogenic growth of tantalum thin films for low-loss superconducting circuits”. In: *Phys. Rev. Appl.* 23 (3 Mar. 2025), p. 034025. DOI: 10.1103/PhysRevApplied.23.034025 (cit. on p. 166).

[324] M. Grassl, T. Beth, and T. Pellizzari. “Codes for the quantum erasure channel”. In: *Phys. Rev. A* 56 (1 July 1997), pp. 33–38. DOI: 10.1103/PhysRevA.56.33 (cit. on p. 171).

[325] J. D. Teoh, P. Winkel, H. K. Babla, B. J. Chapman, J. Claes, S. J. de Graaf, et al. “Dual-rail encoding with superconducting cavities”. In: *Proceedings of the National Academy of Sciences* 120.41 (2023), e2221736120. DOI: 10.1073/pnas.2221736120 (cit. on p. 171).

[326] Z. Wang, T. Miyamura, Y. Sunada, K. Sunada, J. Ilves, K. Matsuura, et al. “Generation of Frequency-Bin-Encoded Dual-Rail Cluster States via Time-Frequency Multiplexing of Microwave Photonic Qubits”. In: *PRX Quantum* 7 (1 Feb. 2026), p. 010330. DOI: 10.1103/rrct-dpfv (cit. on p. 171).

[327] P. Kurpiers, M. Pechal, B. Royer, P. Magnard, T. Walter, J. Heinsoo, et al. “Quantum Communication with Time-Bin Encoded Microwave Photons”. In: *Phys. Rev. Appl.* 12 (4 Oct. 2019), p. 044067. DOI: 10.1103/PhysRevApplied.12.044067 (cit. on p. 171).

[328] J. Dilley, P. Nisbet-Jones, B. W. Shore, and A. Kuhn. “Single-photon absorption in coupled atom-cavity systems”. In: *Phys. Rev. A* 85 (2 Feb. 2012), p. 023834. DOI: 10.1103/PhysRevA.85.023834 (cit. on p. 172).

[329] A. Almanakly, B. Yankelevich, M. Hays, B. Kannan, R. Assouly, A. Greene, et al. “Deterministic remote entanglement using a chiral quantum interconnect”. In: *Nature physics* 21.5 (2025), pp. 825–830. DOI: 10.1038/s41567-025-02811-1 (cit. on p. 172).